

One-dimensional numerical model for layered shallow water flow in highly stratified estuaries

Krvavica, Nino

Doctoral thesis / Disertacija

2016

Degree Grantor / Ustanova koja je dodijelila akademski / stručni stupanj: **University of Rijeka, Faculty of Civil Engineering in Rijeka / Sveučilište u Rijeci, Građevinski fakultet u Rijeci**

Permanent link / Trajna poveznica: <https://urn.nsk.hr/urn:nbn:hr:157:923959>

Rights / Prava: [Attribution-NonCommercial-NoDerivatives 4.0 International/Imenovanje-Nekomercijalno-Bez prerada 4.0 međunarodna](#)

Download date / Datum preuzimanja: **2024-09-20**



Repository / Repozitorij:

[Repository of the University of Rijeka, Faculty of Civil Engineering - FCERI Repository](#)



UNIVERSITY OF RIJEKA
FACULTY OF CIVIL ENGINEERING

Nino Krvavica

**ONE-DIMENSIONAL NUMERICAL
MODEL FOR LAYERED SHALLOW
WATER FLOW IN HIGHLY
STRATIFIED ESTUARIES**

DOCTORAL THESIS

Supervisor: Prof. Nevenka Ožanić, PhD

Co-supervisor: Assoc. Prof. Vanja Travaš, PhD

Rijeka, 2016

Mentor rada: Prof. dr. sc. Nevenka Ožanić

Komentor rada: Izv. prof. dr. sc. Vanja Travaš

Doktorski rad obranjen je dana _____ na Građevinskom fakultetu Sveučilišta u Rijeci, pred povjerenstvom u sastavu:

1. Izv. prof. dr. sc. Goran Lončar, Građevinski fakultet Sveučilišta u Zagrebu, vanjski član, predsjednik,

2. Doc. dr. sc. Elvis Žic, Građevinski fakultet Sveučilišta u Rijeci, član,

3. Prof. dr. sc. Nevenka Ožanić, Građevinski fakultet Sveučilišta u Rijeci, član i mentorica.

*This thesis is dedicated to the memory of my father
Bruno Krvavica
who always believed in me and inspired me to find pleasure in discovering new things.*

Acknowledgements

Personal

First of all, I would like to express sincere gratitude to my advisor Nevenka Ožanić for giving me the opportunity to join the Faculty of Civil Engineering in Rijeka and for continuous support and encouragement during my PhD study. I would like to thank my co-advisor Vanja Travaš for his time and patience in listening to my research problems and ideas. His advices, comments and careful reviews are greatly appreciated. I am grateful to Nenad Ravlić for introducing me to the exciting world of research and numerical modelling, as well as for his guidance during the first years of my PhD study. I appreciate the time and effort by committee members Goran Lončar and Elvis Žic. Their insightful comments and suggestions improved the quality of this thesis.

I would also like to thank my colleagues from the faculty. I am thankful to Ivica Kožar for his valuable suggestions and assistance in publishing one of my first papers. Suggestions and comments given by Josip Rubinić have also been a great help at various stages of my research. I greatly appreciate both personal and technical advices received from Gordan Jelenić and Željko Arbanas. I am particularly thankful to Igor Ružić for his assistance during several field measurements, but more importantly, for his initial idea to measure and examine the salinity structure in the Rječina River estuary. I especially appreciate the help from Goran Volf, Elvis Žic, Maja Radišić, Miran Tuhtan, Natalija Bede, Nina Čeh, Paulo Šćulac, and Petra Đomlija with an important field measurement at the Rječina River on one extremely hot summer day. Also, a big thank you goes to Leo, Maja, Nikola, Nina, and Vedran for their company and friendship, and for listening to my problems and questions, especially those that had no answers. Petra, there are many ways in which you have helped me, in both private and academic life, but above all, thank you for being such a good friend.

I would like to thank my family – my mother and grandparents – without their support and understanding throughout my education, this would be a much harder journey. And finally, Marina, thank you for your unconditional support, love, and delicious food.

Institutional

This work has been supported by Ministry of Science, Education and Sports of the Republic of Croatia under the project Hydrology of Sensitive Water Resources in Karst (114-0982709-2549) and Research Infrastructure for Campus-based Laboratories at the University of Rijeka (RC.2.2.06-0001), which was co-funded from the European Fund for Regional Development (ERDF). A part of the research was conducted with the help from the bilateral Croatian-Japanese project Risk Identification and Land-use Planning for Disaster Mitigation of Landslides and Floods in Croatia. The support has also been provided in part by the University of Rijeka under the project Hydrology of Water Resources and Risk Identification from Floods and Mudflows in Karst Areas (13.05.1.1.03).

Abstract

A numerical model for simulating freshwater and seawater flow in highly stratified estuaries was developed and validated. The governing equations for one-dimensional, two-layer, and time-dependant shallow water flow were derived from the laws of conservation of mass and linear momentum. The resulting equations are written as a system of non-linear, hyperbolic, partial differential equations. To solve this system, a finite volume method was used; specifically, a well-balanced Q-scheme for two-layer shallow water flow in channels with irregular geometry was extended to resolve additional friction and entrainment terms. Particular emphasis was placed on the selection and validation of appropriate boundary conditions and the numerical treatment of wet-dry transitions.

To assess the performance of the proposed model and examine the main physical processes, a field sampling campaign was conducted during 2014-15 in the Rječina River estuary. Entrainment rates were estimated from observed salinity profiles and flow rates by a two-layer box model. Interfacial friction factors were determined by fitting the numerical results to observed salt-wedge profiles. A steady arrested salt-wedge model, based on a finite difference method, was used for this purpose. When the interfacial friction factor was calibrated, the numerical results agreed favourably against field observations for both steady and variable flow conditions.

The combination of field observations and numerical experiments allowed for a more detailed investigation of the main physical processes in microtidal estuaries. The salt-wedge dynamics in the Rječina River estuary depends mainly on the river flow rate, while the sea-level and channel geometry impose a second-order control. Furthermore, a strong stratification persisted under all observed flow conditions. Finally, none of the existing entrainment and interfacial friction laws proved adequate; therefore, new empirical equations were proposed.

Keywords: *estuaries, salt-wedge, shallow water flow, Q-scheme, finite volume method, stratification, entrainment, interfacial friction.*

Prošireni sažetak

Izrađen je i validiran numerički model za simuliranje tečenja slane i slatke vode u izrazito stratificiranim ušćima. Vladajuće jednačbe za jednodimenzijnski, dvoslojni i nestacionarni tok plitkih voda u koritima nepravilne geometrije, izvedene su iz zakona očuvanja mase i količine gibanja. Rezultirajuće jednačbe čine sustav nelinearnih, hiperboličnih, parcijalnih diferencijalnih jednačbi, a mogu se zapisati u vektorskom obliku kao zakon održanja s izvornim članom.

Za rješavanje navedenih jednačbi koristila se metoda konačnih volumena, odnosno dobro balansirana Q-shema za dvoslojno tečenje u koritima nepravilne geometrije, koja je modificirana kako bi se uključili dodatni članovi koji opisuju trenje i vertikalno miješanje. Posebna pozornost je posvećena validiranju fizikalno relevantnog nizvodnog rubnog uvjeta, definiranog dubinom gornjeg sloja na ušću rijeke ili na mjestima naglog suženja korita. Također je riješen i problem pomicanja fronte donjeg sloja, koji u numeričkom smislu predstavlja prijelaz između suhog i mokrog dijela domene. Numerički model je verificiran za slučaj prizmatičnog korita s ravnim dnom, za koji postoje analitička rješenja te za slučaj neprizmatičnog korita, usporedbom s jednostavnijim stacionarnim numeričkim modelom temeljenim na metodi konačnih razlika, odnosno implicitnoj trapeznoj metodi.

Terenska mjerenja na ušću Rječine provedena su tijekom 2014. i 2015. godine pri različitim razinama mora i protocima rijeke, pri čemu su mjerena fizikalna svojstva vode na nekoliko profila duž ušća. U tu svrhu, prvenstveno su se koristile CTD sonde koje mjere tlak, temperaturu i električnu provodljivost po dubini vode. Iz navedenih podataka izračunati su saliniteti i gustoća vode pomoću poznatih empirijskih izraza. Ulazni protoci određivali su se prema razini vode na pragu uzvodno od ušća, za koji je poznata protočna krivulja. Akustični Dopplerov strujomjer se povremeno koristio kako bi se validirali uzvodni protoci rijeke i izračunate brzine u pojedinim slojevima.

Intenziteti miješanja među slojevima određeni su pomoću dvoslojnog Knudsenovog modela na osnovu izmjerenih protoka i saliniteta vode u svakom sloju. Koeficijenti trenja na razdjelnici slojeva dobiveni su metodom prilagodbe numeričkih rezultata izmjerenim dubinama haloklina duž ušća Rječine. Uz kalibrirane koeficijente trenja, poklapanja numeričkih rezultata i terenskih mjerenja su zadovoljavajuća, što ukazuje na vrlo dobru prognostičku moć predloženog modela u izrazito stratificiranim uvjetima.

Kombinacija terenskih mjerenja i numeričkih simulacija omogućila je detaljniji uvid u relevantne fizikalne procese u izrazito stratificiranim ušćima. Pokazalo se kako protok rijeke ima dominantni utjecaj na dinamiku slanog klina, dok u manjoj mjeri utjecaj imaju razina mora i geometrija korita. Smanjenje protoka rijeke te podizanje morske razine može uzrokovati jači prodor slanog klina uzvodno. Također, tijekom svih mjerenja zabilježena je kontinuirana stratifikacija stupca vode, neovisno o mareografskim i hidrološkim uvjetima.

Postojeći parametrizacijski modeli za intenzitet miješanja u stratificiranim sredinama nisu se pokazali dovoljno pouzdanima na ušću Rječine. Detaljnije analize sugeriraju kako je intenzitet miješanja moguće zadovoljavajuće prognozirati tek na osnovu kombinacije poznatih bezdimenzionalnih parametara toka i koeficijenta trenja. Parametrizacijski modeli za koeficijent trenja na razdjelnici pokazali su se još manje pouzdanima. Analize izmjerenih podataka sugeriraju kako se koeficijent trenja povećava s protokom rijeke, što je u suprotnosti s postojećim saznanjima. Zaključno, predloženi su novi empirijski izrazi za prognoziranje intenziteta miješanja i koeficijenta trenja na razdjelnici u izrazito stratificiranim ušćima.

Ključne riječi: *ušće, slani klin, jednadžba plitkih voda, Q-shema, metoda konačnih volumena, stratifikacija, intenzitet miješanja, koeficijent trenja.*

Contents

1	Introduction	1
1.1	Background and Motivation	2
1.2	Hypothesis	5
1.3	Objective of the thesis	6
1.4	Thesis outline	7
2	Literature review	8
2.1	Two-layer hydraulic theory	9
2.1.1	Arrested salt-wedge models	11
2.1.2	Time-dependant salt-wedge models	12
2.2	Interfacial processes	13
2.2.1	Interfacial friction	14
2.2.2	Entrainment	17
3	Governing equations for two-layer flow in salt-wedge estuaries	20
3.1	Governing equations for time-dependant salt-wedges	21
3.1.1	Conservation of mass	24
3.1.2	Conservation of linear momentum	25
3.1.3	Vector form of the governing equations	31
3.2	Governing equations for arrested salt-wedges	33
3.2.1	System of ODEs for arrested salt-wedges	34
3.2.2	Single ODE for arrested salt-wedges	35
3.2.3	Analytical equation for arrested salt-wedges	36
4	One-dimensional numerical schemes	37
4.1	FDM for arrested salt-wedges	38
4.1.1	Implicit trapezoidal method	38
4.1.2	Boundary conditions for arrested salt-wedges	40
4.1.3	Calibration of the interfacial friction factor λ_i	41
4.2	FVM for time-dependant salt-wedges	41
4.2.1	FVM for hyperbolic conservation laws	42

4.2.2	Godunov method and approximate Riemann solvers	44
4.2.3	Modified Q-scheme for two-layer salt-wedge flow	47
4.2.4	Wet-dry fronts in channels with irregular geometry	55
4.2.5	Boundary conditions for time-dependant salt-wedges	58
5	Numerical model performance assessment	59
5.1	Code verification	60
5.1.1	Comparison with analytical solutions	60
5.1.2	Comparison between FDM and FVM models	61
5.2	Well-balanced property of FVM model	65
5.2.1	Verification of the C-property	65
5.2.2	Verification of the extended C-property	67
5.3	Numerical model sensitivity	69
5.3.1	Influence of interfacial friction	69
5.3.2	Influence of bed friction	70
5.3.3	Influence of entrainment	70
5.3.4	Influence of density ratio	72
6	Field study in the Rječina River estuary	74
6.1	Rječina River	75
6.2	Adriatic Sea	77
6.3	Field observations in the Rječina River estuary	78
6.3.1	Salinity, temperature and density	79
6.3.2	Flow rates and velocities	84
6.4	Knudsen's hydrographic theory	86
6.5	Channel bathymetry	87
6.5.1	Digital terrain model	89
6.5.2	Cross-section geometry parameters	91
7	Application to the Rječina River estuary	93
7.1	Results of arrested salt-wedges	94
7.1.1	Field observations of arrested salt-wedges	94
7.1.2	FDM results of arrested salt-wedges	97
7.1.3	FVM results of arrested salt-wedges	99
7.2	Results of time-dependant salt-wedges	101
7.2.1	Fields observations of time-dependant salt-wedges	102
7.2.2	FVM results of time-dependant salt-wedges	103

8	Discussion of salt-wedge dynamics	107
8.1	Discussion of interfacial processes	108
8.1.1	Entrainment parametrisation	111
8.1.2	Interfacial friction parametrisation	114
8.2	Discussion of hydraulic control	117
8.3	Discussion of stratification strength	118
8.4	Discussion of salt-wedge propagation rates	119
9	Conclusion	121
9.1	Summary	122
9.1.1	Numerical models	122
9.1.2	Salt-wedge dynamics	124
9.2	Future work	127
	Bibliography	128
	Appendices	
A	Additional numerical results	137
	List of abbreviations and symbols	145
	List of Tables	148
	List of Figures	149

1

Introduction

Contents

1.1	Background and Motivation	2
1.2	Hypothesis	5
1.3	Objective of the thesis	6
1.4	Thesis outline	7

Abstract

This chapter gives an introduction to the thesis. A general background and motivation for researching the numerical modelling of highly stratified estuaries is presented. Next, the hypothesis, objectives, and main research questions are stated and discussed. Finally, a short thesis outline is available at the end of the chapter.

1.1 Background and Motivation

Estuaries are transitional areas between river and marine environments. They are influenced by different forcing mechanisms, such as tides, waves, river flows, and even the channel geometry [85]. Freshwater in estuaries flows towards the river mouth over a denser underlying seawater, which intrudes upstream. Depending on the intensity of vertical mixing between these two fluids, estuaries are classified as [30]:

- a) highly stratified estuaries,
- b) partially mixed estuaries,
- c) well-mixed estuaries.

Figure 1.1 illustrates the main differences between these types: (a) *highly stratified estuaries* are characterized by a strong vertical salinity and density stratification, *i.e.*, an upper layer of freshwater separated from a lower layer of seawater by a thin interfacial layer (halocline and pycnocline), (b) *partially mixed estuaries* are characterized by both horizontal and vertical salinity and density gradients, and (c) *well-mixed estuaries* are characterized by horizontal salinity and density gradients and nearly uniform water column.

In this thesis the focus is placed only on highly stratified estuaries, which, according to traditional classification by Hansen and Rattray [42], consist of *salt wedges* and *fjords*. Salt-wedge estuaries are considered the most dynamic and variable of all estuarine systems [36]. They usually develop at the mouths of coastal rivers, where the ratio of river to tidal flow is high enough to maintain a strong density stratification [30]. Highly stratified conditions are therefore preserved by either high river flow rates or weak tidal dynamics. Under ideal conditions, an upper layer of freshwater is separated from a lower seawater wedge by a sharp halocline, with the overriding flow pushing the underlying one towards the river mouth until an equilibrium is achieved between the buoyancy pressure gradient, friction forces, and inertial forces [84]. For steady-flow conditions, *i.e.*, constant sea-levels and river flow rates, a so-called *arrested salt-wedge* is eventually established, where only the upper layer is active. However, because of constant tidal motions, steady states rarely occur in natural estuaries.

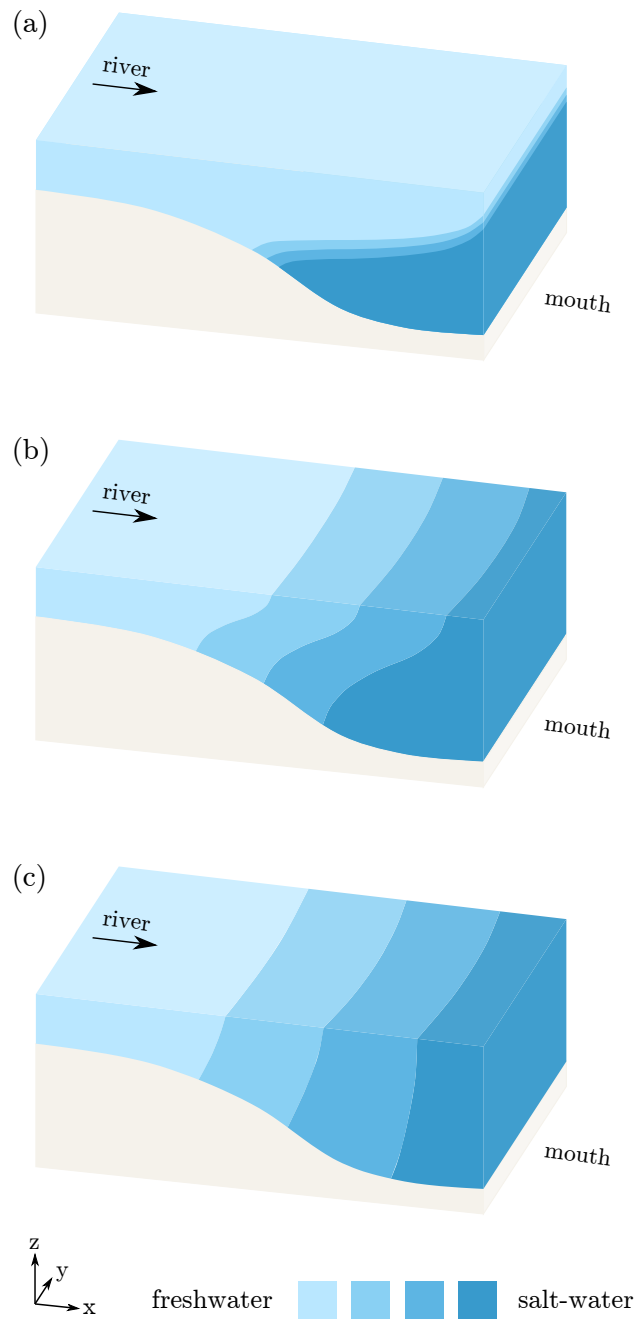


Figure 1.1: Types of estuaries depending on the intensity of vertical mixing: (a) highly stratified estuary, (b) partially mixed estuary, and (c) well-mixed estuary, as described in [30] and [85].

Fjords, on the other hand, are deep estuaries often containing shallow sills that separate them from the ocean. In contrast to salt-wedges, the salinity difference between the upper and lower layer is weaker. They do, however, exhibit similar dynamic characteristics as salt-wedges [36].

Pronounced vertical stratification is found in many salt-wedge estuaries worldwide. Recent studies have focused mostly on *macrotidal* salt-wedge estuaries, such as the Hudson [77], Fraser [64], Merrimack [78], and Snohomish River [104]. In these environments, high river flow rates maintain a strong stratification by suppressing the vertical mixing caused by tidal dynamics. In fact, the salt-wedge structure in the Fraser Estuary is observed only during high river flow rates [64]. Whereas, in microtidal seas, where tidal amplitudes do not exceed 2 m [48], estuaries are highly stratified even for relatively low river flow rates. A typical example of a microtidal salt-wedge estuary is the Ebro River in Spain [48] or Neretva River in Croatia [62].

Understanding physical processes in salt-wedges is important in many engineering and environmental activities, such as predicting the impact of channel dredging or widening in coastal areas, planning freshwater intake positions, defining structural measures for seawater intrusion, or managing pollutant and sediment transport. Furthermore, important agricultural lands are regularly developed around estuaries (*e.g.*, Neretva River in Croatia [62]); therefore, the mechanism of salt-wedge intrusion is not a mere hydraulic curiosity, but an integral part of social and economic development.

The mechanism of salt-wedge dynamics, in particular the bottom layer water renewal, is also important from the ecological and water-quality point of view. The halocline divides an estuary in two regions that differ not only in contrasting salinity, but also in temperature, turbidity, turbulence, and direction of the flow. Furthermore, hypoxic or anoxic conditions may develop in the stagnant lower layer of arrested salt-wedges [36].

Many approaches are available when modelling the dynamics of salt-wedge estuaries, namely: analytical models, empirical equations, one-dimensional (1D), two-dimensional (2D) and three-dimensional (3D) numerical models, as well as laboratory experiments. Today, 3D numerical models are most frequently used to simulate various dynamic estuarine processes [105, 60, 78, 104]; although, their computational cost may sometimes become too expensive for engineering purposes. This is especially true

for salt-wedge estuaries, where a fine vertical discretization is needed to adequately resolve a thin interface between the layers.

Three-dimensional numerical models may be necessary to realistically simulate partially or well-mixed estuaries, where the main physical properties vary in both the vertical and horizontal direction. However, one-dimensional two-layer numerical models should accurately resolve the main physical processes in salt-wedge estuaries if the stratification is strong enough to suppress the vertical mixing, and the interfacial layer is much thinner than the upper and lower layer.

1.2 Hypothesis

Considering the current state of research in coastal and estuarine numerical modelling, the following hypothesis is stated:

Under highly stratified conditions, it is justified to use a one-dimensional two-layer shallow water model to predict the main physical processes in salt-wedge estuaries.

This hypothesis is based on (a) the fact that the vertical exchange between the layers in salt-wedges is minimal compared to the extent of advective processes within each layer [36], (b) current trends in the literature that show how 1D two-layer numerical models accurately capture the main features of the *exchange flow in sea straits*, such as the Strait of Gibraltar [18], and (c) the assumption that salt-wedge estuaries show more similarities to the exchange flow in sea straits than to partially or well-mixed estuaries. The hypothesis was tested by developing a one-dimensional two-layer shallow water model and then comparing numerical solutions against field observations of a salt-wedge in the Rječina River estuary in Croatia.

The main similarity between salt-wedge estuaries and the exchange flow in sea straits is the salinity and density structure characterized by an upper layer of less dense fluid flowing over a lower layer of more dense fluid, which are separated by a thin interfacial layer. There are, however, some notable differences between them. First, salt-wedges are under the influence of many different forcing mechanisms, such as tidal, fluvial, and estuarine. The upper layer in salt-wedge estuaries is usually more active than the lower one, which can be motionless or flow in the same or the opposite direction. The salt-wedge flow, in contrast to the exchange flow in sea straits,

is more sensitive to the interfacial shear stress. And finally, although the vertical mixing in salt-wedge estuaries is reduced by a strong stratification, it may nonetheless exhibit significant influence on the lower layer circulation.

1.3 Objective of the thesis

The objective of this thesis is to develop a 1D two-layer numerical model for simulating the dynamic response of salt-wedge estuaries under the influence of variable river flow rates and sea levels. A good predictive model should only need river flow rate Q , fluid density ρ , and total depth at the mouth H as input parameters. Furthermore, the model should be stable, accurate, and capable of simulating both steady and highly variable flow conditions, including shock propagations.

Considering the hypothesis and objectives of this thesis, the main research question was:

1. How well can a 1D numerical model predict salt-wedge dynamics under various flow conditions?

However, to develop a suitable numerical model, several more practical questions also required an answer:

2. Which boundary conditions should be imposed in a 1D two-layer numerical model for salt-wedge estuaries?
3. How to numerically treat the transition between the wet and dry part of the domain in channels with irregular geometry?
4. How to deal with the possible loss of hyperbolicity when interfacial instabilities appear?
5. How to include and approximate *friction* and *vertical mixing*?

The last question posed additional challenges, not only when approximating these terms in a numerical model, but also when computing interfacial friction factors and entrainment rates based on known flow parameters. Therefore, an additional aim was to critically evaluate the existing parametrization equations for interfacial processes in stratified flow.

1.4 Thesis outline

The thesis is organized as follows. **Chapter 2** presents systematized published studies on salt-wedge estuaries, two-layer numerical models, interfacial friction, and vertical mixing.

Chapter 3 derives a system of governing equations for salt-wedge estuaries represented by a two-layer shallow water flow. **Chapter 4** defines and discusses the numerical schemes used to solve the governing equations. This chapter presents two numerical schemes; the first one is based on a *finite difference method* (FDM), and used to estimate a steady-state flow in arrested salt-wedges, and the second one is based on a *finite volume method* (FVM), and used to solve a time-dependant salt-wedge flow. **Chapter 5** verifies both numerical schemes against analytical models and between each other. Furthermore, it investigates the model sensitivity on the main input parameters, namely friction, entrainment, and density difference. **Chapter 6** describes the Rječina River estuary and provides detailed information on the methodology for field observations of the salinity, temperature, density, flow rate, velocity, and sea level, as well as a method for estimating the vertical mixing.

The results from applying the proposed numerical models on the salt-wedge in the Rječina River estuary are given in **Chapter 7**. The model was validated by comparing the computed salt-wedge profiles against measured interface depths along the estuary under different flow conditions.

Based on a combination of field observations and numerical simulations, **Chapter 8** discusses the key physical processes in microtidal salt-wedge estuaries. An important part of this chapter is the mechanism of interfacial processes and the parametrization of interfacial friction factor λ_i and entrainment rate E .

Finally, **Chapter 9** summarizes and concludes the thesis by presenting key scientific contributions and a list of possible future work topics.

2

Literature review

Contents

2.1	Two-layer hydraulic theory	9
2.1.1	Arrested salt-wedge models	11
2.1.2	Time-dependant salt-wedge models	12
2.2	Interfacial processes	13
2.2.1	Interfacial friction	14
2.2.2	Entrainment	17

Abstract

This chapter presents the literature review of two-layer hydraulic theory and numerical models for salt-wedge estuaries. Furthermore, published studies on interfacial physical processes in stratified environments, namely interfacial friction and entrainment, are also presented and discussed.

2.1 Two-layer hydraulic theory

Two-layer hydraulic theory is based on the *shallow water equations* (SWE) and the assumption that a salt-wedge is adequately represented by two-layers of immiscible fluid separated by a pycnocline of zero thickness. Schijf and Schönfeld [86] and Stommel and Farmer [91] were among first to develop a mathematical theory for two-layer flows in salt-wedge estuaries.

The governing equations, for a two-layer shallow water flow in channels with rectangular cross-sections of constant width (Fig. 2.1), are written as a coupled system of *continuity* and *momentum* equations, as follows [86]:

$$\frac{\partial h_1}{\partial t} + u_1 \frac{\partial h_1}{\partial x} + h_1 \frac{\partial u_1}{\partial x} = 0, \quad (2.1)$$

$$\frac{\partial h_2}{\partial t} + u_2 \frac{\partial h_2}{\partial x} + h_2 \frac{\partial u_2}{\partial x} = 0, \quad (2.2)$$

$$\frac{\partial u_1}{\partial t} + g \frac{\partial h_1}{\partial x} + g \frac{\partial h_2}{\partial x} + u_1 \frac{\partial u_1}{\partial x} + g \frac{db}{dx} + \frac{\tau_i - \tau_s}{\rho_1 h_1} = 0, \quad (2.3)$$

$$\frac{\partial u_2}{\partial t} + r g \frac{\partial h_1}{\partial x} + g \frac{\partial h_2}{\partial x} + u_2 \frac{\partial u_2}{\partial x} + g \frac{db}{dx} + \frac{\tau_b - \tau_i}{\rho_2 h_2} = 0, \quad (2.4)$$

where coordinate x refers to the axis of the channel, t is time, g is acceleration of gravity, h_1 and h_2 are the respective upper and lower layer thickness, u_1 and u_2 are the respective upper and lower layer velocity in the direction of the flow, $r = \rho_1/\rho_2$ is the ratio of the upper ρ_1 to lower ρ_2 layer density, b is the channel bed elevation, and τ_s , τ_i , and τ_b are the respective surface, interface, and channel bed shear stress.

Although Stommel and Farmer [91] suggested some general principles for two-layer flow, it was not until a few decades later that a more systematic theory was presented. Armi and Farmer, in a series of studies [4, 5, 31], further developed the hydraulic theory for two-layer flows. They focused specifically on the issue of flow regimes and the influence of channel contractions, sills, and their combination.

Armi [4] described flow regimes in a two-layer exchange flow similarly as in a single layer. The only difference is that, instead of a regular Froude number $Fr = u_1/\sqrt{gh_1}$, a *composite Froude number* G was used:

$$G^2 = Fd_1^2 + Fd_2^2 - (1 - r)Fd_1^2Fd_2^2, \quad (2.5)$$

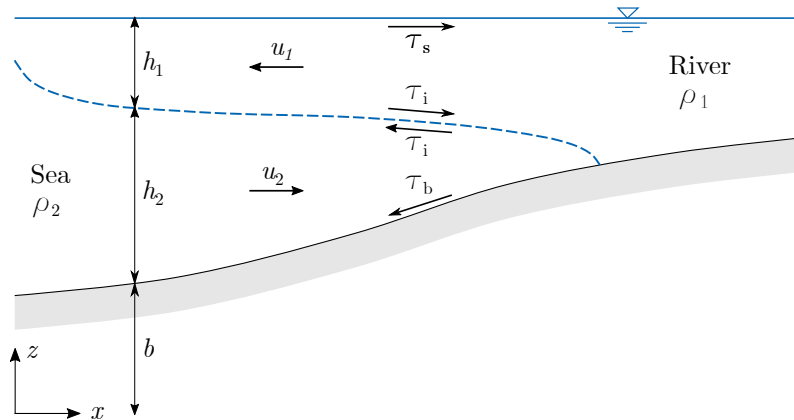


Figure 2.1: Longitudinal scheme of a two-layer salt-wedge flow, as defined by Schijf and Schönfeld [86].

where

$$Fd_1 = \frac{u_1}{\sqrt{g(1-r)h_1}} \quad \text{and} \quad Fd_2 = \frac{u_2}{\sqrt{g(1-r)h_2}} \quad (2.6)$$

are the respective upper and lower layer *densimetric Froude numbers* for channels with rectangular cross-sections. When $G^2 < 1$, the flow is *internally subcritical*, indicating that the baroclinic perturbations, *e.g.*, internal waves, propagate in both directions. On the other hand, when $G^2 > 1$, the flow is *internally supercritical*, and all internal waves propagate only in the downstream direction. The hydraulic control is established at a point where the flow is *internally critical*, which occurs for $G^2 = 1$. In the latter case, a unique relationship exists between the flow rate and the interfacial depth [4]. When only the upper layer is active, the densimetric Froude number $Fd = Fd_1$ is used instead of G .

Armi and Farmer [5] and Farmer and Armi [31] further examined the influence of channel contractions and a combination of sills and contractions in a two-layer exchange flow. They found that a critical condition was established at the narrowest and shallowest section of the channel. However, the presence of relatively strong barotropic flow, such as tides or river waves, may move the position of the hydraulic control upstream or downstream.

Although these findings are true for flows in sea straits, in which both layers are equally active and flow in opposite directions, they also apply for salt-wedge

flows [73]. Pawlak and Armi [73] examined in more details two-layer hydraulics in salt-wedge estuaries, and found that the friction may also influence the exact position of the hydraulic control. In particular, increased friction may move the control downstream from the narrowest section.

2.1.1 Arrested salt-wedge models

Early investigators used the two-layer theory to develop simple analytical models and predict the arrested salt-wedge intrusion length [43, 91]. These models were derived from SWE (2.1)-(2.4) by assuming a prismatic channel, rectangular cross-sections, and horizontal bed slope, as well as neglecting lower layer dynamics and bed friction. Under these assumptions, the salt-wedge length L was found to be a function of interfacial friction factor λ_i and river densimetric Froude number F_0 [43]:

$$L = \frac{H_0}{4\lambda_i} \left(3F_0^{2/3} - \frac{6}{5}F_0^{4/3} - 2 + \frac{1}{5}F_0^{-2} \right), \quad (2.7)$$

with $F_0 = u_0/\sqrt{g(1-r)H_0}$, where u_0 and H_0 are the respective river velocity and depth, upstream from the salt-wedge tip.

In subsequent years, various authors extended and improved these simple arrested salt-wedge models. Rattray and Mitsuda [79] developed a 1D steady two-layer model, which accounts for bed slope and bed friction. Dermissis and Partheniades [29] also considered the interfacial and bed friction, and they analysed dominant shear stresses in arrested salt-wedges.

Balloffet and Borah [7] developed a 1D steady two-layer numerical model by including the interfacial and bed friction, and assuming that a river channel can be represented by a series of rectangular cross-sections with variable widths. They found that, when λ_i is calibrated, the model accurately predicts the arrested salt-wedge length in the Mississippi River.

Arita and Jirka [2, 3] extended the existing models to include the bed friction, vertical mixing, and lower layer convective acceleration. In this way the circulation in the lower layer, that occurs as a results of mixing, was included. Furthermore, they proposed a semi-empirical friction model, which links the entrainment rate E with λ_i . Grubert [40, 41] developed a similar model to Arita and Jirka's by considering

turbulent mixing, which allowed for the momentum transport in both directions, from the lower layer to the upper one, and *vice versa*.

Finally, Sorgard [88] found that the thickness of the interfacial layer increases with the intensity of vertical mixing. Sorgard, therefore, developed a 1D three-layer numerical model, that includes the interfacial, bed and wind shear stress, mixing between the layers, and rectangular cross-sections of variable width. Sorgard [88] also found a good agreement between the three-layer model and field observations in the Glomma River estuary in Norway. Hogg *et al.* [46] further extended Sorgard's model to allow densities in the interfacial layer to vary according to the intensity of vertical mixing.

Unfortunately, arrested salt-wedge models have limited application in field conditions, and only time-dependant models can adequately capture all relevant physical processes in salt-wedge estuaries.

2.1.2 Time-dependant salt-wedge models

Dazzi and Tomasino [28] extended the Schijf and Schönfeld's theory [86], and developed a first 1D time-dependent two-layer numerical model to study salt-wedge dynamics in the Po River. Although their model described the main features of the tidal flow, it neglected the convective acceleration terms in the momentum equations.

Since then, several two-layer models solving full SWE successfully simulated the salt-wedge dynamics under gradually changing flow conditions. Sierra *et al.* [87] used a commercial MIKE 12 model to simulate salt-wedge dynamics in the Ebro River estuary. The model was calibrated with field observations and reproduced a general behaviour of the estuary, especially the salt-wedge intrusion length. Ljubenkovic and Vranješ [62] developed a 1D two-layer numerical model based on a *finite element method* (FEM) and successfully applied it to the Neretva River [62] and Jadro River [61] estuaries in Croatia. Liu *et al.* [59] applied a 1D two-layer numerical model based on a FDM and analysed the salt-water intrusion in the Shinkawa River in Japan. Although these models show good agreement with field observations for gradual changes in tidal and river flows, they are not shock-capturing; therefore, they are unable to correctly describe internally transcritical flows, which may occur under highly dynamic conditions at the mouth, sills, or channel contractions [5, 31].

Recently, several studies presented and discussed shock-capturing numerical models for single-layer shallow water flows, which were based on a FVM and a well-balanced Q -scheme [9, 101]. Castro *et al.* [18] extended these models and presented a general formulation for a 1D two-layer exchange flow in channels with irregular geometry. Their model was successfully validated against analytical steady-state solutions [18], and used to simulate the exchange flow through the Strait of Gibraltar. The numerical solutions agreed favourably with the observed data, especially for the propagation of internal bores [19].

Two-dimensional two-layer shallow water models can also resolve irregular and variable channel geometry (*e.g.*, [57]). However, in regulated channels, such as the Rječina River estuary, average cross-section widths are fairly uniform and the flow is mainly unidirectional; hence, a simpler 1D two-layer model that accounts for irregular cross-sections of the channel should be adequate.

2.2 Interfacial processes

The *stratification* and the stability of *internal waves* govern the interfacial processes in stratified flows [1]. The stratification is especially important in estuarine environments because it controls the intensity of vertical mixing. In fact, strong stratification may reduce vertical mixing by several orders of magnitude [90]. Reduced mixing in highly stratified estuaries, however, usually results in much stronger vertical shear stresses in comparison to partially or well-mixed estuaries [36]. Although vertical mixing is suppressed by stratification, strong shear stress at the interface is known to locally intensify turbulent production and mixing between the layers through the formation of Kelvin-Helmholtz (K-H) instabilities [64].

The stability of internal waves govern both the shear stress and the vertical mixing. For low and stable flow conditions, the interface between layers remains smooth and laminar. When the freshwater velocity rises, internal waves form at the interface, which increases the apparent roughness. If the velocity exceeds a certain value, stability is compromised, and the internal waves brake and generate mixing, causing an interfacial layer to develop. Once a stable interfacial layer is established, density and velocity gradients become weaker, internal waves stabilize, and the turbulent mixing is reduced. The interfacial shear stress varies according

to the stage of the interfacial layer development under the influence of turbulence generated at the bed and the interface [1].

Vertical mixing in two-layer flow is classified either as *entrainment* or *turbulent mixing* [15]. When the interfacial layer is in a subcritical state, *entrainment mixing* takes place. If one of the layers is non-turbulent, the one-way process occurs from a non-turbulent to a turbulent layer (*pure entrainment*). If both layers are turbulent, a two-way process occurs, usually called *net entrainment*, which is computed as the difference between the rate of upward and downward entrainment. *Turbulent mixing* occurs when the interfacial layer is in a critical or supercritical state, with equal amounts of fluid being exchanged between the layers [41]. Sargent and Jirka [84] found that the turbulent energy in salt-wedges is larger in freshwater layer than in the underlying salt-water wedge. This difference results in entrainment directed from the lower to the upper layer.

Recent findings [64] suggest that turbulent production and mixing in salt-wedge estuaries are adequately described by the respective interfacial friction factor λ_i and entrainment rate E . The key question, however, is how to quantify these factors based on known flow parameters? The following subsections explore the existing equations for λ_i and E in more details.

2.2.1 Interfacial friction

The quadratic friction law defines the interfacial shear stress τ_i as

$$\tau_i = \lambda_i \rho_1 \Delta u^2, \quad (2.8)$$

where λ_i is the interfacial friction factor (equal to 1/8 of the Darcy-Weisbach friction factor f), ρ_1 is the upper layer fluid density, and $\Delta u = u_1 - u_2$ is the difference between the upper and lower layer velocities.

A comprehensive review of λ_i is given by Karelse *et al.* [51], Abraham *et al.* [1], and Arita and Jirka [2]. Many attempts have been made to combine data from different sources and find the dependence of λ_i on flow parameters. Notable examples [51, 94, 2] considered a densimetric Froude number Fd , Reynolds number $Re = u_1 R_{h,1} / \nu$ (where $R_{h,1}$ is hydraulic radius and ν is kinematic viscosity), or Keulegan number $K = Re Fd^2$. Unfortunately, because of extensive data scattering around the proposed equations, a commonly accepted friction law is still not established.

Based on laboratory experiments, several authors [43, 1] found that λ_i reduces with increasing Re . Those experiments, however, are valid only for laminar flow and small Re , and therefore are unsuitable for field conditions.

Lofquist [63] carried out extensive experiments in stratified flow, where Re ranged from 10^3 to 10^4 . His results suggest that interfacial shear stress depends both on Re and Fd . The experiments also showed that both *turbulent* τ_T and *viscous* τ_V shear stress contribute to the total interfacial shear stress τ_i , and that the turbulent contribution increases with Re and Fd .

Tamai [94] compiled laboratory and field data from several estuaries in Japan and proposed that λ_i is proportional to $(ReFd^5)^{-1/2}$. The scattering of the compiled data, however, was too extensive, especially at large Re .

Dermissis and Partheniades [29] found that correlating λ_i with either Re , Fd , or K resulted in wide scattering of the observed data. They minimized the scattering by linking λ_i with $ReFr^2$, with additional independent parameter $\Delta\rho/\rho$. Similarly to previous studies, the proposed constitutive model lacked validation at large Re .

Arita and Jirka [2] assumed that λ_i is proportional to E , and proposed a new semi-empirical friction model (Fig. 2.2). The equation (2.9) consisted of laminar (viscous) and turbulent contribution, and was probably inspired by the *Moody diagram* for friction flows in pipes [68]. As the viscous shear stress is dominant for $Re < 10^4$, Eq. (2.9) suggests that λ_i is reduced as Re increases. Namely, when Re increases, the flow becomes more turbulent, and τ_T and τ_V become equally important; hence, λ_i should be a function of both Re and Fd . As Re increases even further, τ_T becomes dominant, and λ_i gradually becomes independent from Re and increases with Fd . Arita and Jirka [2] proposed the following equations to be solved:

$$\lambda_i = 0.076 \left(1 - \frac{Ri}{\sqrt{Ri^2 + Ri_{cr}^2}} \right) + \frac{2}{Re} \frac{z_1}{\delta_u}, \quad (2.9)$$

with

$$\frac{\delta_u}{z_1} = \left(\frac{500}{Re} \right)^{1/2} + \frac{Ri_{cr}}{\sqrt{Ri^2 + Ri_{cr}^2}} \left[1 - \left(\frac{500}{Re} \right)^{1/2} \right], \quad (2.10)$$

where $Ri_{cr} = 1/4$ is the critical Richardson number and Ri is the bulk Richardson number, defined as

$$Ri = \frac{g(1-r)h_1}{\Delta u^2}. \quad (2.11)$$

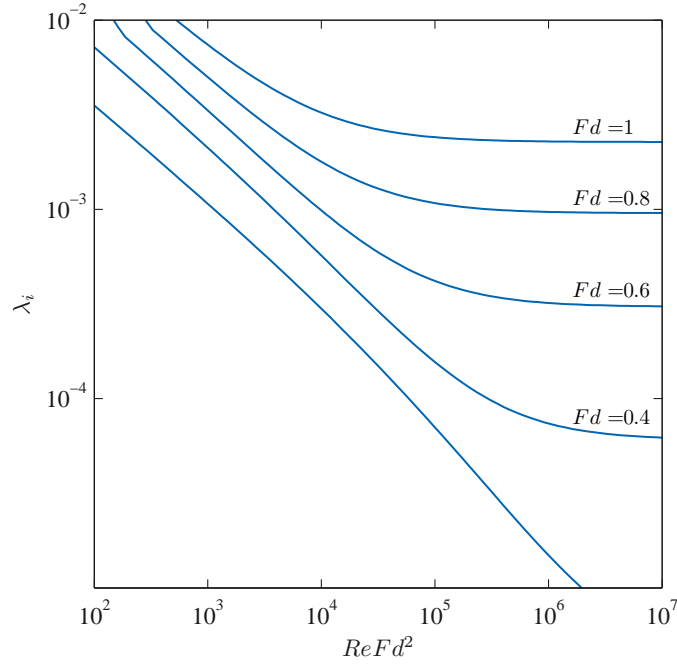


Figure 2.2: Arita and Jirka’s [2] friction law; interfacial friction factor λ_i dependence on $ReFd^2$.

Note that for the arrested salt wedge, $u_2 \approx 0$; therefore, $\Delta u \approx u_1$ and $Ri \approx Fd^{-2}$.

Arita and Jirka [2] acknowledged, however, that the dependence of λ_i on governing parameters for the transition between the laminar and turbulent states is purely empirical. Furthermore, Sargent and Jirka [84] found surprisingly high viscous contribution in the total stress in their salt-wedge experiments. They suggested that the stratified flow may experience *local laminarization* at the interface even at large Re numbers, which makes the efforts to derive a suitable parametrization even more complicated. Although the model by Arita and Jirka (Fig. 2.2) shows good agreement with laboratory data, it suffers from insufficient data sets from the field, which are needed to instil more confidence and assess its accuracy for large Reynolds numbers ($Re > 10^4$).

Field studies are scarce, unfortunately, and they are usually limited to only a few single values (*e.g.*, [89, 64, 62, 61]). The main difficulties in obtaining a relevant set of λ_i from the field can be identified in (a) time-dependent flow conditions in natural estuaries, (b) inability to conduct measurements under systematic variation of the main flow parameters, and (c) high sensitivity of λ_i to the slope of the interface, which can sometimes be difficult to accurately measure in the field.

In recent years, many authors [76, 46] who studied two-layer models showed that numerical solutions are sensitive to λ_i , and that more field measurements are needed to validate existing friction equations [88, 35]. Unfortunately, since Arita and Jirka in 1987 [2] no attempts were made to derive a suitable parametrisation of interfacial friction factor, and no additional data sets from the field were provided to re-evaluate existing equations.

2.2.2 Entrainment

A good review of entrainment in stratified flows can be found in [26, 40, 32]. Earlier studies mainly focused on the entrainment parametrization, *i.e.*, the relationship between the governing non-dimensional parameters, such as Fd or Ri , and entrainment rate E , defined as

$$E = \frac{w_e}{\Delta u}, \quad (2.12)$$

where w_e is the entrainment velocity.

Christodoulou [26] compiled the data from previous experiments on mixing in stratified flows. Based on flow regimes he proposed different equations; for low Ri , entrainment rate was found to be constant, but as Ri increases, different power law dependencies were found between E and Ri , depending on the mixing mechanism. All entrainment equations suggest that E reduces with increasing Ri , so that

$$E \propto Ri^{-a}, \quad (2.13)$$

where a is a positive power law coefficient, which varies according to the flow regime.

Fernando [32] reviewed numerous published entrainment equations, including the ones by Christodoulou [26], and found little or no consensus between them. Furthermore, depending on the type of stratified flow, the shear entrainment rate $E_* = w_e/u_*$ is sometimes used instead of E , and the shear Richardson number $Ri_* = g(1-r)h_1/u_*^2$ instead of Ri , where $u_* = \sqrt{\tau/\rho}$ is the shear velocity. Fernando suggested that the question of what form of Richardson number is the most appropriate still seems to be open, even for similar types of flow.

Grubert [41] examined the data from laboratory experiments and the field, and suggested that no reliable entrainment law can be found based on laboratory

experiments alone. In field conditions, the shear stress may become the main source of mixing; not only does it influence the turbulent production, but it can also cause the development of wave instabilities at the interface [41]. Therefore, he proposed to link the entrainment rate with flow parameters and the average shear stress, *e.g.*, $E = f(Ri, \lambda)$ or $E = f(Ri, Ri_*)$.

Strang and Fernando [92] studied the turbulent mixing in stratified flow and discovered that for low Richardson number ($Ri < 1.5$) Kelvin-Helmholtz waves develop and entrainment rate is independent from Ri . As Ri increases, a power law dependence of E on Ri is found (similar to Eq. 2.13), and interfacial instabilities gradually change from K-H to asymmetric Holmboe waves ($3.2 < Ri < 5.8$), then to symmetric Holmboe waves ($Ri > 5.8$).

Cenedese and Aduce [24] presented the most recent parametrisation for entrainment rate, which is based on bulk flow parameters. In this study, E is linked to non-dimensional bulk parameters, which were averaged vertically and longitudinally. Based on laboratory and ocean data, they derived the following empirical equation for the entrainment rate based on Fd and Re (Fig. 2.3):

$$E = \frac{\min + AFd^\alpha}{1 + AC(Fd + Fd_0)^\alpha}, \quad (2.14)$$

where the best fit with the experimental and field data was found for $\min = 4 \times 10^{-5}$, $A = 3.4 \times 10^{-3}$, $Fd_0 = 0.51$, $\alpha = 7.18$, and $C = f(Re)$.

Recent studies, however, focused more on the fundamental understanding of the complex interaction between the stratification, interfacial shear, and turbulent mixing [92, 37, 78]. The local strength of stratification is usually quantified by a squared Brunt-Väisälä or *buoyancy frequency* N^2 , defined as follows [90]:

$$N^2 = -\frac{g}{\bar{\rho}} \frac{\partial \rho(z)}{\partial z}, \quad (2.15)$$

where $\bar{\rho}$ is the mean density, and $\rho(z)$ is the density at depth z . The shear S_h can be expressed in the same units (s) as follows [90]:

$$S_h = \frac{\partial u(z)}{\partial z}. \quad (2.16)$$

Shear and stratification influence the turbulent mixing in opposite ways; stronger stratification dampens the turbulent energy, whereas the shear stress initiates the production of the turbulent energy and increases the mixing [90].

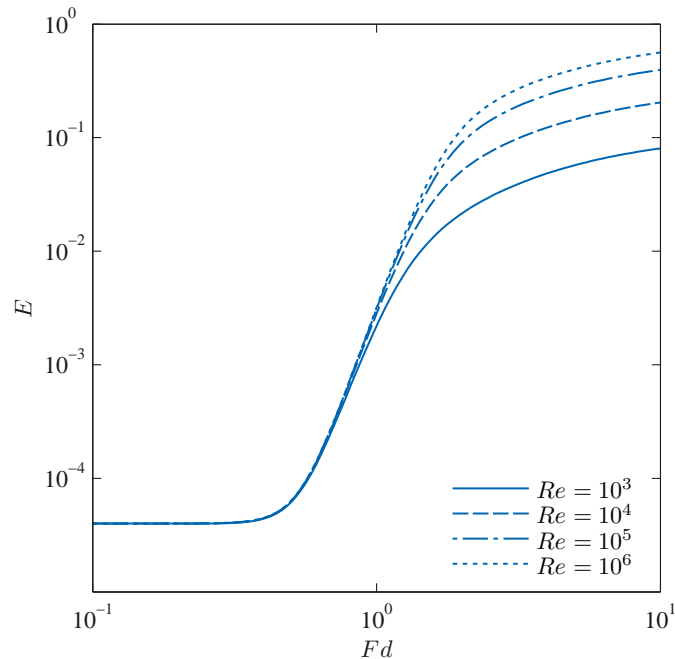


Figure 2.3: Cenedese and Adduce’s [24] entrainment law; entrainment rate E dependence on densimetric Froude number Fd .

The ratio of stratification and shear stress is expressed through the *gradient Richardson number* defined as

$$Ri_g = \frac{N^2}{S_h^2} = -\frac{\frac{g}{\rho} \frac{\partial \rho(z)}{\partial z}}{\left(\frac{\partial u(z)}{\partial z}\right)^2}. \quad (2.17)$$

Gradient Richardson number therefore provides a more physical interpretation of the interfacial dynamics; it represents a ratio of stabilizing to destabilizing forces and indicates whether the flow is prone to instabilities and mixing [90]. As Ri_g increases, the effects of stratification becomes more prominent and the turbulent mixing should be reduced [90].

Numerous studies of interfacial mixing in stratified flows provide valuable insight, but exact mechanisms are not yet completely understood, and quantitative discrepancies are present when the results are combined [32, 50]. While current trends in the literature, which use different turbulence closure schemes, are crucial in understanding the mechanism of turbulent mixing, in many numerical models λ_i and E are still determined from bulk flow parameters. This is especially true in layered shallow water models.

3

Governing equations for two-layer flow in salt-wedge estuaries

Contents

3.1	Governing equations for time-dependant salt-wedges . . .	21
3.1.1	Conservation of mass	24
3.1.2	Conservation of linear momentum	25
3.1.3	Vector form of the governing equations	31
3.2	Governing equations for arrested salt-wedges	33
3.2.1	System of ODEs for arrested salt-wedges	34
3.2.2	Single ODE for arrested salt-wedges	35
3.2.3	Analytical equation for arrested salt-wedges	36

Abstract

This chapter presents the governing equations for time-dependant two-layer shallow water flows in salt-wedge estuaries with irregular geometry, including interfacial friction and entrainment. The resulting equations are written in the vector form as a system of conservation laws with source terms. Furthermore, several simplifications are introduced to derive a system of ordinary differential equations for steady two-layer flows in arrested salt-wedges.

3.1 Governing equations for time-dependant salt-wedges

A one dimensional time-dependant flow was assumed, and the fluid consisted of two layers of different densities. The *partial differential equations* (PDE) for a two-layer salt-wedge flow are written as a coupled system of shallow water equations. These equations, also called the *Saint-Venant equations*, are derived from the law of the conservation of mass and linear momentum. They are applied to each layer of a *control volume* and then averaged over depth [25].

It is appropriate to define the main notations first (Fig. 3.1 and 3.2). The coordinate x refers to the axis of the channel, y is the coordinate normal to the axis, z is the vertical coordinate, and t is time. In general, index $j = 1$ refers to the upper layer, whereas $j = 2$ refers to the lower layer. By describing the two-layer flow by a system of SWE, the following assumptions or simplifications are introduced [25]:

- The flow is one-dimensional along the channel axis x , and velocity $u_j(x, t)$ is uniform over the layer cross-section:

$$u_1(x, t) = \frac{1}{h_1(x, t)} \int_{b+h_2}^{b+h_2+h_1} u(x, z, t) dz,$$

$$u_2(x, t) = \frac{1}{h_2(x, t)} \int_b^{b+h_2} u(x, z, t) dz,$$

where $h_1(x, t)$ and $h_2(x, t)$ are the respective upper and lower layer thickness, and $b(x)$ is the channel bed elevation.

- The density $\rho_j(x, t)$ is also uniform over the layer cross-section:

$$\rho_1(x, t) = \frac{1}{h_1(x, t)} \int_{b+h_2}^{b+h_2+h_1} \rho(x, z, t) dz,$$

$$\rho_2(x, t) = \frac{1}{h_2(x, t)} \int_b^{b+h_2} \rho(x, z, t) dz,$$

- The streamline curvature is small and vertical accelerations are negligible; hence, the pressure $p_j(x, z, t)$ is hydrostatic:

$$p_1(x, z, t) = \rho_1 g (b(x) + h_2(x, t) + h_1(x, t) - z),$$

$$p_2(x, z, t) = \rho_1 g h_1(x, t) + \rho_2 g (b(x) + h_2(x, t) - z),$$

where g is the acceleration of gravity.

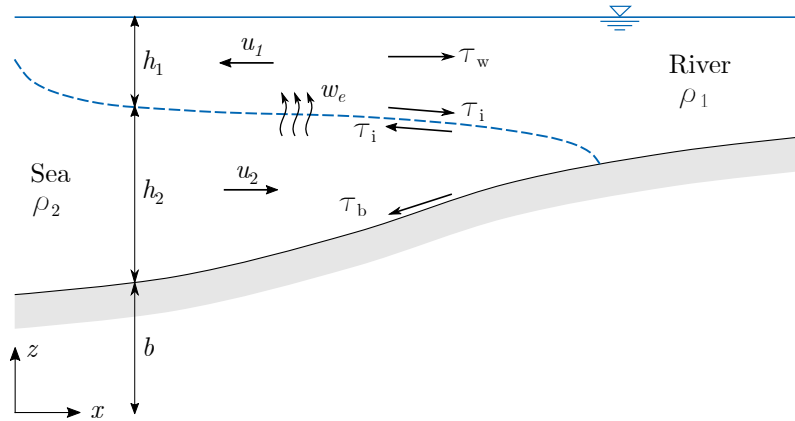


Figure 3.1: Longitudinal scheme of a two-layer salt-wedge flow including friction and entrainment in channels with irregular geometry.

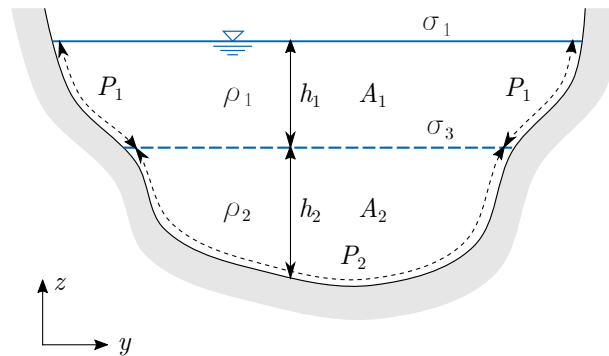


Figure 3.2: Cross-section scheme of a two-layer salt-wedge flow including friction and entrainment in channels with irregular geometry.

- The bottom slope is small enough, so that a cosine of angle θ between the bottom slope and the horizontal is approximated by unity:

$$\cos\theta \approx 1 \quad \text{and} \quad \sin\theta \approx \tan\theta \approx \theta.$$

- Resistance laws adequately estimate viscous effects, *i.e.* friction and turbulence.

In addition to these general assumption, the atmospheric pressure was assumed to be constant and equal to zero, and the surface stress was also assumed to be zero, although this condition can be relaxed if needed.

Furthermore, the respective upper and lower layer cross-section area relates to the layer thickness and width $\sigma(x, z)$, as follows:

$$A_1(x, t) = \int_{b+h_2}^{b+h_2+h_1} \sigma(x, z) dz, \quad (3.1)$$

$$A_2(x, t) = \int_b^{b+h_2} \sigma(x, z) dz. \quad (3.2)$$

The respective surface and interface cross-section width relates to the layer thickness, as follows:

$$\sigma_1(x, t) = \sigma(x, b + h_2 + h_1), \quad (3.3)$$

$$\sigma_3(x, t) = \sigma(x, b + h_2). \quad (3.4)$$

The respective upper and lower layer flow rates are

$$Q_1(x, t) = A_1(x, t)u_1(x, t), \quad (3.5)$$

$$Q_2(x, t) = A_2(x, t)u_2(x, t). \quad (3.6)$$

Finally, the entrainment velocity $w_e(x, t)$ denotes the vertical transport velocity from the lower to the upper layer.

To derive the governing equations for two-layer flow, let us consider a control volume of fluid Ω between two cross-sections (at x_A and x_B), which consists of two fluids of different densities (Fig. 3.3). The cross section surfaces $\Gamma_{A,1}$ and $\Gamma_{B,1}$, interface Γ_i separating the fluids, channel bed/wall Γ_w , and free water surface Γ_s bound the upper layer control volume Ω_1 . The cross section surfaces $\Gamma_{A,2}$ and $\Gamma_{B,2}$, interface Γ_i , and channel bed Γ_b bound the lower layer control volume Ω_2 .

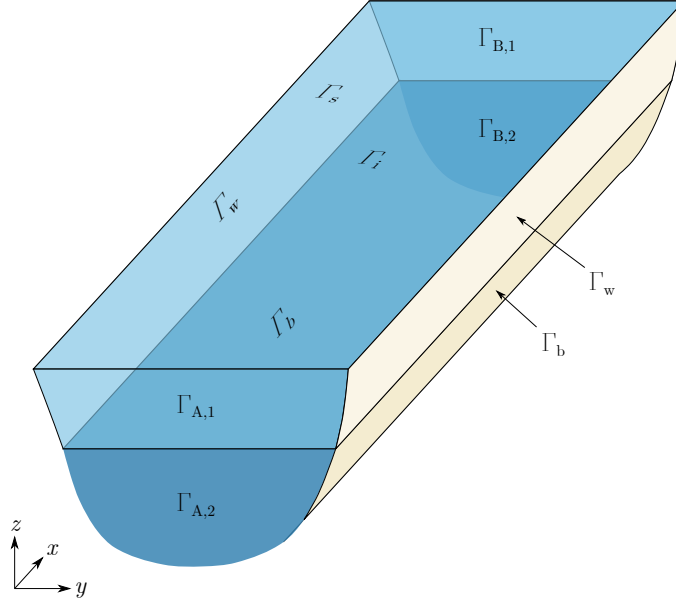


Figure 3.3: Control volume of a two-layer flow in channels with irregular geometry.

3.1.1 Conservation of mass

The law of conservation of mass states that *no mass is generated or annihilated in the volume* Ω , which means that the time rate of change of mass in volume Ω is equal to the net mass flux through the boundaries of the same volume [97].

Upper layer

The integral form of the law of conservation of mass for the upper layer states

$$\begin{aligned} \frac{d}{dt} \int_{\Omega_1} \rho_1 dV = & - \int_{\Gamma_{A,1}} \rho_1 \mathbf{u}_1 \cdot \mathbf{n} dA - \int_{\Gamma_{B,1}} \rho_1 \mathbf{u}_1 \cdot \mathbf{n} dA \\ & - \int_{\Gamma_i} \rho_2 \mathbf{w}_e \cdot \mathbf{n} dA, \end{aligned} \quad (3.7)$$

where the left term is the time rate of change of mass in the upper layer volume Ω_1 , the first term on the right is the mass inflow in the upper layer through boundary $\Gamma_{A,1}$, the second term is the mass outflow from the upper layer through the boundary $\Gamma_{B,1}$, the third term is the mass inflow from the lower to the upper layer through the interface Γ_i , \mathbf{u}_1 is the upper layer velocity vector, \mathbf{w}_e is the entrainment velocity vector, and \mathbf{n} is the outward unit normal vector.

Under one-dimensional framework, Eq. (3.7) is rewritten in the form of linear integrals along the channel axis, from x_A to x_B , as follows:

$$\int_{x_A}^{x_B} \rho_1 \frac{\partial A_1}{\partial t}(x, t) dx = - \int_{x_A}^{x_B} \rho_1 \frac{\partial Q_1}{\partial x}(x, t) dx + \int_{x_A}^{x_B} \rho_2 w_e(x, t) \sigma_3(x, t) dx. \quad (3.8)$$

Assuming that the flow variables are sufficiently smooth, density is constant along the control volume $\rho_j(x, t) = \text{const.}$, and Ω is arbitrary, Eq. (3.8) is divided by ρ_1 and written in differential form as follows:

$$\frac{\partial A_1}{\partial t}(x, t) + \frac{\partial Q_1}{\partial x}(x, t) = \frac{1}{r} w_e(x, t) \sigma_3(x, t). \quad (3.9)$$

where $r = \rho_1/\rho_2$ is the ratio of upper to lower layer density.

The lower layer

Similarly, the integral form of the law of conservation of mass for the lower layer states

$$\begin{aligned} \frac{d}{dt} \int_{\Omega_2} \rho_2 dV = & - \int_{\Gamma_{A,2}} \rho_2 \mathbf{u}_2 \cdot \mathbf{n} dA - \int_{\Gamma_{B,2}} \rho_2 \mathbf{u}_2 \cdot \mathbf{n} dA \\ & - \int_{\Gamma_1} \rho_2 \mathbf{w}_e \cdot \mathbf{n} dA, \end{aligned} \quad (3.10)$$

where \mathbf{u}_2 is the lower layer velocity vector. Equation (3.10) is rewritten in the form of linear integrals along the channel axis as follows:

$$\int_{x_A}^{x_B} \rho_2 \frac{\partial A_2}{\partial t}(x, t) dx = - \int_{x_A}^{x_B} \rho_2 \frac{\partial Q_2}{\partial x}(x, t) dx - \int_{x_A}^{x_B} \rho_2 w_e(x, t) \sigma_3(x, t) dx. \quad (3.11)$$

Again, assuming that the flow variables are sufficiently smooth, density is constant along the control volume $\rho_j(x, t) = \text{const.}$, and Ω is arbitrary, Eq. (3.11) is divided by ρ_2 and written in differential form as follows:

$$\frac{\partial A_2}{\partial t}(x, t) + \frac{\partial Q_2}{\partial x}(x, t) = -w_e(x, t) \sigma_3(x, t). \quad (3.12)$$

3.1.2 Conservation of linear momentum

The law of conservation of linear momentum results from the Newton's second law and states that *the time rate of change of the momentum in the control volume Ω is equal to the total forces acting on the same volume* [97].

Upper layer

The integral form of the law of conservation of linear momentum states

$$\begin{aligned}
 \frac{d}{dt} \int_{\Omega_1} \rho_1 u_1(x, t) dV &= - \int_{\Gamma_{A,1}} \rho_1 u_1(x_A, t) \mathbf{u}_1(x_A, t) \cdot \mathbf{n} dA \\
 &\quad - \int_{\Gamma_{B,1}} \rho_1 u_1(x_B, t) \mathbf{u}_1(x_B, t) \cdot \mathbf{n} dA \\
 &\quad - \int_{\Gamma_i} \rho_1 u_1(x, t) \mathbf{w}_e(x, t) \cdot \mathbf{n} dA \\
 &\quad - \int_{\partial\Omega_1} p_1(x, z, t) n_1 dA + \int_{\partial\Omega_1} \tau_1(x, t) dA,
 \end{aligned} \tag{3.13}$$

where the first term on the left is the time rate of change of the momentum in volume Ω_1 , the first term on the right is the momentum inflow through the boundary $\Gamma_{A,1}$, the second term is the momentum outflow through the boundary $\Gamma_{B,1}$, the third term is the momentum inflow from the lower to the upper layer through the interface Γ_i , the fourth term are the pressure forces, n_1 is the first component of the outward unit vector normal to corresponding surfaces, and the last term are the friction forces due to shear stress $\tau_1(x, t)$.

The pressure terms are defined as follows [18]:

$$\int_{\Gamma_{A,1}} p_1(x, z, t) n_1 dA = -\rho_1 g I_{1,1}(x_A, t), \tag{3.14}$$

$$\int_{\Gamma_{B,1}} p_1(x, z, t) n_1 dA = \rho_1 g I_{1,1}(x_B, t), \tag{3.15}$$

$$\int_{\Gamma_w} p_1(x, z, t) n_1 dA = -\rho_1 g \int_{x_A}^{x_B} I_{2,1}(x, t) dx, \tag{3.16}$$

$$\int_{\Gamma_i} p_1(x, z, t) n_1 dA = \rho_1 g \int_{x_A}^{x_B} h_1(x, t) \sigma_3(x, t) \frac{\partial}{\partial x} (b + h_2) dx, \tag{3.17}$$

$$\int_{\Gamma_s} p_1(x, z, t) n_1 dA = 0, \tag{3.18}$$

where

$$I_{1,1}(x, t) = \int_{b(x)+h_2(x,t)}^{b(x)+h_2(x,t)+h_1(x,t)} [b(x) + h_2(x, t) + h_1(x, t) - z] \sigma(x, z) dz, \tag{3.19}$$

$$I_{2,1}(x, t) = \int_{b(x)+h_2(x,t)}^{b(x)+h_2(x,t)+h_1(x,t)} [b(x) + h_2(x, t) + h_1(x, t) - z] \frac{\partial \sigma}{\partial x}(x, z) dz. \tag{3.20}$$

The shear stresses consist of bed/wall τ_w , interfacial τ_i and surface τ_s shear stress, which are defined either by Manning's equation and roughness coefficient n_M or by quadratic friction law and factor λ , as follows [25]:

$$\begin{aligned}\tau_w &= -\rho_1 g n_M^2 |u_1| u_1 R_{h,1}^{-1/3} \\ &= -\rho_1 \lambda_w |u_1| u_1,\end{aligned}\tag{3.21}$$

$$\tau_i = -\rho_1 \lambda_i |u_1 - u_2| (u_1 - u_2),\tag{3.22}$$

$$\tau_s = 0,\tag{3.23}$$

where λ_w is the bed/wall friction factor, $R_{h,1} = A_1/P_1$ is the upper layer hydraulic radius, and P_1 is the upper layer wetted perimeter.

Under 1D framework, the momentum conservation law for the upper layer (Eq. 3.13) is rewritten in the form of linear integrals along the channel axis as follows:

$$\begin{aligned}\int_{x_A}^{x_B} \rho_1 \frac{\partial Q_1}{\partial t}(x, t) dx &= - \int_{x_A}^{x_B} \rho_1 \frac{\partial(Q_1 u_1)}{\partial x}(x, t) dx \\ &+ \int_{x_A}^{x_B} \rho_1 u_1(x, t) w_e(x, t) \sigma_3(x, t) dx \\ &- \int_{x_A}^{x_B} \rho_1 g \frac{\partial I_{1,1}}{\partial x}(x, t) dx + \int_{x_A}^{x_B} \rho_1 g I_{2,1}(x, t) dx \\ &- \int_{x_A}^{x_B} \rho_1 g h_1(x, t) \sigma_3(x, t) \frac{\partial}{\partial x}(b + h_2) dx \\ &+ \int_{x_A}^{x_B} [\tau_i \sigma_3(x, t) + \tau_w P_2(x, t)] dx.\end{aligned}\tag{3.24}$$

Assuming that the flow variables are sufficiently smooth, density is constant along the control volume $\rho_j(x, t) = \text{const.}$, and Ω is arbitrary, Eq. (3.24) is divided by ρ_1 and written in differential form as follows:

$$\begin{aligned}\frac{\partial Q_1}{\partial t}(x, t) &= - \frac{\partial(Q_1 u_1)}{\partial x}(x, t) + u_1(x, t) w_e(x, t) \sigma_3(x, t) - g \frac{\partial I_{1,1}}{\partial x}(x, t) + g I_{2,1}(x, t) \\ &- g h_1(x, t) \sigma_3(x, t) \frac{\partial}{\partial x}(b + h_2) + \frac{1}{\rho_1} \tau_i \sigma_3(x, t) + \frac{1}{\rho_1} \tau_w P_2(x, t).\end{aligned}\tag{3.25}$$

Equation (3.25) is then rewritten as a function of the conserved variables Q_j and A_j , $j = 1, 2$ and their derivatives. Note that the dependence on x and t will be left out where introduced previously to reduce the excess notation. Also, the friction and entrainment terms are dropped for now and introduced later when the final form is obtained.

First, we rewrite Eq. (3.25) without friction and entrainment terms as follows:

$$\frac{\partial Q_1}{\partial t} + \frac{\partial}{\partial x} \left(\frac{Q_1^2}{A_1} + gI_{1,1} \right) = gI_{2,1} - gh_1\sigma_3 \frac{\partial}{\partial x} (b + h_2). \quad (3.26)$$

Next, Leibniz integral rule [106] for $\partial I_{1,1}/\partial x$ gives

$$\begin{aligned} \frac{\partial I_{1,1}}{\partial x} &= \int_{b+h_2}^{b+h_2+h_1} \frac{\partial}{\partial x} [(b + h_2 + h_1 - z) \sigma(x, z)] dz - h_1\sigma_3 \frac{\partial}{\partial x} (b + h_2) \\ &= \frac{\partial}{\partial x} (b + h_2 + h_1) A_1 + I_{2,1} - h_1\sigma_3 \frac{\partial}{\partial x} (b + h_2), \end{aligned} \quad (3.27)$$

and momentum equation (3.26) is simplified to

$$\frac{\partial Q_1}{\partial t} + \frac{\partial}{\partial x} \left(\frac{Q_1^2}{A_1} \right) = -gA_1 \frac{\partial}{\partial x} (b + h_2 + h_1). \quad (3.28)$$

Again, Leibniz rule for derivatives of Eq. (3.1) and (3.2) gives

$$\begin{aligned} \frac{\partial A_1}{\partial x} &= \int_{b+h_2}^{b+h_2+h_1} \frac{\partial \sigma}{\partial x}(x, z) dz + \sigma_1 \frac{\partial}{\partial x} (b + h_2 + h_1) - \sigma_3 \frac{\partial}{\partial x} (b + h_2) \\ &= I_{3,1} + \sigma_1 \frac{\partial h_1}{\partial x} + (\sigma_1 - \sigma_3) \frac{\partial}{\partial x} (b + h_2), \end{aligned} \quad (3.29)$$

and

$$\begin{aligned} \frac{\partial A_2}{\partial x} &= \int_b^{b+h_2} \frac{\partial \sigma}{\partial x}(x, z) dz + \sigma_3 \frac{\partial}{\partial x} (b + h_2) \\ &= I_{3,2} + \sigma_3 \frac{\partial}{\partial x} (b + h_2), \end{aligned} \quad (3.30)$$

where

$$I_{3,1} = \int_{b+h_2}^{b+h_2+h_1} \frac{\partial \sigma}{\partial x}(x, z) dz, \quad (3.31)$$

$$I_{3,2} = \int_b^{b+h_2} \frac{\partial \sigma}{\partial x}(x, z) dz, \quad (3.32)$$

therefore, we have

$$\frac{\partial h_1}{\partial x} = \frac{1}{\sigma_1} \frac{\partial A_1}{\partial x} - \frac{1}{\sigma_1} \left[I_{3,1} + (\sigma_1 - \sigma_3) \frac{\partial}{\partial x} (b + h_2) \right], \quad (3.33)$$

and

$$\frac{\partial h_2}{\partial x} = \frac{1}{\sigma_3} \left(\frac{\partial A_2}{\partial x} - I_{3,2} \right) - \frac{db}{dx}. \quad (3.34)$$

Using Eqs. (3.33) and (3.34) and after some calculation the momentum equation (3.28) reads

$$\frac{\partial Q_1}{\partial t} + \frac{\partial}{\partial x} \left(\frac{Q_1^2}{A_1} \right) = -\frac{gA_1}{\sigma_1} \frac{\partial}{\partial x} (A_1 + A_2) + \frac{gA_1}{\sigma_1} (I_{3,1} + I_{3,2}), \quad (3.35)$$

and, finally, we can write the conservative differential form of the upper layer momentum equation and introduce back the friction and entrainment terms, as follows:

$$\begin{aligned} \frac{\partial Q_1}{\partial t} + \frac{\partial}{\partial x} \left(\frac{Q_1^2}{A_1} + \frac{gA_1^2}{2\sigma_1} \right) = & - \frac{gA_1}{\sigma_1} \frac{\partial A_2}{\partial x} + \frac{gA_1^2}{2} \frac{\partial}{\partial x} \left(\frac{1}{\sigma_1} \right) + \frac{gA_1}{\sigma_1} (I_{3,1} + I_{3,2}) \\ & + \frac{1}{\rho_1} \tau_i \sigma_3 + \frac{1}{\rho_1} \tau_w P_2 + \frac{Q_1}{A_1} w_e \sigma_3. \end{aligned} \quad (3.36)$$

The lower layer

The integral form of the law of conservation of linear momentum for the lower layer states

$$\begin{aligned} \frac{d}{dt} \int_{\Omega_2} \rho_2 u_2(x, t) dV = & - \int_{\Gamma_{A,2}} \rho_2 u_2(x_A, t) \mathbf{u}_2(x_A, t) \cdot \mathbf{n} dA \\ & - \int_{\Gamma_{B,2}} \rho_2 u_2(x_B, t) \mathbf{u}_2(x_B, t) \cdot \mathbf{n} dA \\ & - \int_{\Gamma_i} \rho_2 u_2(x, t) \mathbf{w}_e(x, t) \cdot \mathbf{n} dA \\ & - \int_{\partial\Omega_2} p_2(x, z, t) n_1 dA + \int_{\partial\Omega_2} \tau_2(x, t) dA. \end{aligned} \quad (3.37)$$

The pressure terms in the lower layer are defined as follows [18]:

$$\int_{\Gamma_{A,2}} p_2(x, z, t) n_1 dA = -\rho_1 g h_1(x_A, t) A_2(x_A, t) - \rho_2 g I_{1,2}(x_A, t), \quad (3.38)$$

$$\int_{\Gamma_{B,2}} p_2(x, z, t) n_1 dA = \rho_1 g h_1(x_B, t) A_2(x_B, t) + \rho_2 g I_{1,2}(x_B, t), \quad (3.39)$$

$$\int_{\Gamma_b} p_2(x, z, t) n_1 dA = -\rho_1 g \int_{x_A}^{x_B} h_1(x, t) I_{3,2}(x, t) dx - \rho_2 g \int_{x_A}^{x_B} I_{2,2}(x, t) dx \quad (3.40)$$

$$\int_{\Gamma_i} p_2(x, z, t) n_1 dA = -\rho_1 g \int_{x_A}^{x_B} h_1(x, t) \sigma_3(x, t) \frac{\partial}{\partial x} (b + h_2) dx, \quad (3.41)$$

where

$$I_{1,2}(x, t) = \int_b^{b+h_2} [b(x) + h_2(x, t) - z] \sigma(x, z) dz, \quad (3.42)$$

$$I_{2,2}(x, t) = \int_b^{b+h_2} [b(x) + h_2(x, t) - z] \frac{\partial \sigma}{\partial x}(x, z) dz, \quad (3.43)$$

$$I_{3,2}(x, t) = \int_b^{b+h_2} \frac{\partial \sigma}{\partial x}(x, z) dz. \quad (3.44)$$

The shear stresses consist of τ_i (Eq. 3.22) and bed shear stress τ_b , defined as [25]:

$$\begin{aligned} \tau_b = & -\rho_2 g n_M^2 |u_2| u_2 R_{h,2}^{-1/3} \\ = & -\rho_2 \lambda_b |u_2| u_2, \end{aligned} \quad (3.45)$$

where λ_b is the bed friction factor, $R_{h,2} = A_2/P_2$ is the lower layer hydraulic radius, and P_2 is the lower layer wetted perimeter.

The momentum conservation law for the lower layer (Eq. 3.37) is rewritten in the form of linear integrals along the channel axis as follows:

$$\begin{aligned}
 \int_{x_A}^{x_B} \rho_2 \frac{\partial Q_2}{\partial t}(x, t) dx &= - \int_{x_A}^{x_B} \rho_2 \frac{\partial Q_2 u_2}{\partial x}(x, t) dx \\
 &\quad - \int_{x_A}^{x_B} \rho_2 u_2(x, t) w_e(x, t) \sigma_3(x, t) dx \\
 &\quad - \int_{x_A}^{x_B} \rho_1 g \frac{\partial(h_1 A_2)}{\partial x}(x, t) dx - \int_{x_A}^{x_B} \rho_2 g \frac{\partial I_{1,2}}{\partial x}(x, t) dx \\
 &\quad + \int_{x_A}^{x_B} \rho_1 g h_1(x, t) I_{3,2}(x, t) dx + \int_{x_A}^{x_B} \rho_2 g I_{2,2}(x, t) dx \\
 &\quad + \int_{x_A}^{x_B} \rho_1 g h_1(x, t) \sigma_3(x, t) \frac{\partial}{\partial x}(b + h_2) dx \\
 &\quad + \int_{x_A}^{x_B} [\tau_b P_2(x, t) - \tau_i \sigma_3(x, t)] dx.
 \end{aligned} \tag{3.46}$$

Assuming that the flow variables are sufficiently smooth, density is constant along the control volume $\rho_j(x, t) = \text{const.}$, and Ω is arbitrary, Eq. (3.46) is divided by ρ_2 and written in differential form as follows:

$$\begin{aligned}
 \frac{\partial Q_2}{\partial t}(x, t) &= - \frac{\partial(Q_2 u_2)}{\partial x}(x, t) - u_2(x, t) w_e(x, t) \sigma_3(x, t) - r g \frac{\partial(h_1 A_2)}{\partial x}(x, t) \\
 &\quad - g \frac{\partial I_{1,2}}{\partial x}(x, t) + r g h_1(x, t) I_{3,2}(x, t) + g I_{2,2}(x, t) \\
 &\quad + r g h_1(x, t) \sigma_3(x, t) \frac{\partial}{\partial x}(b + h_2) + \frac{1}{\rho_2} \tau_b P_2(x, t) - \frac{1}{\rho_2} \tau_i \sigma_3(x, t).
 \end{aligned} \tag{3.47}$$

Once more, Eq. (3.47) is rewritten as a function of conserved variables Q_j and A_j , $j = 1, 2$ and their derivatives only. Note that the dependence on x and t is, again, left out where introduced previously to reduce the excess notation. Also, the friction and entrainment terms are dropped for now and introduced later when the final form is obtained.

First, Eq. (3.47) is rewritten as follows:

$$\begin{aligned}
 \frac{\partial Q_2}{\partial t} + \frac{\partial}{\partial x} \left(\frac{Q_2^2}{A_2} + g I_{1,2} \right) &= - r g h_1 \frac{\partial A_2}{\partial x} - r g A_2 \frac{\partial h_1}{\partial x} + r g h_1 I_{3,2} + g I_{2,2} \\
 &\quad + r g h_1 \sigma_3 \frac{\partial}{\partial x}(b + h_2)
 \end{aligned} \tag{3.48}$$

Next, Leibniz rule for $\partial I_{1,2}/\partial x$ gives

$$\begin{aligned}\frac{\partial I_{1,2}}{\partial x} &= \int_b^{b+h_2} \frac{\partial}{\partial x} [(b+h_2-z)\sigma(x,z)] dz \\ &= \frac{\partial}{\partial x} (b+h_2) A_2 + I_{2,2},\end{aligned}\quad (3.49)$$

and momentum equation (3.48) is simplified to

$$\begin{aligned}\frac{\partial Q_2}{\partial t} + \frac{\partial}{\partial x} \left(\frac{Q_2^2}{A_2} \right) &= -gA_2 \frac{\partial}{\partial x} (b+h_2) - rgh_1 \frac{\partial A_2}{\partial x} - rgA_2 \frac{\partial h_1}{\partial x} \\ &\quad + rgh_1 I_{3,2} + rgh_1 \sigma_3 \frac{\partial}{\partial x} (b+h_2).\end{aligned}\quad (3.50)$$

Using the definitions for $\partial h_1/\partial x$ (Eq. 3.33) and $\partial h_2/\partial x$ (Eq. 3.34), and after some calculation the momentum equation (3.50) reads

$$\begin{aligned}\frac{\partial Q_2}{\partial t} + \frac{\partial}{\partial x} \left(\frac{Q_2^2}{A_2} \right) &= -\frac{gA_2}{\sigma_3} \frac{\partial A_2}{\partial x} - \frac{rgA_2}{\sigma_1} \frac{\partial A_1}{\partial x} + \frac{rgA_2}{\sigma_3} \frac{\partial A_2}{\partial x} - \frac{rgA_2}{\sigma_1} \frac{\partial A_2}{\partial x} \\ &\quad + \frac{rgA_2}{\sigma_1} I_{3,1} + \frac{gA_2}{\sigma_3} I_{3,2} - \frac{rgA_2}{\sigma_3} I_{3,2} + \frac{rgA_2}{\sigma_1} I_{3,2},\end{aligned}\quad (3.51)$$

and, finally, we can write the conservative differential form of the lower layer momentum equation and introduce back the friction and entrainment terms as follows:

$$\begin{aligned}\frac{\partial Q_2}{\partial t} + \frac{\partial}{\partial x} \left(\frac{Q_2^2}{A_2} + \frac{gA_2^2}{2\sigma_2} \right) &= -\frac{rgA_2}{\sigma_1} \frac{\partial A_1}{\partial x} + \frac{gA_2^2}{2} \frac{\partial}{\partial x} \left(\frac{1}{\sigma_2} \right) + \frac{rgA_2}{\sigma_1} I_{3,1} + \frac{gA_2}{\sigma_2} I_{3,2} \\ &\quad + \frac{1}{\rho_2} \tau_b P_2(x,t) - \frac{1}{\rho_2} \tau_i \sigma_3 - \frac{Q_2}{A_2} w_e \sigma_3,\end{aligned}\quad (3.52)$$

where σ_2 is weighted harmonic mean of σ_1 and σ_3 :

$$\frac{1}{\sigma_2} = \frac{1-r}{\sigma_3} + \frac{r}{\sigma_1}.\quad (3.53)$$

3.1.3 Vector form of the governing equations

Equations (3.9), (3.12), (3.36) and (3.52) are written in the vector form as a coupled system of conservation laws with source terms, as follows:

$$\frac{\partial \mathbf{w}}{\partial t} + \frac{\partial \mathbf{f}(\boldsymbol{\sigma}, \mathbf{w})}{\partial x} = \mathbf{B}(\boldsymbol{\sigma}, \mathbf{w}) \frac{\partial \mathbf{w}}{\partial x} + \mathbf{v}(\boldsymbol{\sigma}, \mathbf{w}) + \mathbf{g}(\boldsymbol{\sigma}, \mathbf{w}) + \mathbf{s}(\boldsymbol{\sigma}, \mathbf{w}),\quad (3.54)$$

where \mathbf{w} is the vector of conserved variables:

$$\mathbf{w} = \{A_1 \quad Q_1 \quad A_2 \quad Q_2\}^T,\quad (3.55)$$

vector $\boldsymbol{\sigma}$ contains characteristic channel cross-section widths:

$$\boldsymbol{\sigma} = \left\{ \sigma_1 \quad \sigma_2 \quad \sigma_3 \right\}^T, \quad (3.56)$$

vector $\mathbf{f}(\boldsymbol{\sigma}, \mathbf{w})$ is the flux:

$$\mathbf{f}(\boldsymbol{\sigma}, \mathbf{w}) = \begin{pmatrix} Q_1 \\ \frac{Q_1^2}{A_1} + \frac{g}{2\sigma_1} A_1^2 \\ Q_2 \\ \frac{Q_2^2}{A_2} + \frac{g}{2\sigma_2} A_2^2 \end{pmatrix}, \quad (3.57)$$

and term $\mathbf{B}(\boldsymbol{\sigma}, \mathbf{w}) \frac{\partial \mathbf{w}}{\partial x}$ appears as a result of coupling the two-layer system, where matrix $\mathbf{B}(\boldsymbol{\sigma}, \mathbf{w})$ is defined as

$$\mathbf{B}(\boldsymbol{\sigma}, \mathbf{w}) = \begin{bmatrix} 0 & 0 & 0 & 0 \\ 0 & 0 & -g \frac{A_1}{\sigma_1} & 0 \\ 0 & 0 & 0 & 0 \\ -g \frac{A_2}{\sigma_1} & 0 & 0 & 0 \end{bmatrix}. \quad (3.58)$$

The additional source terms have been split into three parts; the first vector $\mathbf{v}(\boldsymbol{\sigma}, \mathbf{w})$ corresponds to derivatives of $\boldsymbol{\sigma}$:

$$\mathbf{v}(\boldsymbol{\sigma}, \mathbf{w}) = \begin{pmatrix} 0 \\ \frac{g}{2} \frac{\partial}{\partial x} \left(\frac{1}{\sigma_1} \right) A_1^2 \\ 0 \\ \frac{g}{2} \frac{\partial}{\partial x} \left(\frac{1}{\sigma_2} \right) A_2^2 \end{pmatrix}, \quad (3.59)$$

the second vector $\mathbf{g}(\boldsymbol{\sigma}, \mathbf{w})$ corresponds to the channel bed, width, and wetted cross-section area (*i.e.*, irregular geometry):

$$\mathbf{g}(\boldsymbol{\sigma}, \mathbf{w}) = \begin{pmatrix} 0 \\ \frac{gA_1}{\sigma_1} (I_{3,1} + I_{3,2}) \\ 0 \\ \frac{rgA_2}{\sigma_1} I_{3,1} + \frac{gA_2}{\sigma_2} I_{3,2} \end{pmatrix}, \quad (3.60)$$

and the third vector $\mathbf{s}(\boldsymbol{\sigma}, \mathbf{w})$ corresponds to the friction and entrainment:

$$\mathbf{s}(\boldsymbol{\sigma}, \mathbf{w}) = \mathbf{s}_F(\boldsymbol{\sigma}, \mathbf{w}) + \mathbf{s}_E(\boldsymbol{\sigma}, \mathbf{w}), \quad (3.61)$$

$$\mathbf{s}_F(\boldsymbol{\sigma}, \mathbf{w}) = \begin{pmatrix} 0 \\ \frac{\tau_w}{\rho_1} P_1 + \frac{\tau_i}{\rho_1} \sigma_3 \\ 0 \\ \frac{\tau_b}{\rho_2} P_2 - \frac{\tau_i}{\rho_2} \sigma_3 \end{pmatrix}, \quad (3.62)$$

$$\mathbf{s}_E(\boldsymbol{\sigma}, \mathbf{w}) = \begin{Bmatrix} \frac{1}{2}w_e\sigma_3 \\ \frac{Q_1}{A_1}w_e\sigma_3 \\ -w_e\sigma_3 \\ -\frac{Q_2}{A_2}w_e\sigma_3 \end{Bmatrix}. \quad (3.63)$$

Notice that densities in each layer remain constant in time and space, and are unaffected by the entrainment ($\rho_j(x, t) = \text{const.}$, $j = 1, 2$). This assumption is a first step approximation necessary to model the entrainment effects in salt-wedge estuaries, *i.e.*, the circulation in the lower layer in arrested salt wedge and the vertical transfer of momentum for highly dynamic flow conditions. Furthermore, the entrainment is mostly confined to the interfacial layer; although vertical mixing may increase its thickness, the density of the upper and lower layer are rarely affected globally [64].

Before proceeding further, notice that a practical difficulty may appear when solving the integrals appearing in Eq. (3.60). To simplify the computation, the integrals in Eq. (3.60) are replaced by corresponding derivatives. First, let us recall the following equalities from Eqs. (3.29) and (3.30):

$$I_{3,1} = -\frac{\partial A_1}{\partial x} + \sigma_1 \frac{\partial h_1}{\partial x} + (\sigma_1 - \sigma_3) \frac{\partial}{\partial x} (b + h_2), \quad (3.64)$$

$$I_{3,2} = -\frac{\partial A_2}{\partial x} + \sigma_3 \frac{\partial}{\partial x} (b + h_2). \quad (3.65)$$

Using Eqs. (3.64) and (3.65) the source term (Eq. 3.60) now reads

$$\mathbf{g}(\boldsymbol{\sigma}, \mathbf{w}) = \begin{Bmatrix} 0 \\ gA_1 \left[\frac{1}{\sigma_1} \frac{\partial}{\partial x} (A_1 + A_2) - \frac{\partial}{\partial x} (b + h_2 + h_1) \right] \\ 0 \\ gA_2 \left[\frac{1}{\sigma_2} \frac{\partial A_2}{\partial x} + \frac{r}{\sigma_1} \frac{\partial A_1}{\partial x} - \frac{\partial}{\partial x} (b + h_2 + rh_1) \right] \end{Bmatrix}. \quad (3.66)$$

3.2 Governing equations for arrested salt-wedges

For steady-state conditions, *i.e.*, constant sea levels and river flow, an equilibrium is established between the buoyancy pressure gradients, friction forces, and inertial forces [84], and eventually an arrested salt-wedge forms. This section presents the governing equations for this steady-state type of estuary.

3.2.1 System of ODEs for arrested salt-wedges

To derive governing equations for the arrested salt-wedge, in which only the upper layer is fully active, we first write Eq. (3.54) in steady-state form as the following system of *ordinary differential equations* (ODE):

$$\frac{dQ_1}{dx} = \frac{1}{r} w_e \sigma_3, \quad (3.67)$$

$$\frac{dQ_2}{dx} = -w_e \sigma_3, \quad (3.68)$$

$$\begin{aligned} \frac{d}{dx} \left(\frac{Q_1^2}{A_1} + \frac{g}{2\sigma_1} A_1^2 \right) &= -g \frac{A_1}{\sigma_1} \frac{dA_2}{dx} + \frac{g}{2} \frac{d}{dx} \left(\frac{1}{\sigma_1} \right) A_1^2 \\ &+ gA_1 \left[\frac{1}{\sigma_1} \frac{d}{dx} (A_1 + A_2) - \frac{d}{dx} (b + h_2 + h_1) \right] \\ &+ \frac{\tau_w}{\rho_1} P_1 + \frac{\tau_i}{\rho_1} \sigma_3 + \frac{Q_1}{A_1} w_e \sigma_3, \end{aligned} \quad (3.69)$$

$$\begin{aligned} \frac{d}{dx} \left(\frac{Q_2^2}{A_2} + \frac{g}{2\sigma_2} A_2^2 \right) &= -g \frac{A_2}{\sigma_1} \frac{dA_1}{dx} + \frac{g}{2} \frac{d}{dx} \left(\frac{1}{\sigma_2} \right) A_2^2 \\ &+ gA_2 \left[\frac{1}{\sigma_2} \frac{dA_2}{dx} + \frac{r}{\sigma_1} \frac{dA_1}{dx} - \frac{d}{dx} (b + h_2 + rh_1) \right] \\ &+ \frac{\tau_b}{\rho_2} P_2 - \frac{\tau_i}{\rho_2} \sigma_3 - \frac{Q_2}{A_2} w_e \sigma_3. \end{aligned} \quad (3.70)$$

The momentum equations (3.69) and (3.70) are simplified to

$$\frac{d}{dx} \left(\frac{Q_1^2}{A_1} \right) = -gA_1 \frac{d}{dx} (b + h_2 + h_1) + \frac{\tau_w}{\rho_1} P_1 + \frac{\tau_i}{\rho_1} \sigma_3 + \frac{Q_1}{A_1} w_e \sigma_3, \quad (3.71)$$

$$\frac{d}{dx} \left(\frac{Q_2^2}{A_2} \right) = -gA_2 \frac{d}{dx} (b + h_2 + rh_1) + \frac{\tau_b}{\rho_2} P_2 - \frac{\tau_i}{\rho_2} \sigma_3 - \frac{Q_2}{A_2} w_e \sigma_3. \quad (3.72)$$

Dividing these equations by gA_1 and gA_2 , respectively, and after some simple calculation, the momentum equations are written as

$$\frac{d}{dx} \left(\frac{Q_1^2}{2gA_1^2} + b + h_2 + h_1 \right) = \frac{\tau_w}{\rho_1 g A_1} P_1 + \frac{\tau_i}{\rho_1 g A_1} \sigma_3 + \frac{Q_1}{gA_1^2} w_e \sigma_3, \quad (3.73)$$

$$\frac{d}{dx} \left(\frac{Q_2^2}{2gA_2^2} + b + h_2 + rh_1 \right) = \frac{\tau_b}{\rho_2 g A_2} P_2 - \frac{\tau_i}{\rho_2 g A_2} \sigma_3 - \frac{Q_2}{gA_2^2} w_e \sigma_3. \quad (3.74)$$

The continuity equations (3.67) and (3.68) with the momentum equations (3.73) and (3.74) can be used to compute the arrested salt-wedge profile in channels with irregular geometry, including friction and entrainment processes.

3.2.2 Single ODE for arrested salt-wedges

If entrainment is neglected ($w_e(x, t) = 0$), the flow rate in the lower layer becomes $Q_2(x, t) = 0$, and the upper layer becomes stationary ($dQ_1/dx = 0$); hence, the arrested salt-wedge is described by momentum equations

$$\frac{d}{dx} \left(\frac{Q_1^2}{2gA_1^2} + b + h_2 + h_1 \right) = \frac{\tau_w}{\rho_1 g A_1} P_1 + \frac{\tau_i}{\rho_1 g A_1} \sigma_3 \quad (3.75)$$

and

$$\frac{d}{dx} (b + h_2 + r h_1) = -\frac{\tau_i}{\rho_2 g A_2} \sigma_3. \quad (3.76)$$

For a prismatic channel with rectangular cross sections, in which $\sigma_{1,2,3}(x) = \sigma$ and $A_j(x) = \sigma h_j(x)$, $j = 1, 2$, a single ODE is obtained. First, since $dQ_1/dx = 0$, Eq. (3.76) is rewritten so that the only unknowns are h_1 and h_2 ; therefore

$$\begin{aligned} \frac{Q_1^2}{2g\sigma^2} \frac{d}{dx} \left(\frac{1}{h_1^2} + b + h_2 + h_1 \right) &= \frac{\tau_w}{\rho_1 g A_1} 2h_1 + \frac{\tau_i}{\rho_1 g A_1} \sigma \\ -\frac{Q_1^2}{g\sigma^2 h_1^3} \frac{dh_1}{dx} + \frac{db}{dx} + \frac{dh_2}{dx} + \frac{dh_1}{dx} &= \frac{\tau_w}{\rho_1 g A_1} 2h_1 + \frac{\tau_i}{\rho_1 g A_1} \sigma. \end{aligned} \quad (3.77)$$

Equation (3.76) is subtracted from Eq. (3.77), which results in

$$-\frac{Q_1^2}{g\sigma^2 h_1^3} \frac{dh_1}{dx} + \frac{dh_1}{dx} - r \frac{dh_1}{dx} = \frac{\tau_w}{\rho_1 g A_1} 2h_1 + \frac{\tau_i}{\rho_1 g A_1} \sigma + \frac{\tau_i}{\rho_2 g A_2} \sigma. \quad (3.78)$$

Using definitions for shear stress from Eqs. (3.21) and (3.22), a single ODE describes the slope of the interface from the mouth upstream ($u_1 < 0$, $u_2 = 0$) as follows:

$$\left(1 - r - \frac{u_1^2}{gh_1} \right) \frac{dh_1}{dx} = \frac{\lambda_w u_1^2}{gA_1} 2h_1 + \frac{\lambda_i u_1^2}{gA_1} \sigma + r \frac{\lambda_i u_1^2}{gA_2} \sigma, \quad (3.79)$$

and finally we have

$$\frac{dh_1}{dx} = \frac{Fd^2}{1 - Fd^2} \left[\lambda_i \left(1 + r \frac{h_1}{h_2} \right) + \lambda_w \frac{2h_1}{\sigma} \right], \quad (3.80)$$

where $Fd = u_1 / \sqrt{g(1-r)h_1}$ is the densimetric Froude number in channels with rectangular cross-sections and stagnant lower layer.

3.2.3 Analytical equation for arrested salt-wedges

Equation (3.80) may be further simplified by neglecting λ_w and considering a horizontal channel bed ($b(x) = \text{const}$). Under these assumptions the following non-dimensional parameters are introduced:

$$\varphi = h_1/H_0, \quad \chi = x/H_0, \quad (3.81)$$

where H_0 is a constant total depth in a horizontal channel. Also, the upstream squared densimetric Froude number is

$$F_0^2 = \frac{Q^2}{g(1-r)\sigma^2 H_0^3} = Fd^2\varphi^3. \quad (3.82)$$

Substituting the parameters defined by Eqs. (3.81) and (3.82), and using the *Boussinesq approximation*, which neglects the density ratio r everywhere except where multiplied by g [100], Eq. (3.80) becomes

$$\frac{d\varphi}{d\chi} = \frac{F_0^2}{\varphi^3 - F_0^2} \lambda_i \left(\frac{1}{1 - \varphi} \right). \quad (3.83)$$

Equation (3.83) is then integrated over depth, as follows:

$$\chi = \int_{\varphi_1}^{\varphi_2} \left[\frac{F_0^2}{\varphi^3 - F_0^2} \lambda_i \left(\frac{1}{1 - \varphi} \right) \right]^{-1} d\varphi. \quad (3.84)$$

The integration between the boundary conditions $\varphi_1 = 1$ at the tip of the salt-wedge and a critical condition $\varphi_2 = F_0^{2/3}$ at the river mouth leads to a well-known analytical equation (2.7) for the length of the salt-wedge. The shape of the salt-wedge can, similarly, be computed in a discrete form by solving Eq. (3.84), where $\varphi_1 = 1$ and $\varphi_2 = \varphi_1 - \Delta\varphi$. Here $\Delta\varphi$ is a vertical spatial step; therefore, φ_2 is the upper layer thickness at any distance χ from the tip of the salt-wedge.

4

One-dimensional numerical schemes

Contents

4.1 FDM for arrested salt-wedges	38
4.1.1 Implicit trapezoidal method	38
4.1.2 Boundary conditions for arrested salt-wedges	40
4.1.3 Calibration of the interfacial friction factor λ_i	41
4.2 FVM for time-dependant salt-wedges	41
4.2.1 FVM for hyperbolic conservation laws	42
4.2.2 Godunov method and approximate Riemann solvers	44
4.2.3 Modified Q-scheme for two-layer salt-wedge flow	47
4.2.4 Wet-dry fronts in channels with irregular geometry	55
4.2.5 Boundary conditions for time-dependant salt-wedges	58

Abstract

This chapter presents two numerical schemes for solving arrested and time-dependant salt-wedge flows. The first scheme is based on a FDM, namely the implicit trapezoidal method, while the second scheme is based on a FVM, namely the modified Q-scheme of Roe. Furthermore, stability and well-balanced properties of the FVM scheme are discussed. A well-balanced treatment of source terms at wet-dry fronts in channels with irregular geometry is also presented. And finally, physically relevant boundary conditions for salt-wedge models are proposed.

4.1 FDM for arrested salt-wedges

The arrested salt-wedge model was developed to compute interface profiles and to calibrate the interfacial friction factor. The governing equations for steady-state flow are written as a system of four ODEs (Eq. 3.67, 3.68, 3.73, and 3.74). There are a number of ways to numerically solve a system of ODEs, the simplest being the finite difference method, which approximates the derivatives of an unknown function. Among many forms of FDM, such as the forward Euler, backward Euler, and central difference, the most commonly used for steady gradually varied shallow water flow is the *implicit trapezoidal method* [93].

4.1.1 Implicit trapezoidal method

A first step in applying the implicit trapezoidal method is to divide the spatial domain by M nodes, with a step $\Delta x = x_{i+1} - x_i$. Spatial steps of equal length are considered here, although this method is easily applied to irregular meshes. The proposed method for solving ODE of a general form

$$\frac{dy}{dx} = f(x, y) \quad (4.1)$$

is written as follows [93]:

$$y_{i+1} = y_i + \frac{\Delta x}{2} (f(x_i, y_i) + f(x_{i+1}, y_{i+1})), \quad (4.2)$$

where y_{i+1} and y_i are the values of the unknown function at nodes i and $i + 1$, respectively, and $f(x_i, y_i)$ and $f(x_{i+1}, y_{i+1})$ are the values of the derivatives of a function $y(x)$ at nodes i and $i + 1$, respectively (see Fig. 4.1).

Application of the implicit trapezoidal method (Eq. 4.2) to solve the system of equations (3.67), (3.68), (3.73) and (3.74) results in the following equations:

$$Q_{i+1,1} = Q_{i,1} + \frac{\Delta x}{2r} (w_{e,i+1}\sigma_{i+1,3} + w_{e,i}\sigma_{i,3}), \quad (4.3)$$

$$Q_{i+1,2} = Q_{i,2} - \frac{\Delta x}{2} (w_{e,i+1}\sigma_{i+1,3} + w_{e,i}\sigma_{i,3}), \quad (4.4)$$

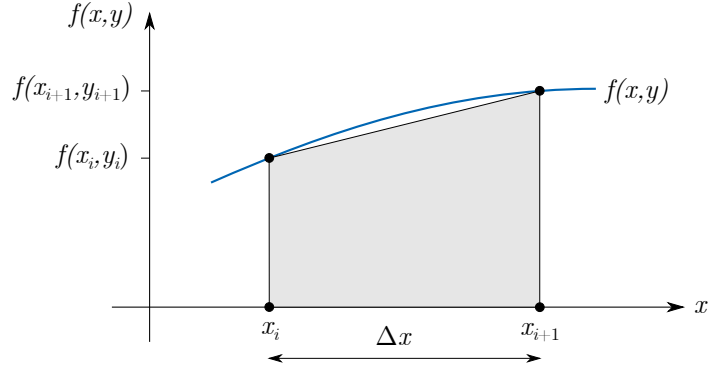


Figure 4.1: Implicit trapezoidal method interpretation.

$$\begin{aligned}
 \left(\frac{Q_1^2}{2gA_1^2} + b + h_2 + h_1 \right)_{i+1} &= \left(\frac{Q_1^2}{2gA_1^2} + b + h_2 + h_1 \right)_i - \\
 &\frac{\Delta x}{2} \left(\frac{\lambda_{w,i+1}|u_{i+1,1}|u_{i+1,1}}{gA_{i+1,1}} P_{i+1,1} + \frac{\lambda_{w,i}|u_{i,1}|u_{i,1}}{gA_{i,1}} P_{i,1} \right) - \\
 &\frac{\Delta x}{2} \left(\frac{(\lambda_i)_{i+1}|u_{i+1,1} - u_{i+1,2}|(u_{i+1,1} - u_{i+1,2})}{gA_{i+1,1}} \sigma_{i+1,3} \right. \\
 &\quad \left. + \frac{(\lambda_i)_i|u_{i,1} - u_{i,2}|(u_{i,1} - u_{i,2})}{gA_{i,1}} \sigma_{i,3} \right) + \\
 &\frac{\Delta x}{2} \left(\frac{Q_{i+1,1}}{gA_{i+1,1}^2} w_{e,i+1} \sigma_{i+1,3} + \frac{Q_{i,1}}{gA_{i,1}^2} w_{e,i} \sigma_{i,3} \right), \tag{4.5}
 \end{aligned}$$

$$\begin{aligned}
 \left(\frac{Q_2^2}{2gA_2^2} + b + h_2 + rh_1 \right)_{i+1} &= \left(\frac{Q_2^2}{2gA_2^2} + b + h_2 + rh_1 \right)_i - \\
 &\frac{\Delta x}{2} \left(\frac{\lambda_{b,i+1}|u_{i+1,2}|u_{i+1,2}}{gA_{i+1,2}} P_{i+1,2} + \frac{\lambda_{b,i}|u_{i,2}|u_{i,2}}{gA_{i,2}} P_{i,2} \right) + \\
 &\frac{\Delta x}{2} \left(\frac{(\lambda_i)_{i+1}|u_{i+1,1} - u_{i+1,2}|(u_{i+1,1} - u_{i+1,2})}{gA_{i+1,2}} r \sigma_{i+1,3} \right. \\
 &\quad \left. + \frac{(\lambda_i)_i|u_{i,1} - u_{i,2}|(u_{i,1} - u_{i,2})}{gA_{i,2}} r \sigma_{i,3} \right) - \\
 &\frac{\Delta x}{2} \left(\frac{Q_{i+1,2}}{gA_{i+1,2}^2} w_{e,i+1} \sigma_{i+1,3} + \frac{Q_{i,2}}{gA_{i,2}^2} w_{e,i} \sigma_{i,3} \right). \tag{4.6}
 \end{aligned}$$

The approximate solution is found by solving the system of four algebraic equations (4.3)-(4.6) for four unknowns Q_1 , Q_2 , h_1 , and h_2 . The entrainment velocity w_e and friction factors λ_w , λ_b , and λ_i are either known input parameters given as

constant values, or they are computed at each node from additional entrainment and friction equations. The resulting equations are non-linear; hence, an iterative *Newton-Raphson method* [8] was applied.

The main advantages of using the implicit trapezoidal method are that it ensures a 2nd order of accuracy, it requires only the cross-section geometry data at nodes i and $i+1$, and it can be applied for non-prismatic channels with arbitrary cross-sections [93]. Furthermore, it should be noted that the implicit trapezoidal rule applied to a single shallow water equation is identical to the *standard step method* [25], which is derived from the energy equation; it is thoroughly validated and widely used in hydraulic practice to calculate the steady-state water-depth profiles along natural channels [93].

4.1.2 Boundary conditions for arrested salt-wedges

Flow rates in the upper Q_1 and lower Q_2 layer, as well as the upper layer thickness h_1 and total water depth $H = h_1 + h_2$ should be specified at the downstream boundary. The difference between the upper and lower layer flow rate should be equal to the river flow rate $Q = Q_1 - Q_2$, where Q_2 in a steady-state flow can be estimated from a known entrainment rate E .

In arrested salt-wedge models it is usually assumed that the flow in the upper layer is internally critical at the mouth, which is defined by $Fd^2 = 1$ [86, 7]. If entrainment is considered, both layers are active; therefore, a composite Froude number G (Eq. 2.5) should be used instead. The internally critical condition, defined by $G^2 = 1$, was solved iteratively for known Q_1 and Q_2 to obtain the critical upper layer thickness $h_{c,1}$. The implicit trapezoidal method, unfortunately, is unsuitable for transcritical flows, which may occur at the downstream boundary. Therefore, once the internally critical upper layer thickness $h_{c,1}$ was computed, the boundary condition was specified by $h_1 = 1.05h_{c,1}$ to ensure a subcritical flow $G^2 < 1$.

The salt-wedge tip represents an upstream boundary for a two-layer system; however, the model is able to compute the water surface profile along the entire spatial domain. This was achieved by defining a tolerance parameter ξ , so that when a lower layer thickness is $h_2 < \xi$, the computation of a two-layer system is stopped, and a solver for a single layer SWE [25] continues until the upstream boundary is reached.

4.1.3 Calibration of the interfacial friction factor λ_i

Steady-state salt-wedge models were widely used in the past for predicting the arrested salt-wedge length in the field, and even for simulating quasi-steady salt-wedge dynamics under gradual changes of the river flow rate (*e.g.*, the Mississippi River [7]). Today, the arrested salt-wedge models are mostly used for preliminary analyses or calibration of the interfacial friction factor. Obviously, Eq. (2.7) or (3.80) are much more attractive than the system of Eqs. (3.67), (3.68), (3.73) and (3.74); λ_i is directly obtained from the normalized length of the salt-wedge L/H or the interface slope dh_1/dx . Many interfacial friction studies [94, 29, 89, 76, 56] were based on such, or very similar, equations. In this thesis a different approach is proposed.

The salt-wedge profile was computed by solving the system of Eqs. (4.3)-(4.6). The interfacial friction factor was assumed constant along the wedge, and was systematically varied until the best fit between numerical results and observed interfacial depths was achieved. In the process of finding the best fit, λ_i varied over the range 10^{-5} - 10^{-2} by the increment of 10^{-5} . The best fit was determined by the visual inspection and by the smallest *root mean square error*, defined as

$$\text{RMSE} = \sqrt{\frac{1}{N} \sum (X_{\text{obs}} - X_{\text{mod}})^2}, \quad (4.7)$$

where N is the total number of observations along the wedge, X_{obs} is the observed interface depth, and X_{mod} is the computed interface depth. This approach allowed for a more accurate representation of the variable channel geometry, lower layer dynamics, bed friction, entrainment, and in the end resulted in more accurate results.

4.2 FVM for time-dependant salt-wedges

The time-dependant model was developed to simulate salt-wedge dynamics under steady and highly variable flow conditions. The numerical model for salt-wedges should be stable, fully conservative, and shock-capturing; therefore, a finite volume method was the most appropriate choice.

Finite volume methods have become popular in recent years, especially in hydrodynamic modelling for systems of *conservation laws*. Although similar to finite difference methods and often interpreted as FDM approximations of differential equations, a FVM

is derived from the integral form of the conservation law, which shows many advantages over the differential form [58]. The integral form of conservation laws naturally holds for many physical laws, such as the conservation of mass, momentum, or energy. A more detailed description of a FVM and its applications can be found in [58, 97].

4.2.1 FVM for hyperbolic conservation laws

The following one-dimensional first-order hyperbolic PDE is an example of a *conservation law*:

$$\frac{\partial \mathbf{w}(x, t)}{\partial t} + \frac{\partial \mathbf{f}(\mathbf{w})}{\partial x} = 0, \quad (4.8)$$

where $\mathbf{w}(x, t)$ is the *conserved quantity* vector and $\mathbf{f}(\mathbf{w})$ is the *convective flux* vector. When a conservation law has a non-zero right-hand side (RHS) it is called a *balance law* or a *conservative law with source terms*. If the Jacobian of the flux $\mathbf{J}(\mathbf{w}) = \partial \mathbf{f} / \partial \mathbf{w}$ has real eigenvalues, then the system is called *hyperbolic*, and if they are also distinct, then it is called *strictly hyperbolic* [58].

The PDE (4.8) is easily derived from the following, more fundamental, integral form of a conservation law if $\mathbf{w}(x, t)$ and $\mathbf{f}(\mathbf{w})$ are sufficiently smooth [58]:

$$\frac{d}{dt} \int_{x_A}^{x_B} \mathbf{w}(x, t) dx = \mathbf{f}(\mathbf{w}(x_A, t)) - \mathbf{f}(\mathbf{w}(x_B, t)), \quad (4.9)$$

which states that the time-rate change of conserved quantity \mathbf{w} between two points x_A and x_B can occur only due to fluxes $\mathbf{f}(\mathbf{w})$ at endpoints. The main advantage of the integral equation (4.9) is that it admits discontinuous solutions, in contrast to partial differential equations [58].

In a 1D finite volume method the spatial domain is divided into M control volumes or cells denoted by $C_i = [x_{i-1/2}, x_{i+1/2}]$, for $i = 1..M$, where x_i is the centre of the cell, and $x_{i+1/2}$ is the *intercell* between the cells C_i and C_{i+1} (Fig. 4.2). If we assume that all cells are equal in size, then $\Delta x = x_{i+1/2} - x_{i-1/2}$ denotes the cell size, although, a FVM is easily applied for irregular meshes.

In general, index i refers to average values in cell C_i , and index $i + 1/2$ refers to intermediate state at the edges between cells C_i and C_{i+1} (Fig. 4.3). Symbol Δt denotes the time step, and the upper index n corresponds to values at time $t^n = n\Delta t$.

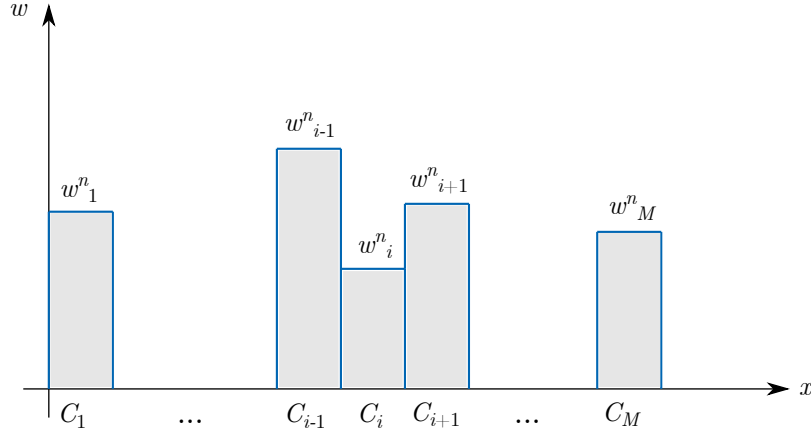


Figure 4.2: Graphical interpretation of a piecewise constant function $\mathbf{w}^n(x)$.

As illustrated in Fig. 4.2, the value \mathbf{w}_i^n denotes the average value of $\mathbf{w}(x, t)$ over cell C_i at time t_n , as follows:

$$\mathbf{w}_i^n = \frac{1}{\Delta x} \int_{C_i} \mathbf{w}(x, t_n) dx = \frac{1}{\Delta x} \int_{x_{i-1/2}}^{x_{i+1/2}} \mathbf{w}(x, t_n) dx. \quad (4.10)$$

Therefore, a FVM approximate solution to Eq. (4.8) is a piecewise constant, written as

$$\mathbf{w}^n(x) = \mathbf{w}_i^n \quad \text{for } x \in C_i. \quad (4.11)$$

These conserved values are updated at each time step by the fluxes through the edges of each cell. To develop an explicit numerical scheme, Eq. (4.9) is written for $\mathbf{w}(x, t)$ in each cell and integrated over time from t_n to t_{n+1} , as follows:

$$\int_{C_i} \mathbf{w}(x, t_{n+1}) dx - \int_{C_i} \mathbf{w}(x, t_n) dx = \int_{t_n}^{t_{n+1}} [\mathbf{f}(\mathbf{w}(x_{i-1/2}, t)) - \mathbf{f}(\mathbf{w}(x_{i+1/2}, t))] dt. \quad (4.12)$$

For a fully discrete form, the time average flux at intercell $i + 1/2$ between time t^n and t^{n+1} is denoted by [58]:

$$\mathbf{f}_{i+1/2}^n = \frac{1}{\Delta t} \int_{t_n}^{t_{n+1}} \mathbf{f}(\mathbf{w}(x_{i+1/2}, t)) dt. \quad (4.13)$$

Using Eqs. (4.10) and (4.13), and dividing Eq. (4.12) by Δx , we finally obtain the following explicit finite volume scheme [58]:

$$\mathbf{w}_i^{n+1} = \mathbf{w}_i^n - \frac{\Delta t}{\Delta x} (\mathbf{f}_{i+1/2}^n - \mathbf{f}_{i-1/2}^n). \quad (4.14)$$

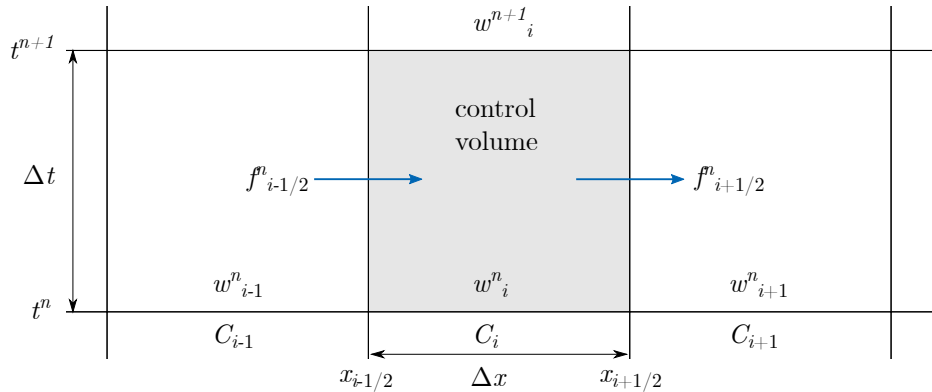


Figure 4.3: Graphical interpretation of a three-point explicit finite volume method.

In hyperbolic PDEs, perturbations (*e.g.* waves in SWE) propagate with finite speeds; therefore, it is reasonable to assume that flux $\mathbf{f}_{i+1/2}^n$ is some function \mathcal{F} of quantities \mathbf{w}_{i+1}^n and \mathbf{w}_i^n in neighbouring cells [58]:

$$\mathbf{f}_{i+1/2}^n = \mathcal{F}(\mathbf{w}_i^n, \mathbf{w}_{i+1}^n). \quad (4.15)$$

The main problem in FVM is finding \mathcal{F} that adequately approximates the actual physical flux. Regardless of the choice for \mathcal{F} , Eq. (4.14) is in general a three-point explicit method [58], which means that the solution for \mathbf{w}_i^{n+1} depends on values from three neighbouring cells \mathbf{w}_{i-1}^n , \mathbf{w}_i^n , and \mathbf{w}_{i+1}^n , obtained from the previous times step (Fig. 4.3).

Furthermore, Eq. (4.14) is considered a *conservative numerical scheme* because the same flux function is used to update the quantities in neighbouring cells \mathbf{w}_i^n and \mathbf{w}_{i+1}^n . In other words, the same quantity which enters the cell C_{i+1} must leave the cell C_i , so that the total quantity is preserved over the entire domain, up to the boundaries [97]. However, since Eq. (4.9) is exact, the accuracy of the numerical scheme depends on the choice of \mathcal{F} .

4.2.2 Godunov method and approximate Riemann solvers

A *Riemann problem* is a hyperbolic conservation law (Eq. 4.8) with the following initial condition defined by a single discontinuity at $x = 0$:

$$\mathbf{w}(x, 0) = \begin{cases} \mathbf{w}_i^n & \text{if } x < 0 \\ \mathbf{w}_{i+1}^n & \text{if } x > 0 \end{cases} . \quad (4.16)$$

The *Godunov method* [39] is an upwind finite volume scheme which exactly solves the Riemann problem at each intercell $x_{i+1/2}$, to determine \mathcal{F} at a given time step t_n . The Godunov intercell flux is therefore a function of the conserved quantity \mathbf{w} evaluated at the intercell $x_{i+1/2}$ [97]:

$$\mathcal{F} = \mathbf{f}\left(\mathbf{w}(x_{i+1/2}, t_n)\right) = \mathbf{f}\left(\mathbf{w}_{i+1/2}^n\right). \quad (4.17)$$

The solution to the Riemann problem is based on a quasi-linear form of the conservation law [97]:

$$\frac{\partial \mathbf{w}}{\partial t} + \mathbf{J}(\mathbf{w}) \frac{\partial \mathbf{w}}{\partial x} = 0, \quad (4.18)$$

where $\mathbf{J}(\mathbf{w}) = \partial \mathbf{f} / \partial \mathbf{w}$ is the Jacobian matrix of the flux, which is derived by applying the chain rule for $\partial \mathbf{f}(\mathbf{w}) / \partial x$ in Eq. (4.8):

$$\frac{\partial \mathbf{f}(\mathbf{w})}{\partial x} = \frac{\partial \mathbf{f}}{\partial \mathbf{w}} \frac{\partial \mathbf{w}}{\partial x} = \mathbf{J}(\mathbf{w}) \frac{\partial \mathbf{w}}{\partial x}. \quad (4.19)$$

For linear conservation laws, the Riemann problem is solved exactly at each intercell based on eigenvalues and eigenvectors of the constant coefficient Jacobian matrix $\mathbf{J}(\mathbf{w}) = \mathbf{J}$. For non-linear conservation laws, however, Jacobian matrix $\mathbf{J}(\mathbf{w})$ is a function of \mathbf{w} , and obtaining the exact solution to the Riemann problem can become computationally too expensive. Therefore, *approximate Riemann solvers* were eventually introduced [58].

Roe [81] introduced an idea to replace the original Jacobian matrix $\mathbf{J}(\mathbf{w})$ by an approximate Jacobian matrix $\tilde{\mathbf{J}}(\mathbf{w}_i^n, \mathbf{w}_{i+1}^n)$. Constant coefficients of the matrix $\tilde{\mathbf{J}}(\mathbf{w}_i^n, \mathbf{w}_{i+1}^n)$ depend only on known values \mathbf{w}_{i+1}^n and \mathbf{w}_i^n ; therefore, the Riemann problem becomes a linear hyperbolic system. Since perturbation speeds depend on eigenvalues ψ of the Jacobian matrix, the numerical flux at the intercell is evaluated in an upwind manner as [58]:

$$\mathbf{f}_{i+1/2}^- = \mathbf{f}(\mathbf{w}_i^n) + \tilde{\mathbf{J}}^-(\mathbf{w}_i^n, \mathbf{w}_{i+1}^n) \Delta \mathbf{w} \quad (4.20)$$

and

$$\mathbf{f}_{i+1/2}^+ = \mathbf{f}(\mathbf{w}_{i+1}^n) - \tilde{\mathbf{J}}^+(\mathbf{w}_i^n, \mathbf{w}_{i+1}^n) \Delta \mathbf{w}, \quad (4.21)$$

with

$$\Delta \mathbf{w} = \mathbf{w}_{i+1}^n - \mathbf{w}_i^n. \quad (4.22)$$

4. One-dimensional numerical schemes

Averaging Eqs. (4.20) and (4.21) gives

$$\mathbf{f}_{i+1/2} = \frac{1}{2} [\mathbf{f}(\mathbf{w}_i^n) + \mathbf{f}(\mathbf{w}_{i+1}^n)] - \frac{1}{2} |\tilde{\mathbf{J}}(\mathbf{w}_i^n, \mathbf{w}_{i+1}^n)| \Delta \mathbf{w}, \quad (4.23)$$

which is a general way of writing the numerical flux at the intercell $x_{i+1/2}$ in the original Q -scheme [101]. Notice that the numerical flux consists of a centred part $\frac{1}{2} [\mathbf{f}(\mathbf{w}_i) + \mathbf{f}(\mathbf{w}_{i+1})]$ and additional term defined by the matrix $\tilde{\mathbf{J}}(\mathbf{w}_i^n, \mathbf{w}_{i+1}^n)$, which is used to upwind the flux. The following definitions are also presented for clarity:

$$\tilde{\mathbf{J}}(\mathbf{w}_i^n, \mathbf{w}_{i+1}^n) = \mathbf{K} \Psi \mathbf{K}^{-1} \quad \text{and} \quad \tilde{\mathbf{J}}^\pm(\mathbf{w}_i^n, \mathbf{w}_{i+1}^n) = \mathbf{K} \Psi^\pm \mathbf{K}^{-1}, \quad (4.24)$$

where Ψ is a diagonal matrix having as coefficients the eigenvalues of $\tilde{\mathbf{J}}(\mathbf{w}_i^n, \mathbf{w}_{i+1}^n)$, and \mathbf{K} denotes a matrix containing eigenvectors, which correspond to those eigenvalues. Also

$$\Psi^\pm = \begin{bmatrix} \psi_1^\pm & & 0 \\ & \ddots & \\ 0 & & \psi_4^\pm \end{bmatrix}, \quad (4.25)$$

where

$$\psi_l^\pm = \frac{1}{2} (\psi_l \pm |\psi_l|), \quad 1 \leq l \leq 4, \quad (4.26)$$

so that

$$|\Psi| = \Psi^+ - \Psi^- \quad \text{and} \quad |\tilde{\mathbf{J}}| = \tilde{\mathbf{J}}^+ - \tilde{\mathbf{J}}^-. \quad (4.27)$$

For a hyperbolic conservation law, the Roe's Jacobian matrix $\tilde{\mathbf{J}}(\mathbf{w}_i^n, \mathbf{w}_{i+1}^n)$ should satisfy the following properties [97]:

a) *Hyperbolicity* of the PDE system.

All eigenvalues of matrix $\tilde{\mathbf{J}}(\mathbf{w}_i, \mathbf{w}_{i+1})$ should be real.

b) *Consistency* with the original Jacobian:

$$\tilde{\mathbf{J}}(\mathbf{w}_i, \mathbf{w}_{i+1}) \longrightarrow \mathbf{J}(\mathbf{w}) \quad \text{when} \quad \mathbf{w}_i, \mathbf{w}_{i+1} \longrightarrow \mathbf{w}$$

c) *Conservation* across discontinuities:

$$\mathbf{f}(\mathbf{w}_{i+1}) - \mathbf{f}(\mathbf{w}_i) = \tilde{\mathbf{J}}(\mathbf{w}_i, \mathbf{w}_{i+1}) \Delta \mathbf{w}$$

To satisfy the latter condition, the constant coefficient matrix $\tilde{\mathbf{J}}(\mathbf{w}_i^n, \mathbf{w}_{i+1}^n)$ is approximated at some average state [97]:

$$\tilde{\mathbf{J}}(\mathbf{w}_i^n, \mathbf{w}_{i+1}^n) = \mathbf{J}(\tilde{\mathbf{w}}_{i+1/2}^n) = \mathbf{J}_{i+1/2}^n, \quad (4.28)$$

where $\tilde{\mathbf{w}}_{i+1/2}^n$ is the Roe's average of \mathbf{w}_i^n and \mathbf{w}_{i+1}^n evaluated at intercell $x_{i+1/2}$, which depends on the specific problem at hand.

4.2.3 Modified Q-scheme for two-layer salt-wedge flow

The governing equations for a single layer shallow water flow through a prismatic channel with rectangular cross-sections, horizontal bed, and no friction are written as a system of conservation laws, and a standard approximate Riemann solver, such as the original Q-scheme, can be applied [9]. However, when sloped bed, variable cross-section, or friction is considered, as in the governing system of equations (3.54), the corresponding system becomes a conservation law with source terms, and standard solvers may fail in computing steady-state flow [9].

The problem of source terms corresponding to bed elevations and variable width was successfully solved for a single layer shallow water flow through non-prismatic channels with rectangular cross-sections by introducing a modified Q-scheme with upwind treatment of the source terms [9, 101]. Castro *et al.* also adapted the Q-scheme to deal with coupled two-layer systems in channels with rectangular cross-sections [21] and later in channels with arbitrary cross-sections [18].

The first difficulty in approximating the system of two-layer SWE in channels with irregular geometry is that the flux $\mathbf{f}(\boldsymbol{\sigma}, \mathbf{w})$ in Eq. (3.54) depends, not only on \mathbf{w} , but also on the channel width $\boldsymbol{\sigma}$. The chain rule for the partial derivative of $\mathbf{f}(\boldsymbol{\sigma}, \mathbf{w})$ therefore states

$$\frac{\partial \mathbf{f}(\boldsymbol{\sigma}, \mathbf{w})}{\partial x} = \frac{\partial \mathbf{f}}{\partial \mathbf{w}} \frac{\partial \mathbf{w}}{\partial x} + \frac{\partial \mathbf{f}}{\partial \boldsymbol{\sigma}} \frac{\partial \boldsymbol{\sigma}}{\partial x} = \mathbf{J}(\boldsymbol{\sigma}, \mathbf{w}) \frac{\partial \mathbf{w}}{\partial x} + \mathbf{v}(\boldsymbol{\sigma}, \mathbf{w}). \quad (4.29)$$

Another difficulty arises from the fact that the source terms corresponding to derivatives of the conserved quantity $\mathbf{B}(\boldsymbol{\sigma}, \mathbf{w}) \frac{\partial \mathbf{w}}{\partial x}$ in Eq. (3.54) should be considered when computing eigenvalues. Castro *et al.* [21] treated this source term *locally* as a flux term, so that the governing equation (3.54) with Eq. (4.29), and without source terms $\mathbf{g}(\boldsymbol{\sigma}, \mathbf{w})$ and $\mathbf{s}(\boldsymbol{\sigma}, \mathbf{w})$, is rewritten as:

$$\frac{\partial \mathbf{w}}{\partial t} + \mathbf{Q}(\boldsymbol{\sigma}, \mathbf{w}) \frac{\partial \mathbf{w}}{\partial x} = 0, \quad (4.30)$$

where $\mathbf{Q}(\boldsymbol{\sigma}, \mathbf{w}) = \mathbf{J}(\boldsymbol{\sigma}, \mathbf{w}) - \mathbf{B}(\boldsymbol{\sigma}, \mathbf{w})$, and $\mathbf{J}(\boldsymbol{\sigma}, \mathbf{w})$ is the Jacobian matrix, defined as:

$$\mathbf{J}(\boldsymbol{\sigma}, \mathbf{w}) = \frac{\partial \mathbf{f}}{\partial \mathbf{w}} = \begin{bmatrix} 0 & 1 & 0 & 0 \\ -\frac{Q_1^2}{A_1^2} + \frac{g}{\sigma_1} A_1 & 2\frac{Q_1}{A_1} & 0 & 0 \\ 0 & 0 & 0 & 1 \\ 0 & 0 & -\frac{Q_2^2}{A_2^2} + \frac{g}{\sigma_2} A_2 & 2\frac{Q_2}{A_2} \end{bmatrix} \quad (4.31)$$

An approximate Riemann solver can therefore be applied to Eq. (3.54).

Numerical scheme

In the present work, the Q-scheme of Castro *et al.* [18] for a two-layer flow through channels with irregular geometry was extended to solve the governing equation (3.54). The additional terms accounting for friction (Eq. 3.62) and entrainment (Eq. 3.63) were considered as source terms, and treated in a similar upwind manner as terms accounting for irregular geometry (Eq. 3.66). The idea to upwind the friction terms in channels with rectangular cross-sections was proposed in [34]. Likewise, Cea *et al.* [23] showed that mass terms, such as lateral inflows should also be upwinded to reduce discretization errors introduced by upwinding the flux terms, and to ensure the stability of the numerical scheme.

The proposed numerical model is explicit in time and first order accurate, although, it is second order accurate for steady-state solutions [9]. Using a combination of numerical techniques presented in [18, 21, 23, 34, 101], the following numerical scheme is proposed to solve Eq. (3.54):

$$\begin{aligned}
 \mathbf{w}_i^{n+1} = & \mathbf{w}_i^n + \frac{\Delta t}{\Delta x} \left(\mathbf{f}_{i-1/2} - \mathbf{f}_{i+1/2} \right) \\
 & + \frac{\Delta t}{2\Delta x} \left[\mathbf{B}_{i-1/2}(\mathbf{w}_i^n - \mathbf{w}_{i-1}^n) + \mathbf{B}_{i+1/2}(\mathbf{w}_{i+1}^n - \mathbf{w}_i^n) \right] \\
 & + \frac{\Delta t}{2\Delta x} \left(\mathbf{v}_{i-1/2} + \mathbf{v}_{i+1/2} \right) \\
 & + \frac{\Delta t}{\Delta x} \left(\mathbf{P}_{i-1/2}^+ \mathbf{g}_{i-1/2} + \mathbf{P}_{i+1/2}^- \mathbf{g}_{i+1/2} \right) \\
 & + \Delta t \left(\mathbf{P}_{i-1/2}^+ \mathbf{s}_{i-1/2} + \mathbf{P}_{i+1/2}^- \mathbf{s}_{i+1/2} \right),
 \end{aligned} \tag{4.32}$$

with numerical fluxes defined as follows [18]:

$$\mathbf{f}_{i+1/2} = \frac{1}{2} \left[\mathbf{f}(\boldsymbol{\sigma}_i^n, \mathbf{w}_i^n) + \mathbf{f}(\boldsymbol{\sigma}_{i+1}^n, \mathbf{w}_{i+1}^n) \right] - \frac{1}{2} |\mathcal{Q}_{i+1/2}| (\mathbf{w}_{i+1}^n - \mathbf{w}_i^n), \tag{4.33}$$

$$\mathbf{f}_{i-1/2} = \frac{1}{2} \left[\mathbf{f}(\boldsymbol{\sigma}_{i-1}^n, \mathbf{w}_{i-1}^n) + \mathbf{f}(\boldsymbol{\sigma}_i^n, \mathbf{w}_i^n) \right] - \frac{1}{2} |\mathcal{Q}_{i-1/2}| (\mathbf{w}_i^n - \mathbf{w}_{i-1}^n), \tag{4.34}$$

and the following projection matrices used to upwind source terms [18]:

$$\mathbf{P}_{i+1/2}^\pm = \frac{1}{2} \mathbf{K}_{i+1/2} \left(\mathbf{Id} \pm \text{sgn}(\boldsymbol{\Psi}_{i+1/2}) \right) \mathbf{K}_{i+1/2}^{-1}, \tag{4.35}$$

$$\mathbf{P}_{i-1/2}^\pm = \frac{1}{2} \mathbf{K}_{i-1/2} \left(\mathbf{Id} \pm \text{sgn}(\boldsymbol{\Psi}_{i-1/2}) \right) \mathbf{K}_{i-1/2}^{-1}, \tag{4.36}$$

where \mathbf{Id} is 4×4 identity matrix, and

$$\text{sgn}(\mathbf{\Psi}_{i+1/2}) = \begin{bmatrix} \text{sgn}(\psi_{i+1/2,1}) & & & 0 \\ & \ddots & & \\ & & & \text{sgn}(\psi_{i+1/2,4}) \\ 0 & & & \end{bmatrix}. \quad (4.37)$$

Note that the projection matrices are derived from the eigenvalues and eigenvectors of the matrix $\mathbf{Q}_{i+1/2}$. The eigenvalues $\psi_{i+1/2,l}$, $1 \leq l \leq 4$, are categorized as two external and two internal eigenvalues, which relate to wave speeds. The analytical solutions for eigenvalues are unknown; therefore, the QZ algorithm [67] was used.

If the signs of internal eigenvalues are the same, the flow is internally supercritical, if one of them is equal to zero, the flow is internally critical, and if the signs differ, the flow is internally subcritical. Castro *et al.* [18] deduced from the matrix $\mathbf{Q}(\boldsymbol{\sigma}, \mathbf{w})$ that internally critical, subcritical, and supercritical flow, corresponding to $G^2 = 1$, $G^2 < 1$, and $G^2 > 1$, respectively, is defined for irregular cross sections as

$$G^2 = Fd_1^2 + Fd_2^2 - (1-r) \frac{\sigma_2}{\sigma_3} Fd_1^2 Fd_2^2, \quad (4.38)$$

with

$$Fd_1^2 = \frac{Q_1^2 \sigma_1}{g(1-r)A_1^3} \frac{\sigma_3}{\sigma_2} \quad \text{and} \quad Fd_2^2 = \frac{Q_2^2 \sigma_3}{g(1-r)A_2^3}, \quad (4.39)$$

where Fd_1 and Fd_2 are respective upper and lower layer densimetric Froude numbers in channels with irregular cross section geometry [18].

Intermediate states

Once the solutions \mathbf{w}_i^n are known at each cell i at a given time step t^n , the intermediate values are computed at intercells to linearise the system. The Q-scheme of Roe approximates the intermediate states for SWE in channels with irregular geometry as follows [18]:

$$\mathbf{w}_{i+1/2}^n = \left\{ A_{i+1/2,1}^n \quad Q_{i+1/2,1}^n \quad A_{i+1/2,2}^n \quad Q_{i+1/2,2}^n \right\}^T, \quad (4.40)$$

where

$$A_{i+1/2,j}^n = \frac{A_{i,j}^n + A_{i+1,j}^n}{2}, \quad (4.41)$$

$$u_{i+1/2,j}^n = \frac{u_{i,j}^n \sqrt{A_{i,j}^n} + u_{i+1,j}^n \sqrt{A_{i+1,j}^n}}{\sqrt{A_{i,j}^n} + \sqrt{A_{i+1,j}^n}}, \quad (4.42)$$

$$Q_{i+1/2,j}^n = A_{i+1/2,j}^n u_{i+1/2,j}^n, \quad (4.43)$$

and also

$$\mathcal{Q}_{i+1/2}^n = \mathbf{J}_{i+1/2}^n - \mathbf{B}_{i+1/2}^n, \quad (4.44)$$

where matrices $\mathbf{J}_{i+1/2}^n$ and $\mathbf{B}_{i+1/2}^n$ correspond to $\mathbf{J}(\boldsymbol{\sigma}_{i+1/2}^n, \mathbf{w}_{i+1/2}^n)$ and $\mathbf{B}(\boldsymbol{\sigma}_{i+1/2}^n, \mathbf{w}_{i+1/2}^n)$, respectively, with

$$\sigma_{i+1/2,1}^n = \frac{\sigma_{i,1}^n + \sigma_{i+1,1}^n}{2}, \quad (4.45)$$

$$\sigma_{i+1/2,3}^n = \frac{\sigma_{i,3}^n + \sigma_{i+1,3}^n}{2}, \quad (4.46)$$

$$\frac{1}{\sigma_{i+1/2,2}^n} = \frac{1-r}{\sigma_{i+1/2,3}^n} + \frac{r}{\sigma_{i+1/2,1}^n}. \quad (4.47)$$

To satisfy the *conservation property* (C-property) [9], *i.e.*, to exactly preserve the steady-state solution for water at rest ($Q_{i,j} = 0$, $\eta_i = b_i + h_{i,1} + h_{i,2} = \text{const.}$), the following equality must be true [18]:

$$\mathcal{Q}_{i+1/2}(\mathbf{w}_{i+1} - \mathbf{w}_i) = \mathbf{f}(\mathbf{w}_{i+1}) - \mathbf{f}(\mathbf{w}_i) - \mathbf{v}_{i+1/2} - \mathbf{B}_{i+1}(\mathbf{w}_{i+1} - \mathbf{w}_i). \quad (4.48)$$

Condition (4.48) is satisfied when $\mathbf{v}_{i+1/2}^n$ is equal to $\{0 \ v_{i+1/2,1}^n \ 0 \ v_{i+1/2,2}^n\}^T$ [18], where

$$\begin{aligned} v_{i+1/2,j}^n &= \frac{g}{2} \left(\frac{1}{\sigma_{i+1,j}^n} - \frac{1}{\sigma_{i+1/2,j}^n} \right) (A_{i+1,j}^n)^2 + \\ &\frac{g}{2} \left(\frac{1}{\sigma_{i+1/2,j}^n} - \frac{1}{\sigma_{i,j}^n} \right) (A_{i,j}^n)^2. \end{aligned} \quad (4.49)$$

The intermediate states for source terms are computed in a similar manner. The source term corresponding to irregular geometry is approximated as [18]:

$$\mathbf{g}_{i+1/2}^n = \begin{Bmatrix} 0 \\ g_{i+1/2,1}^n \\ 0 \\ g_{i+1/2,2}^n \end{Bmatrix}, \quad (4.50)$$

where

$$\begin{aligned} g_{i+1/2,1}^n &= g \frac{A_{i+1/2,1}^n}{\sigma_{i+1/2,1}^n} (A_{i+1,1}^n + A_{i+1,2}^n - A_{i,1}^n - A_{i,2}^n) \\ &- g A_{i+1/2,1}^n (b_{i+1} + h_{i+1,2}^n + h_{i+1,1}^n - b_i - h_{i,2}^n - h_{i,1}^n) \end{aligned} \quad (4.51)$$

and

$$g_{i+1/2,2}^n = \frac{gA_{i+1/2,2}^n}{\sigma_{i+1/2,2}^n} (A_{i+1,2}^n - A_{i,2}^n) + \frac{rgA_{i+1/2,2}^n}{\sigma_{i+1/2,1}^n} (A_{i+1,1}^n - A_{i,1}^n) \quad (4.52)$$

$$- gA_{i+1/2,2}^n (b_{i+1} + h_{i+1,2}^n + rh_{i+1,1}^n - b_i - h_{i,2}^n - rh_{i,1}^n).$$

An additional effort in this thesis was made to evaluate intermediate states for friction and entrainment terms. Let us recall that the second source term (3.61) accounts for friction and entrainment, as follows:

$$\mathbf{s}_{i+1/2}^n = \left\{ \begin{array}{l} \mathbf{s}_{\text{E},i+1/2,1[1]}^n \\ \mathbf{s}_{\text{F},i+1/2,1}^n + \mathbf{s}_{\text{E},i+1/2,1[2]}^n \\ \mathbf{s}_{\text{E},i+1/2,2[1]}^n \\ \mathbf{s}_{\text{F},i+1/2,2}^n + \mathbf{s}_{\text{E},i+1/2,2[2]}^n \end{array} \right\}. \quad (4.53)$$

The intermediate friction source terms are therefore approximated as:

$$s_{\text{F},i+1/2,1}^n = -gA_{i+1/2,1}^n \frac{n_{\text{M}}^2 u_{i+1/2,1}^n |u_{i+1/2,1}^n|}{(R_{h,i+1/2,1}^n)^{4/3}} \quad (4.54)$$

$$- \lambda_i (u_{i+1/2,1}^n - u_{i+1/2,2}^n) |u_{i+1/2,1}^n - u_{i+1/2,2}^n| \sigma_{i+1/2,3}^n$$

$$s_{\text{F},i+1/2,1}^n = -\lambda_w (u_{i+1/2,1}^n) |u_{i+1/2,1}^n| P_{i+1/2,1}^n$$

$$- \lambda_i (u_{i+1/2,1}^n - u_{i+1/2,2}^n) |u_{i+1/2,1}^n - u_{i+1/2,2}^n| \sigma_{i+1/2,3}^n,$$

and

$$s_{\text{F},i+1/2,2}^n = -gA_{i+1/2,2}^n \frac{n_{\text{M}}^2 u_{i+1/2,2}^n |u_{i+1/2,2}^n|}{(R_{h,i+1/2,2}^n)^{4/3}} \quad (4.55)$$

$$- r\lambda_i (u_{i+1/2,2}^n - u_{i+1/2,1}^n) |u_{i+1/2,2}^n - u_{i+1/2,1}^n| \sigma_{i+1/2,3}^n$$

$$s_{\text{F},i+1/2,2}^n = -\lambda_b (u_{i+1/2,2}^n) |u_{i+1/2,2}^n| P_{i+1/2,2}^n$$

$$- r\lambda_i (u_{i+1/2,2}^n - u_{i+1/2,1}^n) |u_{i+1/2,2}^n - u_{i+1/2,1}^n| \sigma_{i+1/2,3}^n.$$

Whereas, the entrainment intermediate states are approximated as:

$$s_{\text{E},i+1/2,1[1]}^n = \frac{1}{r} w_e \sigma_{i+1/2,3}^n, \quad (4.56)$$

$$s_{\text{E},i+1/2,1[2]}^n = w_e u_{i+1/2,1}^n \sigma_{i+1/2,3}^n, \quad (4.57)$$

$$s_{\text{E},i+1/2,2[1]}^n = -w_e \sigma_{i+1/2,3}^n, \quad (4.58)$$

$$s_{\text{E},i+1/2,2[2]}^n = -w_e u_{i+1/2,2}^n \sigma_{i+1/2,3}^n. \quad (4.59)$$

Harten regularization

For either internally or externally critical flow, one of the eigenvalues is equal to zero and numerical viscosity of the Q-scheme may vanish. To prevent this, Castro *et al.* [18] proposed to apply the Harten regularization [44] and redefined Eq. (4.33) as follows:

$$\mathbf{f}_{i+1/2} = \frac{1}{2} \left[\mathbf{f}(\boldsymbol{\sigma}_i^n, \mathbf{w}_i^n) + \mathbf{f}(\boldsymbol{\sigma}_{i+1}^n, \mathbf{w}_{i+1}^n) \right] - \frac{1}{2} |\mathcal{Q}_{i+1/2}|_\epsilon (\mathbf{w}_{i+1}^n - \mathbf{w}_i^n), \quad (4.60)$$

where

$$|\mathcal{Q}_{i+1/2}|_\epsilon = \mathbf{K}_{i+1/2} |\boldsymbol{\Psi}_{i+1/2}|_\epsilon \mathbf{K}_{i+1/2}^{-1}. \quad (4.61)$$

Each diagonal coefficient of matrix $|\boldsymbol{\Psi}_{i+1/2}|_\epsilon$ is modified as follows:

$$|\psi_{i+1/2,l}|_\epsilon = |\psi_{i+1/2,l}| + 0.5 \left[1 + \text{sgn}(\epsilon - |\psi_{i+1/2,l}|) \right] \left(\frac{\psi_{i+1/2,l}^2 + \epsilon^2}{2\epsilon} - |\psi_{i+1/2,l}| \right), \quad (4.62)$$

where $1 \leq l \leq 4$ and ϵ is a correction parameter, usually chosen to be around 0.1 [18].

On hyperbolicity and interfacial instabilities

Sometimes complex eigenvalues may appear in the matrix \mathcal{Q} , and then Eq. (3.54) loses its hyperbolic character. This problem is related to the occurrence of shear driven instabilities, such as Kelvin-Helmholtz or Holmboe waves [16]. In real flows, these instabilities usually initiate interfacial mixing, which then dissipates some of the turbulent energy. Unfortunately, the considered model breaks down if complex eigenvalues appear, and cannot simulate unstable flows. Adequate friction, however, can reduce some of the locally confined shear instabilities enough to maintain the hyperbolic character of the PDE system. The practical problem is that too much friction may result in excessively diffused results and even produce spurious oscillations in the flow.

Castro *et al.* [16] presented a different strategy for maintaining the hyperbolic character. This numerical technique uses a predictor/corrector algorithm, which adds an extra friction term only to those individual cells where complex eigenvalues are detected at each time step [16]. The additional friction should represent the loss of momentum due to mixing, which is expected in real flows as a result of interfacial instabilities. However, this method is justified only if instabilities are confined in space and time.

A generalized solution for this problem should include a more physical interpretation of interfacial processes and a numerical model that accounts for both friction and entrainment terms, which are variable in space and time. In the present study, adding physically relevant friction and entrainment terms prevented the appearance of complex eigenvalues and maintained the hyperbolic character in all examined cases.

Stability of the explicit scheme

The explicit schemes are stable only if Δx and Δt satisfy the *Courant-Friedrichs-Lewy* (CFL) condition [97]. Castro *et al.* [18] included eigenvalues of the matrix \mathcal{Q} in a CFL-like condition to ensure the scheme's stability:

$$\max \left(|\psi_{i+1/2,l}| \right) \frac{\Delta t}{\Delta x} \leq \text{CFL} \leq 1.0, \quad (4.63)$$

where $1 \leq l \leq 4$ and $1 \leq i \leq M$.

However, friction may sometimes become dominant in shallow water flow, and it is essential to impose an additional stability condition. Burguete *et al.* [14] proposed the following condition for a single layer:

$$-\frac{s_i}{2} \Delta x - \frac{(Q_i)^2}{A_i} \leq 0, \quad (4.64)$$

where s_i is the source term accounting for friction. For arrested salt-wedge and no entrainment $w_e = 0$, the lower layer is stagnant $Q_2 = 0$, and only the friction source term for the upper layer remains $s_i = s_{F,i,1}$; therefore, the condition (4.64) for a two-layer case is written as follows:

$$\left[\frac{\lambda_w}{2} \frac{Q_{i,1}^2}{A_{i,1}^2} P_{i,1} + \frac{\lambda_i}{2} \frac{Q_{i,1}^2}{A_{i,1}^2} \sigma_{i,3} \right] \Delta x - \frac{(Q_{i,1})^2}{A_{i,1}} \leq 0, \quad (4.65)$$

which is further simplified to

$$\Delta x \leq \frac{2R_{h,i,1}}{\lambda_i \frac{\sigma_{i,3}}{P_{i,1}} + \lambda_w}, \quad 1 \leq i \leq M. \quad (4.66)$$

This condition implies that the grid size is limited by the sum of interfacial and bed/wall friction factor, as well as the upper layer hydraulic radius. It also implies that denser meshes have fewer problems with instabilities caused by the friction.

Conservation property

Bermudez and Vázquez [9] showed that a central discretization of source terms may results in spurious oscillations, *i.e.*, non-physical waves; therefore, the source terms should be upwinded. The same authors proposed a well-balanced condition called *conservation property* (C-property), which prevents the appearance of non-physical oscillations. A numerical scheme is said to satisfy the C-property if it exactly preserves the steady-state solution for water at rest, as illustrated in Fig. 4.4,

$$Q_{i,1} = 0, \quad Q_{i,2} = 0, \quad (4.67)$$

$$\eta_{i,1} = b_i + h_{i,2} + h_{i,1} = \text{const.}, \quad (4.68)$$

$$\eta_{i,2} = b_i + h_{i,2} = \text{const.}, \quad (4.69)$$

with $1 \leq i \leq M$.

Castro *et al.* [18] demonstrated that a Q-scheme applied to a two-layer flow in channels with arbitrary cross-sections satisfies the C-property if the following equalities hold:

$$\mathcal{Q}_{i+1/2}(\mathbf{w}_{i+1} - \mathbf{w}_i) = \mathbf{f}(\mathbf{w}_{i+1}) - \mathbf{f}(\mathbf{w}_i) - \mathbf{v}_{i+1/2} - \mathbf{B}_{i+1}(\mathbf{w}_{i+1} - \mathbf{w}_i) \quad (4.70)$$

and

$$\mathcal{Q}_{i+1/2}(\mathbf{w}_{i+1} - \mathbf{w}_i) = \mathbf{g}_{i+1/2} + \mathbf{s}_{i+1/2}. \quad (4.71)$$

The first condition is true because the numerical treatment of the term $\mathbf{v}_{i+1/2}$ (Eq. 4.49) was derived specifically to satisfy Eq. (4.70) [18].

On the other hand, to prove the second condition (4.71), the non-zero components of the source terms (Eqs. 4.50 and 4.53) for steady-state flow corresponding to water at rest are written as follows:

$$g_{i+1/2,1} = g \frac{A_{i+1/2,1}}{\sigma_{i+1/2,1}} (A_{i+1,1} + A_{i+1,2} - A_{i,1} - A_{i,2}), \quad (4.72)$$

$$g_{i+1/2,2} = g \frac{A_{i+1/2,2}}{\sigma_{i+1/2,2}} (A_{i+1,2} - A_{i,2}) + rg \frac{A_{i+1/2,2}}{\sigma_{i+1/2,1}} (A_{i+1,1} - A_{i,1}), \quad (4.73)$$

$$s_{F,i+1/2,1} = 0, \quad s_{F,i+1/2,2} = 0, \quad (4.74)$$

$$s_{E,i+1/2,1} = \{0 \ 0\}^T, \quad s_{E,i+1/2,2} = \{0 \ 0\}^T. \quad (4.75)$$

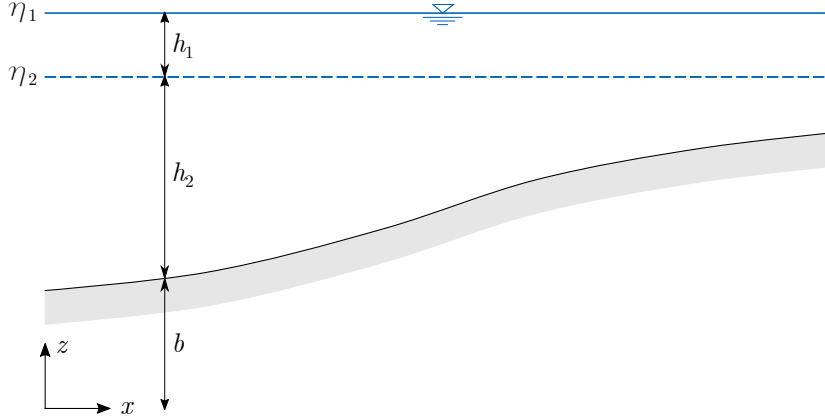


Figure 4.4: Longitudinal section of the channel corresponding to water at rest.

Similarly, the matrix $\mathcal{Q}_{i+1/2}$ for the same conditions is written as:

$$\mathcal{Q}_{i+1/2} = \begin{bmatrix} 0 & 1 & 0 & 0 \\ \frac{g}{\sigma_{i+1/2,1}} A_{i+1/2,1} & 0 & \frac{g}{\sigma_{i+1/2,1}} A_{i+1/2,1} & 0 \\ 0 & 0 & 0 & 1 \\ \frac{rg}{\sigma_{i+1/2,1}} A_{i+1/2,2} & 0 & \frac{g}{\sigma_{i+1/2,2}} A_{i+1/2,2} & 0 \end{bmatrix}. \quad (4.76)$$

Therefore, with $\mathbf{w}_i = \{A_{i,1} \ 0 \ A_{i,2} \ 0\}^T$ and $\mathbf{w}_{i+1} = \{A_{i+1,1} \ 0 \ A_{i+1,2} \ 0\}^T$ it is easy to verify that Eq. (4.71) is also true, and the numerical scheme satisfies the C-property.

4.2.4 Wet-dry fronts in channels with irregular geometry

Wet-dry fronts appear at the intercell between a dry and a wet cell, *i.e.* a salt-wedge front. Various numerical techniques were developed to deal with dry cells [11, 10, 17, 20, 22]. In this thesis a fixed mesh was considered, and the cells were allowed to be wetted by either both layers or by the upper layer alone. A tolerance parameter ε was defined to avoid instabilities and negative depths. When $h_{i,2} < \varepsilon$, the cell C_i was considered wetted only by the upper layer, and the lower layer velocity was set to zero $u_{i,2} = 0$; however, the layer thickness $h_{i,2}$ remains unchanged in order to preserve the mass conservation property of the scheme. Note that the value of ε should be chosen as small as possible for more accurate results (in this work the range of values 0.01 - 0.05 m has proved adequate).

It is said that the treatment of wet-dry fronts is appropriate if the numerical scheme satisfies the *extended C-property* [17]. This condition implies that a numerical

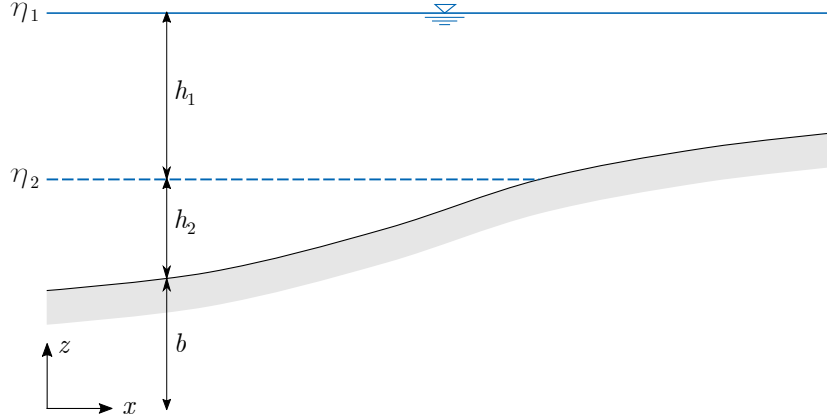


Figure 4.5: Longitudinal section of the channel corresponding to water at rest with wet-dry transition in the lower layer.

steady-state solution for water at rest including wet-dry fronts has to exactly conserve the mass and momentum equations without any spurious oscillations. Otherwise, dry cells may become artificial wetted and non-physical flow may appear. Brufau [11] presented a numerical scheme for one-layer flow that satisfies the extended C-property, and Castro *et al.* [17] derived a modification for two-layer flow through channels with rectangular cross-sections. This modification for a two-layer case was extended here for a more general case of a two-layer flow through channels with irregular cross sections.

First, let us show that the extended C-property is not satisfied when a lower layer wet-dry front appears in channels with irregular cross-sections. Consider a steady-state flow corresponding to water at rest as illustrated in Fig. 4.5. The lower layer source term (Eq. 4.52) is written as follows:

$$g_{i+1/2,2} = g \frac{A_{i+1/2,2}}{\sigma_{i+1/2,2}} (A_{i+1,2} - A_{i,2}) + rg \frac{A_{i+1/2,2}}{\sigma_{i+1/2,1}} (A_{i+1,1} - A_{i,1}) - gA_{i+1/2,2} (b_{i+1} + rh_{i+1,1} - b_i - rh_{i,1} - h_{i,2}), \quad (4.77)$$

and the matrix $\mathcal{Q}_{i+1/2}$ is equal to Eq. (4.76). Therefore, Eq. (4.71) is not true $\mathcal{Q}_{i+1/2}(\mathbf{w}_{i+1} - \mathbf{w}_i) \neq \mathbf{g}_{i+1/2} + \mathbf{s}_{i+1/2}$, and spurious oscillations may appear in a steady-state flow.

However, the source terms can be modified to satisfy the extended C-property if function $b(x)$ is regular enough. Assuming a piecewise bed elevation function,

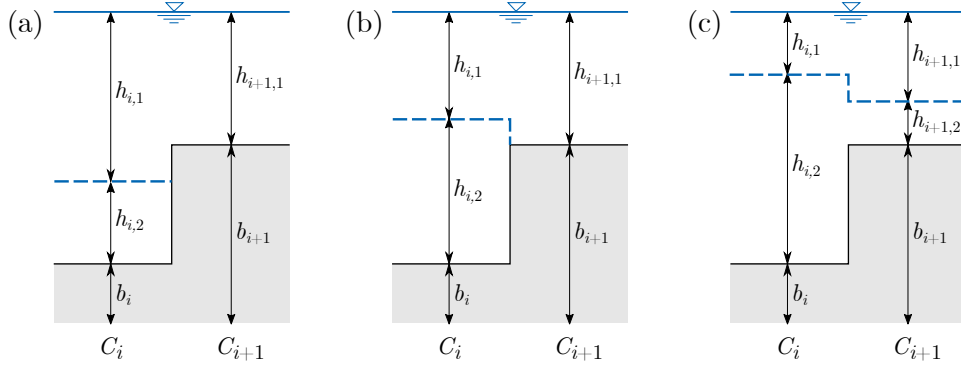


Figure 4.6: Wet-dry fronts: (a) bed elevation redefinition and reflective condition is needed, (b) and (c) no redefinition needed.

with discontinuities at cell interfaces, the numerical source term for bed elevation is redefined and appropriate reflection conditions are set (Fig. 4.6). For the wet-dry transition occurring at the interface $x_{i+1/2}$, between cells C_i and C_{i+1} , one part of the lower layer source term (Eq. 4.52) accounting for bed elevations, $\Delta b = b_{i+1} - b_i$, is modified as follows:

$$\Delta b = \begin{cases} r(b_{i+1} - b_i) + (1-r)h_{i,2} & \text{if } h_{i+1,2} < \epsilon \text{ and } h_{i,2} \leq \Delta b \\ r(b_{i+1} - b_i) - (1-r)h_{i+1,2} & \text{if } h_{i,2} < \epsilon \text{ and } h_{i+1,2} \leq -\Delta b \\ b_{i+1} - b_i & \text{otherwise} \end{cases} \quad (4.78)$$

Under general assumption that the cell C_i is wetted only by the upper layer ($h_{i,2} < \epsilon$), the reflection condition is imposed to ensure that the wet-dry front is not allowed to advance until $h_{i,2}$ becomes larger than the bed step Δb . This condition states

$$Q_{i+1/2,2} = \begin{cases} 0 & \text{if } h_{i+1,2} < \epsilon \text{ and } h_{i,2} \leq \Delta b \\ 0 & \text{if } h_{i,2} < \epsilon \text{ and } h_{i+1,2} \leq -\Delta b \\ A_{i+1/2,2}u_{i+1/2,2} & \text{otherwise} \end{cases} \quad (4.79)$$

Notice that only the intercell flow rate $Q_{i+1/2,2}$ is set to zero, while the flow rate in the wetted cell is computed as usual from Eq. (3.54).

We can now easily verify that the non-zero components of the lower layer source term (Eq. 4.52) redefined by Eq. (4.78) is written as:

$$g_{i+1/2,2} = g \frac{A_{i+1/2,2}}{\sigma_{i+1/2,2}} (A_{i+1,2} - A_{i,2}) + rg \frac{A_{i+1/2,2}}{\sigma_{i+1/2,1}} (A_{i+1,1} - A_{i,1}). \quad (4.80)$$

Therefore, Eq. (4.71) is true and the extended C-property is satisfied when a lower layer wet-dry front appears. A similar treatment of the upper layer wet-dry front can be applied, although such redefinition is not needed in salt-wedge models.

The problem of wetting and drying in two-layer flows is still not completely resolved, especially if high accuracy in computing the propagation speed of wet-dry fronts is required. Recently, Castro *et al.* [20] proposed a more physically accurate treatment for a single layer; a non-linear Riemann problem is solved at all intercells where a wet-dry front is detected. Unfortunately, this numerical treatment is not easily extended for a two-layer case [20]. Besides, the largest differences in propagation velocities of the wet-dry front for a single layer, between the original treatment [17] and the more advanced treatment that solves non-linear Riemann problem [20] was under 5% for all experiments presented by Castro *et al.* [20]. This difference in accuracy is considered minimal in field applications.

4.2.5 Boundary conditions for time-dependant salt-wedges

The upstream boundary condition in salt-wedge estuaries is usually defined by either the stage or flow hydrograph, which are both easily implemented [58]. The downstream boundary condition, however, deserves more discussion.

As mentioned before, in arrested salt-wedge models it is usually assumed that the flow in the upper layer is critical at the mouth [86, 7]. Similarly, in time-dependant salt-wedge models both layers are active, and the critical flow should be described by a composite Froude number G (Eq. 4.38). Therefore, the equality $G^2 = 1$ is solved iteratively for known values of Q_1 and Q_2 . The flow rates in both layer are set to a zero-gradient condition, where $Q_{M,j}^n = Q_{M-1,j}^n$, $j = 1, 2$.

Sometimes, it is difficult to determine the exact position of the mouth for the realistic geometry of the salt-wedge estuaries. However, Armi and Farmer [5] showed that in two-layer flows an internally critical flow (hydraulic control) may also be located at a point of strong channel contractions, which are more easily identified. In this thesis a downstream boundary was positioned near the mouth at a point where bridge abutments formed a strong channel contraction.

5

Numerical model performance assessment

Contents

5.1	Code verification	60
5.1.1	Comparison with analytical solutions	60
5.1.2	Comparison between FDM and FVM models	61
5.2	Well-balanced property of FVM model	65
5.2.1	Verification of the C-property	65
5.2.2	Verification of the extended C-property	67
5.3	Numerical model sensitivity	69
5.3.1	Influence of interfacial friction	69
5.3.2	Influence of bed friction	70
5.3.3	Influence of entrainment	70
5.3.4	Influence of density ratio	72

Abstract

This chapter presents several numerical experiments that verify the properties of two proposed schemes. Numerical solutions are compared against analytical solutions of arrested salt-wedges, and between two different numerical schemes. Furthermore, well-balanced property of the FVM model is discussed and verified in practice. Numerical sensitivity to interfacial friction, bed friction, entrainment, and density ratio is also investigated.

5.1 Code verification

Verification of two-layer numerical models is not an easy task because the exact solutions for salt-wedge profiles are unknown. The only exception is a simplified case of an arrested salt-wedge in a prismatic channel with rectangular cross-sections and a horizontal bed, where the bed friction and entrainment are neglected. Therefore, both proposed models were first verified for this simplified case, by comparing the numerical results to analytical solutions. The proposed models were also verified for salt-wedge flow in non-prismatic channels with variable depth, by comparing the numerical results from two different models between each other.

5.1.1 Comparison with analytical solutions

For a simplified case of an arrested salt-wedge in a prismatic channel with rectangular cross-sections and a horizontal bed, exact solutions are given by Eq. (2.7). Unfortunately, in the process of deriving Eq. (2.7), the Boussinesq approximation is used, which disregards the density ratio r everywhere except where multiplied by g . Hence, the numerical and exact solution will always slightly disagree. Nevertheless, solutions by FDM and FVM models were compared to exact solutions (for r close to 1) to qualitatively assess their performance.

First, the FDM model was used to compute interface profiles of the arrested salt-wedge for different river flow rates. A 10 km long prismatic channel was considered, defined by rectangular cross-sections of constant depth $b(x) = 0.5$ m and width $\sigma(x) = 20$ m, as illustrated in Fig. 5.1. The spatial step was set to $\Delta x = 10$ m, the interfacial friction factor to $\lambda_i = 10^{-3}$, and the density ratio to $r = 0.975$. The downstream boundary condition was forced by a total water depth $H = 1.5$ m and the upper layer thickness h_1 , which was computed from the critical flow condition $Fd^2 = 1$.

The FVM model was also applied for the same flow conditions. A 10 km long prismatic channel was considered as previously (Fig. 5.1). The spatial step was set to $\Delta x = 100$ m and the temporal step to $\Delta t = 5$ s, which gives an average CFL ≈ 0.5 . The interfacial friction factor was set to $\lambda_i = 10^{-3}$ and the density ratio to $r = 0.975$. The upstream boundary condition was forced by a constant river flow rate $Q(x_M, t) = Q(x_M, 0)$. The downstream boundary condition was forced by a constant total water depth $H(x_0, t) = 1.5$ m and upper layer thickness $h_1(x_0, t)$,

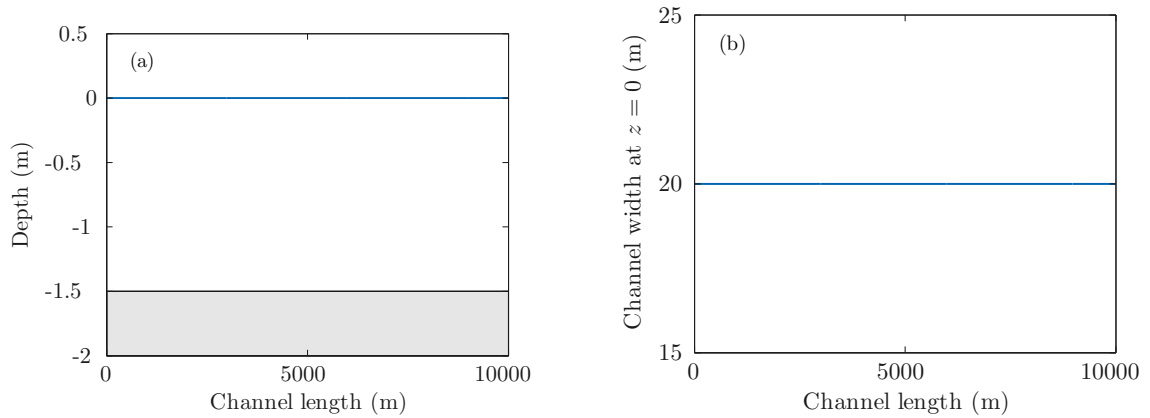


Figure 5.1: Prismatic channel geometry defined by (a) horizontal bed and (b) rectangular cross-sections of constant width.

which was computed from the critical flow condition $G^2(x_0, t) = 1$. The solution from the FDM model was used as the initial condition, and the simulation ended when a steady-state flow was reached.

Figure 5.2 shows computed steady-state solutions by the proposed FDM and FVM models compared against the exact solution of an arrested salt-wedge for flow rates 1.6, 2.1, and 3.0 $\text{m}^3 \text{s}^{-1}$. The agreement between both models and the exact solution is satisfactory in all cases. Slightly shorter salt-wedge length, computed by the analytical model, is probably the results of the Boussinesq approximation. Solutions obtained by the FDM and FVM models, on the other hand, look almost the same.

5.1.2 Comparison between FDM and FVM models

The aim of this numerical experiment is to assess the ability of both models to correctly compute steady-state solutions of an arrested salt-wedge in non-prismatic channels, defined by rectangular cross-sections with variable depth and width, that also includes the bed friction. As the exact solution is unknown, the numerical solutions obtained by two different numerical models (FDM and FVM) were compared between each other.

The geometry of 1000 m long channel was defined by the following bed elevation function (Fig. 5.3a):

$$b(x) = \frac{2.3}{\cosh^2(x/600)}, \quad (5.1)$$

5. Numerical model performance assessment

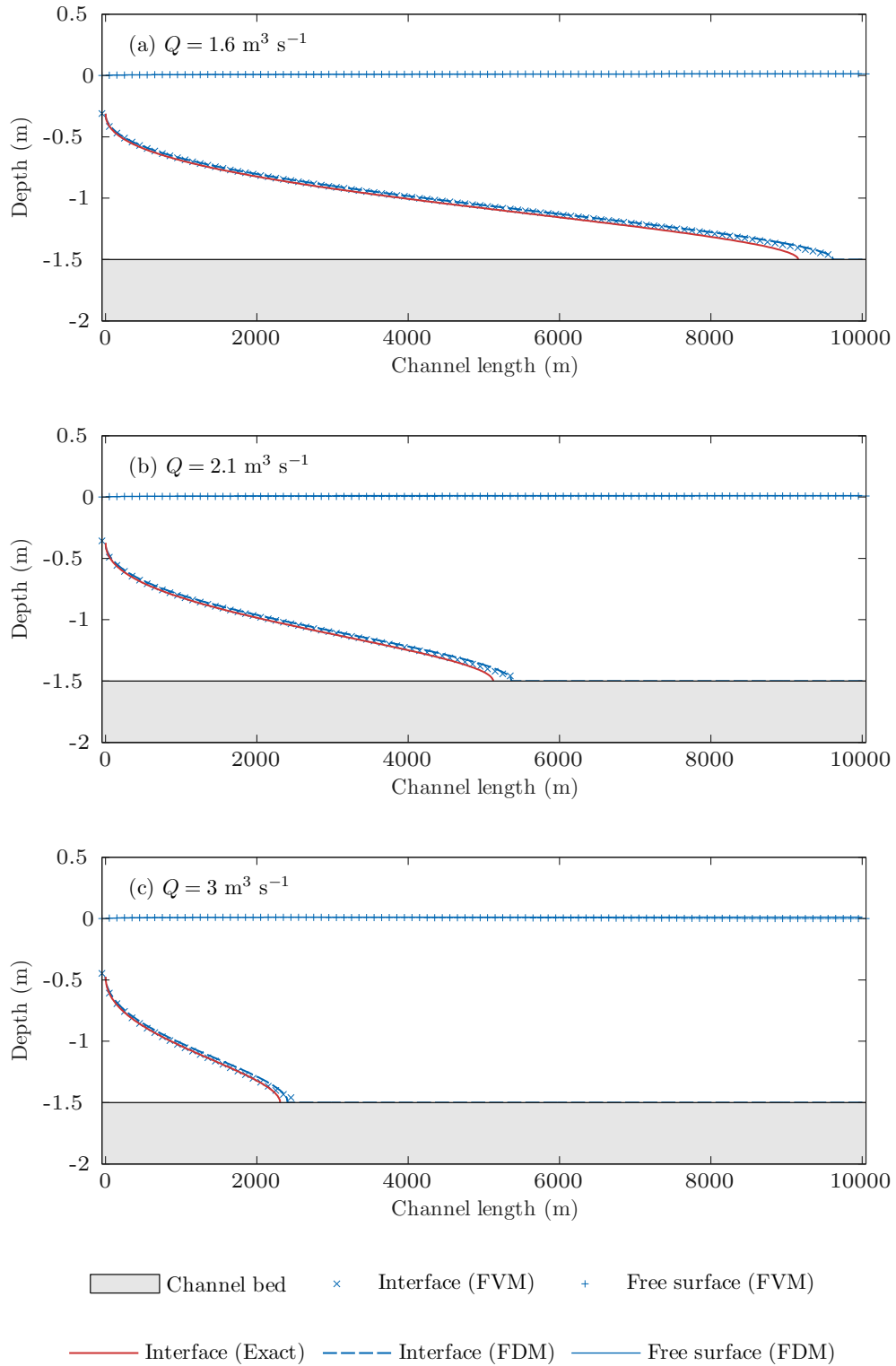


Figure 5.2: Numerical solutions for the arrested salt-wedge obtained by a steady FDM and a time-dependant FVM model, and their agreement with the exact solution for (a) $Q = 1.6 \text{ m}^3 \text{ s}^{-1}$, (b) $Q = 2.1 \text{ m}^3 \text{ s}^{-1}$ and (c) $Q = 3.0 \text{ m}^3 \text{ s}^{-1}$.

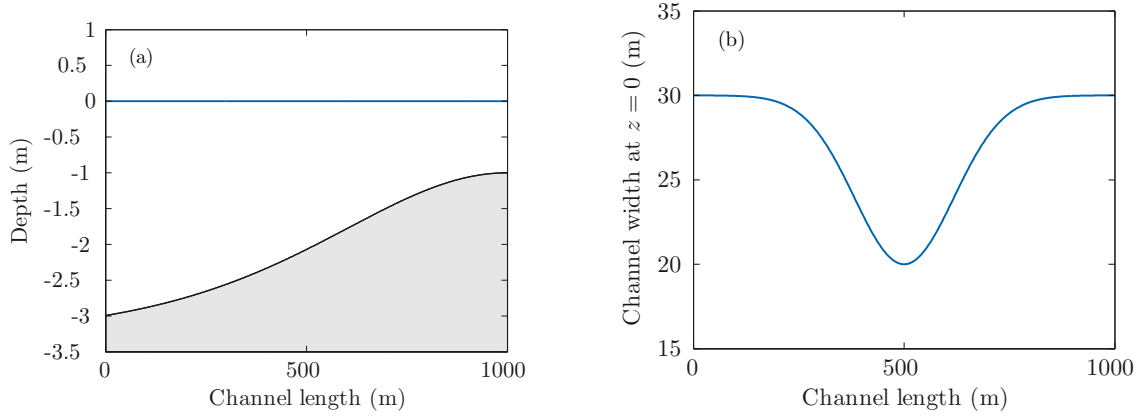


Figure 5.3: Non-prismatic channel geometry defined by (a) variable bed slope and (b) rectangular cross-sections of variable width.

and rectangular cross-sections with a contraction located at the middle of the channel (Fig. 5.3b):

$$\sigma(x) = 20 + 10 \left[1 - \exp \left(-9 \left(\frac{x}{500} - 1 \right)^2 \right) \right]. \quad (5.2)$$

As previously, the FDM model was used to compute the interface profile of an arrested salt-wedge for different river flow rates. The spatial step was set to $\Delta x = 10$ m, the interfacial friction factor to $\lambda_i = 10^{-3}$, the bed and wall friction were defined by Manning's roughness coefficient $n_M = 0.025 \text{ m}^{-1/3} \text{ s}$, and the density ratio was $r = 0.975$. The downstream boundary condition was forced by a total depth $H = 3.0$ m and the upper layer thickness at the mouth h_1 , which was computed from the critical flow condition $Fd^2 = 1$.

The FVM model was also applied for the same flow conditions. The spatial step was set to $\Delta x = 10$ m and the temporal step to $\Delta t = 0.5$ s, which gives an average CFL ≈ 0.5 . The friction factors and the density ratio were the same as in the FDM model. The upstream boundary condition defined a constant river flow rate $Q(x_M, t) = Q(x_M, 0)$. Whereas, the downstream boundary condition was forced by a constant total water depth $H(x_0, t) = 3.0$ m and a critical flow at the mouth. The solution from the FDM model was used as the initial condition, and the simulation ended when a steady-state flow was reached.

Figure 5.4 shows the steady-state solutions of an arrested salt wedge, in a channel with variable geometry, computed by both FDM and FVM model for flow rates 4, 9

5. Numerical model performance assessment

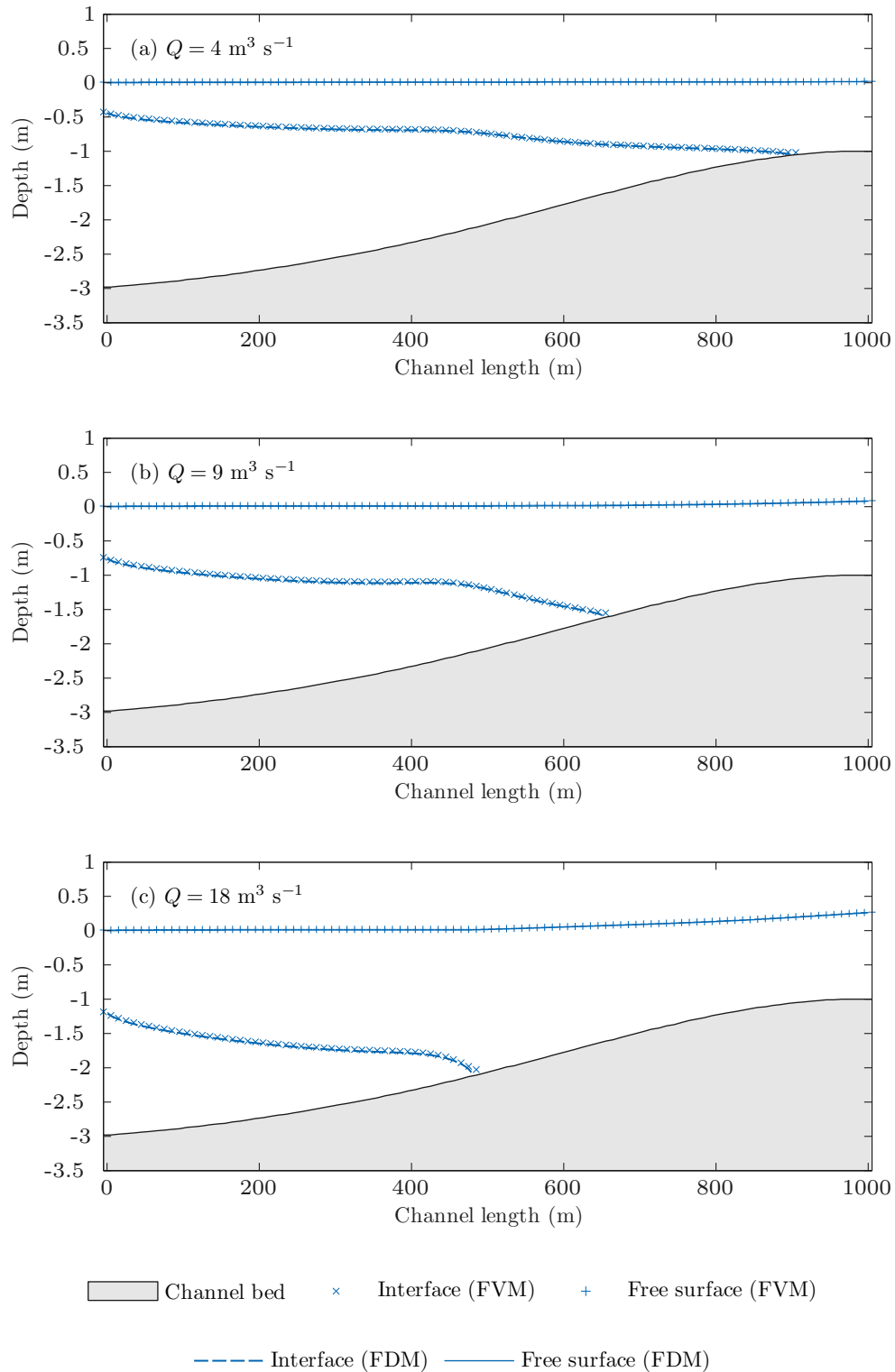


Figure 5.4: Numerical solutions for the arrested salt-wedge obtained by a steady FDM and a time-dependant FVM model, for (a) $Q = 4 \text{ m}^3 \text{ s}^{-1}$, (b) $Q = 9 \text{ m}^3 \text{ s}^{-1}$ and (c) $Q = 18 \text{ m}^3 \text{ s}^{-1}$.

and $18 \text{ m}^3 \text{ s}^{-1}$. As it can be seen, the agreement between two models is satisfactory for all three cases. The influence of the channel contraction is noticeable in all examples as a local deformation of the interface profile near $x \approx 500 \text{ m}$ (Fig. 5.4).

5.2 Well-balanced property of FVM model

This section examines the time-dependant model based on a FVM and assess whether the conservation properties (C-property and extended C-property) are satisfied in practice.

5.2.1 Verification of the C-property

The Q-scheme is well-balanced if it satisfies the C-property, which states that the numerical scheme should exactly preserve the steady-state solution for water at rest in channels with irregular geometry, without generating any non-physical oscillations [18]. One of the previous subsections (4.2.3) demonstrated that the proposed Q-scheme exactly preserves the mass and momentum equations by showing that Eqs. (4.70) and (4.71) are true for steady-state flow corresponding to water at rest. This subsection presents a numerical experiment to verify whether the proposed numerical scheme actually preserves the steady-state for water at rest in a practical application.

A 10 m long channel is considered, defined by a series of triangular cross-sections with randomly generated depths and widths, as illustrated in Fig. 5.5a,b. The spatial step was set to $\Delta x = 0.05 \text{ m}$ and the temporal step to $\Delta t = 0.004 \text{ s}$, which gives an average CFL ≈ 0.9 . The boundary conditions were set to a zero-gradient for flow rates in both layers and the total depth was constant. The initial condition was a steady-state solution representing water at rest ($Q_{i,1} = Q_{i,2} = 0$, $\eta_{i,1} = b_i + h_{i,1} + h_{i,2} = \text{const.}$), where the lower layer is always non-zero $h_{i,2} > 0$, so that no dry cells appear inside the domain. Figure 5.5c,d shows the upper and lower layer depth, as well as the flow rate in each layer at the initial time. Finally, Fig. 5.5e,f shows the same parameters 10 seconds after the start of the simulation; although, the results are the same for every other time step.

These results indicate that the proposed numerical scheme exactly preserves the steady-state solution for water at rest in channels with irregular geometry. The free water surface and the interface remained constant during the simulation. Some

5. Numerical model performance assessment

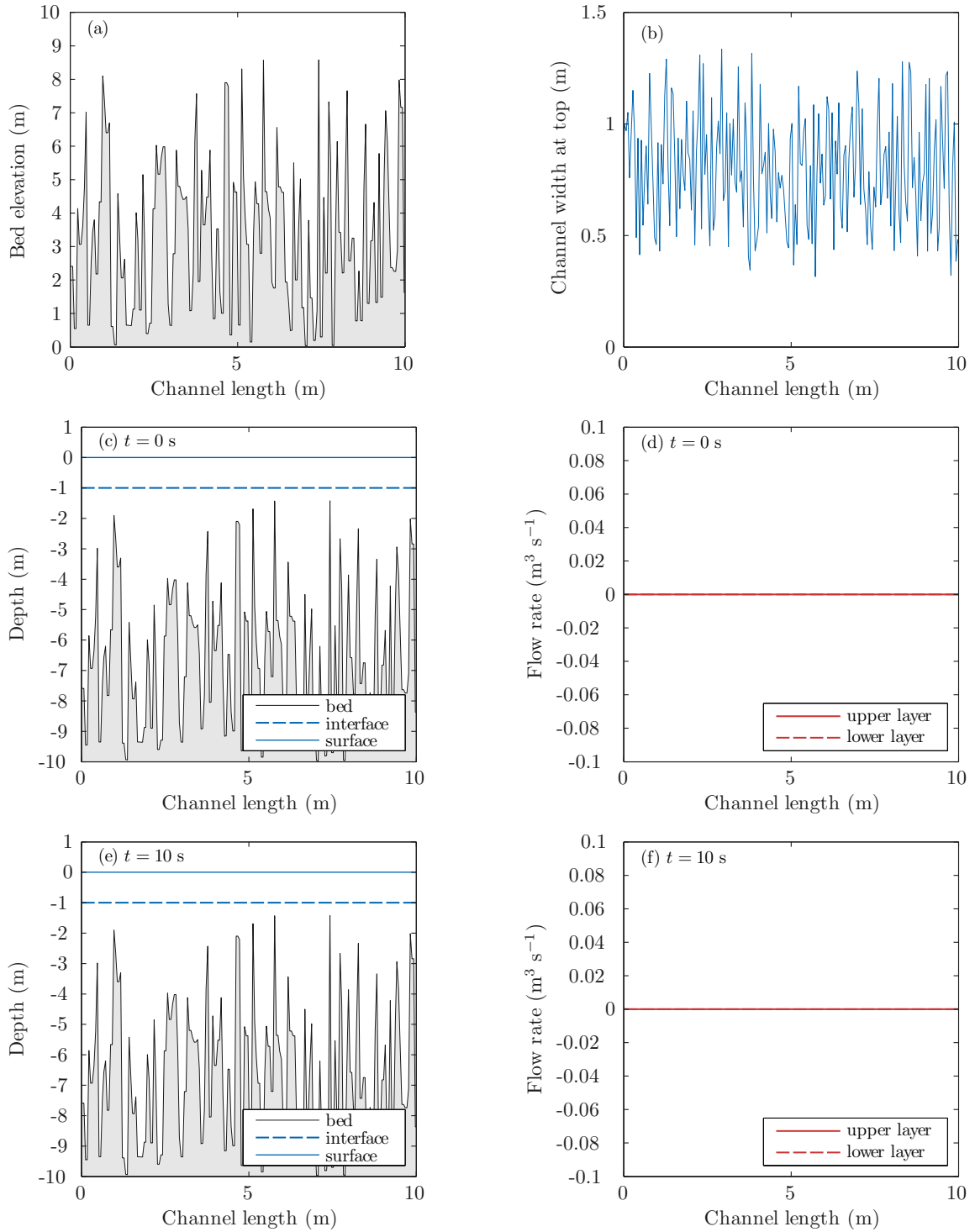


Figure 5.5: C-property verification test for water at rest in an irregular channel: (a) bed elevation, (b) channel width, (c) and (d) initial conditions (water depth and flow rate), and (e) and (f) results after $t = 10$ s (water depths and flow rates).

non-zero flow rates did appear, however, but they were of the order of the numerical round-off error ($\approx 10^{-12}$) and did not grow with time. Furthermore, no spurious oscillations were generated. It is therefore reasonable to conclude that the C-property is also satisfied in practical applications.

5.2.2 Verification of the extended C-property

When dry cells appear in either the upper or lower layer, non-physical oscillations may be generated even though the C-property is satisfied. One of the previous subsections (4.2.4) demonstrated the importance of modifying the source term at the intercell between wet and dry cells. This subsection shows two numerical experiments for steady-state flow corresponding to water at rest in channels with irregular geometry and wet-dry transitions; the first one, illustrates that the spurious oscillations may appear in practice if the original approximation of the source terms (Eq. 4.52) is considered, and the second one, examines whether the steady-state flow is actually preserved when the source terms at the salt-wedge front are modified by Eq. (4.78).

Again, a 10 m long channel is considered, defined by a series of triangular cross-sections with randomly generated depths and widths, as illustrated in Fig. 5.5a,b. The spatial step was set to $\Delta x = 0.05$ m and the temporal step to $\Delta t = 0.004$ s, which gives an average CFL ≈ 0.9 . The boundary conditions were set to zero-gradient for flow rate in both layers and the total depth was considered to be constant. The initial condition was a steady-state solution representing water at rest ($Q_{i,1} = Q_{i,2} = 0$, $\eta_{i,1} = b_i + h_{i,1} + h_{i,2} = \text{const.}$), but in contrast to the previous experiment, the lower layer dries out at several cells, so that wet-dry transitions appear in the channel (Fig. 5.6a,b).

Figure 5.6a,b shows the upper and lower layer depth, as well as the flow rate in each layer at the initial time. Figure 5.6c,d shows the same parameters 1 second after the start of simulation when the original source term approximation is applied (after 1 second the numerical scheme becomes unstable and the computation stops). Finally, Figure 5.6e,f shows the same parameters 10 seconds after the start of simulation with the modified source terms, as described in section (4.2.4). Again, the results are the same for all other time steps.

These results indicate that the proposed numerical scheme with adequate treatment of wet-dry fronts exactly preserves the steady-state solution for water at rest in channels

5. Numerical model performance assessment

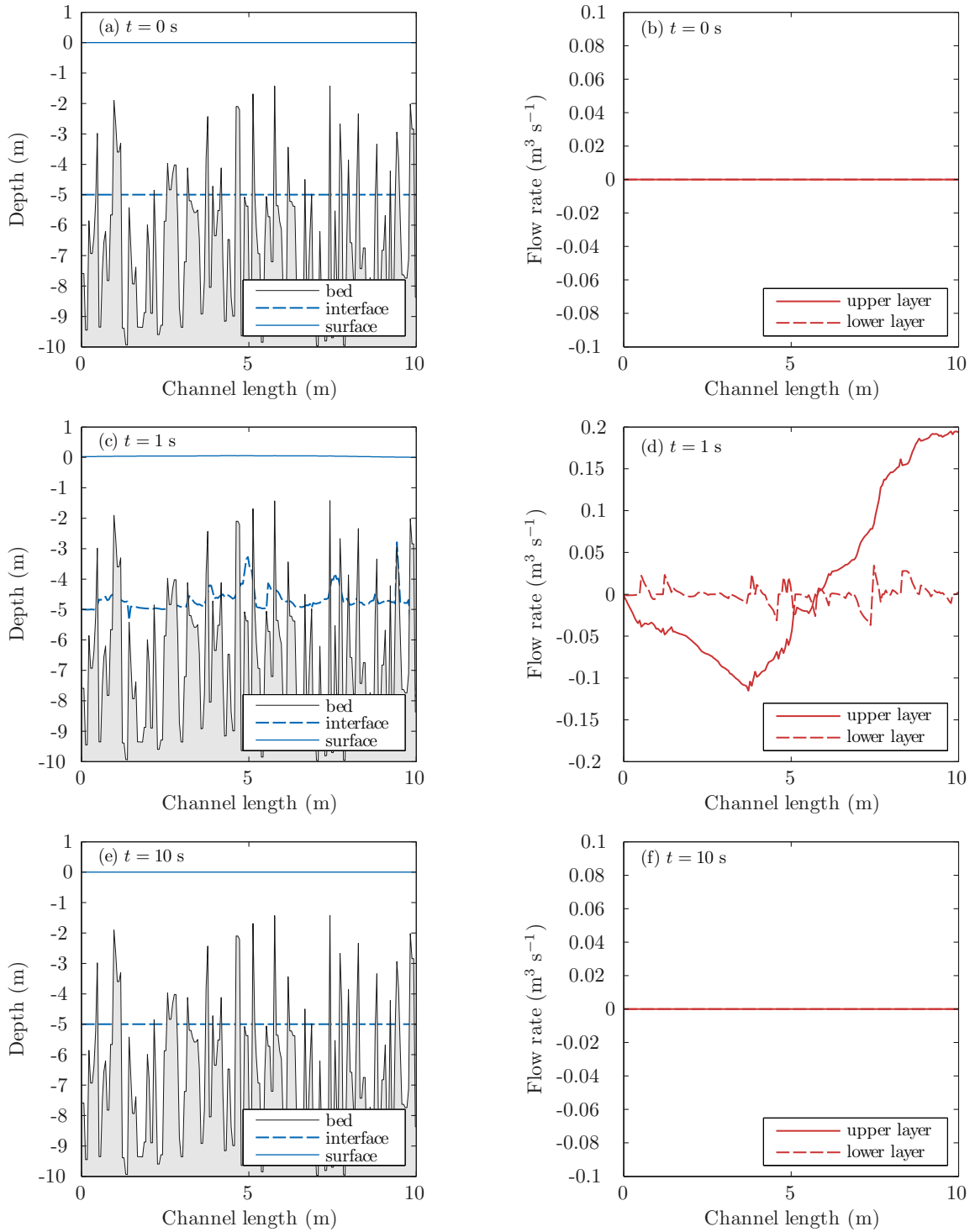


Figure 5.6: Extended C-property verification test for water at rest in an irregular channel with lower layer wet-dry transitions: (a) and (b) initial conditions (water depths and flow rates), (c) and (d) results at $t = 1$ s when the original source terms are considered and spurious oscillations appear, and (e) and (f) results at $t = 10$ s when the source term approximation is applied.

with irregular geometry and lower layer wet-dry fronts. If the original treatment of the source terms is applied, non-physical oscillations may appear, which destabilizes the numerical scheme. On the other hand, if wet-dry fronts are adequately treated and the source term is modified, as described in section (4.2.4), the free water surface and the interface remain constant in time. The extended C-property is therefore also satisfied in practical application.

5.3 Numerical model sensitivity

This section investigates the model sensitivity to the main input parameters, in particular, the influence of the interfacial friction, bed friction, entrainment, and density ratio. To do so, a 10 km long prismatic channel was considered, defined by a rectangular cross-section of constant depth and width, as illustrated previously in Fig. 5.1. The FDM model results are presented here, although, the same results were obtained by the FVM model. The spatial step was set to $\Delta x = 10$ m. The downstream boundary condition was forced by the total water depth $H = 1.5$ m and the upper layer thickness h_1 at the mouth, which corresponded to the critical flow condition $Fd^2 = 1$ (or $G^2 = 1$ when entrainment was considered).

5.3.1 Influence of interfacial friction

Interfacial friction factor is one of the most important parameters in salt-wedge models [2]. Let us recall that the solution for the salt-wedge length in simplified prismatic channels, defined by a horizontal bed and cross-sections of constant width, is given by Eq. (2.7). Clearly, L is inversely proportional to the interfacial friction factor λ_i . In other words, for the same H and Q , L increases at a same rate as λ_i is reduced.

To illustrate this dependence and high sensitivity of numerical models to λ_i , Fig. 5.7 presents five numerical examples for constant river flow rate $Q = 2.0 \text{ m}^3 \text{ s}^{-1}$, where λ_i varied from 1×10^{-3} to 2.1×10^{-3} by a $\sim 20\%$ increase. Figure 5.7 shows that as λ_i increases the salt-wedge length is reduced by approximately the same amount, so that L for $\lambda_i = 2.1 \times 10^{-3}$ is 2.1 times shorter than L for $\lambda_i = 1.0 \times 10^{-3}$. Considering that λ_i may vary in the same estuary as much as an order of magnitude, it is clear that solutions for the arrested salt-wedge are highly sensitive to the interfacial friction factor.

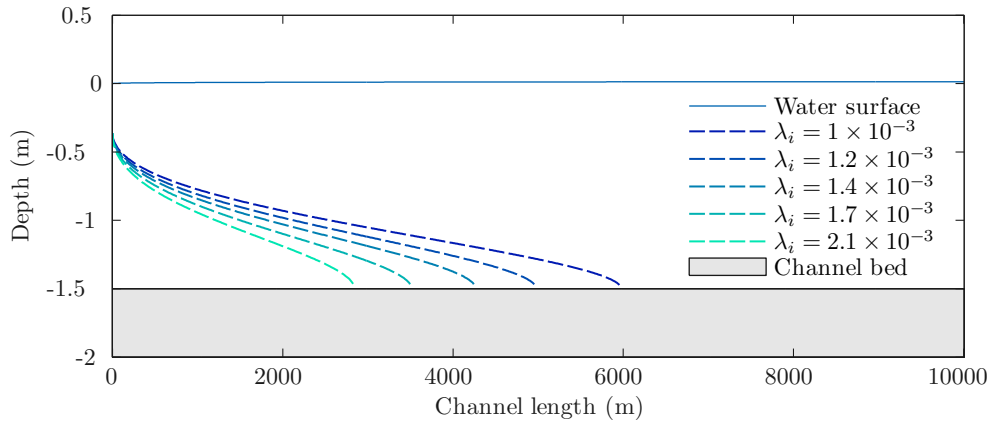


Figure 5.7: Sensitivity of the numerical model on the interfacial friction factor λ_i , for $Q = 2.0 \text{ m}^3 \text{ s}^{-1}$ and $r = 0.975$, without bed friction or entrainment.

5.3.2 Influence of bed friction

Simple arrested salt-wedge models often neglect bed friction; the influence of the bed friction in the upper layer in wide channels is often an order of magnitude smaller than the interfacial friction. Furthermore, the bed friction in the stagnant lower layer is always zero under the assumption of no mixing between the layers. However, bed friction may influence the movement of the salt-wedge under variable river or tidal flow.

Figure 5.8 presents five numerical examples to assess the influence of the bed friction on the arrested salt-wedge length. The river flow rate was constant $Q = 2.0 \text{ m}^3 \text{ s}^{-1}$, the interfacial friction factor was $\lambda_i = 10^{-3}$, and the Manning's roughness coefficient varied from 0.02 to 0.08 by an increment of 0.02. Figure 5.8 shows that as n_M increases the salt-wedge length is reduced, so that L for $n_M = 0.08$ is about 40% shorter than L for $n_M = 0.02$. However, examined values for n_M span almost the entire range of values that can be expected in estuaries – from concrete finishing, the excavated channels covered in gravel and rocks, to unmaintained natural channels covered completely in weed and dense brushes [95]. The bed friction is clearly less important than the interfacial friction, but it should be considered in estuarine models. Furthermore, in time-dependant flow the influence of n_M may become even more pronounced.

5.3.3 Influence of entrainment

Salt-wedge models also often neglect entrainment, because in highly stratified conditions the vertical mixing is weak and usually confined to the interfacial layer.

5. Numerical model performance assessment

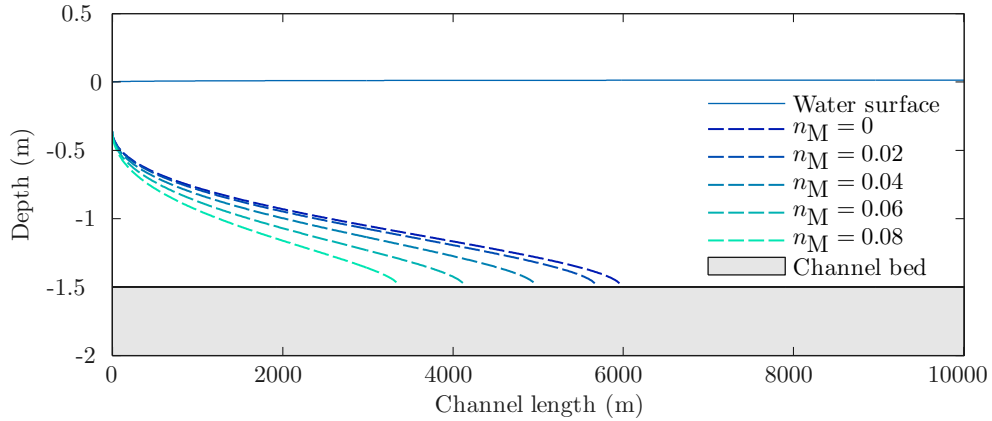


Figure 5.8: Sensitivity of the numerical model on the Manning's roughness coefficient n_M , for $Q = 2.0 \text{ m}^3 \text{ s}^{-1}$, $\lambda_i = 10^{-3}$ and $r = 0.975$, without entrainment.

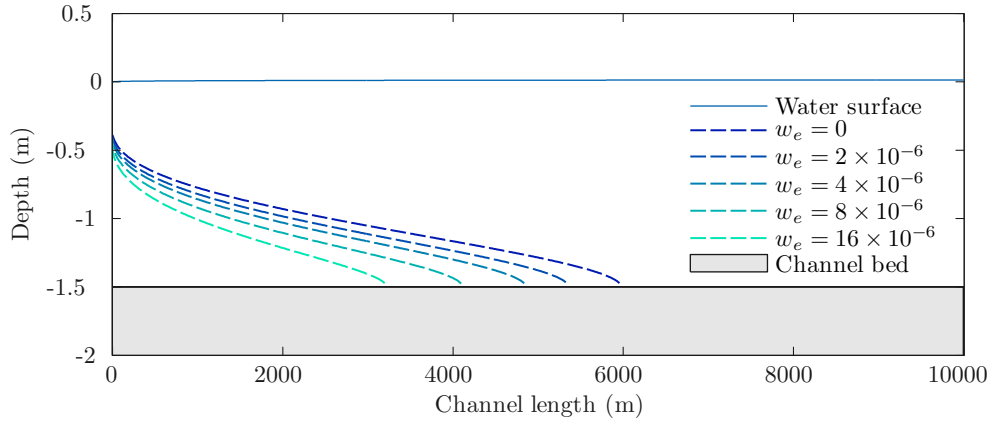


Figure 5.9: Sensitivity of the numerical model on the entrainment velocity w_e (m s^{-1}), for $Q = 2.0 \text{ m}^3 \text{ s}^{-1}$, $\lambda_i = 10^{-3}$ and $r = 0.975$, without bed friction.

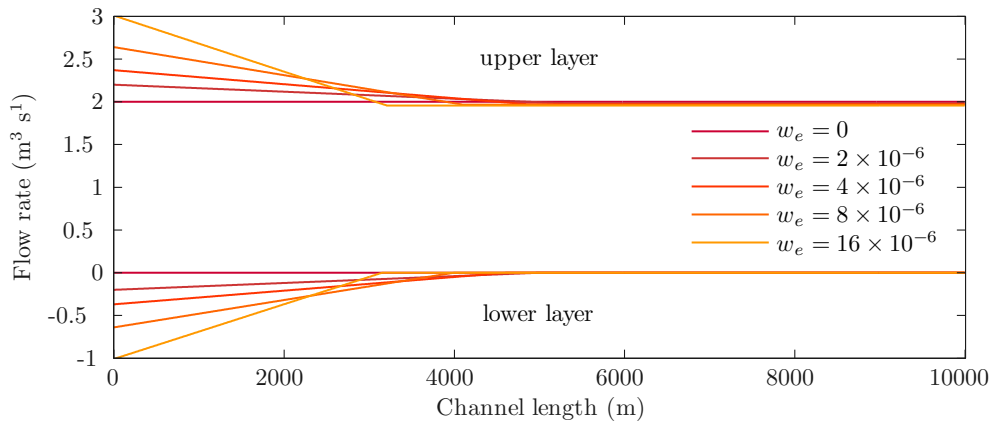


Figure 5.10: The resulting upper and lower layer flow rates for different entrainment velocities w_e (m s^{-1}), for $Q = 2.0 \text{ m}^3 \text{ s}^{-1}$, $\lambda_i = 10^{-3}$ and $r = 0.975$, without bed friction.

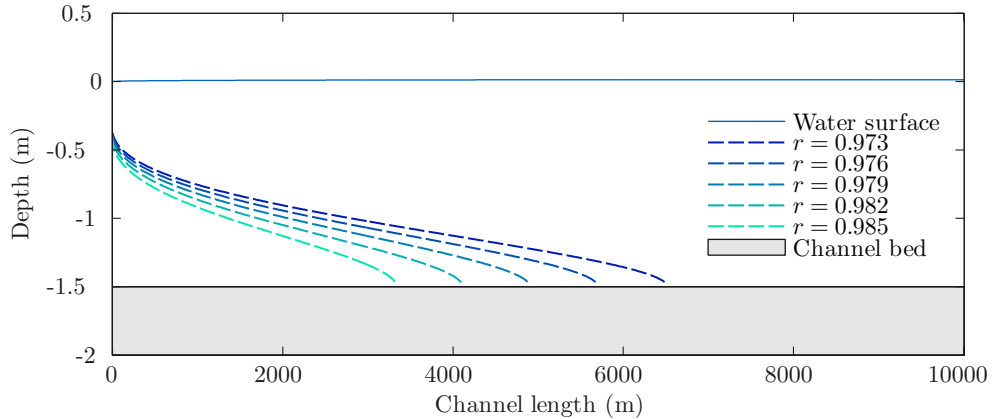


Figure 5.11: Sensitivity of the numerical model on the density ratio r , for $Q = 2.0 \text{ m}^3 \text{ s}^{-1}$, $\lambda_i = 10^{-3}$, without bed friction or entrainment.

Arita and Jirka [2] showed that entrainment, although weaker in salt-wedges than in partially-mixed estuaries, may somewhat influence the lower layer circulation.

Figure 5.9 presents five numerical examples to assess the influence of the entrainment on the arrested salt-wedge length. The river flow rate was constant $Q = 2.0 \text{ m}^3 \text{ s}^{-1}$, the interfacial friction factor was $\lambda_i = 10^{-3}$, and the entrainment velocity increased exponentially from 2×10^{-6} to $16 \times 10^{-6} \text{ m s}^{-1}$. It seems that the increase in w_e results in shorter salt-wedge lengths. However, the entrainment mostly influences the continuity equations by initiating a vertical mass transport from the lower to the upper layer. As a result, a recirculation is established, in which the flow rate in the lower layer is negative and reduces gradually to zero at the tip of the salt-wedge. Flow in the upper layer, on the other hand, is positive and increases towards the mouth. Figure 5.10 illustrates the variations in the upper and lower layer flow rates, as a result of entrainment. It seems that the change in the flow rate is the primary cause of different salt-wedge lengths shown in Fig. 5.9; therefore, the entrainment appears to only impose an indirect influence on the salt-wedge length, albeit, a noticeable one. Furthermore, the longer the salt-wedge is, the more pronounced influence of the entrainment should be.

5.3.4 Influence of density ratio

Finally, the influence of the density ratio is investigated. As defined before, r is the ratio of upper to lower layer density. The upper freshwater layer density is

fairly constant in the field and ranges from 998 to 1000 kg m⁻³, depending on the temperature. Whereas, the lower salt-water layer additionally depends on the salinity and may span over a wider range of values, usually from 1015 to 1030 kg m⁻³.

Figure 5.11 presents five numerical examples to assess the influence of r on the salt-wedge length. The river flow rate was constant $Q = 2.0 \text{ m}^3 \text{ s}^{-1}$, and the interfacial friction factor was $\lambda_i = 10^{-3}$. The density ratio r varied from 0.973 to 0.985 by an increment of 0.003, corresponding to respective density differences $\Delta\rho = \rho_2 - \rho_1 = 28, 24, 21, 18, \text{ and } 15 \text{ kg m}^{-3}$. It seems that r also plays an important role in salt-wedge models; an increase in the salt-water density results in a noticeably stronger salt-wedge intrusion.

6

Field study in the Rječina River estuary

Contents

6.1	Rječina River	75
6.2	Adriatic Sea	77
6.3	Field observations in the Rječina River estuary	78
	6.3.1 Salinity, temperature and density	79
	6.3.2 Flow rates and velocities	84
6.4	Knudsen's hydrographic theory	86
6.5	Channel bathymetry	87
	6.5.1 Digital terrain model	89
	6.5.2 Cross-section geometry parameters	91

Abstract

This chapter presents physical characteristics of the Rječina River and the Adriatic Sea. Furthermore, approaches and methods used in field observations of the Rječina River estuary are described. Also, the Knudsen's box model for estimating the entrainment velocities is presented. Finally, the chapter documents the generation of the digital terrain model and the derivation of the cross-section geometry.

6.1 Rječina River

The Rječina River is 18.6 km long karst river located in the northern coastal part of Croatia, and it originates from a strong karst spring Rječina situated 325 m above sea-level (ASL) [82]. In its lower reaches, the river flows through a narrow canyon, and then continues through an alluvial plain in the city centre of Rijeka, where it finally enters the Adriatic Sea [102]. Water drawn from the Rječina River is mainly used for Rijeka's water supply system (WSS) and electricity production at the Hydropower Plant Rijeka (Rijeka HPP) [52]. The main intake is located at Rječina spring, from which $0.69 \text{ m}^3 \text{ s}^{-1}$ is used on average for WSS, except in the summer months, when the spring usually dries out [82]. During these dry months, from June to August, the water is drawn from the second intake located at Zvir spring (at $\sim 2.5 \text{ m ASL}$), next to the Rječina River channel at a distance of 1.4 km from the river mouth (Fig. 6.1). The mean annual intake from Zvir spring is $0.21 \text{ m}^3 \text{ s}^{-1}$ [82].

The water regime in the Rječina River significantly changed after the construction of the Valići dam and reservoir in the middle reaches of the river [52]. Water drawn from the reservoir is used for the electricity production at the Rijeka HPP, located in the city centre, near Zvir spring. The maximum operating capacity of the Rijeka HPP is $21 \text{ m}^3 \text{ s}^{-1}$, and the overflowed water is discharged back into the Rječina River at 1.3 km from the mouth (Fig. 6.1).

Observations at the most downstream gauging station Tvornica have, unfortunately, not been conducted continuously, mostly because of poor maintenance and frequent malfunctions. Tvornica gauging station is located downstream from the Rijeka HPP outflow at 1.2 km from the mouth (Fig. 6.1). Considering the significance of the lower reaches of the Rječina River, located in the city centre, the observations were resumed in 1998, which allowed for a more recent hydrological analysis over a 16-year period (1999-2015). For the period from 2003 to 2009, only the water stage was observed; therefore, the flow rates were computed from the available water stage data and the official rating curve.

The mean annual flow rate for the analysed period 1999-2015 at Tvornica gauging station was $11.1 \text{ m}^3 \text{ s}^{-1}$, which is slightly lower than $12.9 \text{ m}^3 \text{ s}^{-1}$ observed in the previous hydrological period (1961-1990) [82]. This difference may be explained by a

6. Field study in the Rječina River estuary

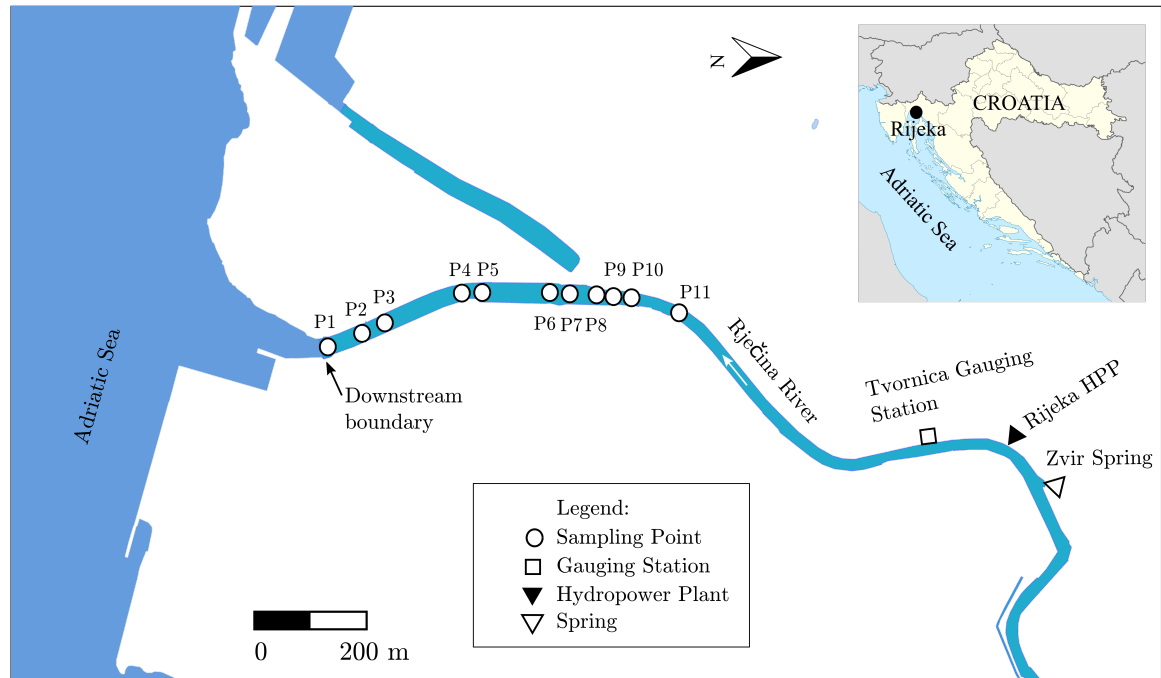


Figure 6.1: Map of the Rječina River estuary with sampling points and inflow locations

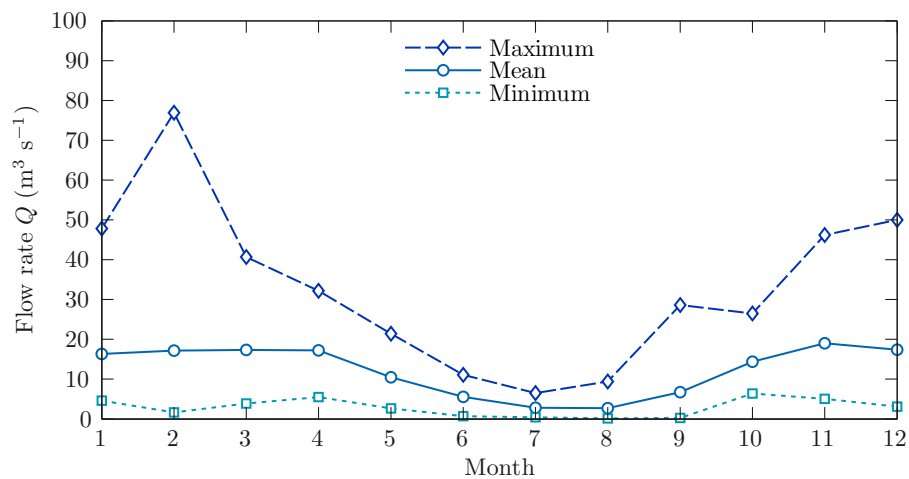


Figure 6.2: Inter-annual variations of the minimum, mean and maximum monthly flow rates at Tvornica gauging station (1999-2015)

relatively short series of years covered by the more recent analysis, which includes three extremely dry years (2003, 2007 and 2012).

Figure 6.2 shows the variations in the minimum, mean and maximum monthly flow rate throughout the year. The base flow at this gauging station consists of overflowed water from Rječina spring and Zvir spring, in about equal parts when the mean annual flow is considered [82]. However, during the summer months, when Rječina Spring usually dries out, only Zvir spring provides the base flow, with overflows ranging from a daily minimum $Q < 0.1 \text{ m}^3 \text{ s}^{-1}$, observed in August 2003, to an average 1 - 2 $\text{m}^3 \text{ s}^{-1}$. Whereas, during the wet period (November to February), overflowed water from Zvir spring amounts up to 20 $\text{m}^3 \text{ s}^{-1}$, contributing in part to the total water flow rate at Tvornica gauging station, where a maximum daily flow rate of 184 $\text{m}^3 \text{ s}^{-1}$ was observed in February of 2014. Inter-daily oscillations also occur in the lower reaches, depending on outflows from the Rijeka HPP.

6.2 Adriatic Sea

The Adriatic Sea is a semi-enclosed body of water connected to the Mediterranean Sea through the Strait of Otranto. Climatologically, the Adriatic is usually divided into three regions: the northern, middle and southern Adriatic. The northern part of the Adriatic is the shallowest of the three and most sensitive to seasonal variations [27].

The water column in the northern Adriatic consists of a seasonal surface water layer, characterized by low salinity and high temperatures in the summer, and deep water layer, characterized by high salinity and low temperatures [27]. A pycnocline, separating these two layers, is present at the depth of 30 m during the spring and summer [6]. In autumn, the upper layer begins to cool, whereas, in the winter season the temperature stability is renewed, and the whole column cools down [6].

The northern Adriatic shows slightly lower salinities than the southern part. However, the average salinity of the Adriatic Sea is relatively high compared to other seas [6]. The salinity also exhibits seasonal character; in the spring the freshwater inflow increases, and the water column shows lower salinities at the surface and a well-developed vertical stratification [27]. The deep water layer in the northern Adriatic shows average values of temperature $T = 11.4 \pm 1.4 \text{ }^\circ\text{C}$, practical salinity $S = 38.3 \pm 0.3$, and density $\rho = 1029.2 \text{ kg m}^{-3}$ [6].

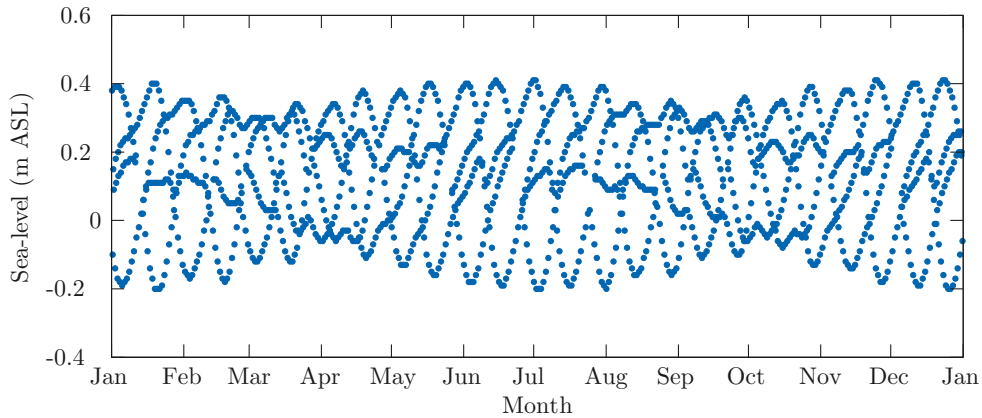


Figure 6.3: Daily minimum and maximum sea-level amplitudes at Bakar tidal gauging station in 2015 (according to [45]).

The tides in the Adriatic Sea are of a mixed type with relatively low amplitudes [80]. The maximum astronomical tidal amplitude recorded between 1953 and 2006, at the Bakar tidal gauging station, which is located only 12 km from the Rijeka city centre, was 123 cm; however, mean tidal amplitudes do not exceed 30 cm [80]. Figure 6.3 shows daily tidal amplitudes at Bakar tidal gauging station in 2015 [45].

6.3 Field observations in the Rječina River estuary

The Rječina River estuary is located in the city centre of Rijeka, at $45^{\circ}20'$ N and $14^{\circ}27'$ E (Fig. 6.4). This estuary is a typical example of a microtidal salt-wedge where a variable river flow rate, rather than tides, is the main source of its time dependence. Krvavica *et al.* [54] observed highly stratified conditions in the Rječina River estuary even for low river flow rates. They also computed that the salt-wedge is expelled from the estuary when $Q \gtrsim 38 \text{ m}^3 \text{ s}^{-1}$. Furthermore, an arrested salt-wedge frequently forms in the estuary because of a specific combination of low tidal amplitudes, partially controlled freshwater flow rate, and its relatively short length [54].

Field observations in the Rječina River estuary were carried out during the period from February to September 2014 and from April to August 2015. The main aim was to measure the salinity structure along the salt-wedge during different river flow rates and sea levels. Eleven sampling points were selected along the estuary (Fig. 6.4), with most of them located at bridges traversing it. Thirty sampling campaigns covered



Figure 6.4: Digital orthophoto of the Rječina River estuary with sampling points.

various flow conditions, with sea-levels ranging from -0.5 to $+0.75$ m ASL and river flow rates ranging from 1.3 to 31.3 $\text{m}^3 \text{s}^{-1}$. For this range of flow rates the salt-wedge was always present in the estuary ($Q < 38$ $\text{m}^3 \text{s}^{-1}$). The changes in the tidal-driven sea-levels during the measurements were always under 3–4 cm. Only the observations made under steady-state conditions were considered, however. Steady states were identified by Q being constant for several hours before and after the measurements, and by a minimal influence of wind or waves. A total of 22 out of 30 data sets remained for further analysis of the arrested salt-wedge after the selection.

An additional sampling campaign, conducted on 1 July 2015, provided more insight in the salt-wedge response to changes of the river flow rate, which were caused by variable discharges from the Rijeka HPP. This observation differed from previous ones for several reasons: (a) the propagation of the salt-wedge was observed (*i.e.*, time-dependent changes in the salt-wedge shape), in contrast to the stationary arrested salt-wedge shape, (b) the vertical salinity profiles were measured continuously along the estuary every 5 – 15 minutes during a period of 12 hours, in contrast to a single set of measurements along the estuary for the arrested salt-wedge, and (c) vertical velocity profiles were measured near the mouth.

6.3.1 Salinity, temperature and density

Vertical profiles of conductivity C and temperature T were measured by a Schlumberger CTD diver (Conductivity-Temperature-Depth). This device records continuously

measured conductivity, temperature, and pressure data. By lowering the diver into the water at a pace of $\sim 5 \text{ cm s}^{-1}$, a detailed vertical $C - T$ profile was measured.

Salinity dependence on conductivity, temperature and pressure

The practical salinity S was calculated from the observed water conductivity C , temperature T and pressure p using empirical equations given in [33], as follows:

$$S = a_0 + a_1 R_t^{1/2} + a_2 R_t + a_3 R_t^{3/2} + a_4 R_t^2 + a_5 R_t^{5/2} + \Delta S, \quad (6.1)$$

where

$$\Delta S = \frac{T - 15}{1 + k(T - 15)} \left(b_0 + b_1 R_t^{1/2} + b_2 R_t + b_3 R_t^{3/2} + b_4 R_t^2 + b_5 R_t^{5/2} \right), \quad (6.2)$$

and

$$R = R_t r_t R_p = \frac{C(S, T, p)}{C(35, 15, 0)}, \quad (6.3)$$

with

$$r_t = c_0 + c_1 T + c_2 T^2 + c_3 T^3 + c_4 T^4, \quad (6.4)$$

and

$$R_p = 1 + \frac{e_1 p + e_2 p^2 + e_3 p^3}{1 + d_1 T + d_2 T^2 + (d_3 + d_4 T) R}, \quad (6.5)$$

where T is temperature in degrees Celsius, p is pressure in decibars, coefficients a_i , b_i , c_i are given in Table 6.1, coefficient d_i , e_i and k are given in Table 6.2, $C(S, T, p)$ is water conductivity at a given salinity S , temperature T and pressure p , and $C(35, 15, 0) = 42.914 \text{ mS cm}^{-1}$ is conductivity of standard seawater of practical salinity 35, temperature $15 \text{ }^\circ\text{C}$ at atmospheric pressure. Equation (6.1) is considered valid for $-2 < T < 35 \text{ }^\circ\text{C}$ and $2 < S < 42$ [33]. Figure 6.5 shows the salinity dependence on conductivity and temperature at 1 m depth.

Density dependence on salinity and temperature

Water density ρ was calculated from the observed practical salinity S and temperature T at atmospheric pressure using empirical equations given in [66], as follows:

$$\rho(S, T) = \rho_w + AS + BS^{3/2} + CS, \quad (6.6)$$

with

$$A = a_0 + a_1 T + a_2 T^2 + a_3 T^3 + a_4 T^4, \quad (6.7)$$

Table 6.1: Empirical coefficients a_i , b_i , and c_i for computing salinity from measured conductivity, temperature and pressure [33]

coeff.	value	coeff.	value	coeff.	value
a_0	0.008	b_0	0.0005	c_0	0.67661
a_1	-0.1692	b_1	-0.0056	c_1	0.020066
a_2	25.3851	b_2	-0.0066	c_2	1.10426×10^{-4}
a_3	14.0941	b_3	-0.0375	c_3	-6.9698×10^{-7}
a_4	-7.026	b_4	0.0636	c_4	1.0031×10^{-9}
a_5	2.7081	b_5	-0.0144		

Table 6.2: Empirical coefficients d_i , e_i , and k for computing salinity from measured conductivity, temperature and pressure [33]

coeff.	value	coeff.	value	coeff.	value
d_0	3.426×10^{-2}	e_0	2.07×10^{-5}	k	1.62×10^{-2}
d_1	4.464×10^{-4}	e_1	-6.37×10^{-10}		
d_2	4.215×10^{-1}	e_2	3.989×10^{-15}		
d_3	-3.107×10^{-3}				

and

$$B = b_0 + b_1T + b_2T^2, \quad (6.8)$$

where S is practical salinity, T is temperature in degrees Celsius, coefficient a_i and b_i are given in Table 6.3, $C = 4.8314 \times 10^{-3}$, and ρ_w is pure water density in kg m^{-3} computed from

$$\rho_w(T) = 999.8426 + d_0T + d_1T^2 + d_2T^3 + d_3T^4 + d_4T^5, \quad (6.9)$$

where coefficients d_i are also given in Table 6.3. Equation (6.6) is considered valid for $-2 < T < 40$ °C and $0 < S < 42$ [66]. Figure 6.6 illustrates the dependence of ρ on S and T .

Table 6.3: Empirical coefficients a_i , b_i , and d_i for computing density of salt-water from measured salinity and temperature at atmospheric pressure [66]

coeff.	value	coeff.	value	coeff.	value
a_0	8.24493×10^{-1}	b_0	-5.72466×10^{-3}	d_0	6.79395×10^{-2}
a_1	-4.08990×10^{-3}	b_1	1.02270×10^{-4}	d_1	-9.09530×10^{-3}
a_2	7.64380×10^{-5}	b_2	-1.65460×10^{-6}	d_2	1.00168×10^{-4}
a_3	-8.24670×10^{-7}			d_3	-1.12008×10^{-6}
a_4	5.38750×10^{-9}			d_4	6.53634×10^{-9}

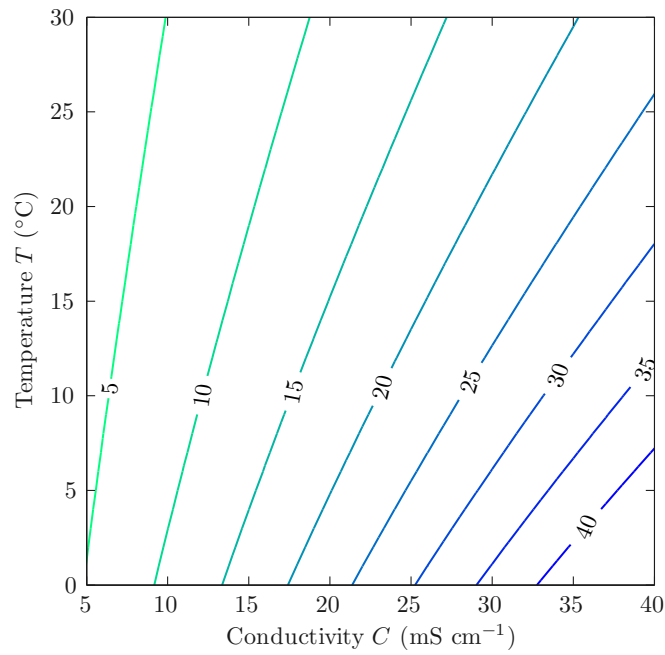


Figure 6.5: Practical salinity S dependence on conductivity C (mS cm^{-1}) and temperature T ($^{\circ}\text{C}$) at 1 m depth, computed from [33].

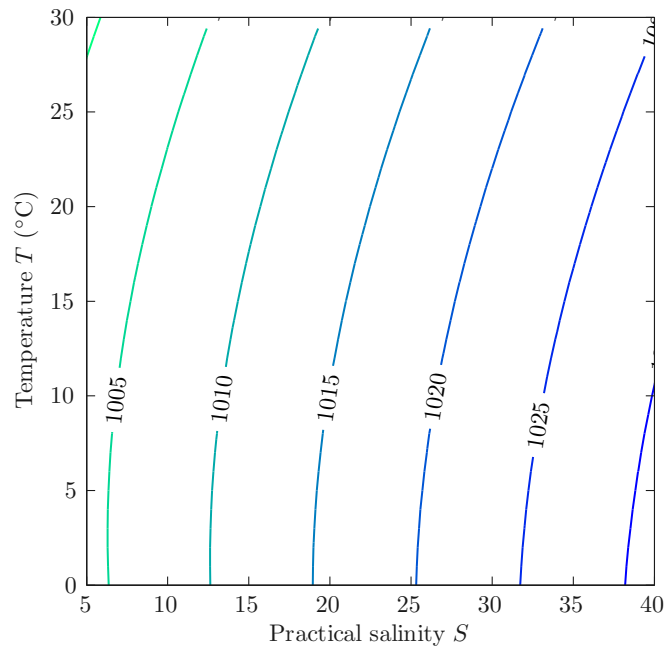


Figure 6.6: Density ρ (kg m^{-3}) dependence on practical salinity S and temperature T ($^{\circ}\text{C}$), computed from [66].

Kinematic viscosity dependence on density and temperature

Kinematic viscosity ν of pure water was computed as a ratio of dynamic viscosity μ and water density ρ , as follows:

$$\nu = \frac{\mu}{\rho}. \quad (6.10)$$

The dynamic viscosity μ was calculated from the observed temperature T at atmospheric pressure using empirical equations given in [47], as follows:

$$\mu(T) = \sum_{i=1}^4 a_i \tilde{T}^{b_i}, \quad (6.11)$$

where $\tilde{T} = T/300$ K, T is temperature in Kelvin, and coefficient a_i and b_i are given in Table 6.4. Equation (6.11) is recommended for temperature range $253.15 < T < 383.15$ K ($-20 < T < 110$ °C) [47].

Table 6.4: Empirical coefficients a_i and b_i for computing dynamic viscosity μ from measured temperature at atmospheric pressure [47]

coeff.	value	coeff.	value
a_1	280.68	b_1	-1.9
a_2	511.45	b_2	-7.7
a_3	61.131	b_3	-19.6
a_4	0.459	b_4	-40

Salinity profiles

During the preliminary analyses, observations were made at several points along each channel cross-section; however, the measurements revealed minimal variations in the salinity structure over a cross-section width [55]. Therefore, a single vertical profile, measured at the centre of each cross-section, was considered to be adequate for the purpose of this thesis.

Figure 6.7 shows a characteristic observed salinity profile and the method for estimating interfacial layer thickness δ_i , and average salinities in the upper S_1 and lower S_2 layer. First, an average salinity gradient inside the interfacial layer was computed as

$$\frac{\Delta S}{\delta_i} = \frac{S_{25\%} - S_{75\%}}{z_{S25\%} - z_{S75\%}}, \quad (6.12)$$

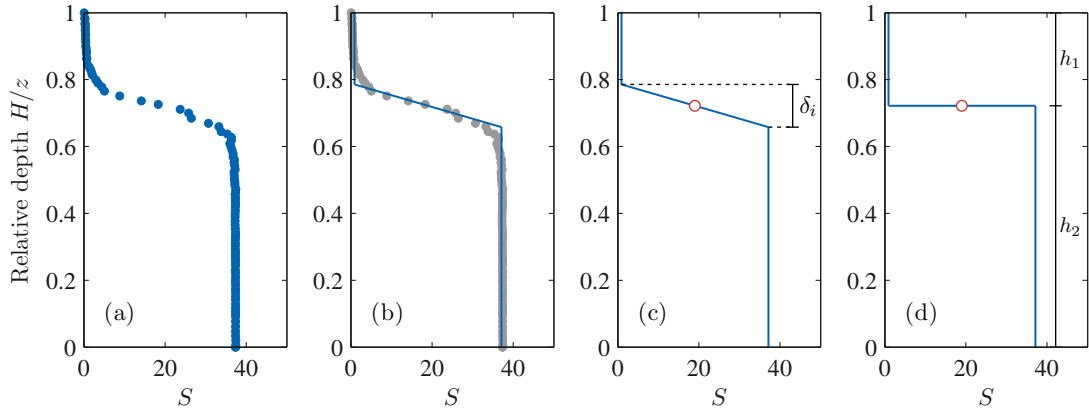


Figure 6.7: Salinity profiles for flow rate $Q = 17.2 \text{ m}^3 \text{ s}^{-1}$: (a) observed salinity S profile, (b) linearized salinity profile, (c) interface thickness and depth, and (d) approximated constant salinity S in the upper and lower layer.

where $S_{25\%} = 0.25S_{\max}$, $S_{75\%} = 0.75S_{\max}$, $S_{\max} = \max(S)$, $z_{S_{25\%}}$ and $z_{S_{75\%}}$ are the corresponding vertical coordinates. Next, the average salinities in the upper layer $S_1 = \text{mean}(S < 0.05S_{\max})$ and in the lower layer $S_2 = \text{mean}(S > 0.95S_{\max})$ were computed, with salinity difference being $\Delta S = S_2 - S_1$ (Fig. 6.7b). Points where these three lines intersect were considered to be the upper and lower boundaries of the interfacial layer, which define δ_i (Fig. 6.7c). The vertical distance between the water surface and the midpoint of the interfacial layer defined the *interface depth*. For most cases, the interface depth located in the middle of the interfacial layer was close to the midpoint in salinity and to the maximum salinity gradient. Finally, the upper and lower layer thickness was computed (Fig. 6.7d). Therefore, in a two-layer approximation, the interface depth is equal to the upper layer thickness h_1 .

A squared buoyancy frequency (Eq. 2.15) was additionally computed at each sampling point, and the maximum value of N^2 at each transect was used as a measure of the stratification strength.

6.3.2 Flow rates and velocities

River flow rate was estimated from the observed water stage at Tvornica gauging station and a rating curve derived from field measurements during 2013-15 (Fig. 6.8). Using a rating curve for steady or quasi-steady river flow is justified; however, caution is advised in unsteady flow, when a rating curve hysteresis should be considered [98].

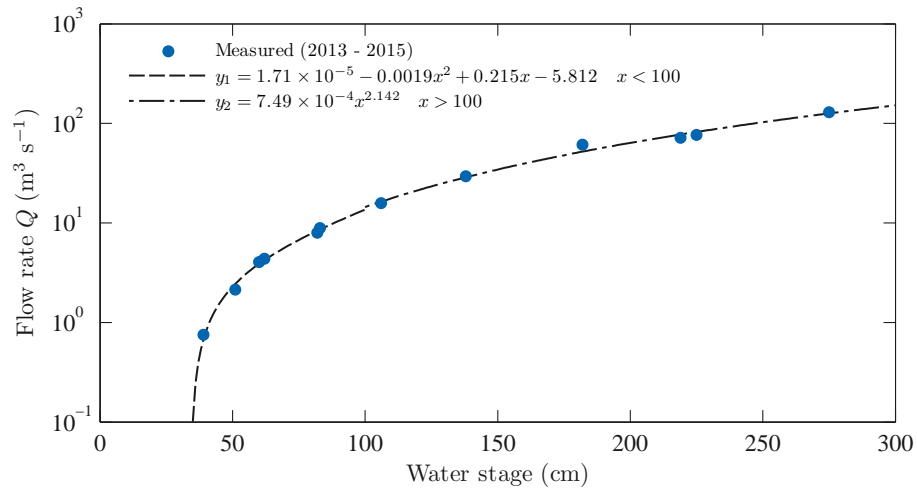


Figure 6.8: Rating curve at Tvornica gauging station obtained from field measurements (2013-2015).

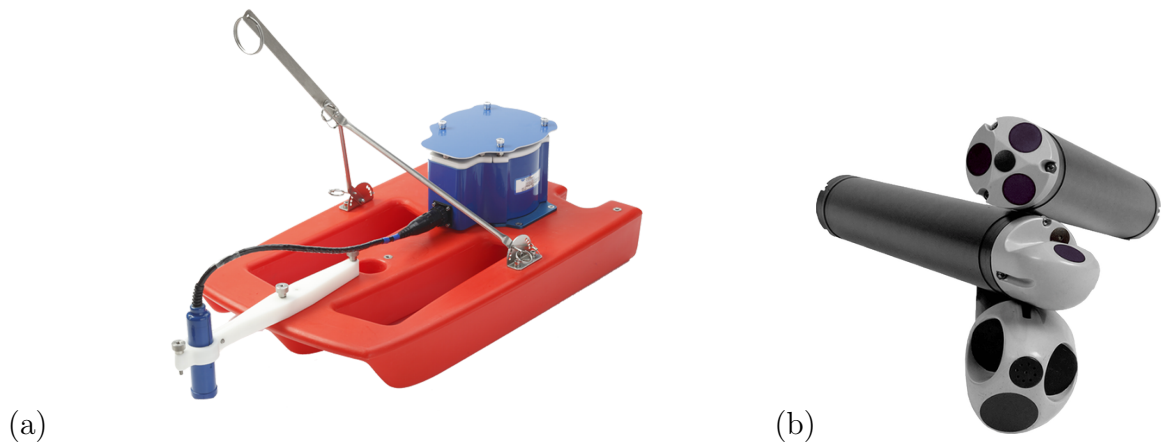


Figure 6.9: ADCP instrument used to measure flow rates and velocities in Rječina River estuary: (a) Teledyn StreamPro and (b) Nortek Aquadopp.

The computed river flow rate was validated on several occasions by the Teledyne StreamPro acoustic Doppler current profiler (ADCP), positioned upstream from the salt-wedge (Fig. 6.9a). StreamPro works at a frequency of 2.0 MHz, it has 4 beams at an angle $\pm 20^\circ$. The cell size ranges from 2 to 10 cm, its resolution is 1 mm s^{-1} , and accuracy is $\pm 1\%$. The instrument was pulled across the river from a bridge to obtain a cross-section area and a series of vertical velocity profiles. The flow rate was computed using the Teledyn software WinRiver II [96]. The differences between the ADCP measurements and flow rates computed from the rating curve were under 15%.

For a time-dependent salt-wedge case, observed on 1 July 2015, an additional Aquadopp ADCP (Fig. 6.9b) was positioned near the river mouth to measure the velocity profiles. Aquadopp also works at a frequency of 2.0 MHz, it has 3 beams, but a finer cell size which ranges from 0.7 to 1.5 cm, and similar accuracy of $\pm 1\%$. This current meter was positioned at the bottom of the channel facing upward, and was continuously recording the velocity profile during the sampling.

6.4 Knudsen's hydrographic theory

A simple two-layer *box model* was applied to compute entrainment velocities from the observed values. This model is based on *Knudsen's hydrographical theorem* for conservation of volume and salt, which is appropriate for strongly stratified estuaries, steady flow conditions, and negligible tidal effects [30]. Given the fact that the Rječina River estuary is relatively short and the channel geometry is fairly uniform, the along-wedge average values were computed. The entire length of the salt-wedge was considered a single box, where the upstream boundary (A) represents the tip of the salt-wedge, and the downstream boundary (B) represents the salt-wedge exit region (Fig. 6.10). Continuity equations for water and salt in the upper and lower layer are written as follows:

$$Q_1^{(A)} + Q_{21} = Q_{12} + Q_1^{(B)}, \quad (6.13)$$

$$Q_2^{(A)} + Q_{21} = Q_{12} + Q_2^{(B)}, \quad (6.14)$$

$$Q_1^{(A)} S_1^{(A)} + Q_{21} \bar{S}_2 = Q_{12} \bar{S}_1 + Q_1^{(B)} S_1^{(B)}, \quad (6.15)$$

$$Q_2^{(A)} S_2^{(A)} + Q_{21} \bar{S}_2 = Q_{12} \bar{S}_1 + Q_2^{(B)} S_2^{(B)}, \quad (6.16)$$

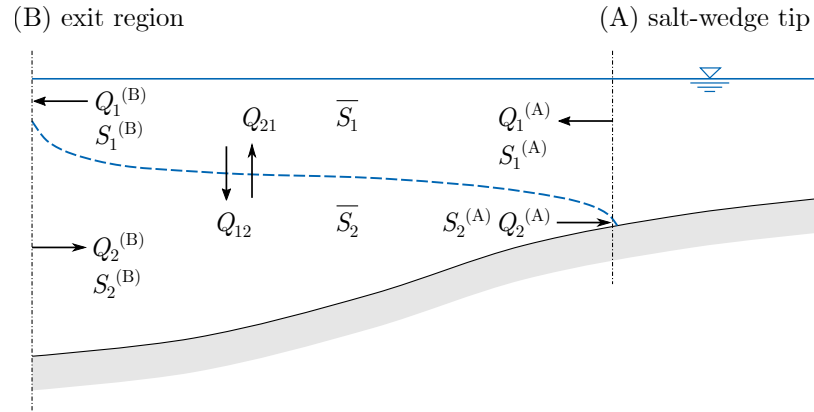


Figure 6.10: Scheme of a two-layer box model for estimating the vertical mixing in salt-wedge estuaries.

where Q_j is the horizontal flow rate; Q_{jj} is the average vertical flow rate inside the box; S_j is the salinity in the j -th layer; \bar{S}_j is the average salinity inside the box; and $j = 1, 2$ denotes the upper and lower layer, respectively.

For the upstream boundary conditions, the following values were used: upper layer flow rate $Q_1^{(A)}$ equals the observed river flow rate; lower layer flow rate $Q_2^{(A)}$ is zero; salinity in the upper layer $S_1^{(A)}$ is also zero; and $S_2^{(A)}$ is equal to the observed value at the most upstream profile. At the downstream boundary, the observed values were used for the upper $S_1^{(B)}$ and lower $S_2^{(B)}$ layer salinities. Finally, the horizontal flow rates $Q_1^{(B)}$ and $Q_2^{(B)}$, as well as downward Q_{12} and upward Q_{21} flow rates, were calculated at each layer by solving the set of equations (6.13) - (6.16).

The vertical volume fluxes w_{12} and w_{21} were estimated by dividing the respective downward and upward flow rates Q_{12} and Q_{21} by the interfacial surface area A_{int} ; therefore, $w_{12} = Q_{12}/A_{int}$ and $w_{21} = Q_{21}/A_{int}$. Finally, the entrainment velocity $w_e = w_{21} - w_{12}$ was obtained from the difference between the upward w_{21} and downward w_{12} volume flux.

6.5 Channel bathymetry

The channel bathymetry was derived from a geodetic survey of cross section depths along the lower reaches of the Rječina River in 2015 using a combination of CTD and a GPS device (Fig. 6.11).

6. Field study in the Rječina River estuary

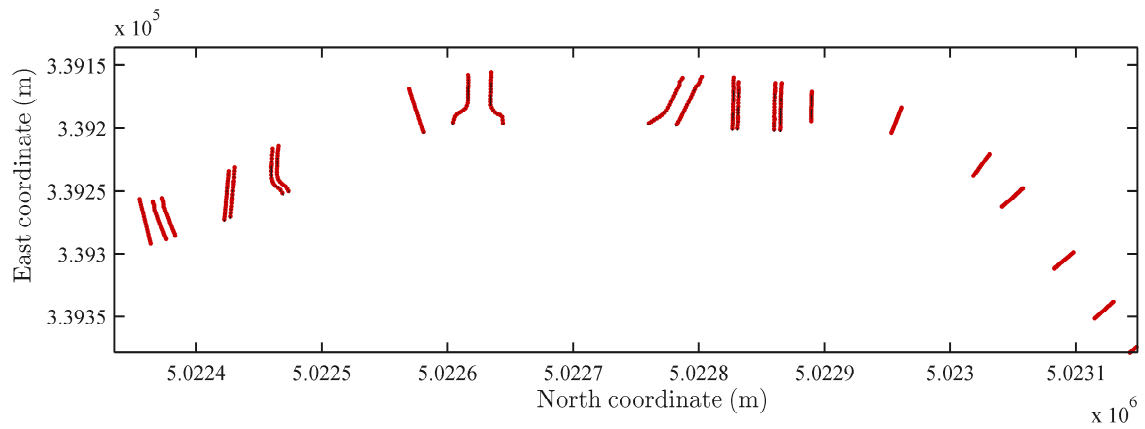


Figure 6.11: Depth measurements (red dots) in the lower reaches of Rječina River.

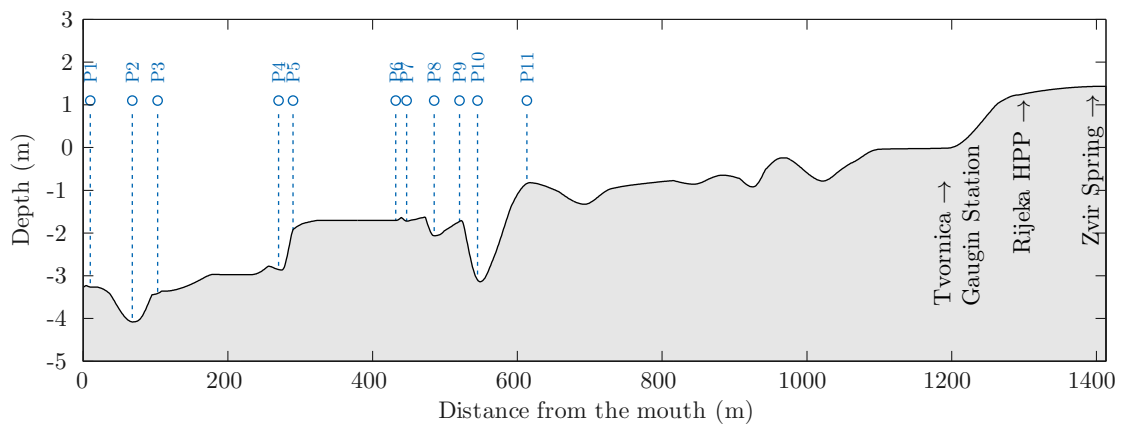


Figure 6.12: Longitudinal section of the Rječina River estuary with bed elevations and locations of sampling points.

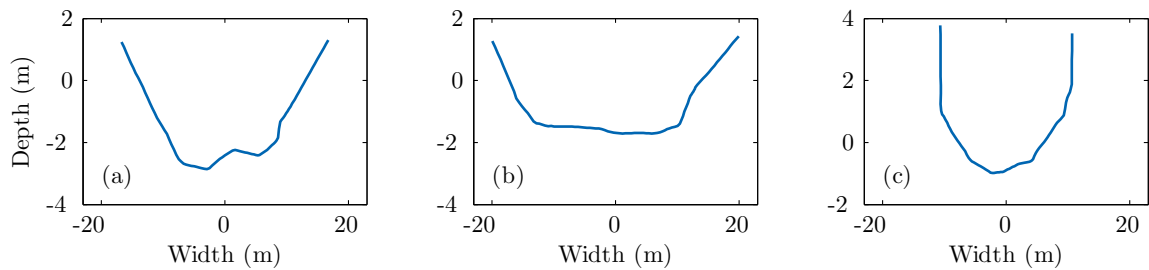


Figure 6.13: The characteristic channel cross-sections in the Rječina River estuary: (a) near the mouth (0+250 m), (b) in the middle reaches (0+325 m), and (c) in the upper reaches (0+650 m).

The survey revealed that the Rječina River estuary is characterized by a relatively short length and a steep bed slope; the maximum observed salt intrusion length during 2014–15 was just under 800 m, the maximum depth near the mouth is 4.2 m, and the average bed slope is $\sim 0.4\%$ (Fig. 6.12). In the upper reaches of the estuary, the channel cross sections are narrower with high vertical walls (Fig. 6.13c), while the cross-sections are wider with mildly sloped sides and a natural bed in the middle and lower parts of the estuary (Fig. 6.13a,b).

6.5.1 Digital terrain model

All numerical models for open channel flow need some form of a *digital terrain model* (DTM) as input data, usually polyline cross-sections or a 3D mesh [83]. In general, survey data consist of cross-section profiles at several characteristic positions along the channel. If a prismatic channel is considered, then only a single cross-section geometry is needed. Even for non-prismatic channels, with rectangular or some other regular cross-sections, only a few characteristic cross-section geometries are sufficient. If irregular and non-prismatic channel is considered, however, some interpolation method is required to approximate the geometric parameters at each node or cell of the computational domain.

There are several interpolation methods for cross-sections along the river channel [12, 65, 83, 99]. The present analysis used a combination of cubic splines and a Bézier curve, similarly as proposed by Travaš *et al.* [99]. To illustrate the method used for the Rječina River estuary, Fig. 6.14 shows an example for a 110 m long segment of the estuary (from 0+440 m to 0+550 m). This is the most complex segment of the estuary, which includes the transition from a narrow cross-section with vertical walls to a semi-natural wide cross-section with sloped sides. It also includes bridge abutments and piers, which reduce the flow area. Although shown as an illustrative example, the same procedure was applied for the entire length of the Rječina River estuary.

A first step was connecting the measured cross-sections with profile lines. Cross-section are usually defined by a different number of segments; hence, they were interpolated by a constant number of points. A linear interpolation was used in this case, because the cross-section were already sufficiently detailed. When the depth measurements are relatively scarce, a cubic spline or Hermite interpolation is more appropriate [99].

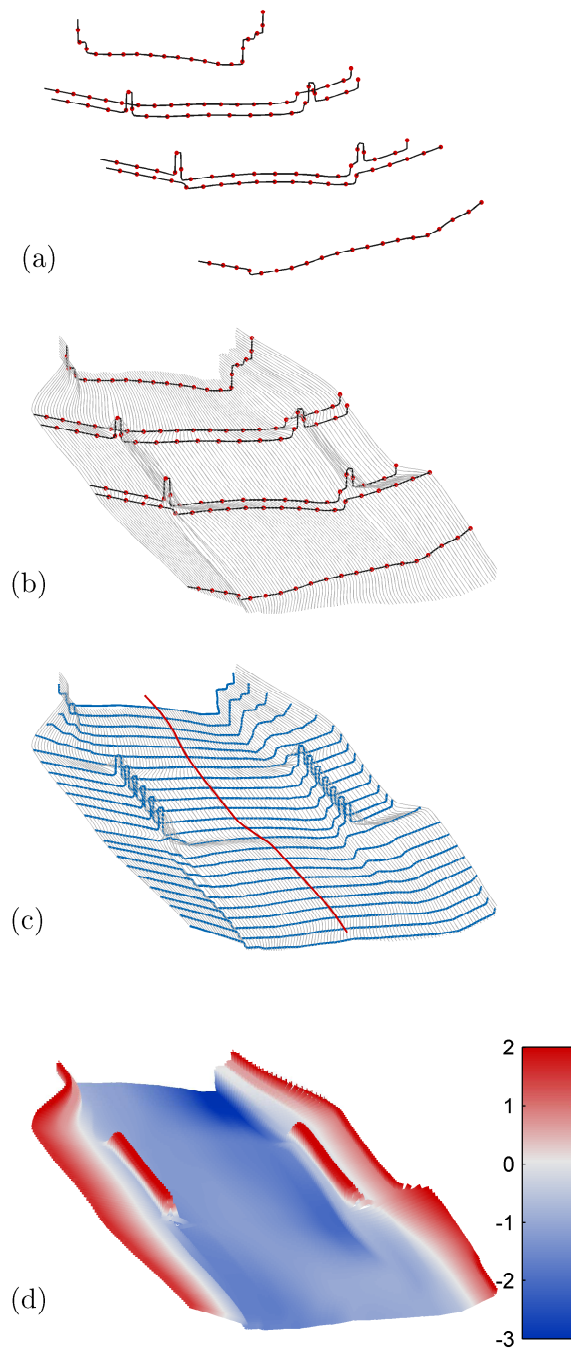


Figure 6.14: Step-by-step illustration of interpolation method for deriving DTM for a segment of the Rječina River estuary (from 0+440 m to 0+550 m): (a) measured cross sections, (b) interpolated profile lines, (c) interpolated cross sections along the centreline, and (d) digital terrain model.

Figure 6.14a shows original six cross-sections for the selected segment of the Rječina River estuary. Notice that two close cross-section were measured to capture the abrupt transitions from a natural to regulated channel, which includes bridge piers. The cross-sections were interpolated by 100 points and then connected by the same number of profile lines using a cubic spline interpolation (Fig. 6.14b). Next, a Bézier curve that connects centres of every cross-section defined the centreline. Along the centreline every 5 m a new interpolated cross-section was derived as an intersection of profile lines with a plane orthogonal to the centreline (Fig. 6.14c). A DTM was finally interpolated, based on a series of equidistant cross-sections, as illustrated in Fig. 6.14d.

6.5.2 Cross-section geometry parameters

Both numerical models used in this thesis need a definition of a functional relationship between the water depth $h(x)$ and the cross-section geometry, *i.e.*, the wetted area $A(h, x)$, width $\sigma(h, x)$, and wetted perimeter $P(h, x)$. The most convenient approach is to define cross-sections at every node i or cell C_i , and to tabulate geometric parameters at each cross-section for h ranging from z_{\min} to z_{\max} with some interval Δz [93].

Figure 6.15 shows the graphical representation of the tabulated array values of A , σ and P . In this array, i -th column represents geometrical values for a cross-section located at a distance $(i - 1)\Delta x$ from the downstream boundary, and k -th row in each column represents a geometrical value $f(h_k)$ at depth $(k - 1)\Delta z$. Therefore, for every computed h , all three geometrical values are easily interpolated from:

$$f(h) = h_k + \frac{f(h_{k+1}) - f(h_k)}{h_{k+1} - h_k} (h - h_k) \quad \text{for } h_k \leq h < h_{k+1}, \quad (6.17)$$

where $f(h)$ is a tabulated array of data for $A(h)$, $\sigma(h)$ or $P(h)$ at each cross section, and $1 \leq k < N$, with N being the number of computed values over the water depth.

If cross sections are rectangular or relatively regular, a simple piecewise analytical equation can be used instead of tabulated data. Even if cross sections are not regular, some continuous function can be fitted by the least-square method. However, considering that the Rječina River channel is characterized by semi-natural cross sections and by bridge piers or abutments, the tabulated method was more appropriate. For example, when the following values were set for the Rječina River estuary: $\Delta x = 5$ m, $\Delta z = 0.1$ m, $z_{\min} = -4.1$ m, $z_{\max} = +3.0$ m, and channel length $L = 1410$ m; three 72×283 arrays defined the resulting cross section geometry (Fig. 6.15).

6. Field study in the Rječina River estuary

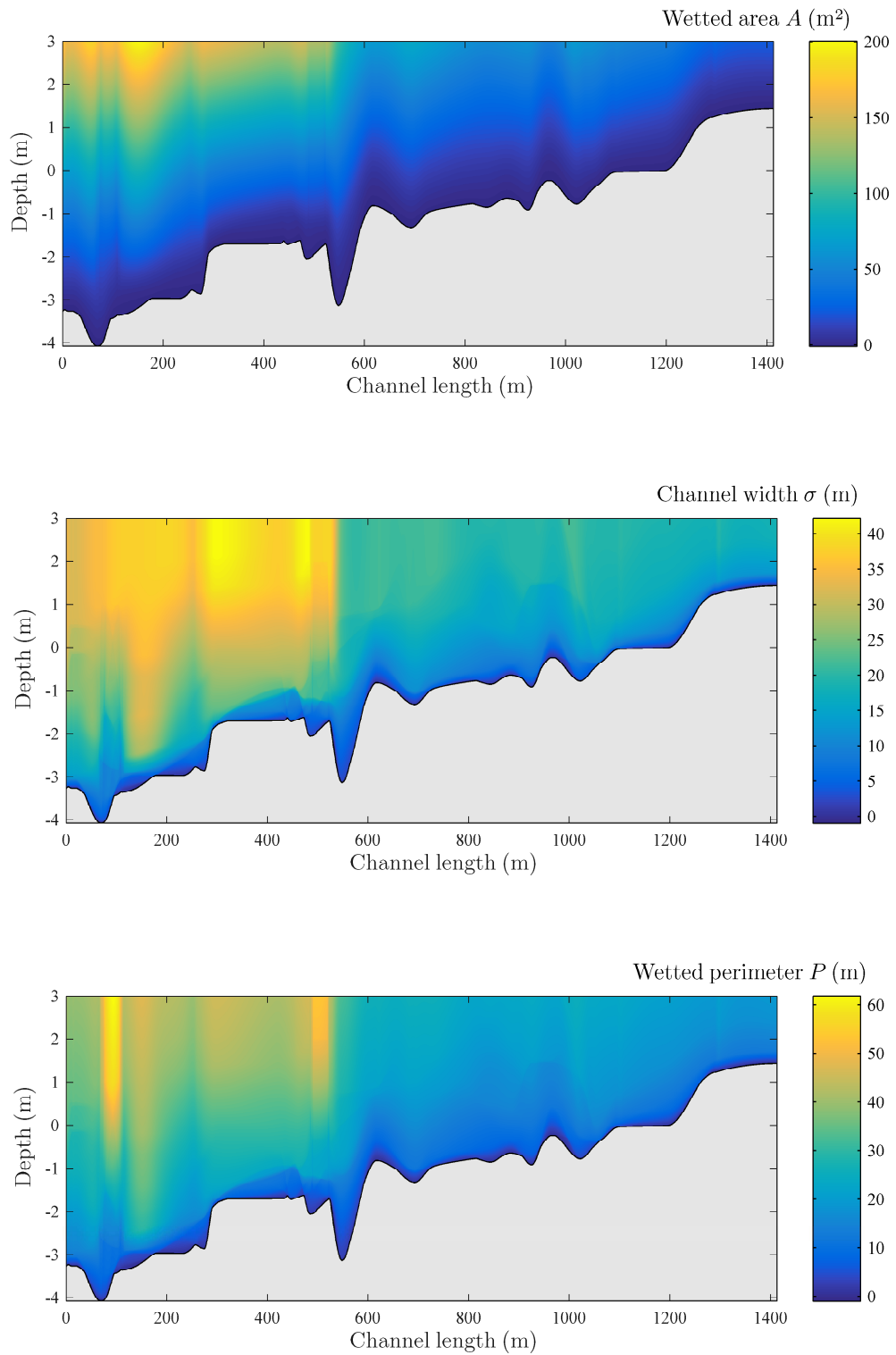


Figure 6.15: Tabulated array of cross-section geometrical values for: (a) wetted area A , (b) channel width σ , and (c) wetted perimeter P .

7

Application to the Rječina River estuary

Contents

7.1 Results of arrested salt-wedges	94
7.1.1 Field observations of arrested salt-wedges	94
7.1.2 FDM results of arrested salt-wedges	97
7.1.3 FVM results of arrested salt-wedges	99
7.2 Results of time-dependant salt-wedges	101
7.2.1 Fields observations of time-dependant salt-wedges	102
7.2.2 FVM results of time-dependant salt-wedges	103

Abstract

This chapter presents the observed salinity structure and numerical results of salt-wedge dynamics in the Rječina River estuary. Both FDM and FVM models were applied to compute the arrested salt-wedge profile under steady flow conditions. The FVM model was additionally applied to compute time-dependant salt-wedge profiles under highly variable flow conditions. Numerical models were validated by comparing the results to field observations under different flow conditions.

7.1 Results of arrested salt-wedges

How far does the seawater intrude in salt-wedge estuaries, how does the salinity structure change under different flow conditions, and more importantly, how well do numerical two-layer models predict the arrested salt-wedge profile in field conditions? All of these questions were answered in the following sections. First, the field observations are presented, in particular, the vertical salinity profiles along the Rječina River estuary under different sea levels and river flow rates. Next, the FDM model was used to calibrate the interfacial friction factor by fitting the numerical results to measured salt-wedge profiles in the field. And finally, the performance of the FVM model was assessed by comparing numerical solutions to measured salt-wedge profiles and flow rates per unit width.

7.1.1 Field observations of arrested salt-wedges

Table 7.1 presents the observed values from sampling campaigns in the Rječina River estuary. River flow rates, measured by the ADCP just upstream from the tip of the salt wedge, ranged from 2.0 to 31.3 m³ s⁻¹, and the sea levels, measured by a water gauge at the mouth, ranged from -0.07 to +0.75 m ASL. The layer-average densities were computed from $S - T$ profiles observed at samplings points along the estuary and linearised as previously shown in Fig. 6.7. The reduced gravity $g(1 - r)$ ranged from 0.235 to 0.271 m s⁻², with $g = 9.81$ m s⁻². The interface thickness δ_i was obtained from salinity profiles using Eq. (6.12), as illustrated in Fig. 6.7, and then averaged along the wedge; it ranged from 0.19 to 0.76 m. The upper and lower layer thickness was computed as a vertical distance between the water surface and the interface, and between the interface and channel bed, respectively. The interface depth was assumed to be located in the middle of the interfacial layer, as illustrated in Fig. 6.7. Maximum squared buoyancy frequency (Eq. 2.15), was computed as a measure of the stratification strength, from the observed vertical density profiles and then averaged along the wedge. In the Rječina River estuary N^2 ranged from 0.4 to 1.7 s⁻², which indicates the presence of a highly stratified water column under all hydrological conditions.

Table 7.1: Observed values in the Rječina River estuary for different flow conditions.

No.	Q ($\text{m}^3 \text{ s}^{-1}$)	sea level (m ASL)	$g(1-r)$ (m s^{-2})	$10^6 \nu$ ($\text{m}^2 \text{ s}^{-1}$)	h_1 (m)	h_2 (m)	δ_i (m)	N^2 (s^{-2})	$10^5 w_e$ (m s^{-1})
1	2.0	0.40	0.257	0.96	0.40	2.54	0.39	0.71	0.99
2	2.8	0.25	0.268	1.34	0.49	2.30	0.19	1.71	0.98
3	4.8	-0.04	0.237	1.18	0.82	1.68	0.33	0.68	2.79
4	4.8	0.10	0.239	1.26	0.75	1.90	0.32	0.77	1.51
5	5.1	0.04	0.253	1.27	0.79	1.79	0.30	0.71	2.24
6	5.3	-0.07	0.245	1.26	0.82	1.65	0.24	0.94	2.69
7	5.7	0.03	0.235	1.19	0.89	1.69	0.43	0.57	3.87
8	7.8	0.60	0.266	1.25	0.97	2.17	0.54	0.52	4.64
9	10.0	0.12	0.249	1.27	1.44	1.22	0.22	0.98	2.70
10	10.0	0.18	0.244	1.23	1.30	1.43	0.23	0.81	5.74
11	11.3	0.14	0.254	1.34	1.48	1.21	0.34	0.87	3.90
12	11.4	0.60	0.264	1.34	1.36	1.79	0.26	1.12	4.00
13	11.5	-0.01	0.255	1.23	1.51	1.04	0.31	0.89	4.53
14	12.3	-0.04	0.251	1.34	1.53	0.98	0.25	0.98	4.37
15	13.4	0.25	0.271	1.35	1.67	1.13	0.36	0.62	6.69
16	14.1	0.50	0.265	1.30	1.52	1.53	0.31	0.95	7.37
17	16.3	0.16	0.248	1.30	1.80	0.92	0.52	0.53	9.42
18	16.8	0.25	0.268	1.35	1.85	0.96	0.76	0.72	7.82
19	17.2	0.45	0.264	1.34	1.86	1.14	0.48	0.60	8.36
20	17.9	0.75	0.265	1.34	1.66	1.64	0.29	0.84	4.98
21	29.8	0.15	0.258	1.34	2.39	0.36	0.62	0.38	25.88
22	31.3	0.35	0.251	1.33	2.53	0.41	0.65	0.39	27.54

Note: River flow rate Q was measured upstream from the salt-wedge by the ADCP, sea level was measured by a water gauge at the mouth, $g = 9.81 \text{ m s}^{-2}$, layer-average density ratio $r = \rho_1/\rho_2$ was computed from the observed density profiles, freshwater viscosity ν was computed from the measured density and temperature profiles, h_1 and h_2 are the respective upper and lower layer thickness (see Fig. 6.7d), δ_i is interfacial thickness (see Fig. 6.7c), N^2 is maximum squared buoyancy frequency (Eq. 2.15), and w_e is entrainment velocity obtained from the box model (Eq. 6.13 - 6.16). All parameters in the columns 4 - 10 are averaged along the salt-wedge.

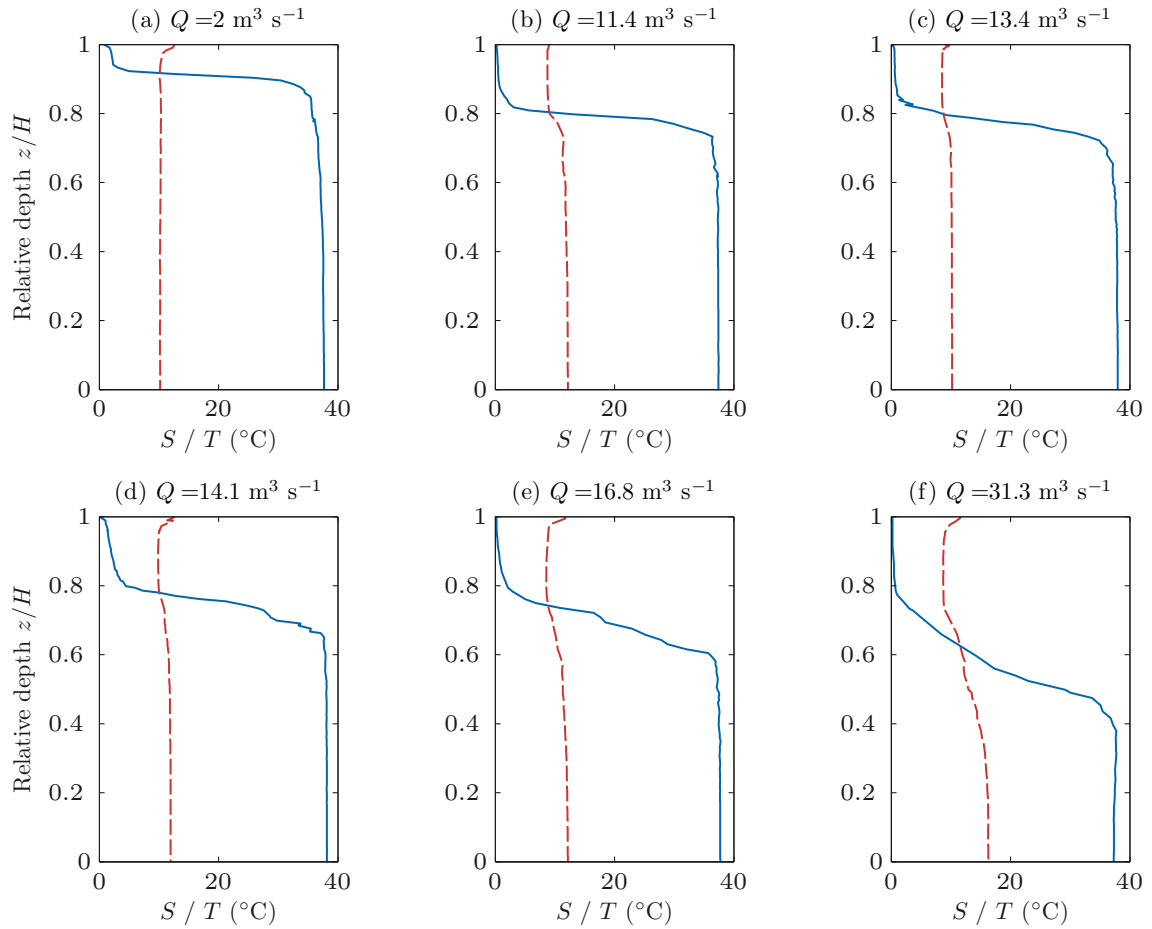


Figure 7.1: Salinity S (solid) and temperature T (dashed) profiles observed in the Rječina River estuary near the mouth (P3) for different river flow rates Q .

Salinity structure and stratification

A typical salinity structure of an arrested salt-wedge in the Rječina River shows nearly constant salinities in each layer along the estuary and strong vertical stratification. Figure 7.1 shows six characteristic vertical $S-T$ profiles, observed near the mouth (P3, Fig. 6.1) during different flow rates. Vertical profiles were consistent along the arrested salt-wedge for steady flow. As expected, the interface depth grows with Q , but the influence of the upper layer flow on the interfacial layer thickness is also noticeable. For lower flow rates, a sharp gradient is preserved, as it can be seen in Fig. 7.1a,b,c. As the flow rate increases above $13 \text{ m}^3 \text{ s}^{-1}$, the interfacial layer becomes more diffusive and its thickness grows, as illustrated in Fig. 7.1d,e. For high flow rates ($Q = 31.3 \text{ m}^3 \text{ s}^{-1}$), the interface is characterized by a well-defined mixed layer, as shown in Fig. 7.1f.

Entrainment

The entrainment velocities were estimated by the box model (Eq. 6.13 - 6.16). The upward water flux w_{21} was a few times to a few orders of magnitude larger than the downward water flux w_{12} , and the corresponding w_e ranged from 1.0×10^{-5} to $27.5 \times 10^{-5} \text{ m s}^{-1}$ (Table 7.1). Similar values of w_e were found at the Ebro River estuary in Spain [49] and the Jadro River estuary in Croatia [61], both microtidal salt-wedges. Whereas, the values in macrotidal salt-wedge estuaries, in particular, the Duwamish River [72] and the Fraser River [64], are one order of magnitude higher, most likely because of stronger tidal mixing. The box model also indicated that the lower layer flow rate ranged from -0.1 to $-1.0 \text{ m}^3 \text{ s}^{-1}$, directed upstream as a result of mixing processes, *i.e.*, Q_2 varied from 3% to 15% of the total river flow rate Q .

7.1.2 FDM results of arrested salt-wedges

The FDM numerical model was used to calibrate λ_i by fitting the computed salt-wedge profiles to observed interface depths along the estuary. Steady flow profiles were obtained by solving the equations (4.3) - (4.6) for different boundary conditions.

The spatial step was set to $\Delta x = 1 \text{ m}$, and the calculation started at the last bridge near the river mouth (P1, Fig. 6.1). The downstream boundary was forced by the flow rates Q_1 and Q_2 , critical upper layer depth h_1 , and total water depth H at the mouth, which corresponded to observed sea levels. Additionally, the model was defined by r , computed from layer-average densities observed in the field (Table 7.1). The entrainment velocity w_e was assumed constant along the wedge, and computed by the box model for each observation (Table 7.1). The wall and bed friction factors were calculated from Manning's roughness factor $n_M = 0.025 \text{ s m}^{-1/3}$ (for channels with gravel bottom and concrete/stone sides). Finally, the numerical solutions were fitted to the observed interface depths by systematically varying λ_i as described earlier. The interfacial friction factor was assumed constant along the wedge, and the best fit was determined by the visual inspection and by the smallest RMSE (Eq. 4.7).

Figure 7.2 shows three numerical solution of arrested salt-wedge profile, for several different Q and sea levels, which are representative of those for a total of 22 simulations performed (see Appendix A for all results). The computed length of the arrested salt-wedge and the slope of the interface is sensitive to λ_i , which needed to be fitted

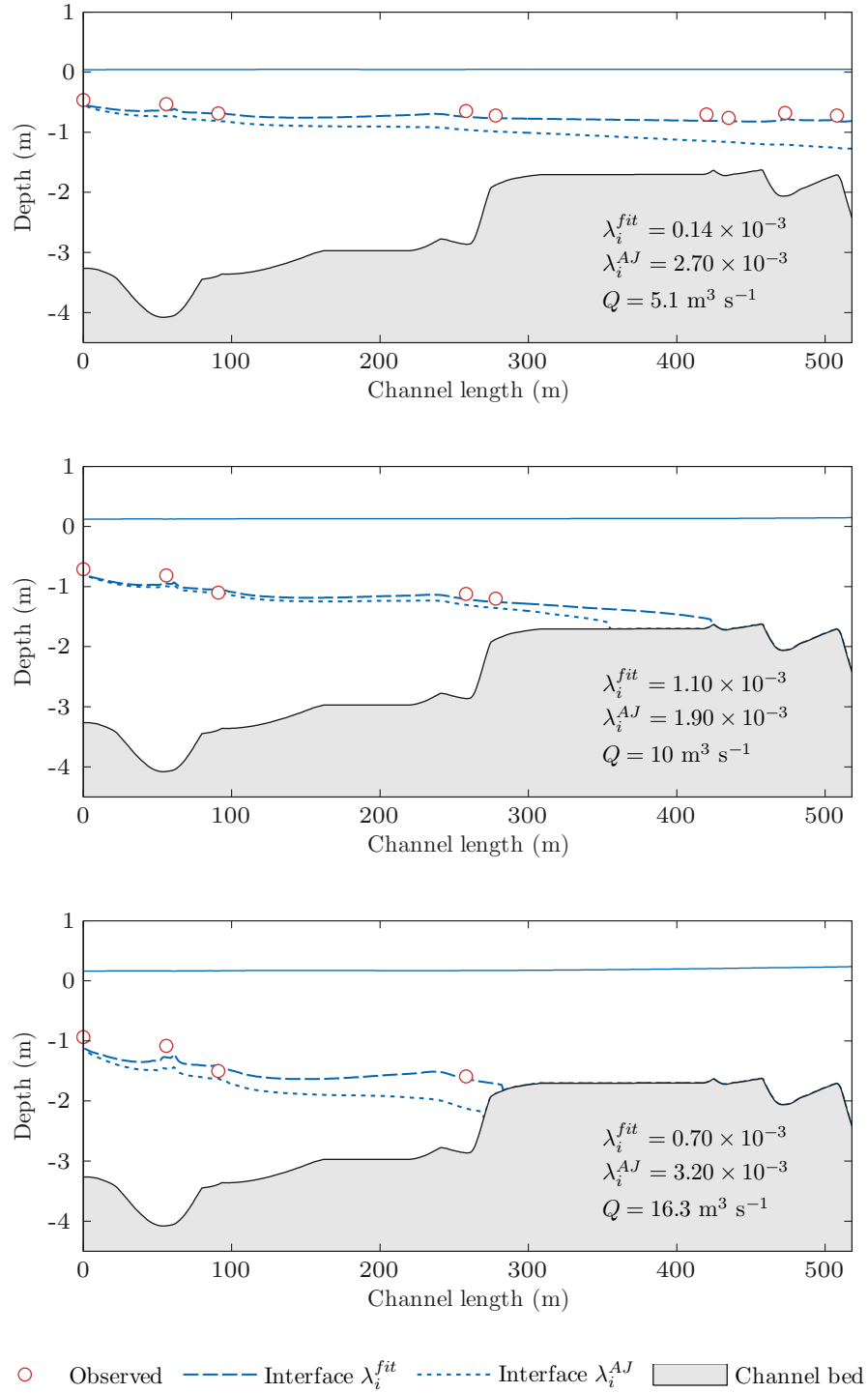


Figure 7.2: Numerical FDM solutions of the salt-wedge shape compared against field observations, for different river flow rates Q . Both λ_i^{fit} (fitted interfacial friction factor) and λ_i^{AJ} (computed from the Arita and Jirka model, Eq. (2.9)) were considered.

to obtain satisfactory agreement with field observations. When existing interfacial friction laws [94, 29, 3] were applied to calculate λ_i , they either overestimated or underestimated the length of the salt-wedge.

The numerical solution computed with two different interfacial friction factors are presented; λ_i^{fit} , obtained by the best fit with the field observations, and λ_i^{AJ} , computed from the Arita and Jirka's friction equation (2.9). Results suggest that the model by Arita and Jirka [2] generally overestimates λ_i and the interface slope, and therefore underestimates the salt-wedge intrusion length (Fig. 7.2). The values of λ_i^{fit} and λ_i^{AJ} sometimes disagreed by an order of magnitude (Fig. 7.2). Sorgard [89] also found that the model by Arita and Jirka [2] underestimates the salt-wedge length in the Glomma River estuary.

7.1.3 FVM results of arrested salt-wedges

The FVM numerical model was used to validate the computed arrested salt-wedge profiles along the Rječina River estuary, under steady flow conditions. The model domain was divided by $M = 80$ cells, with the spatial step $\Delta x = 10$ m and temporal step $\Delta t = 0.5$ s, to satisfy the CFL condition. Density ratio was set on a case-by-case basis, according to the measured upper and lower layer densities; and it ranged from 0.972 to 0.976 (Table 7.1). The entrainment velocity was assumed constant along the wedge, and was computed by the box model for each case (Table 7.1). The wall and bed friction factors were calculated from Manning's roughness factor $n_M = 0.025$ s m^{-1/3}. Finally, fitted λ_i , obtained from the FDM analysis, was used as the interfacial friction factor (Table 8.1). The upstream and downstream boundary conditions were forced by the constant river flow rate $Q_1(x_M, t) = Q_1(x_M, 0)$, the critical upper layer depth $h_1(x_0, t)$, and the total depth $H(x_0, t)$ at the mouth, which corresponded to the observed sea levels. The initial condition was obtained from the previous FDM steady-state solution, for the same flow and sea-level conditions (Fig. 7.2). The simulation lasted until steady-state conditions were reached.

Figure 7.3 shows the computed and observed arrested salt-wedge profiles, for the same three cases as in the previous subsection. In general, for higher Q the arrested salt-wedge length was shorter and the upper layer was thicker. Similarly, for higher sea-level the arrested salt-wedge intruded further upstream. However, these results suggest

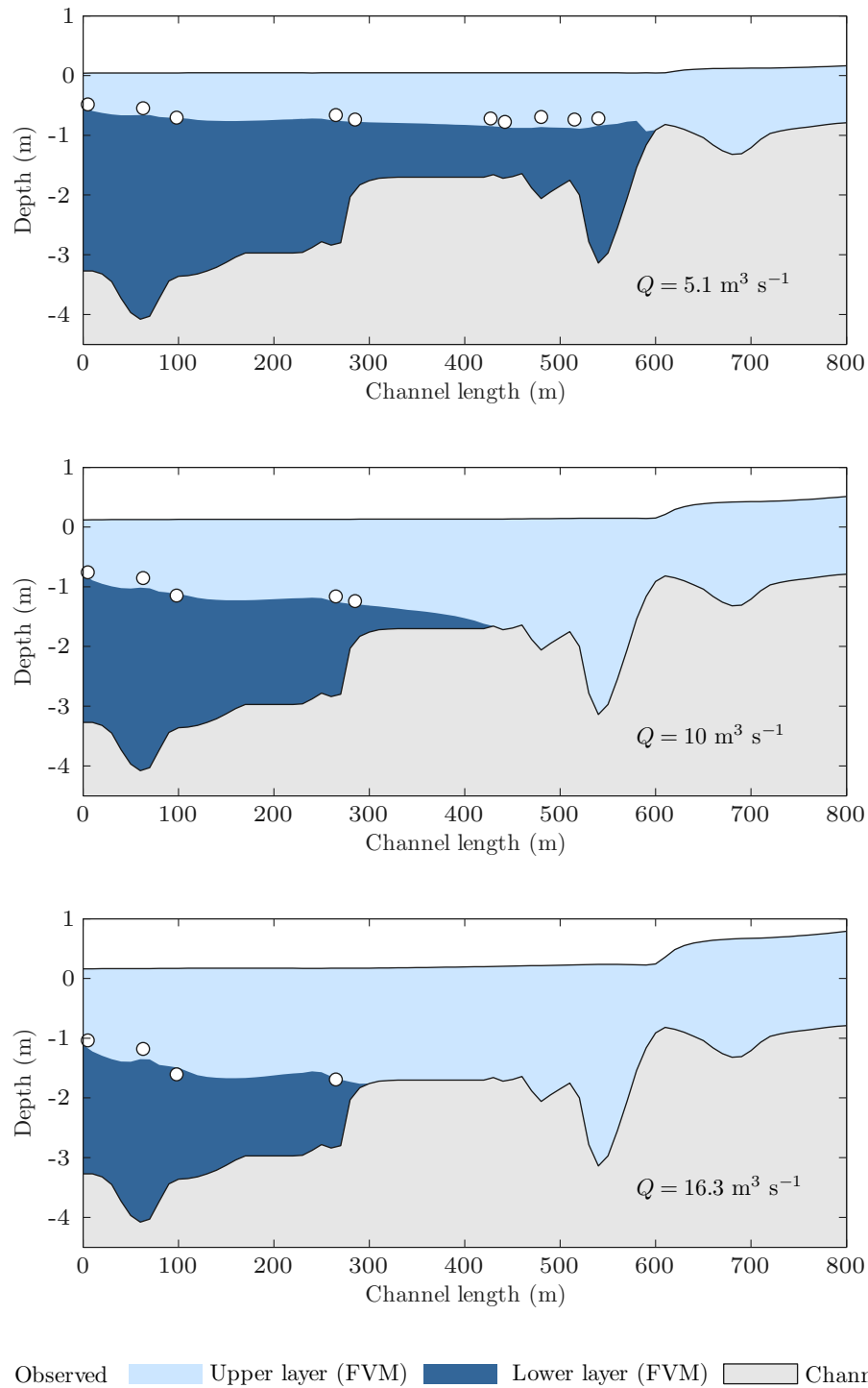


Figure 7.3: Numerical FVM solutions of the arrested salt-wedge shape compared against field observations, for different river inflow rates Q .

that the salt-wedge length depends also on the channel geometry; steeper slopes or sills may limit the salt-wedge from advancing further upstream. The variable slope of the interface was mainly the result of the irregular channel geometry in the estuary.

Model validation

For each arrested salt-wedge case, the computed salt-wedge profile was compared against interface depths observed along the estuary. The following skill metrics were used to validate the numerical model and quantify the agreement between the data: mean absolute error (MAE), correlation coefficient (CC), and skill score (SS), which are respectively defined as follows [70]:

$$\text{MAE} = \frac{1}{N} \sum |X_{\text{mod}} - X_{\text{obs}}|, \quad (7.1)$$

$$\text{CC} = \frac{\sum (X_{\text{mod}} - \bar{X}_{\text{mod}}) (X_{\text{obs}} - \bar{X}_{\text{obs}})}{\sqrt{\sum (X_{\text{mod}} - \bar{X}_{\text{mod}})^2 \sum (X_{\text{obs}} - \bar{X}_{\text{obs}})^2}}, \quad (7.2)$$

$$\text{SS} = 1 - \frac{\sum (X_{\text{mod}} - \bar{X}_{\text{mod}})^2}{\sum (X_{\text{obs}} - \bar{X}_{\text{obs}})^2}, \quad (7.3)$$

where N is the number of data points, X_{mod} is modelled data, X_{obs} is observed data, and overbar represents a mean value. A perfect correlation is indicated by $\text{MAE} = 0$, $\text{CC} = 1$, and $\text{SS} = 1$, whereas $\text{CC} = 0$, $\text{SS} = 0$, and large values of MAE indicate no correlation.

Overall, all skill metrics for arrested salt-wedge profiles indicated a strong agreement between the FVM model results and observed interface depths, with $\text{MAE} = 0.12$ m, $\text{CC} = 0.94$, and $\text{SS} = 0.87$.

7.2 Results of time-dependant salt-wedges

This section presents the observed and computed response of a salt-wedge in the Rječina River estuary to changes in the river flow rate. Furthermore, the FVM numerical model was validated by comparing the solutions against field observations for variable flow conditions.

Krvavica *et al.* [54] showed that the flow rate in the lower reaches of the Rječina River during summer months is highly sensitive to overflows from the Rijeka HPP. On

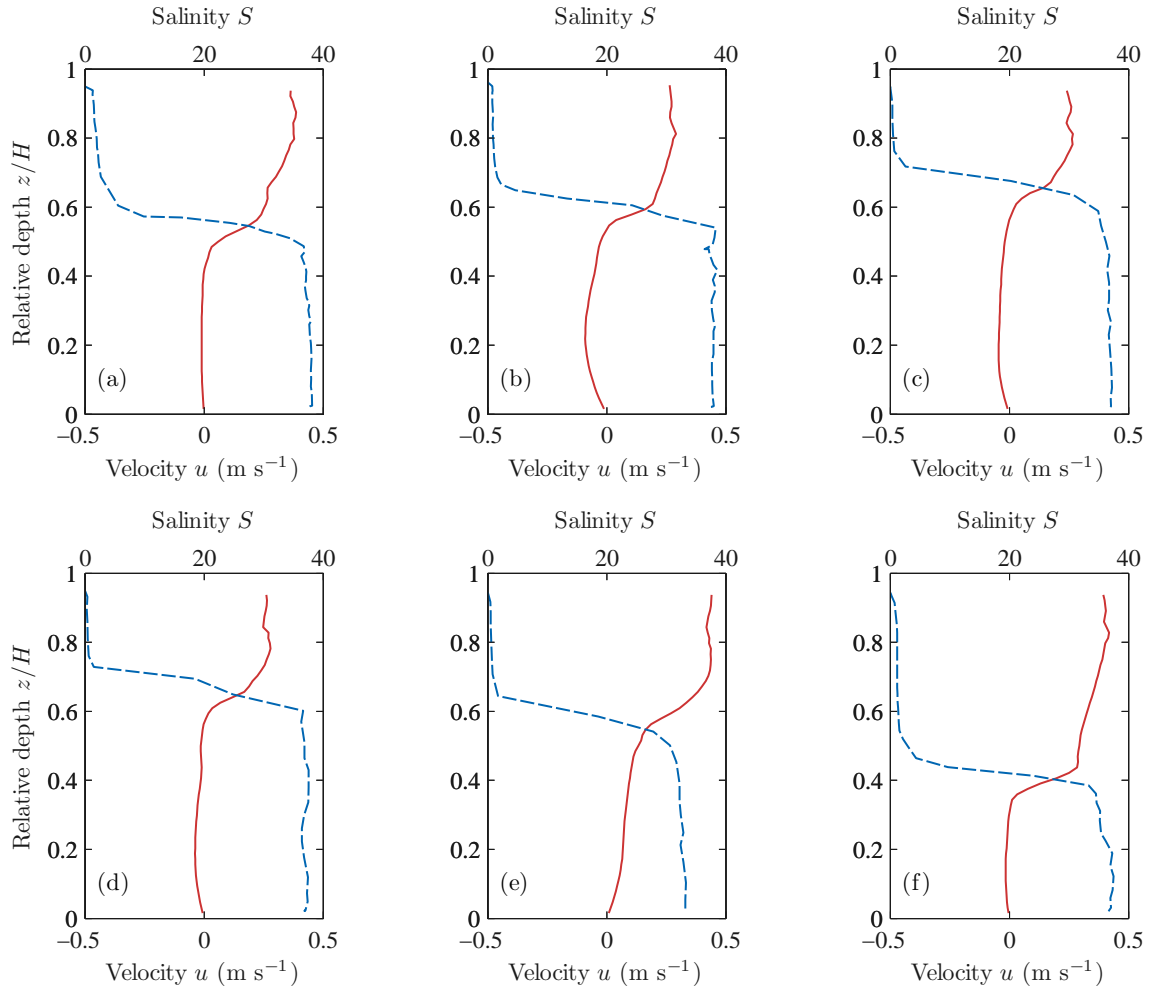


Figure 7.4: Velocity u (solid) and salinity S (dashed) profiles observed in the Rječina River estuary near the mouth (P3): (a) to (c) salt-wedge intrusion caused by a decrease in the river flow rate from 10 to 4.6 $\text{m}^3 \text{s}^{-1}$, and (d) to (f) salt-wedge receding towards the mouth caused by an increase in the river flow rate from 4.2 to 13.4 $\text{m}^3 \text{s}^{-1}$.

1 July 2015 the Rijeka HPP started and stopped on two occasions in an eight-hour period (from 07:00 to 15:00), which caused highly variable conditions to form in the estuary, and the river flow rate ranged between 4.2 and 13.9 $\text{m}^3 \text{s}^{-1}$ (Fig. 7.5a).

7.2.1 Fields observations of time-dependant salt-wedges

Figure 7.4 presents several characteristic salinity and velocity profiles obtained from measurements on 1 July 2015, near the river mouth (P3, Fig. 6.1), and for different flow rates. Velocity profiles obtained under steady-state conditions are characterized by a nearly stagnant lower layer and a characteristic turbulent logarithmic shape

in the upper layer. Figure 7.4a shows $S - u$ profile for the arrested salt-wedge and $Q_1 = 9.8 \text{ m}^3 \text{ s}^{-1}$. During a decrease in the river flow, the salt-wedge advanced upstream, which resulted in negative velocities in the lower layer. Figure 7.4b shows $S - u$ profile for $Q_1 = 6.3 \text{ m}^3 \text{ s}^{-1}$ and $Q_2 = -1.9 \text{ m}^3 \text{ s}^{-1}$. After the equilibrium was established between the inertial forces, pressure gradient and friction forces, the salt-wedge became arrested again. Figure 7.4c shows $S - u$ profile for the arrested salt-wedge, where $Q_1 = 4.6 \text{ m}^3 \text{ s}^{-1}$ and $Q_2 = -0.4 \text{ m}^3 \text{ s}^{-1}$.

Similarly, Fig. 7.4d shows $S - u$ profile for an arrested salt wedge and $Q_1 = 4.2 \text{ m}^3 \text{ s}^{-1}$. As the flow rate increased the salt-wedge was pushed out of the estuary until the force equilibrium was established. Figure 7.4e shows $S - u$ profile for $Q_1 = 9.6 \text{ m}^3 \text{ s}^{-1}$ and $Q_2 = 4.6 \text{ m}^3 \text{ s}^{-1}$, and Fig. 7.4f shows $S - u$ profile for the arrested salt-wedge, with $Q_1 = 13.4 \text{ m}^3 \text{ s}^{-1}$.

7.2.2 FVM results of time-dependant salt-wedges

The FVM numerical model was applied to compute the salt-wedge profiles along the Rječina River estuary under time-dependant flow conditions, and to validate the proposed model. The model domain was divided by $M = 160$ cells, with the spatial step $\Delta x = 5 \text{ m}$ and temporal step $\Delta t = 0.25 \text{ s}$, to satisfy the CFL condition. A denser mesh, in comparison to the steady-state cases, was chosen to accurately capture the salt-wedge movement. The density ratio was set to 0.975, corresponding to the observed layer-averaged freshwater density $\rho_1 = 1000 \text{ kg m}^{-3}$ and salt-water density $\rho_2 = 1026 \text{ kg m}^{-3}$. The entrainment velocity w_e was assumed constant along the wedge but varied in time according to the average flow rate (Table 7.1). The wall and bed friction factors were calculated from Manning's roughness factor $n_M = 0.025 \text{ s m}^{-1/3}$. Finally, a fitted interfacial friction factor was used; λ_i was also considered constant along the wedge, but varied in time corresponding to the upper layer flow rate.

The upstream and downstream boundary conditions were forced by the river inflow $Q_1(x_M, t)$, which corresponded to the observed river hydrograph (Fig. 7.5a), the critical upper layer depth $h_1(x_0, t)$ and the total depth $H(x_0, t)$ at the mouth, which corresponded to the observed sea-levels (Fig. 7.5b). The numerical simulation started at 07:20 and lasted until 15:20 (480 min) to capture all the changes in the salt-wedge shape (at 15:20 the conditions in the estuary became stationary and the arrested salt-wedge was formed).

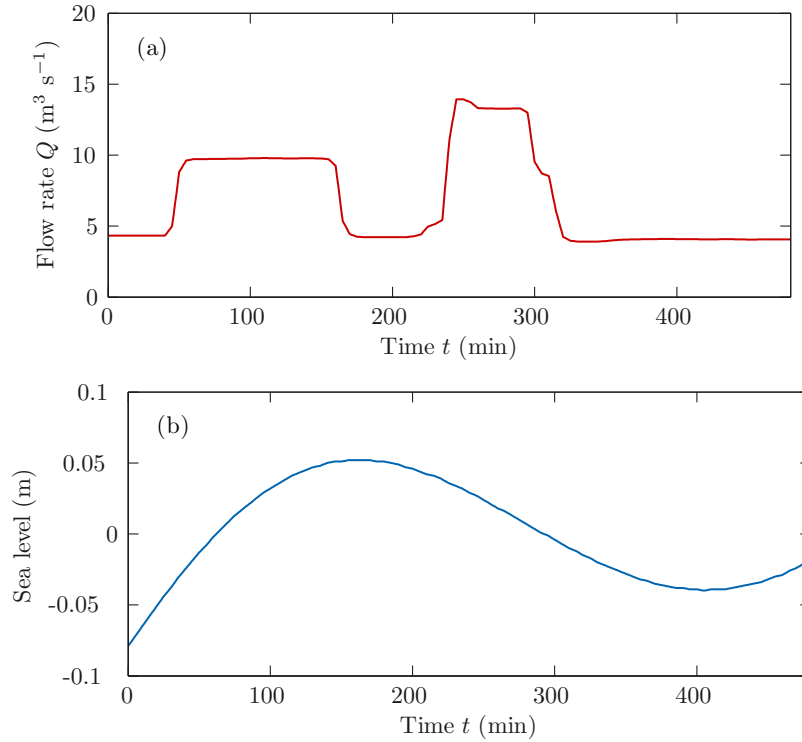


Figure 7.5: Boundary conditions for a time-dependant salt-wedge case: (a) upstream flow rate and (b) downstream sea-level.

Figure 7.6 presents the computed and observed salt-wedge profiles along the estuary at different time steps. Both numerical solutions and field observations showed that the salt-wedge responded almost instantly to changes in the river flow rate by moving along the estuary in either upstream or downstream direction. When Q increased, the salt-wedge receded downstream towards the mouth, and *vice versa*.

Figure 7.7 shows the computed and observed flow rates per unit width in each layer. Near the river mouth the upper layer q_1 varied proportionally to Q ; however, the lower layer q_2 seemed to respond more to the movement of the salt-wedge than to the river flow rate. When Q increased, q_2 was positive and the lower layer receded downstream. Similarly, when Q decreased, q_2 was negative and the lower layer intruded upstream. In both cases, after an equilibrium condition was reached (*i.e.*, an arrested salt-wedge was established), q_2 returned to near-zero values.

Field validation

For time-dependant salt-wedge case, the computed salt-wedge profiles were compared against interface depths observed along the estuary at different time steps. Additionally,

7. Application to the Rječina River estuary

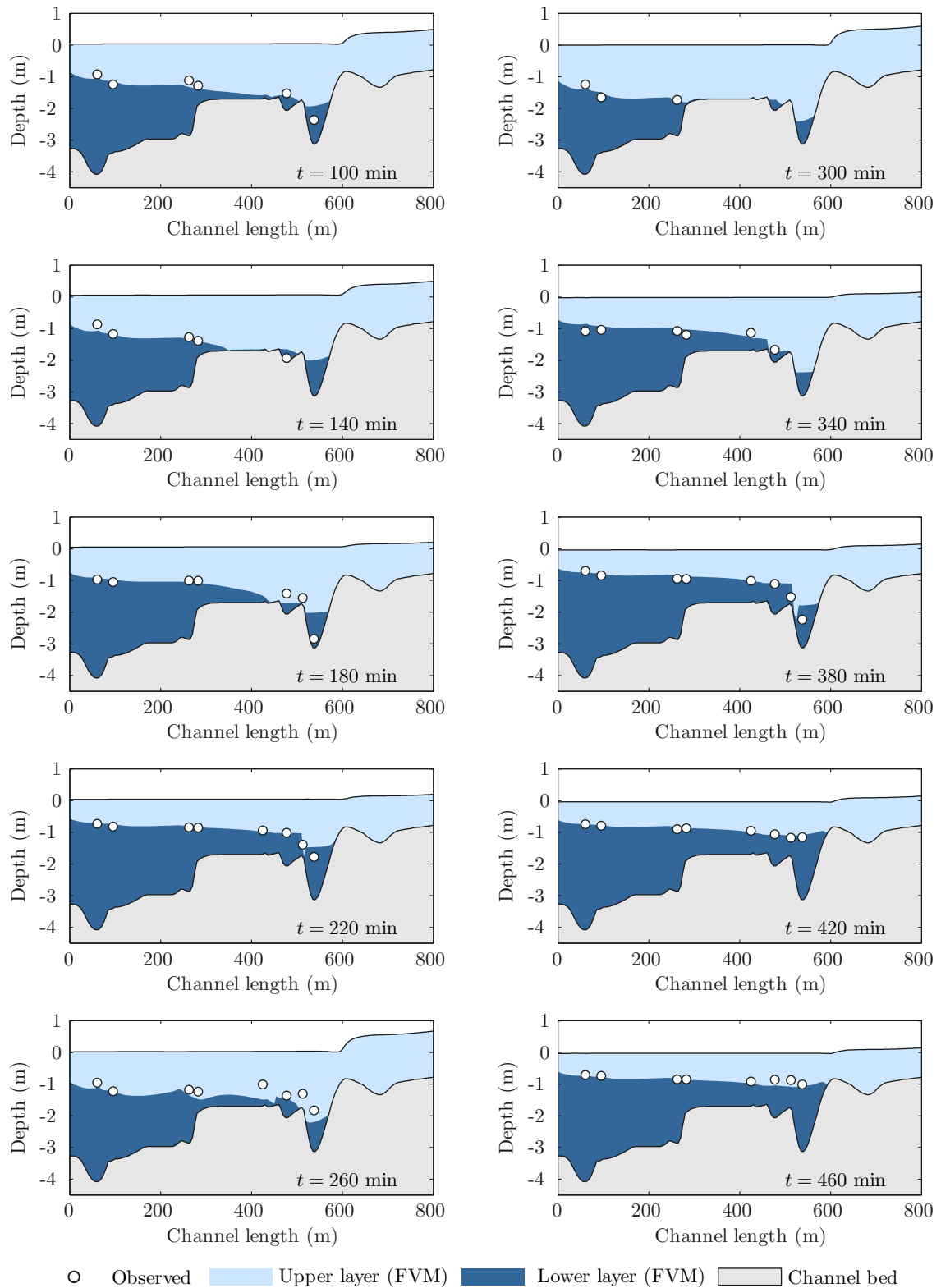


Figure 7.6: Numerical FVM solutions of the time-dependent salt-wedge profile compared against field observations, at different time steps, for variable river flow rate Q .

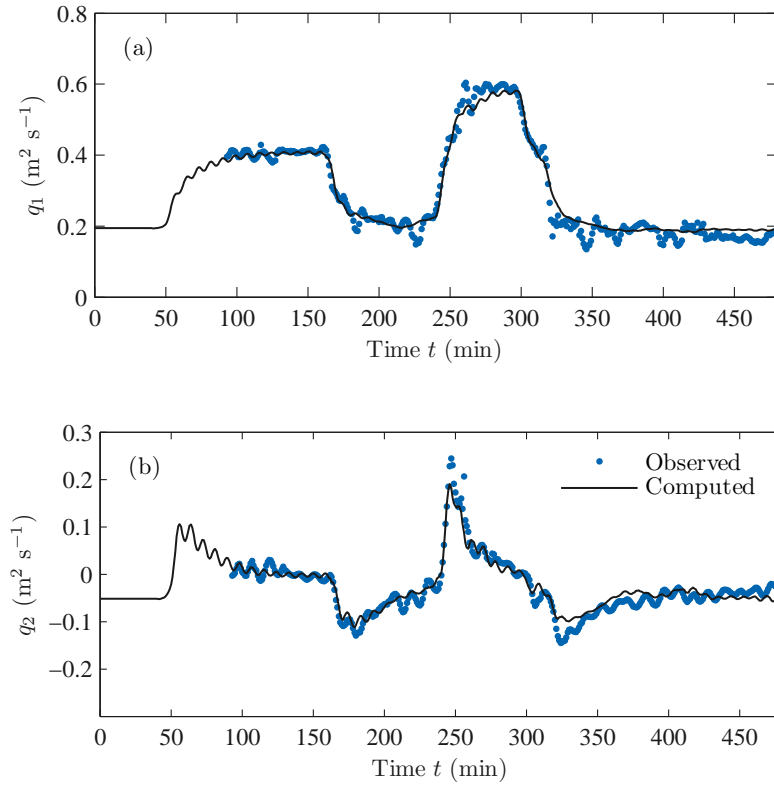


Figure 7.7: Computed and observed changes of flow rates per unit width in the upper (q_1) and lower (q_2) layer, near the mouth (P3, Fig. 6.1).

q_1 and q_2 near the mouth, were also compared against field observations during the simulation. Once more, the following skill metrics were used to validate the model and quantify the agreement between the data: MAE (Eq. 7.1), CC (Eq. 7.2), and SS (Eq. 7.3).

All skill metrics indicated a strong agreement between the modelled and observed data. For h_1 , the MAE was 0.12 m, CC = 0.9, and SS = 0.8. For flow rates per unit width the agreement was even stronger; for q_1 the MAE was $0.018 \text{ m}^2 \text{ s}^{-1}$, CC = 0.99, and SS = 0.97, and for q_2 the MAE was $0.014 \text{ m}^2 \text{ s}^{-1}$, CC = 0.95, and SS = 0.89.

8

Discussion of salt-wedge dynamics

Contents

8.1 Discussion of interfacial processes	108
8.1.1 Entrainment parametrisation	111
8.1.2 Interfacial friction parametrisation	114
8.2 Discussion of hydraulic control	117
8.3 Discussion of stratification strength	118
8.4 Discussion of salt-wedge propagation rates	119

Abstract

This chapter discusses the numerical results presented in the previous chapter. A particular emphasis is placed on the parametrisation of interfacial processes, namely the interfacial friction factor and entrainment rate. Furthermore, the main salt-wedge processes such as the hydraulic control at the downstream boundary, stratification strength under both steady and variable flow conditions, and propagation rates of the salt-wedge front are additionally discussed.

8.1 Discussion of interfacial processes

Field observations and numerical results are discussed and examined here to better understand the interfacial processes in microtidal salt-wedge estuaries. Table 8.1 presents computed flow parameters obtained after fitting numerical solutions to the observed data. All presented values are computed from numerical solutions based on the assumption of zero interfacial layer thickness, and they represent an along-wedge average values.

The bed friction factor $\lambda_b = \lambda_w$ was obtained from Manning's equations with $n_M = 0.025 \text{ s m}^{-1/3}$, and it ranged from 3.4×10^{-3} to 3.9×10^{-3} . Interfacial friction factor was fitted as previously described, and ranged from 7.0×10^{-5} to 1.6×10^{-3} . The agreement between computed and observed interface depths was quantified by RMSE (Eq. 4.7), which showed a mean value of 0.11 m (smaller than the mean value of the interfacial thickness $\bar{\delta}_i = 0.38 \text{ m}$, presented in Table 7.1). The computed velocity difference Δu ranged from 0.17 to 0.47 m s^{-1} . Interfacial shear velocity u_* ranged from 1.6×10^{-3} to $17.7 \times 10^{-3} \text{ m s}^{-1}$, and the entrainment rate E ranged from 0.5×10^{-4} to 6.2×10^{-4} . Non-dimensional parameters showed the following values: Re ranged from 6×10^4 to 6×10^5 , Fd ranged from 0.53 to 0.64, and Ri ranged from 3.3 to 4.5.

Figure. 8.1 illustrates how the governing parameters change with the river flow rate. In general, as Q increases, salt-wedge length becomes shorter and the upper layer is thicker. Both h_1 and Δu increase with Q (Fig. 8.1a,b); therefore, Re also increases with Q . The correlation of h_1 and Δu with Q is non-linear and very strong ($R^2 = 0.98$). However, it seems that as a results of a sloped channel bed and different sea levels, Fd only slightly increases with Q (Fig. 8.1c); therefore, the correlation in this case is relatively weaker ($R^2 = 0.57$).

In most salt-wedge estuaries, strong stratification and even the salt-wedge structure itself is maintained by high river flow, which dampens the vertical mixing caused by tidal motions [36]. In microtidal salt-wedges, on the other hand, an increase in Q may result in high shear velocities at the interface, which produce turbulent energy and increases vertical mixing [90]. The observations show that when the river flow rises and the stratification is reduced (Fig. 8.1d), both w_e (Fig. 8.1e) and u_* (Fig. 8.1f) increase with Q . Whereas, at low Q strong stratification reduces both interfacial shear and the entrainment.

Table 8.1: Fitted friction factors and computed mixing and flow parameters in the Rječina River estuary.

No.	$10^3 \lambda_b$	$10^4 \lambda_i$	RMSE (m)	Δu (m s ⁻¹)	$10^3 u_*$ (m s ⁻¹)	$10^4 E$	$10^{-5} Re$	Fd	Ri
1	3.4	1.0	0.05	0.17	1.7	0.59	0.6	0.54	3.9
2	3.5	0.7	0.05	0.20	1.6	0.50	0.7	0.56	3.6
3	3.7	4.0	0.07	0.22	4.4	1.25	1.3	0.53	4.1
4	3.7	1.2	0.11	0.23	2.5	0.66	1.2	0.56	3.6
5	3.7	1.4	0.08	0.24	2.8	0.94	1.3	0.55	3.7
6	3.7	2.0	0.14	0.24	3.4	1.13	1.4	0.56	3.7
7	3.7	1.8	0.10	0.25	3.2	1.58	1.6	0.56	3.6
8	3.5	2.0	0.03	0.27	3.8	1.69	1.8	0.56	3.6
9	3.8	11.0	0.07	0.28	9.3	0.96	2.4	0.53	4.5
10	3.8	6.0	0.09	0.29	7.1	1.98	2.5	0.56	3.9
11	3.8	7.5	0.07	0.31	8.4	1.27	2.6	0.57	3.9
12	3.6	9.5	0.13	0.30	9.0	1.35	2.5	0.53	4.3
13	3.6	6.0	0.07	0.33	7.9	1.39	2.9	0.60	3.5
14	3.6	5.0	0.07	0.34	7.5	1.29	2.9	0.62	3.3
15	3.6	10.5	0.15	0.33	10.6	2.03	3.0	0.56	4.1
16	3.7	4.0	0.15	0.34	6.7	2.17	3.2	0.57	3.6
17	3.6	7.0	0.12	0.37	9.6	2.53	3.8	0.61	3.3
18	3.6	13.0	0.11	0.37	13.2	2.13	3.7	0.59	3.7
19	3.6	6.0	0.12	0.36	8.8	2.29	3.7	0.59	3.6
20	3.6	2.0	0.04	0.37	5.2	1.33	3.7	0.60	3.3
21	3.9	11.0	0.36	0.47	15.3	5.56	6.2	0.64	3.7
22	3.8	16.0	0.30	0.44	17.7	6.19	6.3	0.61	4.1

Note: bed friction factor $\lambda_b = \lambda_w$ was obtained from Manning's equation with $n_M = 0.025 \text{ sm}^{-1/3}$, interfacial friction factor λ_i was fitted to the observed data, $\Delta u = u_1 - u_2$, where u_1 and u_2 are the respective upper and lower layer velocities computed by the numerical model, $u_* = \sqrt{\tau_{int}/\rho}$ is shear velocity, $E = w_e/\Delta u$ is entrainment rate, Re is Reynolds number, Fd is densimetric Froude number, Ri is bulk Richardson number, and RMSE denotes root mean square error for quantifying the agreement between numerical solutions and observed interface depths.

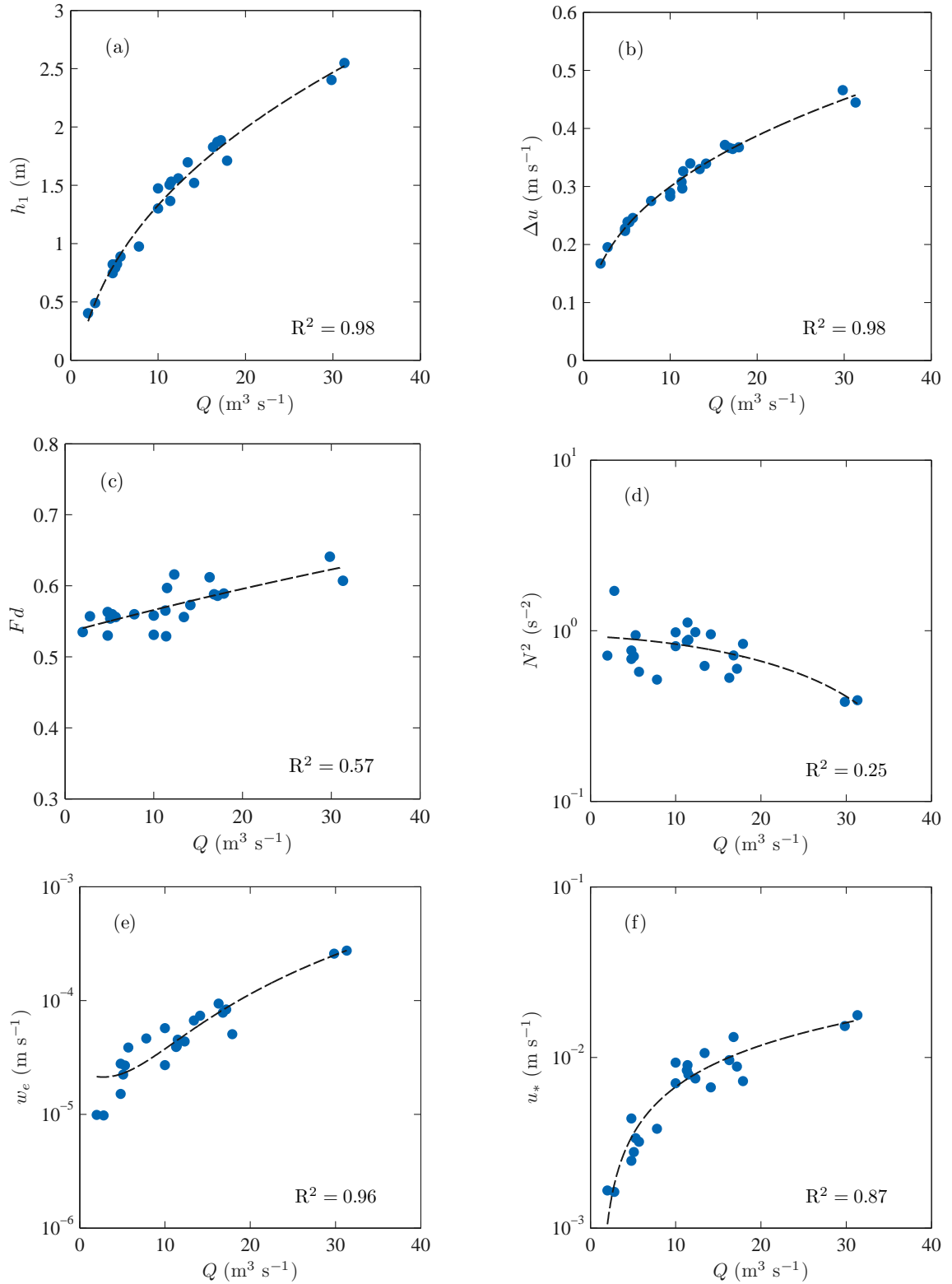


Figure 8.1: Dependence of the: (a) upper layer thickness h_1 , (b) velocity difference Δu , (c) densimetric upper layer Froude number Fd , (d) squared buoyancy frequency N^2 , (e) entrainment velocity w_e , and (f) interfacial shear velocity u_* , on the river flow rate Q .

Note that a strong correlation is also observed between w_e and Q ($R^2 = 0.96$), as well as between u_* and Q ($R^2 = 0.87$), which is surprising considering the complexity of turbulent processes in stratified environments. The strong correlation also justifies numerous attempts to derive a suitable parametrization of these interfacial processes based on bulk flow parameters, which will be further discussed in the following sections.

8.1.1 Entrainment parametrisation

Figure 8.2a shows the entrainment rates plotted against the bulk Richardson numbers and several entrainment laws from the literature. Based on numerous experiments [69, 13, 74, 26, 71, 103] it is generally considered that E reduces with increasing Ri . Surprisingly, in this case, Ri does not seem to be the main governing parameters for E ; the data are in the expected range, but E shows a wide range of values, from 5×10^{-5} to 6×10^{-4} , for a narrow range of bulk Richardson numbers, $3.3 < Ri < 4.5$.

Figure 8.2b shows another comparison between the observed E and the entrainment parametrisation of Cenedese and Adduce (Eq. 2.14). The agreement is also weak in this case, but the values are in the expected range. Once more, the main difficulty is that the observations show a wide range of E for similar densimetric Froude numbers, $0.53 < Fd < 0.64$. According to Eq. (2.14), however, the entrainment rate is expected to increase over the same range as Fd increases from 0.44 to 0.77, which is relatively close to the computed Fd values.

The scattering for similar Ri could be explained by the entrainment in estuaries being intermittent and influenced by local conditions [84]. Another possible explanation could be found in Strang and Fernando's study [92], where a considerable scatter was also observed in the range $3.2 < Ri < 5.8$. They found that as Ri increases from 3.2 to 5.8, interfacial instabilities change from K-H waves to asymmetric Holmboe waves. The resonating K-H and Holmboe waves may be responsible for a wide disparity of entrainment rates. However, statements about the role of specific interfacial instabilities made solely on the range of bulk Richardson numbers is qualitative at best. Both these comparisons suggest that the entrainment rate is difficult to predict based on bulk flow parameters, such as Ri or Fd . Clearly, local gradient measurements are more adequate.

To examine the parameters that govern the mixing processes in more details, the entrainment rates are plotted against N^2 (Fig. 8.3a), u_* (Fig. 8.3b), and their

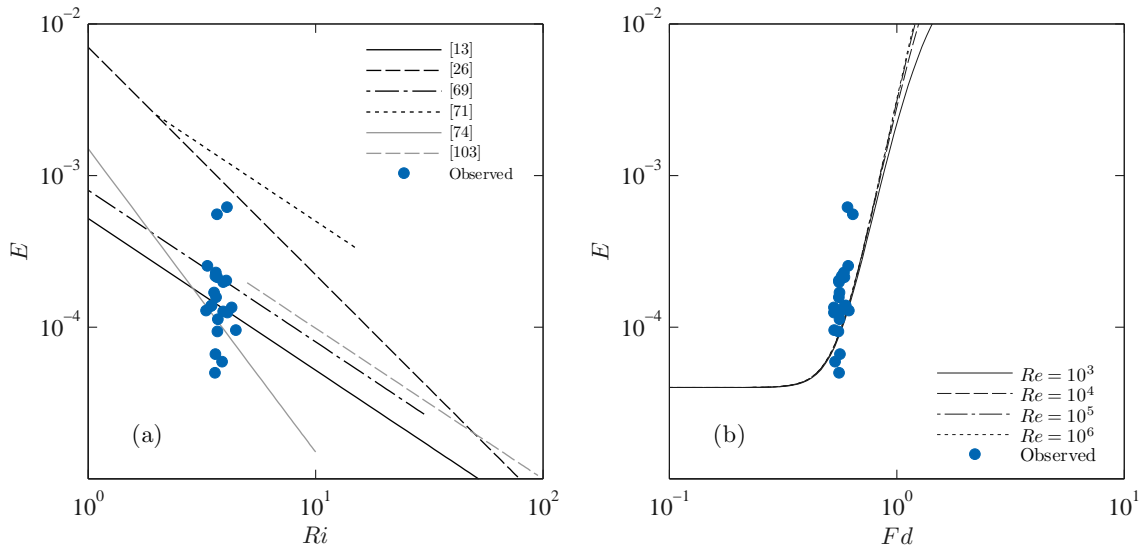


Figure 8.2: Dependence of entrainment rate E on (a) bulk Richardson number Ri (with comparison to equations by Buch [13], Christodoulou [26], Moore and Long [69], Narimousa and Fernando [71], Pedersen [74], and Walker and Hamill [103]) and (b) densimetric Froude number Fd (with comparison to Cenedese and Adduce [24]).

non-dimensional ratio $N^2/(u_*^2/\nu)^2$ (Fig. 8.3c). The latter parameter, although related to, should not be confused with the Richardson gradient number (Eq. 2.17), which requires a detail measurement of the velocity profile. In this case, however, the shear component was approximated by the interfacial shear velocity, *i.e.*, the fitted interfacial friction factor λ_i and computed layer-average velocities. Entrainment rates were found to reduce with increasing stratification, and increase with interfacial shear velocity, which is in agreement with other studies [90]. The dependence of E on the ratio of stratification to shear is strong ($R^2 = 0.84$), suggesting that the entrainment is more easily predicted by gradient, rather than bulk flow parameters.

However, if the average friction factor, $\tilde{\lambda} = (2\lambda_i + \lambda_b)/2$, is combined with Ri , a satisfactory correlation may still be found between E and bulk parameters. Grubert [40, 41] similarly found that shear stress should be included in entrainment parametrisations. Based on the experimental and field data, Grubert proposed the following equation for the entrainment rate, $E = 2.4Ri_*^{-3/2}Ri^{1/2}$, valid for $3.5 < Ri < 20$ [41]. Since $Ri_* = Ri\lambda^{-1}$, a similar dependence of E on bulk parameters Ri and $\tilde{\lambda}$ ($R^2 = 0.66$) was found here:

$$E \propto Ri^{-2}\tilde{\lambda}^{5/2} \quad (8.1)$$

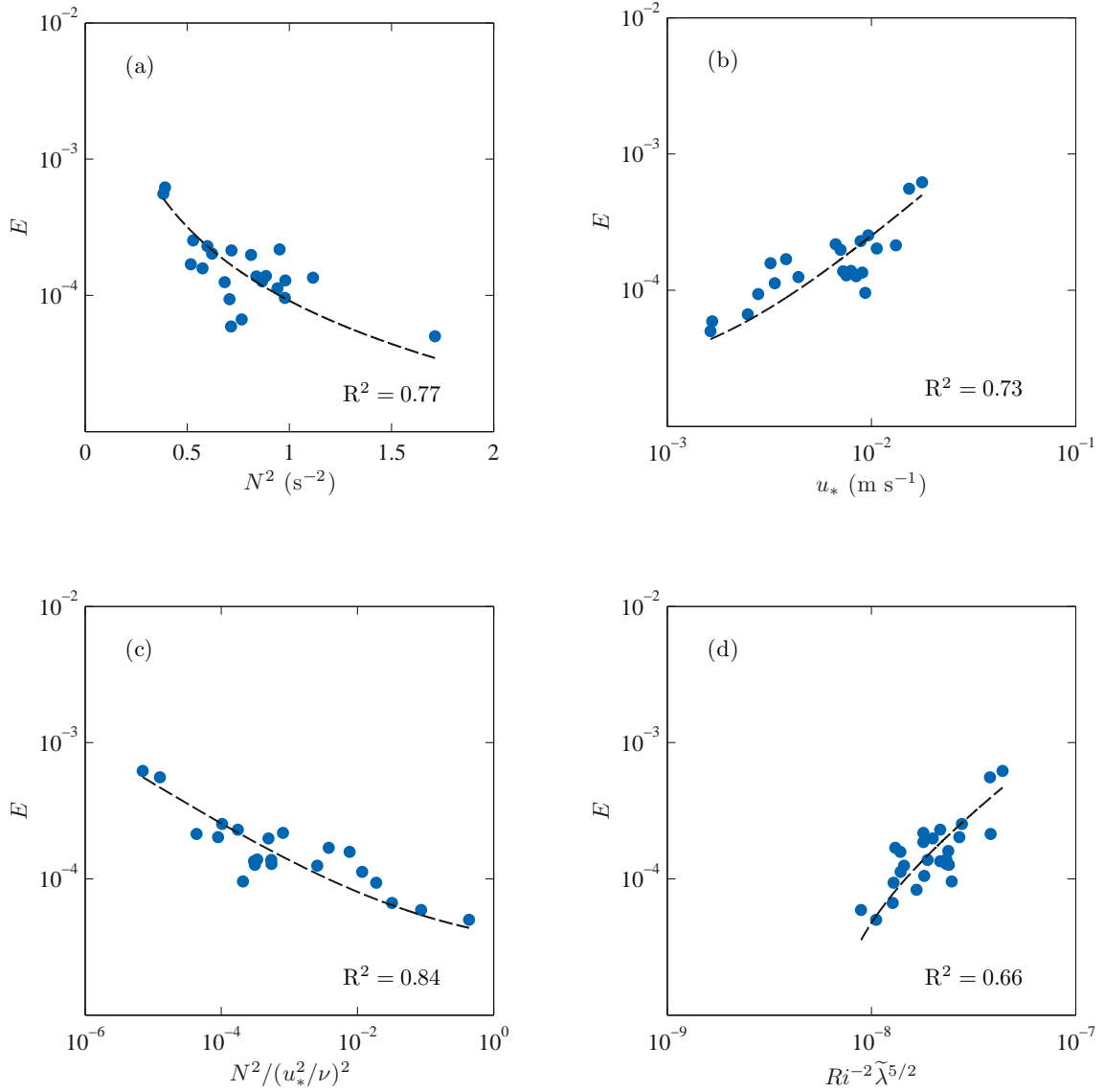


Figure 8.3: Dependence of entrainment rates E on: (a) squared buoyancy frequency N^2 , (b) interfacial shear velocity u_* , (c) non-dimensional ratio of stratification to shear $N^2/(u_*^2/\nu)^2$, and (d) a combination of bulk Richardson number and average interfacial friction factor $Ri^{-2}\tilde{\lambda}^{5/2}$.

Figure 8.3d shows the dependence of E on $Ri^{-2}\tilde{\lambda}^{5/2}$, which supports the conclusions by Grubert [41] that E is not a function of Ri alone, and that some form of friction should also be included. The entrainment in arrested salt-wedges is clearly influenced by the shear stress at the interface and channel bed, which may be the main source of turbulent energy production. In comparison, for macrotidal salt-wedges it was found that during the ebb, the interfacial shear stress was the dominant source of turbulent mixing, while the shear stress at the channel bed was the main source of turbulent mixing during the flood [53]. Furthermore, the shear instabilities at the interface may even be the dominant mechanism for the initial breakdown of the salt-wedge structure itself [104, 78].

8.1.2 Interfacial friction parametrisation

No consensus currently exists on what interfacial friction law should be applied for two-layer salt-wedge models, but the most frequently used is the one by Arita and Jirka [2]. Arita and Jirka [2] extended a two-layer model by including the entrainment, and proposed a new semi-empirical equation, which consists of a laminar and turbulent contribution (Eq. 2.9). The laminar contribution is dominant for small Re , and Eq. (2.9) suggests that λ_i decreases as Re increases. the turbulent contribution, on the other hand, is dominant for large Re , and Eq. (2.9) suggests that λ_i becomes independent from Re and increases with Fd (Fig. 8.4b). The dependence of λ_i on governing parameters is, however, difficult to quantify for the transition between the laminar and turbulent state. Furthermore, Arita [2] found that the stratified flow characterized by large Re numbers may experience local laminarisation at the interface, which makes the efforts to derive a suitable parametrization even more complicated.

Figure 8.4a,b,c shows how λ_i relates to E , $ReFd^2$ (with the Arita and Jirka model given by Eq. 2.9), and Re . Arita and Jirka linked the interfacial friction factor to the entrainment rate, so that the following equality holds $\lambda_i = 2E$ [2]. The observed λ_i does indeed increase with E (Fig. 8.4a); furthermore, it shows a similar ratio $\lambda_i/E \approx 2.8$ as proposed in [2]. The discrepancies between fitted friction factors and Eq. (2.9) are noticeable, however. For the range of governing parameters considered here ($6 \times 10^4 < Re < 6 \times 10^5$ and $0.5 < Fd < 0.7$) we would expect λ_i to be confined to a more limited range of values ($5 \times 10^{-4} < \lambda_i < 8 \times 10^{-4}$). Furthermore, λ_i should be independent from Re or decrease with increasing Re .

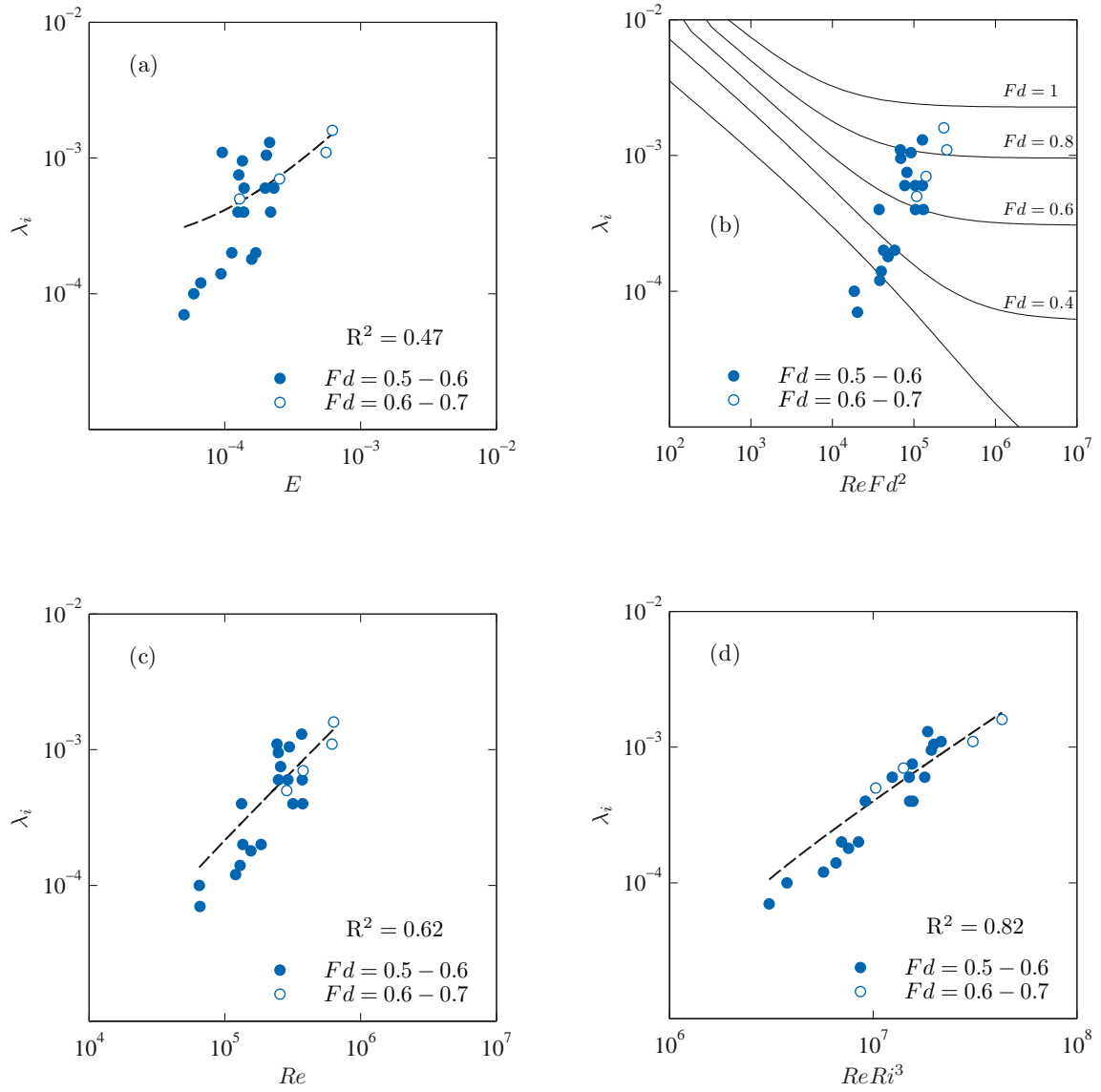


Figure 8.4: Dependence of the interfacial friction factor λ_i on: (a) entrainment rate E , Keulegan number $ReFd^2$ with the Arita and Jirka model [2] (solid lines for different Fd), (c) Reynolds number Re and (d) best fit combination of parameters $ReRi^3$.

In contrast, the observed values of λ_i increase with $ReFd^2$ over a wide range of values, from 7.0×10^{-5} to 1.6×10^{-3} (Fig. 8.4b). It seems, however, that the observed data are in the transitional region of the parameter space, for which Eq. (2.9) is based only on empirical assumptions. When evaluated separately, λ_i shows a wide range of values for similar Fd and a strong positive correlation with Re (Fig. 8.4c, $R^2 = 0.62$).

In search for a more accurate dependence of λ_i on bulk flow parameters, curve fitting resulted in the following empirical relationship, which shows minimal scattering and the strongest correlation coefficient (see Fig. 8.4d):

$$\lambda_i \propto (Re Ri^3)^{0.9} \quad (8.2)$$

Although having high correlation ($R^2 = 0.82$) and a satisfactory predictive capacity for the salt-wedge in the Rječina River estuary, Eq. (8.2) is empirical and should be used with caution in other microtidal salt-wedges. A high exponent for Ri could be explained by a narrow range of Richardson numbers considered here. An increase of λ_i with Re , however, is in contrast to previous studies [29, 2] and deserves more discussion.

Since ν is fairly constant in all considered observations, an increase of λ_i with Re should primarily be seen as an increase with Q and, consequently, with both h_1 and Δu . It seems that interfacial processes in the Rječina River estuary exhibit the following mechanism. As the river flow rate increases, so does the upper layer velocity and the shear velocity at the interface, which increases turbulent mixing; therefore, interfacial layer becomes more diffused and the stratification is weakened (Fig. 8.1). Furthermore, it seems that the turbulent mixing also increases the apparent roughness at the interface; hence, a positive correlation is observed between λ_i and Re . This is, however, only an assumption, and without direct observations of the velocity profile and the Reynolds stress no definite claims can be made.

There are, unfortunately, no similar field data sets available in the literature that are suitable for a comparison; only a few studies provided single values for the interfacial friction factor, *e.g.*, $\lambda_i = 1.6 \times 10^{-4}$ in the Glomma River [89], $\lambda_i = 5 \times 10^{-4}$ in the Fraser River [64], and slightly higher $\lambda_i = 1.5 \times 10^{-3}$ in the Neretva River [62] and $\lambda_i = 2 \times 10^{-3}$ in the Jadro River [61]. These values are comparable to the range of values observed in the Rječina River estuary.

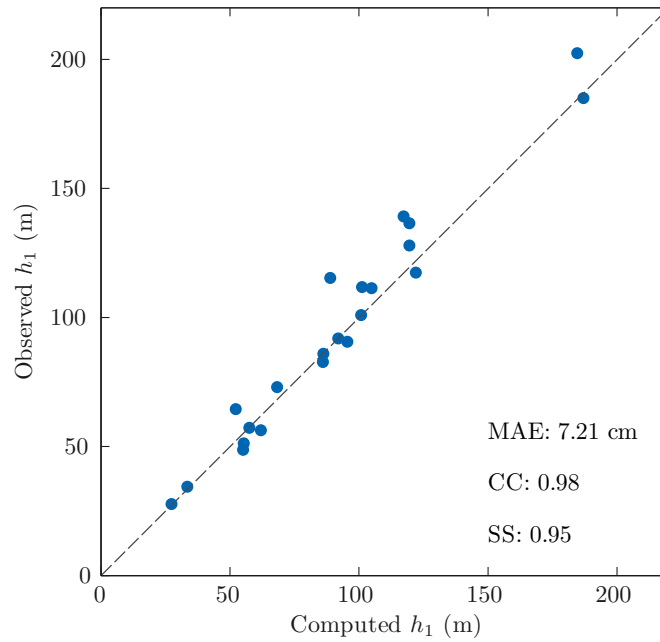


Figure 8.5: Comparison of the computed and observed upper layer thickness h_1 at a control section assumed to be located at the last bridge near the mouth (P1, Fig. 6.1).

8.2 Discussion of hydraulic control

Although some salt-wedge models place a hydraulic control at the river mouth, in the present work an internally critical flow was assumed to be found at the last bridge near the mouth of the Rječina River estuary, *i.e.*, at a location where a strong channel contraction is formed by bridge piers and abutments (P1, Fig. 6.1). To verify how well was this condition satisfied in practice, the observed upper layer thickness at P1 was compared to the computed boundary condition defined by $G^2 = 1$.

Figure 8.5 shows the comparison between the computed and observed upper layer thickness at the last bridge near the mouth for all considered river flow rates in an arrested salt-wedge. The agreement is satisfactory, and all skill metrics indicate a strong correlation, with MAE = 7.2 cm, CC = 0.98, and SS = 0.95. The choice of both position and definition of the downstream boundary condition is therefore justified. These findings suggest that when the exact location of the river mouth is not easily identified, the channel contraction can be used instead.

8.3 Discussion of stratification strength

Geyer *et al.* [37] reported typical values of squared buoyancy frequency as a measure of stratification strength in estuaries. The values range from 0.0025 to 0.01 s⁻² in partially mixed estuaries, and up to 0.1 s⁻² in salt-wedge estuaries [37]. In the Hudson River estuary, for example, N^2 only occasionally reached a maximum of 0.1 s⁻¹ [75]. Similar upper values were also found in other macrotidal salt-wedge estuaries, such as the Columbia River [53] and Snohomish River [104].

In the Rječina River estuary the observed N^2 values ranged from 0.3 up to 1.7 s⁻² (Fig. 8.1d), which is over one order of magnitude larger than any value reported from other field studies. Furthermore, it seems that in the absences of tides, the river flow has a negative influence on the stratification. This is expected, however, because the turbulence produced at the channel bed or interface may also induce vertical mixing [90]. As Q increases, the shear stress exerted on the interface becomes more intense, the interfacial instabilities start to develop and vertical mixing increases. High Q , in this case, actually diffuses the interface layer and weakens the stratification. In the Rječina River estuary N^2 subsides with higher river flow rate until the salt-wedge is completely expelled from the estuary (Fig. 8.1d).

For a time-dependant salt-wedge observed on 1 July 2015 the buoyancy frequency varied slightly from 0.3 to 1.3 s⁻² under variable Q (Fig. 8.6). During the rising flow, the salt-wedge front receded towards the river mouth, and the interface layer became more diffused, which weakened the stratification. After a force equilibrium was established, highly stratified conditions were quickly restored. During the falling river flow, on the other hand, the salt-wedge front advanced upstream, but the stratification was unaffected. The average salinities in the upper and lower layer remained almost constant during all stages of the flow rate variations.

A similar mechanism was observed in the Columbia River estuary [53] under different tidal phases. During the ebb tides, when the salt-wedge front receded, the shear stress at the interface increased the turbulent mixing, which weakened the stratification, but strong longitudinal density gradients quickly restored the salinity structure. During the flood tides, on the other hand, the salt-wedge front advanced upstream, and the shear stress at the channel bed was the dominant source of turbulence.

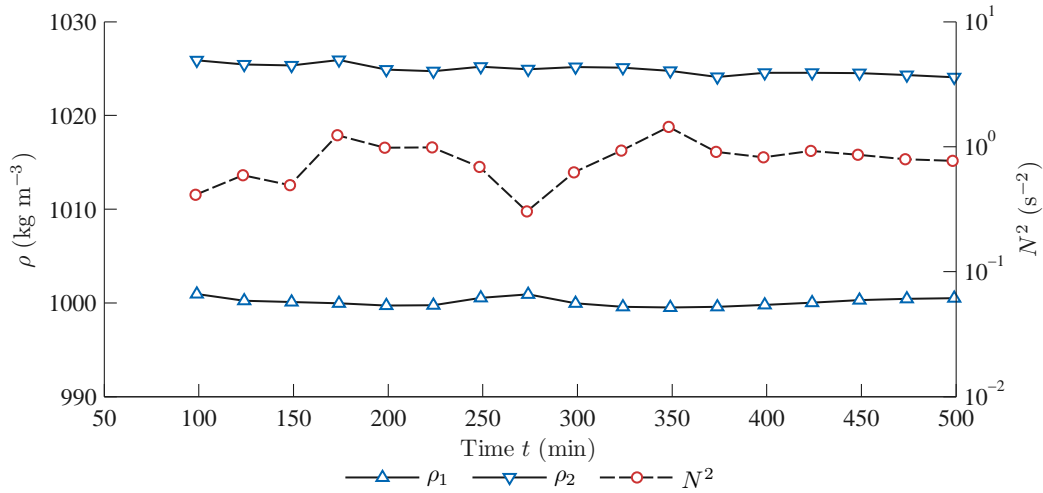


Figure 8.6: Observed density in the upper ρ_1 and lower ρ_2 layer and maximum squared buoyancy frequency N^2 , averaged along the salt-wedge, during a simulation of a time-dependant flow observed on 1 July 2015.

8.4 Discussion of salt-wedge propagation rates

Numerical simulations showed that during a variable river flow, observed on 1 July 2015, the salt-wedge length varied between 600 m for $Q = 4.3 \text{ m}^3 \text{ s}^{-1}$ and 375 m for $Q = 13.9 \text{ m}^3 \text{ s}^{-1}$. Figure 8.7 shows the propagation rates of the salt-wedge front computed from the changes in the salt-wedge length along the estuary. During the first wave, when Q increased from 4.3 to $9.8 \text{ m}^3 \text{ s}^{-1}$, the salt-wedge front receded at a rate of -0.06 m s^{-1} . When Q decreased back to $4.2 \text{ m}^3 \text{ s}^{-1}$, the salt-wedge front advanced upstream at a rate of 0.1 m s^{-1} . Similarly, during the second wave, when Q increased to $13.9 \text{ m}^3 \text{ s}^{-1}$, the salt-wedge front receded at a rate of -0.15 m s^{-1} , and when Q decreased back to $4.2 \text{ m}^3 \text{ s}^{-1}$, the salt-wedge front advanced at a rate of 0.1 m s^{-1} .

Figure 8.7 indicates that the salt-wedge propagation rates are positively correlated with the river flow rate, *i.e.*, higher the increase in the river flow rate, higher the propagation rate. However, this dependence was not true for the upstream propagation rates, which were nearly the same in both cases.

A parallel can therefore be made with the propagation rate of a salt-wedge front during ebb and flood tides. Indeed, Geyer and Farmer [38] showed that the advancement of the salt-wedge front in the Fraser River due to flood tides is mainly influenced by the shear stress at the channel bed. They computed that the salt-wedge front advanced at a rate of 0.7 m s^{-1} , which is a few times larger than the

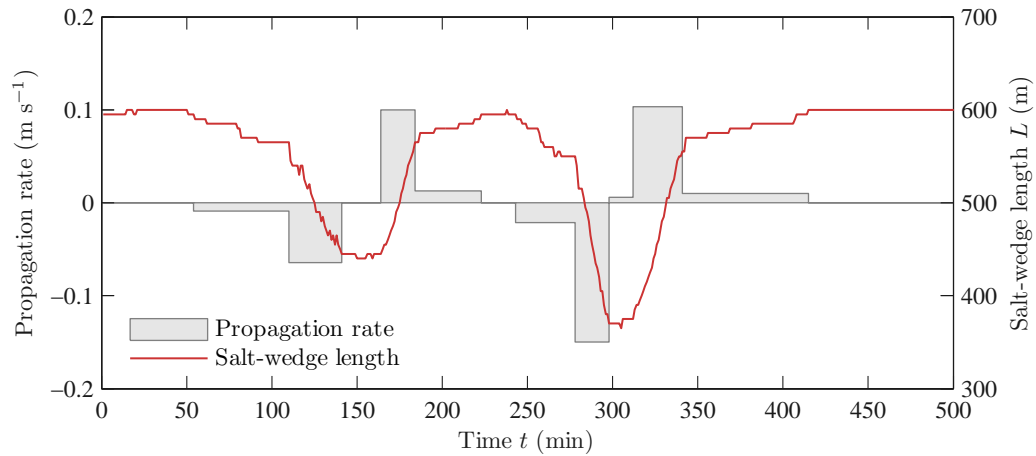


Figure 8.7: Computed movement of the salt-wedge front and corresponding propagation rates during the variable flow observed on 1 July 2015.

values in the Rječina River estuary. Clearly, this comparison can only be made qualitatively because of the different driving forces involved, *i.e.*, river flow in the Rječina River and tides in the Fraser River.

9

Conclusion

Contents

9.1	Summary	122
9.1.1	Numerical models	122
9.1.2	Salt-wedge dynamics	124
9.2	Future work	127

Abstract

This chapter concludes the thesis by summarizing the presented work and emphasizing the specific contributions in regards to proposed numerical models and observed salt-wedge dynamics. Finally, several recommendations for future work in numerical modelling of salt-wedge estuaries are proposed.

9.1 Summary

The goal of this thesis was to develop a 1D two-layer numerical model for computing dynamic processes in salt-wedge estuaries. Two numerical models were proposed; the first one was based on a finite difference method, which was used to compute the arrested salt-wedge profile and to calibrate the interfacial friction factor, whereas the second one was based on a finite volume method and used to simulate both the arrested and time-dependant salt-wedge.

The outstanding questions that needed to be answered and solved were: Which boundary conditions are appropriate for a salt-wedge flow in a two-layer model? How to solve the wet-dry transitions occurring at the salt-wedge front in channels with irregular geometry? How to deal with the possible loss of hyperbolicity? How to numerically treat and quantify the interfacial friction and entrainment? And finally, show how well can a 1D numerical model predict the salt-wedge dynamic processes under steady and time-dependant flow conditions in real-life applications.

All questions were solved and presented in this thesis. The performance of proposed models was verified and validated for both steady and highly variable flow conditions by comparing the numerical solutions against field observations in the Rječina River estuary. A combination of numerical experiments and field observations additionally allowed to further investigate and discuss the main physical processes in microtidal salt-wedge estuaries, such as hydraulic flow regimes, stratification strength, and propagation rates.

The main findings and contributions of this thesis are summarized into two categories; those assessing the performance of numerical models and those examining physical processes in microtidal salt-wedges.

9.1.1 Numerical models

A salt-wedge estuary was simplified to an idealized one-dimensional system composed of two shallow layers of different densities, separated by an interface of zero thickness. Based on the laws for conservation of mass and linear momentum, the governing equations were derived as a two-layer conservative system of shallow water equations with source terms. These partial differential equations were solved by a finite volume

method, or simplified to a steady state, written as a system of ordinary differential equations, and then solved by a finite difference method.

The fundamental assumption made here – a reduction of salt-wedge estuaries to a two-layer shallow water system – was justified. Both models agreed favourably with field observations in the Rječina River estuary. Furthermore, even the flow rates in both layers were successfully validated against field observations under highly variable flow conditions. It should be noted, though, that the Rječina River estuary is influenced by a microtidal sea and that highly stratified water column was preserved under a wide range of flow conditions.

FDM numerical model

The steady-state flow in arrested salt-wedge was successfully solved by the implicit trapezoidal method, which is based on a finite difference method. Inclusion of the irregular channel geometry, friction, and entrainment resulted in a more complex model; a system of four ordinary differential equations had to be solved in comparison to one equation models, which are regularly found in the literature. The results confirmed that additional complexity introduced in the model was justified. The computed salt-wedge profile is more accurate in comparison to single equation models, and the entrainment proved to impart a notable impact on the salt-wedge flow. This model, however, is sensitive to the interfacial friction factor, which needed to be calibrated to obtain good agreement with field observations.

The steady salt-wedge model based on a FDM has its limitations; in addition to being unsuitable for variable flow rates or sea-levels, the model is inadequate to deal with a transcritical flow, which may occur at the salt-wedge front, exit region, or at strong channel contractions. Therefore, time-dependant shock-capturing models are more appropriate in practical applications.

FVM numerical model

The system of partial differential equations describing a time-dependant two-layer flow in salt-wedge estuaries was solved by a modified Q-scheme, which is based on a finite volume method. Numerical treatment of the coupled terms appearing as a result of two layers, and source terms corresponding to irregular geometry was a problem recently solved by Castro et al. [18] for a two-layer exchange flow in sea straits. However, in

the process of developing a similar model for salt-wedge estuaries additional numerical challenges emerged; in particular, the approximation and quantification of friction and entrainment terms, as well as the problem of wet-dry transitions in the lower layer.

The source terms corresponding to friction and entrainment were upwinded similarly as terms corresponding to irregular geometry. This approximation proved successful in satisfying the well-balanced property, both formally and in practical applications. The wet-dry transition was treated by imposing a tolerance depth parameter that controlled the wet/dry state in each cell. Furthermore, the source term corresponding to bed slope was modified at the salt-wedge front to ensure the well-balanced property of the scheme.

The numerical model was verified by comparing the results against analytical models and a steady-state solver for idealized examples, and validated by comparing numerical results to field observations in the Rječina River estuary. When compared to analytical solutions of an arrested salt-wedge flow in simplified channel geometry, the agreement was satisfactory for all considered cases. Furthermore, the solutions were almost identical compared to the FDM model for both simplified and variable channel geometry. Finally, the model validation revealed that the proposed scheme was stable and accurate in computing the arrested salt-wedge profile in the Rječina River estuary. The FVM model also captured time-dependant salt-wedge profiles and flow rates for highly variable flow conditions.

Downstream boundary condition

In both numerical models, the downstream boundary condition was defined by a hydraulic control positioned at the last bridge near the mouth, *i.e.*, a strong channel contraction formed by bridge piers and abutments. The upper layer thickness was computed from the internally critical flow condition defined by a composite Froude number. The agreement with field observations was satisfactory, which indicates that a hydraulic control is established at a point of strong channel contractions.

9.1.2 Salt-wedge dynamics

The following general behaviour of arrested salt-wedges was observed in the Rječina River estuary. As the river flow increases the salt-wedge is pushed out downstream

and the upper layer thickness and velocity also increases. When the river flow decreases, on the other hand, the salt-wedge intrudes further upstream and the upper layer thickness and velocities reduce. Similarly, for lower sea-level the salt-wedge recedes downstream, and *vice versa*.

Propagation rates

Based on numerical solutions of time-dependant salt-wedges, which were validated by field observations, propagation rates of the salt-wedge front were also examined. As expected, the salt-wedge responded almost instantly to the river inflow; when the flow rate increased, the salt-wedge was pushed downstream until a force equilibrium was established and an arrested salt-wedge was formed. When flow rate decreased, the salt-wedge advanced upstream until an arrested salt-wedge was formed.

Propagation rates of the salt-wedge front in the downstream direction, during a flow increase, seem to be influenced by changes in the river flow rate. On the other hand, propagation rates of the salt-wedge front in the upstream direction, during a flow decrease, were nearly constant regardless of the river flow rate.

Stratification strength

The salinity structure and stratification were examined based on field observations of vertical salinity profiles along the estuary. For steady flow, the average salinity in each layer was nearly constant along the salt-wedge, suggesting that the vertical mixing was not strong enough to influence the global salinity structure. The stratification strength, expressed by the squared buoyancy frequency, was among the highest every reported in the literature, reaching up to 1.7 s^{-2} . Even in the time-dependant case, under highly variable river flow, the stratification remained very strong, and N^2 only slightly varied between 0.3 and 1.3 s^{-2} .

In contrast to macrotidal salt-wedges, river flow rates impart a negative influence on the stratification in microtidal salt-wedges. For higher flow rate the interfacial layer was more diffused; therefore, the stratification was weaker. Similar behaviour was also observed under variable river inflow. During the rising flow, the salt-wedge was pushed downstream, the entrainment was intensified, and the interfacial layer became more diffused, which weakened the stratification. After an arrested salt-wedge was formed, entrainment was reduced, and a strong stratification re-established. Whereas,

during the falling river flow and the salt-wedge intrusion there was no noticeable change in the entrainment or the stratification strength.

Entrainment

A strong positive correlation was found between entrainment velocities and river flow rates. Field observations also showed a wide range of E for a narrow range of bulk Richardson numbers. Surprisingly, this is in contrast to many entrainment laws that show how E is reduced with increasing Ri . However, E indicated a strong negative correlation with the ratio of squared buoyancy frequency to interfacial shear velocity, which can qualitatively be related to the gradient Richardson number. This was expected since gradient parameters are more relevant than bulk parameters.

The analysis also showed that an adequate prediction law can still be formulated based on bulk Richardson numbers when combined with an average friction factor, in particular $Ri^{-2}\tilde{\lambda}^{5/2}$. Entrainment at the interface is clearly not influenced only by bulk flow conditions, but also by the shear stress at the channel bed and interface, which may be the main source of turbulent energy production.

Interfacial friction

Interfacial friction proved to be one of the most important parameters governing numerical solutions of a salt-wedge profile. In this thesis, the interfacial friction factor was calibrated to fit the field observations. When compared to the Arita and Jirka's friction law, fitted values showed a much wider range of values than expected. Furthermore, analysis showed that λ_i may increase with Reynolds number, which is a first confirmation that even qualitative differences exist between laboratory and field conditions. Finally, a new empirical equation was found, linking λ_i with $ReRi^3$, which shows good predictive capabilities in the Rječina River estuary.

A general mechanism of interfacial processes in the Rječina River estuary can be described as follows: the upper layer velocity and interfacial shear velocity increase with river flow rate, which intensifies vertical mixing and therefore diffuses the interfacial layer. Furthermore, it seems that vertical mixing increases the apparent roughness at the interface and also the interfacial friction factor. Therefore, a positive correlation was observed between λ_i and both Q and Re . This is, however, only an assumption, and without direct observations of the velocity profile and the Reynolds stress no definite claims can be made.

9.2 Future work

The numerical model used in this thesis, although extended to include irregular geometry, friction, and entrainment, is still a simplified approximation of the salt-wedge dynamics. One of the main assumptions in the proposed model are constant densities in both layers that seem unaffected by the entrainment. Therefore, the model could be extended by coupling additional advection-diffusion equations for salt concentration, so that density is allowed to vary in both space and time.

Another simplification is the assumption of zero interfacial thickness. Field observations in the Rječina River estuary showed that the interfacial thickness may develop up to half of the upper layer thickness. Furthermore, in the time-dependant case, under highly variable river flow, the interfacial layer thickness increased even more. Including a third intermediate layer would therefore significantly improve the model performance.

And finally, considering the numerical accuracy, an extension to a higher-order numerical scheme should also be a welcomed improvement.

The quantification of the main interfacial physical processes, namely entrainment and interfacial friction, seems to remain an open issue. There are still no reliable and unified parametrisations that can accurately predict neither entrainment rate or interfacial friction factor based on bulk flow parameters. Additional experiments at sufficiently large scale or controlled field observations are clearly needed to better understand the interfacial processes in salt-wedge estuaries.

Bibliography

- [1] ABRAHAM, G., KARELSE, M., AND VAN OS, A. On the magnitude of interfacial shear of subcritical stratified flows in relation with interfacial stability. *Journal of Hydraulic Research* 17, 4 (1979), 273–287.
- [2] ARITA, M., AND JIRKA, G. Two-layer model of saline wedge. I: Entrainment and interfacial friction. *Journal of Hydraulic Engineering* 113, 10 (1987), 1229–1246.
- [3] ARITA, M., AND JIRKA, G. Two-layer model of saline wedge. II: Prediction. *Journal of Hydraulic Engineering* 113, 10 (1987), 1249–1263.
- [4] ARMI, L. The hydraulics of two flowing layers with different densities. *Journal of Fluid Mechanics* 163 (1986), 27–58.
- [5] ARMI, L., AND FARMER, D. Maximal two-layer exchange through a contraction with barotropic net flow. *Journal of Fluid Mechanics* 164 (1986), 27–51.
- [6] ARTEGIANI, A., PASCHINI, E., RUSSO, A., BREGANT, D., RAICICH, F., AND PINARDI, N. The Adriatic Sea general circulation. Part I: Air–sea interactions and water mass structure. *Journal of Physical Oceanography* 27, 8 (1997), 1492–1514.
- [7] BALLOFFET, A., AND BORAH, D. Lower Mississippi salinity analysis. *Journal of Hydraulic Engineering* 111, 2 (1985), 300–315.
- [8] BEN-ISRAEL, A. A Newton-Raphson method for the solution of systems of equations. *Journal of Mathematical Analysis and Applications* 15, 2 (1966), 243–252.
- [9] BERMUDEZ, A., AND VÁZQUEZ-CENDÓN, M. Upwind methods for hyperbolic conservation laws with source terms. *Computers & Fluids* 23, 8 (1994), 1049–1071.
- [10] BRUFAU, P., GARCÍA-NAVARRO, P., AND VÁZQUEZ-CENDÓN, M. Zero mass error using unsteady wetting–drying conditions in shallow flows over dry irregular topography. *International Journal for Numerical Methods in Fluids* 45 (2004), 1047–1082.
- [11] BRUFAU, P., VÁZQUEZ-CENDÓN, M., AND GARCÍA-NAVARRO, P. A numerical model for the flooding and drying of irregular domains. *International Journal for Numerical Methods in Fluids* 39, 3 (2002), 247–275.
- [12] BRUNNER, G. HEC-RAS River Analysis System. Tech. rep., US Army Corps of Engineers, 2010.
- [13] BUCH, E. On entrainment observed in laboratory and field experiments. *Tellus* 34 (1982), 307–311.

- [14] BURGUETE, J., AND GARCÍA-NAVARRO, P. Analysis of the friction term in the one-dimensional shallow-water model. *Journal of Hydraulic Engineering* 133, 9 (2007), 1048–1063.
- [15] CARSTENS, T. Turbulent diffusion and entrainment in two-layer flow. *Journal of the Waterways, Harbors and Coastal Engineering Division* 96, 1 (1970), 97–104.
- [16] CASTRO, M., FERNÁNDEZ-NIETO, E., GONZÁLEZ-VIDA, J., AND PARÉS, C. Numerical treatment of the loss of hyperbolicity of the two-layer shallow-water system. *Journal of Scientific Computing* 48, 1 (2011), 16–40.
- [17] CASTRO, M., FERREIRO FERREIRO, A., GARCÍA-RODRÍGUEZ, J., GONZÁLEZ-VIDA, J., MACÍAS, J., PARÉS, C., AND VÁZQUEZ-CENDÓN, M. The numerical treatment of wet/dry fronts in shallow flows: application to one-layer and two-layer systems. *Mathematical and Computer Modelling* 42, 3-4 (2005), 419–439.
- [18] CASTRO, M., GARCIA-RODRIGUEZ, J., GONZÁLEZ-VIDA, J., MACÍAS, J., PARÉS, C., AND VÁZQUEZ-CENDÓN, M. Numerical simulation of two-layer shallow water flows through channels with irregular geometry. *Journal of Computational Physics* 195, 1 (2004), 202–235.
- [19] CASTRO, M., GARCÍA-RODRÍGUEZ, J., GONZÁLEZ-VIDA, J., AND PARÉS, C. Improved FVM for two-layer shallow-water models: Application to the Strait of Gibraltar. *Advances in Engineering Software* 38, 6 (2007), 386–398.
- [20] CASTRO, M., GONZALES-VIDA, J., AND PARES, C. Numerical treatment of wet/dry fronts in shallow flows with a modified Roe scheme. *Mathematical Models and Methods in Applied Sciences* 16, 6 (2006), 897–934.
- [21] CASTRO, M., MACIAS, J., AND PARÉS, C. A Q-scheme for a class of systems of coupled conservation laws with source term. Application to a two-layer 1D shallow water system. *ESAIM: Mathematical Modelling and Numerical Analysis* 35, 1 (2001), 107–127.
- [22] CEA, L., FRENCH, J., AND VÁZQUEZ-CENDÓN, M. Numerical modelling of tidal flows in complex estuaries including turbulence: an unstructured finite volume solver and experimental validation. *International Journal for Numerical Methods in Engineering* 67, 13 (2006), 1909–1932.
- [23] CEA, L., VÁZQUEZ-CENDÓN, M., PUERTAS, J., AND PENA, L. Numerical treatment of turbulent and mass source terms in the shallow water equations for channels with irregular section. In *European Congress on Computational Methods in Applied Sciences and Engineering (ECCOMAS)* (2004).
- [24] CENEDESE, C., AND ADDUCE, C. A new parameterization for entrainment in overflows. *Journal of Physical Oceanography* 40, 1 (2010), 1835–1850.
- [25] CHAUDHRY, M. *Open-channel flow*. Springer Science & Business Media, 2007.
- [26] CHRISTODOULOU, G. Interfacial mixing in stratified flows. *Journal of Hydraulic Research* 24, 2 (1986), 77–92.

- [27] CUSHMAN-ROISIN, B., GAČIĆ, M., POULAIN, P., AND ARTEGIANI, A. *Physical oceanography of the Adriatic Sea: Past, present and future*. Kluwer Academic Publishers, 2001.
- [28] DAZZI, R., AND TOMASINO, M. Mathematical model of salinity intrusion in the delta of the Po River. *Coastal Engineering Proceedings 134* (1974), 2302–2321.
- [29] DERMISIS, V., AND PARTHENIADES, E. Dominant shear stresses in arrested saline wedges. *Journal of Waterway, Port, Coastal, and Ocean Engineering 111*, 4 (1985), 733–752.
- [30] DYER, K. *Estuaries: a physical introduction*. John Wiley & Sons, London, 1973.
- [31] FARMER, D., AND ARMI, L. Maximal two-layer exchange over a sill and through the combination of a sill and contraction with barotropic flow. *Journal of Fluid Mechanics 164* (1986), 53–76.
- [32] FERNANDO, H. Turbulent mixing in stratified fluids. *Annual Review of Fluid Mechanics 23*, 1 (1991), 455–493.
- [33] FOFONOFF, N., AND MILLARD, R. Algorithms for computation of fundamental properties of seawater. *UNESCO Technical papers in marine science 44* (1983), 53.
- [34] GARCÍA-NAVARRO, P., AND VÁZQUEZ-CENDÓN, M. On numerical treatment of the source terms in the shallow water equations. *Computers & Fluids 29*, 8 (2000), 951–979.
- [35] GARRETT, C. Frictional processes in straits. *Deep-Sea Research Part II: Topical Studies in Oceanography 51*, 4-5 (2004), 393–410.
- [36] GEYER, W., AND RALSTON, D. The dynamics of strongly stratified estuaries. In *Treatise on Estuarine and Coastal Science*, vol. 2. Elsevier Inc., 2011, pp. 37–52.
- [37] GEYER, W., SCULLY, M., AND RALSTON, D. Quantifying vertical mixing in estuaries. *Environmental Fluid Mechanics 8*, 5-6 (2008), 495–509.
- [38] GEYER, W., AND SMITH, J. Shear instability in a highly stratified estuary. *Journal of Physical Oceanography 17* (1987), 1668–1679.
- [39] GODUNOV, S. A difference method for numerical calculation of discontinuous solutions of the equations of hydrodynamics. *Matematicheski Sbornik 89*, 3 (1959), 271–306.
- [40] GRUBERT, J. Interfacial mixing in stratified channel flows. *Journal of Hydraulic Engineering 115*, 7 (1989), 887 – 905.
- [41] GRUBERT, J. Interfacial mixing in estuaries and fjords. *Journal of Hydraulic Engineering 116*, 2 (1990), 176–195.
- [42] HANSEN, D., AND RATTRAY JR, M. New dimensions in estuary classification. *Limnology and Oceanography 11*, 3 (1966), 319–326.
- [43] HARLEMAN, D. *Stratified flow*. McGraw-Hill Book Company, New York. NY, 1961.

- [44] HARTEN, A. On a class of high resolution total-variation-stable finite-difference schemes. *SIAM Journal on Numerical Analysis* 21, 1 (1984), 1–23.
- [45] HHI. *Tide tables: Adriatic Sea - East coast*. Hydrographic Institut of the Republic of Croatia, 2015.
- [46] HOGG, A., HALLWORTH, M., AND HUPPERT, H. On gravity currents driven by constant fluxes of saline and particle-laden fluid in the presence of a uniform flow. *Journal of Fluid Mechanics* 539 (2005), 349.
- [47] HUBER, M., PERKINS, R., LAESECKE, A., FRIEND, D., SENEGERS, J., ASSAEL, M., METAXA, I., VOGEL, E., MAREŠ, R., AND MIYAGAWA, K. New international formulation for the viscosity of H₂O. *Journal of Physical and Chemical Reference Data* 38, 2 (2009), 101–125.
- [48] IBANEZ, C., PONT, D., AND PRAT, N. Characterization of the Ebre and Rhone estuaries: a basis for defining and classifying salt-wedge estuaries. *Limnology and Oceanography* 42, 1 (1997), 89–101.
- [49] IBANEZ, C., SALDANA, J., AND PRAT, N. A model to determine the advective circulation in a three layer, salt wedge estuary: application to the Ebre River estuary. *Estuarine, Coastal and Shelf Science* 48 (1999), 271–279.
- [50] JOHNSON, C., AND HOGG, A. Entraining gravity currents. *Journal of Fluid Mechanics* 731 (2013), 477–508.
- [51] KARELSE, M., VREUGDENHIL, C., DELVIGNE, G., AND BREUSERS, H. Momentum and mass transfer in stratified flows. Tech. rep., DELFT Hydraulics Laboratory, 1974.
- [52] KARLEUŠA, B., MAGAŠ, O., RUBINIĆ, J., AND PALINIĆ, N. Rječina River basin restoration (Croatia). In *International symposium on water management and hydraulic engineering, Ohrid (Macedonia)* (2009), pp. 1–5.
- [53] KAY, D., AND JAY, D. Interfacial mixing in a highly stratified estuary 1. Characteristics of mixing. *Journal of Geophysical Research* 108, C3 (2003), 1–15.
- [54] KRVAVICA, N., MOFARDIN, B., RUŽIĆ, I., AND OŽANIĆ, N. Measurement and analysis of salinization at the Rječina estuary. *Gradevinar* 64, 11 (2012), 923–933.
- [55] KRVAVICA, N., RUŽIĆ, I., OŽANIĆ, N., YAMASHIKI, Y., KARABAIĆ, I., MOFARDIN, B., AND ŠKODA, M. Daily variability of salinity and temperature in the Rječina Estuary. In *2nd Project Workshop on Risk Identification and Land-Use Planning for Disaster Mitigation of Landslides and Floods* (2012), N. Ožanić, Ž. Arbanas, S. Mihalić, H. Marui, and N. Dragičević, Eds., Faculty of Civil Engineering, University of Rijeka, pp. 109–112.
- [56] KRVAVICA, N., TRAVAŠ, V., RAVLIĆ, N., AND OŽANIĆ, N. Hydraulics of stratified two-layer flow in Rječina Estuary. In *Landslide and Flood Hazard Assessment* (Zagreb, Croatia, 2013), S. Mihalić Arbanas and Ž. Arbanas, Eds., Faculty of Mining, Geology and Petroleum Engineering, University of Zagreb and Faculty of Civil Engineering, University of Rijeka, pp. 257–261.

- [57] LA ROCCA, M., ADDUCE, C., SCIORTINO, G., PINZON, A., AND BONIFORTI, M. A two-layer, shallow-water model for 3D gravity currents. *Journal of Hydraulic Research* 50, 2 (2012), 208–217.
- [58] LEVEQUE, R. *Finite volume methods for hyperbolic problems*, vol. 54. Cambridge Texts, 2002.
- [59] LIU, H., YOSHIKAWA, N., MIYAZU, S., AND WATANABE, K. Influence of saltwater wedges on irrigation water near a river estuary. *Paddy and Water Environment* 13, 2 (2015), 179–189.
- [60] LIU, Y., MACCREADY, P., HICKEY, B., DEVER, E., KOSRO, P. M., AND BANAS, N. Evaluation of a coastal ocean circulation model for the Columbia River plume in summer 2004. *Journal of Geophysical Research* 114 (2009), 1–23.
- [61] LJUBENKOV, I. Hydrodynamic modeling of stratified estuary: case study of the Jadro River (Croatia). *Journal of Hydrology and Hydromechanics* 63, 1 (2015), 29–37.
- [62] LJUBENKOV, I., AND VRANJEŠ, M. Numerical model of stratified flow – case study of the Neretva riverbed salination (2004). *Gradevinar* 64, 2 (2012), 101–112.
- [63] LOFQUIST, K. Flow and stress near an interface between stratified liquids. *Physics of Fluids* 3, 2 (1960), 158.
- [64] MACDONALD, D., AND GEYER, W. Turbulent energy production and entrainment at a highly stratified estuarine front. *Journal of Geophysical Research C: Oceans* 109, 5 (2004), 1–17.
- [65] MERWADE, V. *Geospatial description of river channels in three dimensions*. PhD thesis, University of Texas, 2004.
- [66] MILLERO, F., AND POISSON, A. International one-atmosphere equation of state of seawater. *Deep Sea Research Part A, Oceanographic Research Papers* 28, 6 (1981), 625–629.
- [67] MOLER, C., AND STEWART, G. An algorithm for generalized matrix eigenvalue problems. *SIAM Journal on Numerical Analysis* 10, 2 (1973), 241–256.
- [68] MOODY, L. Friction factors for pipe flow. *Transactions of the ASME* 66, 8 (1944), 671–684.
- [69] MOORE, M., AND LONG, R. An experimental investigation of stratified shearing flow. *Journal of Fluid Mechanics* 49, 4 (1971), 635–655.
- [70] MURPHY, A. Skill scores based on the mean square error and their relationships to the correlation coefficient. *Monthly Weather Review* 116, 12 (1988), 2417–2424.
- [71] NARIMOUSA, S., AND FERNANDO, H. On the sheared density interface of an entraining stratified fluid. *Journal of Fluid Mechanics* 174 (1987), 1–22.
- [72] PARTCH, E., AND SMITH, J. Time dependent mixing in a salt wedge estuary. *Estuarine and Coastal Marine Science* 6, 1 (jan 1978), 3–19.

- [73] PAWLAK, G., AND ARMI, L. Hydraulics of two-layer arrested wedge flows. *Journal of Hydraulic Research* 35, 5 (1997), 603–618.
- [74] PEDERSEN, F. *A monograph on turbulent entrainment and friction in two-layer stratified flow*. Institute of Hydrodynamics and Hydraulic Engineering, Technical University of Denmark, 1980.
- [75] PETERS, H. Observations of stratified turbulent mixing in an estuary: Neap-to-spring variations during high river flow. *Estuarine, Coastal and Shelf Science* 45, 1 (1997), 69–88.
- [76] POGGIOLI, A., AND HORNER-DEVINE, A. The sensitivity of salt wedge estuaries to channel geometry. *Journal of Physical Oceanography* 45, 12 (2015), 3169–3183.
- [77] RALSTON, D., GEYER, W., AND LERCZAK, J. Subtidal salinity and velocity in the Hudson River Estuary: Observations and modeling. *Journal of Physical Oceanography* 38, 4 (2008), 753–770.
- [78] RALSTON, D., GEYER, W., AND LERCZAK, J. Turbulent mixing in a strongly forced salt wedge estuary. *Journal of Geophysical Research: Oceans* 115, 12 (2010), 1–19.
- [79] RATTRAY, M., AND MITSUDA, E. Theoretical analysis of conditions in a salt wedge. *Estuarine and coastal marine science* 2 (1974), 375–394.
- [80] REZO, M., AND PAVASOVIĆ, M. Analiza mareografskih podataka o Jadranskom moru od 1953 . do 2006 . godine. *Geodetski list* 4 (2014), 269–290. (In Croatian).
- [81] ROE, P. Approximate Riemann solvers, parameter vectors, and difference schemes. *Journal of Computational Physics* 43, 2 (1981), 357–372.
- [82] RUBINIĆ, J., AND SARIĆ, M. Water resources hydrology of the Rječina catchment area. In *Stručno-poslovni skup s međunarodnim sudjelovanjem-Prošlost, sadašnjost i budućnost vodoopskrbe i odvodnje-Iskustva i izazovi* (2005). (In Croatian).
- [83] SANDERS, B., AND CHRYSIKOPOULOS, C. Longitudinal interpolation of parameters characterizing channel geometry by piece-wise polynomial and universal kriging methods: Effect on flow modeling. *Advances in Water Resources* 27, 11 (2004), 1061–1073.
- [84] SARGENT, F., AND JIRKA, G. Experiments on saline wedge. *Journal of Hydraulic Engineering* 113, 10 (1987), 1307–1323.
- [85] SAVENIJE, H. *Salinity and tides in alluvial estuaries*. Elsevier, 2012.
- [86] SCHIJF, J., AND SCHÖNFELD, J. Theoretical considerations on the motion of salt and fresh water. In *Proceedings of Minnesota International Hydraulics Convention* (1953), pp. 321–333.
- [87] SIERRA, J., SÁNCHEZ-ARCILLA, A., FIGUERAS, P., GONZÁLEZ DEL RÍO, J., RASMUSSEN, E., AND MÖSSO, C. Effects of discharge reductions on salt wedge dynamics of the Ebro River. *River Research and Applications* 20, 1 (2004), 61–77.

- [88] SORGARD, E. A numerical, three-layered, stationary salt wedge model. *Journal of Geophysical Research* 96, C7 (1991), 12739–12754.
- [89] SORGARD, E., MARTINSEN, T., AND AAS, E. Drag coefficient at a stationary salt wedge. *Journal of Geophysical Research* 95, C5 (1990), 7337–7345.
- [90] STACEY, M., RIPPETH, T., AND NASH, J. Turbulence and stratification in estuaries and coastal seas. In *Treatise on Estuarine and Coastal Science*, vol. 2. Elsevier Inc., 2011, pp. 9–36.
- [91] STOMMEL, H., AND FARMER, H. On the nature of estuarine circulation, part 1, chap. 3 and 4. Tech. rep., Woods Hole Oceanographic Institution, Woods Hole, Massachusetts, 1952.
- [92] STRANG, E., AND FERNANDO, H. Entrainment and mixing in stratified shear flows. *Journal of Fluid Mechanics* 428 (2001), 349–386.
- [93] SZYMKIEWICZ, R. *Numerical modeling in open channel hydraulics*. Springer, London, 2010.
- [94] TAMAI, N. Friction at the interface of two-layered flows. *Coastal Engineering Proceedings* 1, 15 (1976), 3169–3188.
- [95] TE CHOW, V. *Open channel hydraulics*. McGraw-Hill Book Company, Inc. New York, 1959.
- [96] TELEDYNE INSTRUMENTS, R. WinRiver II User Guide, 2008.
- [97] TORO, E. *Reimann solvers and numerical methods for fluid dynamics*, vol. 40. Springer, 2001.
- [98] TRAVAŠ, V., KRVAVICA, N., AND RADMAN, I. Numerical analysis of hysteresis in rating curves for open channel flow. *International Journal for Engineering Modelling* 25, 1 (2012), 1–6.
- [99] TRAVAŠ, V., KRVAVICA, N., AND RUBEŠA, J. Modelling of the morphology of open river beds for the implementation of a one-dimensional flow analysis. *Hrvatske vode* 23, 92 (2015), 123–132. (In Croatian).
- [100] TRITTON, D. *Physical fluid dynamics*, second ed. Oxford University Press, 1988.
- [101] VÁZQUEZ-CENDÓN, M. Improved treatment of source terms in upwind schemes for the shallow water equations in channels with irregular geometry. *Journal of Computational Physics* 148, 2 (1999), 497–526.
- [102] VIVODA, M., BENAC, Č., ŽIC, E., ĐOMLIJA, P., AND DUGONJIĆ JOVANČEVIĆ, S. Geohazard u dolini Rječine u prošlosti i sadašnjosti. *Hrvatske vode* 20, 81 (2012), 105–116. (In Croatian).
- [103] WALKER, S., AND HAMILL, G. Temporal observations of interfacial layer between fluids of different density. *Journal of Waterway, Port, Coastal, and Ocean Engineering* 125, 1 (1999), 20–28.

- [104] WANG, B., GIDDINGS, S., FRINGER, O., GROSS, E., FONG, D., AND MONISMITH, S. Modeling and understanding turbulent mixing in a macrotidal salt wedge estuary. *Journal of Geophysical Research* 116, C2 (2011), 1–23.
- [105] WARNER, J., GEYER, W., AND LERCZAK, J. Numerical modeling of an estuary: A comprehensive skill assessment. *Journal of Geophysical Research* 110, C5 (2005), 1–13.
- [106] WOODS, F. *Advanced calculus: a course arranged with special reference to the needs of students of applied mathematics*. Ginn and company, 1926.

Appendices

A

Additional numerical results

Chapter 7.1.2 presented only three numerical results of salt-wedge profiles compared to field observations in the Rječina River estuary. Therefore, the following figures show the numerical results for *all 22 cases* corresponding to the flow conditions detailed in Table 7.1 and fitted data presented in Table 8.1. The FDM steady numerical model was used here, the interfacial friction factor was assumed to be constant along the wedge, and the best fit was determined by the visual inspection and by the smallest RMSE (Eq. 4.7).

A. Additional numerical results

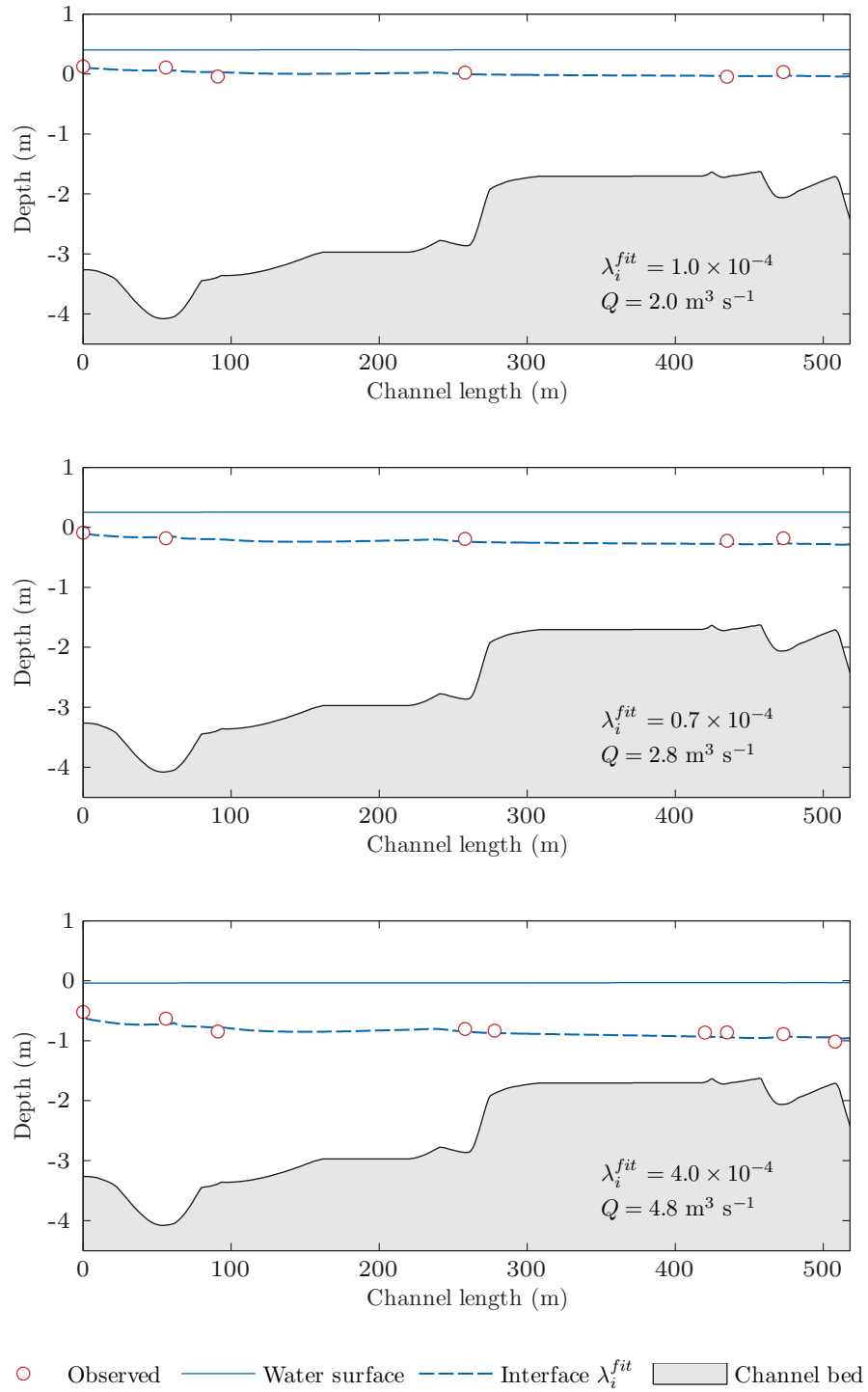


Figure A.1: Numerical FDM solutions of the salt-wedge shape compared against field observations, for different river flow rates Q and fitted interfacial friction factor λ_i^{fit} .

A. Additional numerical results

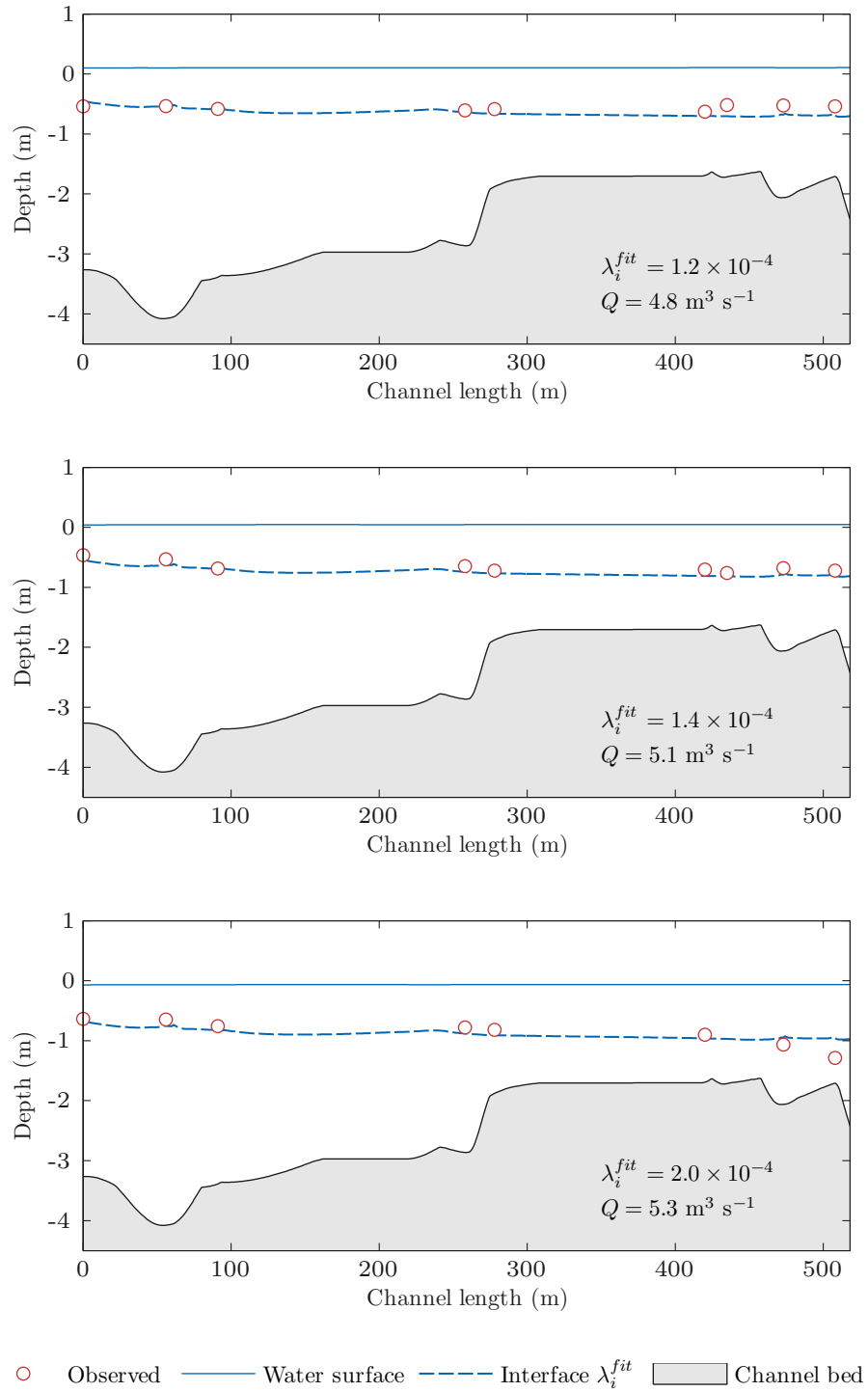


Figure A.2: Numerical FDM solutions of the salt-wedge shape compared against field observations, for different river flow rates Q and fitted interfacial friction factor λ_i^{fit} .

A. Additional numerical results

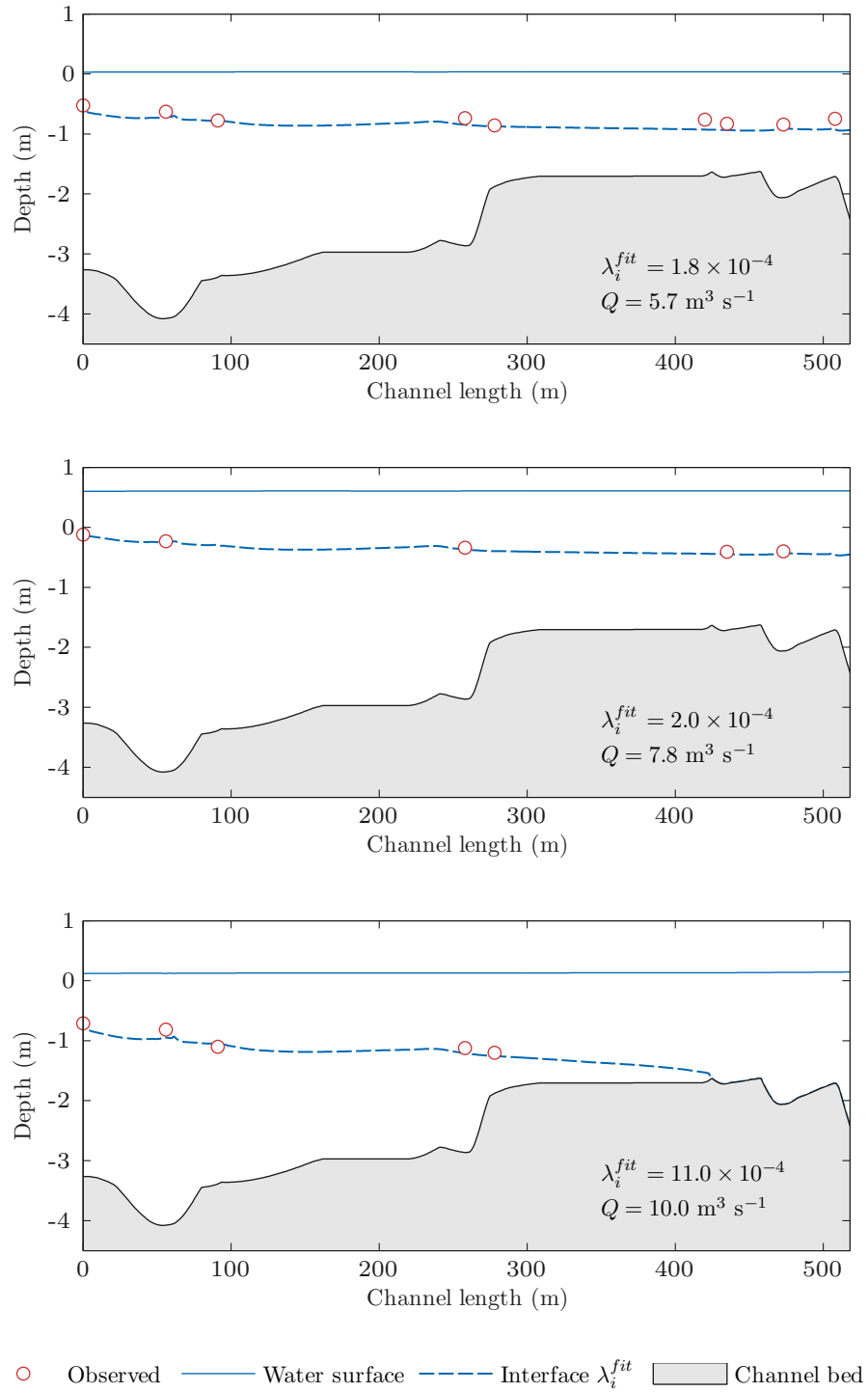


Figure A.3: Numerical FDM solutions of the salt-wedge shape compared against field observations, for different river flow rates Q and fitted interfacial friction factor λ_i^{fit} .

A. Additional numerical results

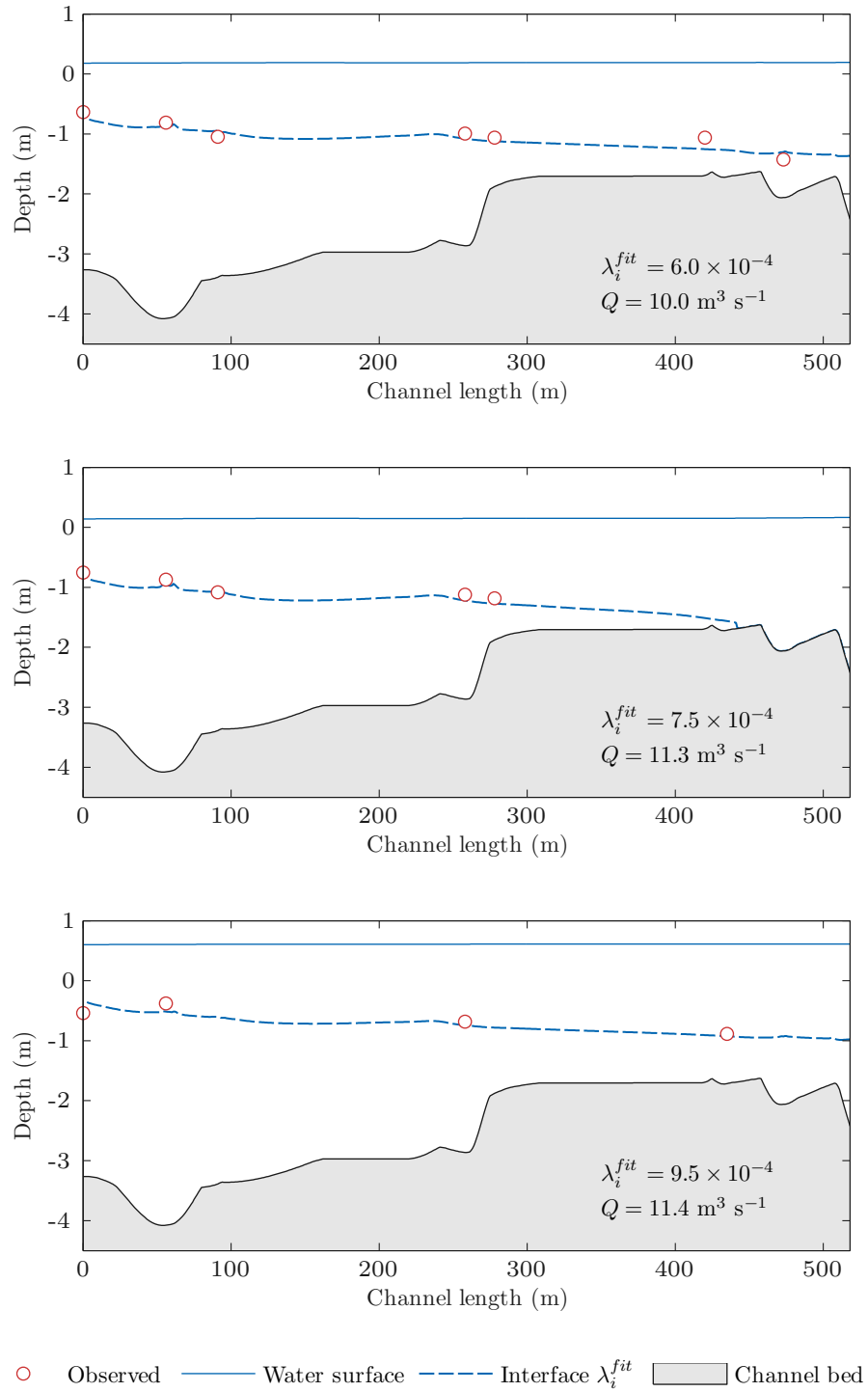


Figure A.4: Numerical FDM solutions of the salt-wedge shape compared against field observations, for different river flow rates Q and fitted interfacial friction factor λ_i^{fit} .

A. Additional numerical results

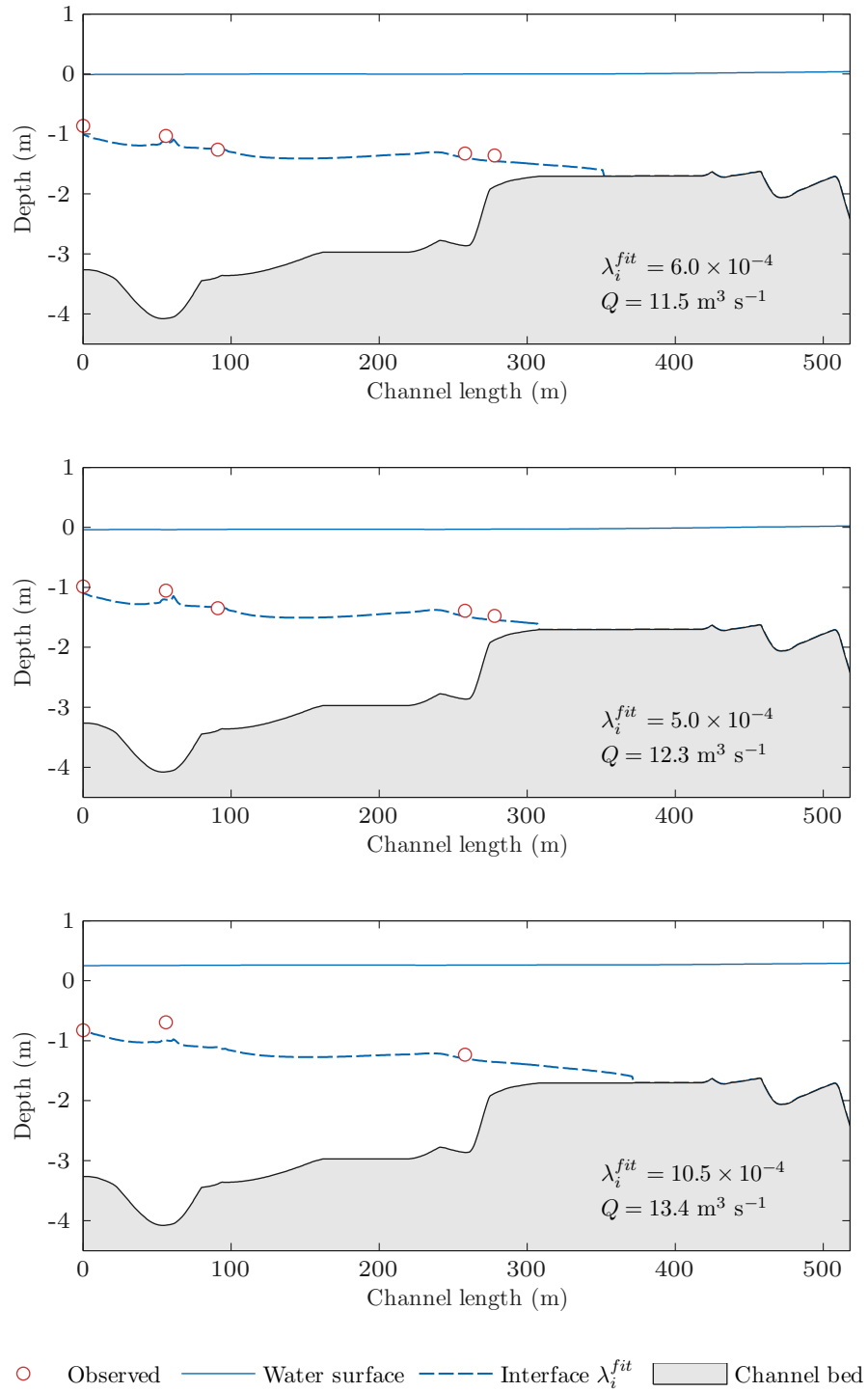


Figure A.5: Numerical FDM solutions of the salt-wedge shape compared against field observations, for different river flow rates Q and fitted interfacial friction factor λ_i^{fit} .

A. Additional numerical results

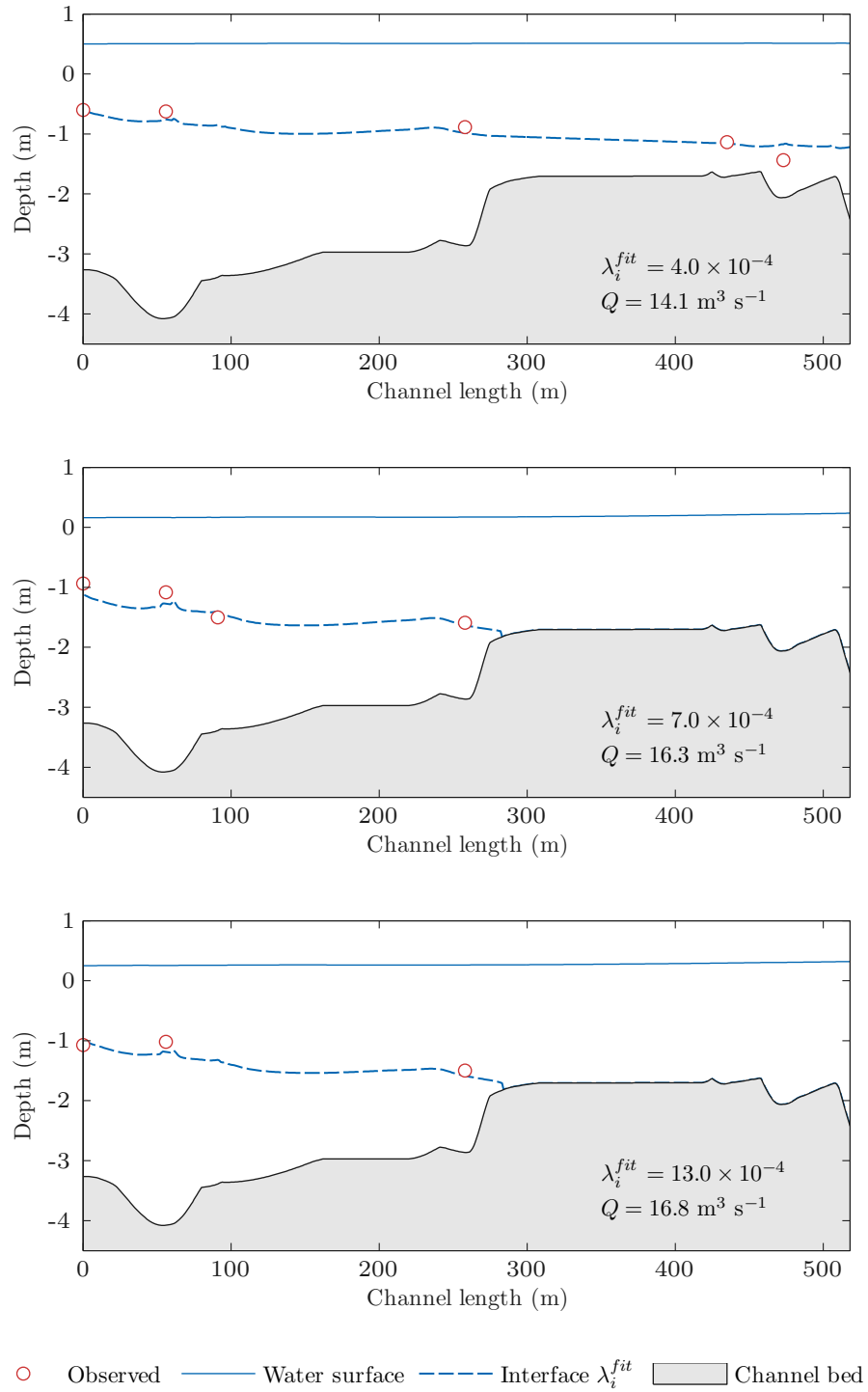


Figure A.6: Numerical FDM solutions of the salt-wedge shape compared against field observations, for different river flow rates Q and fitted interfacial friction factor λ_i^{fit} .

A. Additional numerical results

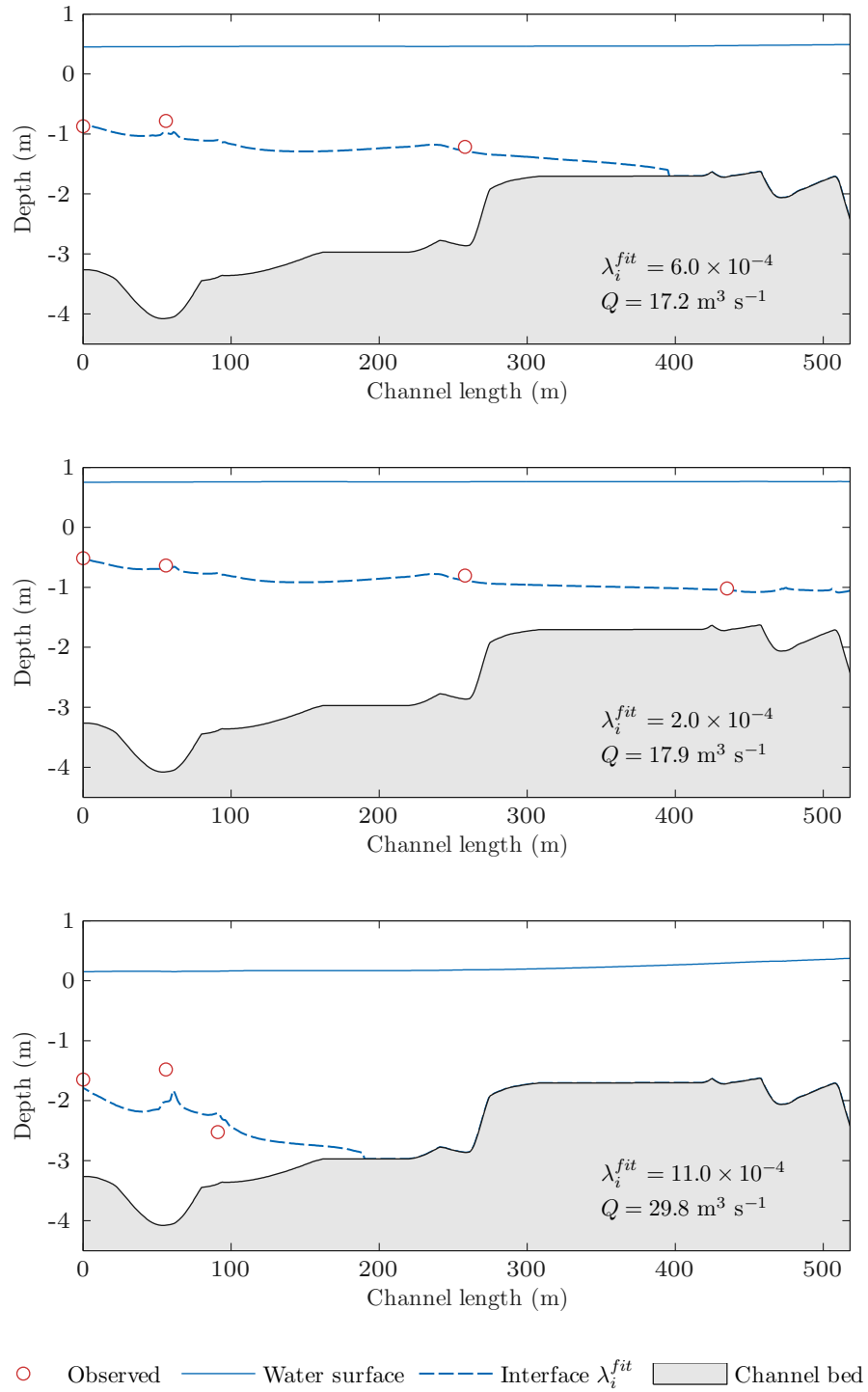


Figure A.7: Numerical FDM solutions of the salt-wedge shape compared against field observations, for different river flow rates Q and fitted interfacial friction factor λ_i^{fit} .

List of abbreviations and symbols

1D	One-dimensional.
2D	Two-dimensional.
3D	Three-dimensional.
ADCP	Acoustic Doppler Current Profiler.
ASL	Above sea-level.
C-property . . .	Conservation Property.
CC	Correlation Coefficient.
CFL	Courant-Friedrich-Lewy.
DTM	Digital Terrain Model.
FDM	Finite Difference Method.
FEM	Finite Element Method.
FVM	Finite Volume Method.
GPS	Global Positioning System.
HPP	Hydro-Power Plant.
K-H	Kelvin-Helmholtz.
MAE	Mean Absolute Error.
No	Number.
ODE	Ordinary Differential Equation.
PDE	Partial Differential Equation.
RHS	Right-Hand Side.
RMSE	Root Mean Square Error.
SS	Skill Score.
SWE	Shallow Water Equation.
WSS	Water Supply System.

List of abbreviations and symbols

Symbol	Dimensions	Description
A	L^2	Wetted cross-section area
\mathbf{B}	–	Two-layer coupling matrix
C	$L^{-3} M^{-1} T^3 I^2$	Electrical conductivity
E	–	Entrainment rate
E_*	–	Shear entrainment rate
F_0	–	River densimetric Froude number
Fr	–	Froude number
Fd	–	Densimetric Froude number
H	L	Total water depth
H_0	L	River depth
\mathbf{J}	–	Jacobian matrix of the flux
\mathbf{K}	–	Matrix of eigenvectors
K	–	Keulegan number
L	L	Length (of the salt-wedge)
M	–	Number of nodes in FDM or cells in FVM
N	T^{-1}	Brünt-Väisälä or buoyancy frequency
\mathbf{P}	–	Upwind projection matrix
P	L	Wetted cross-section perimeter
Q	$L^3 T^{-1}$	Flow rate
\mathcal{Q}	–	Jacobian matrix for coupled two-layer system
R^2	–	Coefficient of determination
R_h	L	Hydraulic radius
Re	–	Reynolds number
Ri	–	Bulk Richardson number
Ri_*	–	Shear Richardson number
Ri_{cr}	–	Critical Richardson number
Ri_g	–	Gradient Richardson number
S	–	Practical salinity
S_h	T^{-1}	Shear stress expressed as a spatial derivation of a vertical velocity profile
T	K	Temperature
X_{mod}		Computed (modelled) quantity
X_{obs}		Observed quantity
b	L	Channel bed elevation
\mathbf{f}	–	Flux vector
\mathbf{g}	–	Irregular geometry source term vector
g	$L T^{-2}$	Acceleration of gravity
h	L	Layer thickness
i	–	Spatial index
j	–	Layer index
n	–	Time index
n_M	$T L^{-1/3}$	Manning's roughness coefficient
p	$M L^{-1} T^{-2}$	Pressure
q	$L^2 T^{-1}$	Flow rate per unit width

List of abbreviations and symbols

r	–	Ratio of upper to lower layer density
\mathbf{s}	–	Friction and entrainment source term vectors
t	T	Time coordinate
\mathbf{v}	–	Cross-section width source term vector
u	L T ⁻¹	Velocity
u_*	L T ⁻¹	Shear velocity
\mathbf{w}	–	Vector of conserved variables
w_e	L T ⁻¹	Entrainment velocity
x	L	Horizontal axis coordinate
z	L	Vertical coordinate
Δx	L	Spatial step
Δt	T	Temporal step
δ_i	L	Interfacial layer thickness
δ_u	L	Shear layer thickness
ϵ	–	Correction parameter in the Harten regularization
ε	L	Tolerance parameter for the disappearance of the lower layer in a FVM
η	L	Free water-surface elevation
λ	–	Friction factor (equal to 1/8 of the Darcy-Weisbach friction factor)
λ_i	–	Interfacial friction factor
λ_b	–	Channel bed friction factor
λ_w	–	Channel bed/wal friction factor
ν	L ² T ⁻¹	Kinematic viscosity
ξ	L	Tolerance parameter for the transition from two-layer to a single layer flow in FDM
ρ	M L ⁻³	Volumetric mass density
$\boldsymbol{\sigma}$	L	Cross-section vector
σ	L	Cross-section width
τ	M L ⁻¹ T ⁻²	Shear stress
τ_T	M L ⁻¹ T ⁻²	Turbulent shear stress
τ_V	M L ⁻¹ T ⁻²	Viscous shear stress
τ_b	M L ⁻¹ T ⁻²	Bed shear stress
τ_i	M L ⁻¹ T ⁻²	Interfacial shear stress
τ_s	M L ⁻¹ T ⁻²	Surface shear stress
φ	–	Non-dimensional depth
χ	–	Non-dimensional length
$\boldsymbol{\Psi}$	–	Diagonal matrix with eigenvalues for Jacobian matrix
ψ	–	Eigenvalues for Jacobian matrix

List of Tables

6.1	Empirical coefficients a_i , b_i , and c_i for computing salinity from measured conductivity, temperature and pressure [33]	81
6.2	Empirical coefficients d_i , e_i , and k for computing salinity from measured conductivity, temperature and pressure [33]	81
6.3	Empirical coefficients a_i , b_i , and d_i for computing density of salt-water from measured salinity and temperature at atmospheric pressure [66]	81
6.4	Empirical coefficients a_i and b_i for computing dynamic viscosity μ from measured temperature at atmospheric pressure [47]	83
7.1	Observed values in the Rječina River estuary for different flow conditions. .	95
8.1	Fitted friction factors and computed mixing and flow parameters in the Rječina River estuary.	109

List of Figures

1.1	Types of estuaries depending on the intensity of vertical mixing: (a) highly stratified estuary, (b) partially mixed estuary, and (c) well-mixed estuary, as described in [30] and [85].	3
2.1	Longitudinal scheme of a two-layer salt-wedge flow, as defined by Schijf and Schönfeld [86].	10
2.2	Arita and Jirka's [2] friction law; interfacial friction factor λ_i dependence on $ReFd^2$	16
2.3	Cenedese and Adduce's [24] entrainment law; entrainment rate E dependence on densimetric Froude number Fd	19
3.1	Longitudinal scheme of a two-layer salt-wedge flow including friction and entrainment in channels with irregular geometry.	22
3.2	Cross-section scheme of a two-layer salt-wedge flow including friction and entrainment in channels with irregular geometry.	22
3.3	Control volume of a two-layer flow in channels with irregular geometry. . .	24
4.1	Implicit trapezoidal method interpretation.	39
4.2	Graphical interpretation of a piecewise constant function $\mathbf{w}^n(x)$	43
4.3	Graphical interpretation of a three-point explicit finite volume method. . .	44
4.4	Longitudinal section of the channel corresponding to water at rest.	55
4.5	Longitudinal section of the channel corresponding to water at rest with wet-dry transition in the lower layer.	56
4.6	Wet-dry fronts: (a) bed elevation redefinition and reflective condition is needed, (b) and (c) no redefinition needed.	57
5.1	Prismatic channel geometry defined by (a) horizontal bed and (b) rectangular cross-sections of constant width.	61
5.2	Numerical solutions for the arrested salt-wedge obtained by a steady FDM and a time-dependant FVM model, and their agreement with the exact solution for (a) $Q = 1.6 \text{ m}^3 \text{ s}^{-1}$, (b) $Q = 2.1 \text{ m}^3 \text{ s}^{-1}$ and (c) $Q = 3.0 \text{ m}^3 \text{ s}^{-1}$	62
5.3	Non-prismatic channel geometry defined by (a) variable bed slope and (b) rectangular cross-sections of variable width.	63
5.4	Numerical solutions for the arrested salt-wedge obtained by a steady FDM and a time-dependant FVM model, for (a) $Q = 4 \text{ m}^3 \text{ s}^{-1}$, (b) $Q = 9 \text{ m}^3 \text{ s}^{-1}$ and (c) $Q = 18 \text{ m}^3 \text{ s}^{-1}$	64
5.5	C-property verification test for water at rest in an irregular channel: (a) bed elevation, (b) channel width, (c) and (d) initial conditions (water depth and flow rate), and (e) and (f) results after $t = 10 \text{ s}$ (water depths and flow rates).	66

5.6	Extended C-property verification test for water at rest in an irregular channel with lower layer wet-dry transitions: (a) and (b) initial conditions (water depths and flow rates), (c) and (d) results at $t = 1$ s when the original source terms are considered and spurious oscillations appear, and (e) and (f) results at $t = 10$ s when the source term approximation is applied.	68
5.7	Sensitivity of the numerical model on the interfacial friction factor λ_i , for $Q = 2.0 \text{ m}^3 \text{ s}^{-1}$ and $r = 0.975$, without bed friction or entrainment.	70
5.8	Sensitivity of the numerical model on the Manning's roughness coefficient n_M , for $Q = 2.0 \text{ m}^3 \text{ s}^{-1}$, $\lambda_i = 10^{-3}$ and $r = 0.975$, without entrainment.	71
5.9	Sensitivity of the numerical model on the entrainment velocity w_e (m s^{-1}), for $Q = 2.0 \text{ m}^3 \text{ s}^{-1}$, $\lambda_i = 10^{-3}$ and $r = 0.975$, without bed friction.	71
5.10	The resulting upper and lower layer flow rates for different entrainment velocities w_e (m s^{-1}), for $Q = 2.0 \text{ m}^3 \text{ s}^{-1}$, $\lambda_i = 10^{-3}$ and $r = 0.975$, without bed friction.	71
5.11	Sensitivity of the numerical model on the density ratio r , for $Q = 2.0 \text{ m}^3 \text{ s}^{-1}$, $\lambda_i = 10^{-3}$, without bed friction or entrainment.	72
6.1	Map of the Rječina River estuary with sampling points and inflow locations	76
6.2	Inter-annual variations of the minimum, mean and maximum monthly flow rates at Tvornica gauging station (1999-2015)	76
6.3	Daily minimum and maximum sea-level amplitudes at Bakar tidal gauging station in 2015 (according to [45]).	78
6.4	Digital orthophoto of the Rječina River estuary with sampling points.	79
6.5	Practical salinity S dependence on conductivity C (mS cm^{-1}) and temperature T ($^{\circ}\text{C}$) at 1 m depth, computed from [33].	82
6.6	Density ρ (kg m^{-3}) dependence on practical salinity S and temperature T ($^{\circ}\text{C}$), computed from [66].	82
6.7	Salinity profiles for flow rate $Q = 17.2 \text{ m}^3 \text{ s}^{-1}$: (a) observed salinity S profile, (b) linearized salinity profile, (c) interface thickness and depth, and (d) approximated constant salinity S in the upper and lower layer.	84
6.8	Rating curve at Tvornica gauging station obtained from field measurements (2013-2015).	85
6.9	ADCP instrument used to measure flow rates and velocities in Rječina River estuary: (a) Teledyn StreamPro and (b) Nortek Aquadopp.	85
6.10	Scheme of a two-layer box model for estimating the vertical mixing in salt-wedge estuaries.	87
6.11	Depth measurements (red dots) in the lower reaches of Rječina River.	88
6.12	Longitudinal section of the Rječina River estuary with bed elevations and locations of sampling points.	88
6.13	The characteristic channel cross-sections in the Rječina River estuary: (a) near the mouth (0+250 m), (b) in the middle reaches (0+325 m), and (c) in the upper reaches (0+650 m).	88
6.14	Step-by-step illustration of interpolation method for deriving DTM for a segment of the Rječina River estuary (from 0+440 m to 0+550 m): (a) measured cross sections, (b) interpolated profile lines, (c) interpolated cross sections along the centreline, and (d) digital terrain model.	90

6.15	Tabulated array of cross-section geometrical values for: (a) wetted area A , (b) channel width σ , and (c) wetted perimeter P	92
7.1	Salinity S (solid) and temperature T (dashed) profiles observed in the Rječina River estuary near the mouth (P3) for different river flow rates Q	96
7.2	Numerical FDM solutions of the salt-wedge shape compared against field observations, for different river flow rates Q . Both λ_i^{fit} (fitted interfacial friction factor) and λ_i^{AJ} (computed from the Arita and Jirka model, Eq. (2.9)) were considered.	98
7.3	Numerical FVM solutions of the arrested salt-wedge shape compared against field observations, for different river inflow rates Q	100
7.4	Velocity u (solid) and salinity S (dashed) profiles observed in the Rječina River estuary near the mouth (P3): (a) to (c) salt-wedge intrusion caused by a decrease in the river flow rate from 10 to 4.6 m ³ s ⁻¹ , and (d) to (f) salt-wedge receding towards the mouth caused by an increase in the river flow rate from 4.2 to 13.4 m ³ s ⁻¹	102
7.5	Boundary conditions for a time-dependant salt-wedge case: (a) upstream flow rate and (b) downstream sea-level.	104
7.6	Numerical FVM solutions of the time-dependant salt-wedge profile compared against field observations, at different time steps, for variable river flow rate Q	105
7.7	Computed and observed changes of flow rates per unit width in the upper (q_1) and lower (q_2) layer, near the mouth (P3, Fig. 6.1).	106
8.1	Dependence of the: (a) upper layer thickness h_1 , (b) velocity difference Δu , (c) densimetric upper layer Froude number Fd , (d) squared buoyancy frequency N^2 , (e) entrainment velocity w_e , and (f) interfacial shear velocity u_* , on the river flow rate Q	110
8.2	Dependence of entrainment rate E on (a) bulk Richardson number Ri (with comparison to equations by Buch [13], Christodoulou [26], Moore and Long [69], Narimousa and Fernando [71], Pedersen [74], and Walker and Hamill [103]) and (b) densimetric Froude number Fd (with comparison to Cenedese and Adduce [24]).	112
8.3	Dependence of entrainment rates E on: (a) squared buoyancy frequency N^2 , (b) interfacial shear velocity u_* , (c) non-dimensional ratio of stratification to shear $N^2/(u_*^2/\nu)^2$, and (d) a combination of bulk Richardson number and average interfacial friction factor $Ri^{-2}\tilde{\lambda}^{5/2}$	113
8.4	Dependence of the interfacial friction factor λ_i on: (a) entrainment rate E , Keulegan number $ReFd^2$ with the Arita and Jirka model [2] (solid lines for different Fd), (c) Reynolds number Re and (d) best fit combination of parameters $ReRi^3$	115
8.5	Comparison of the computed and observed upper layer thickness h_1 at a control section assumed to be located at the last bridge near the mouth (P1, Fig. 6.1).	117
8.6	Observed density in the upper ρ_1 and lower ρ_2 layer and maximum squared buoyancy frequency N^2 , averaged along the salt-wedge, during a simulation of a time-dependant flow observed on 1 July 2015.	119

8.7	Computed movement of the salt-wedge front and corresponding propagation rates during the variable flow observed on 1 July 2015.	120
A.1	Numerical FDM solutions of the salt-wedge shape compared against field observations, for different river flow rates Q and fitted interfacial friction factor λ_i^{fit}	138
A.2	Numerical FDM solutions of the salt-wedge shape compared against field observations, for different river flow rates Q and fitted interfacial friction factor λ_i^{fit}	139
A.3	Numerical FDM solutions of the salt-wedge shape compared against field observations, for different river flow rates Q and fitted interfacial friction factor λ_i^{fit}	140
A.4	Numerical FDM solutions of the salt-wedge shape compared against field observations, for different river flow rates Q and fitted interfacial friction factor λ_i^{fit}	141
A.5	Numerical FDM solutions of the salt-wedge shape compared against field observations, for different river flow rates Q and fitted interfacial friction factor λ_i^{fit}	142
A.6	Numerical FDM solutions of the salt-wedge shape compared against field observations, for different river flow rates Q and fitted interfacial friction factor λ_i^{fit}	143
A.7	Numerical FDM solutions of the salt-wedge shape compared against field observations, for different river flow rates Q and fitted interfacial friction factor λ_i^{fit}	144

Curriculum vitae

Nino Krvavica

Born on 25 December 1982 in Rijeka, Croatia. Attended Andrija Mohorovičić high school in Rijeka from 1997 to 2001. Graduated from the University of Rijeka in 2007 and received a master's degree from the Faculty of Civil Engineering. The master thesis titled *Reinforced Concrete Jetty in the Volosko Port*, supervised by Prof. Nenad Ravlić, was nominated for the Croatian Waters Award for the best master's thesis in Civil engineering.

After graduation, joined the Institute IGH to work on design documentation for construction of coastal structures, water supply and sewage systems, and gain experience in numerical modelling studies. Time spent there resulted in co-authoring first two papers presented at international conferences in Hong Kong, China in 2008 and in Athens, Greece in 2010.

In 2009 entered the postgraduate doctoral study programme in Civil Engineering at the University of Rijeka. The same year started working part time as a teaching assistant in the Urban engineering programme course at the Faculty of Civil Engineering. After leaving the position at the Institute IGH, in 2011 joined the Faculty of Civil Engineering at the University of Rijeka as a full-time research assistant on the scientific project *Hydrology of Sensitive Water Resources in Karst*, financed by the Ministry of Science, Education and Sports of the Republic of Croatia, under the supervision of Prof. Nevenka Ožanić, and continued working as a teaching assistant on several courses in the Hydraulic and Urban engineering programme.

During this time also participated in the bilateral Japanese-Croatian scientific project *Risk Identification and Land-Use Planning for Disaster Mitigation of Landslides and Floods in Croatia* (project manager Prof. Nevenka Ožanić) and international project *Networking for Drinking Water Supply in Adriatic Region - DRINKADRIA* (project manager Prof. Barbara Karleuša). In 2013 spent two months at the University of Kyoto, Japan under the supervision of Prof. Yosuke Yamashiki, researching flood predictions by meteorological radars and physical modelling of debris flow. In June 2016 visited the Hydraulic laboratory of the Faculty of Civil Engineering at the University of Zagreb, Croatia, and collaborated with Prof. Dalibor Carević on the scientific project *Ekomarina*.

List of publications

- [1] GAJIĆ-ČAPKA, M., OŽANIĆ, N., AND KRVAVICA, N. Estimation of maximum short-term precipitation over the Rijeka region. *EGFOS* 5, 9 (2014), 49–59.
- [2] KARLEUŠA, B., OŽANIĆ, N., RUBINIĆ, J., RADMAN, I., DRAGIČEVIĆ, N., VOLF, G., SUŠANJ, I., KRVAVICA, N., RUŽIĆ, I., AND CRNKO, T. Analysing the Possibilities of Drinking Water Supply Improvement in Adriatic Region Through the DRINK ADRIA Project. *Zbornik radova Građevinskog fakulteta Sveučilišta u Rijeci* 17 (2014), 55–67.
- [3] KARLEUŠA, B., RUBINIĆ, J., RADMAN, I., VOLF, G., AND KRVAVICA, N. Cross-Border Water Resources Management in Present Conditions and for Future Scenarios. In *International Symposium Cross-border drinking water management* (Rijeka, Croatia, 2016), B. Karleuša and I. Sušanj, Eds., Faculty of Civil Engineering, University of Rijeka, pp. 59–90.
- [4] KRVAVICA, N., AND ILIĆ, S. Scour around foundations for offshore wind turbines. *Zbornik radova Građevinskog fakulteta Sveučilišta u Rijeci* 15 (2012), 37–57. (In Croatian).
- [5] KRVAVICA, N., KOŽAR, I., TRAVAŠ, V., AND OŽANIĆ, N. Numerical modelling of two-layer shallow water flow in microtidal salt-wedge estuaries: Finite volume solver and field validation. *Journal of Hydrology and Hydromechanics* 65, 1 (2017), 1–11. (In Press).
- [6] KRVAVICA, N., MOFARDIN, B., RUŽIĆ, I., AND OŽANIĆ, N. Measurement and analysis of salinization at the Rječina estuary. *Građevinar* 64, 11 (2012), 923–933.
- [7] KRVAVICA, N., AND MUJAKOVIĆ, N. Solving the problem of water wave motions due to disturbance originating at the surface. *Zbornik radova Građevinskog fakulteta Sveučilišta u Rijeci* 14 (2011), 11–29. (In Croatian).
- [8] KRVAVICA, N., AND RAVLIĆ, N. Non-conservative approach to design of jetties in exposed locations. *Zbornik radova Građevinskog fakulteta Sveučilišta u Rijeci* 12 (2009), 35–54. (In Croatian).
- [9] KRVAVICA, N., RUŽIĆ, I., AND OŽANIĆ, N. Analysis of rainfall intensity assessment using the X-band radar. *Hrvatske vode* 24 (2016), 137–146. (In Croatian).

- [10] KRVAVICA, N., RUŽIĆ, I., OŽANIĆ, N., YAMASHIKI, Y., KARABAIĆ, I., MOFARDIN, B., AND ŠKODA, M. Daily variability of salinity and temperature in the Rječina Estuary. In *2nd Project Workshop on Risk Identification and Land-Use Planning for Disaster Mitigation of Landslides and Floods* (Rijeka, Croatia, 2011), N. Ožanić and Ž. Arbanas, Eds., University of Rijeka, pp. 109–112.
- [11] KRVAVICA, N., AND TRAVAŠ, V. A comparison of method of characteristics and Preissmann scheme for flood propagation modeling with 1D Saint-Venant equations. *Acta Hydrotechnica* 27, 46 (2015), 1–12.
- [12] KRVAVICA, N., TRAVAŠ, V., AND OŽANIĆ, N. Three-layer numerical model for stationary flow in a stratified estuary. In *Zbornik radova šestog susreta Hrvatskog društva za mehaniku* (Rijeka, Croatia, 2014), G. Jelenić and M. Gaćeša, Eds., Croatian Society of Mechanics. (In Croatian).
- [13] KRVAVICA, N., TRAVAŠ, V., AND OŽANIĆ, N. A field study of interfacial friction and entrainment in a microtidal salt-wedge estuary. *Environmental Fluid Mechanics* (2016). (In Press).
- [14] KRVAVICA, N., TRAVAŠ, V., AND OŽANIĆ, N. Salt-wedge response to variable river flow and sea-level rise in the microtidal Rječina River Estuary, Croatia. *Journal of Coastal Research* (2016). (In Press).
- [15] KRVAVICA, N., TRAVAŠ, V., RAVLIĆ, N., AND OŽANIĆ, N. Hydraulics of Stratified Two-layer Flow in Rječina Estuary. In *Landslide and Flood Hazard Assessment* (Zagreb, Croatia, 2013), S. Mihalić Arbanas and Ž. Arbanas, Eds., Faculty of Mining, Geology and Petroleum Engineering, University of Zagreb and Faculty of Civil Engineering, University of Rijeka, pp. 257–261.
- [16] OŽANIĆ, N., KARLEUŠA, B., DRAGIČEVIĆ, N., SUŠANJ, I., ŽIC, E., RUŽIĆ, I., AND KRVAVICA, N. Disaster Mitigation of Floods and Landslides in Croatia through Croatian-Japanese Collaboration. In *Dani gospodarenja vodama 2013: Napredak kroz znanost* (Zagreb, Croatia, 2013), D. Bekić, Ed., Faculty of Civil Engineering, University of Zagreb, pp. 63–93.
- [17] OŽANIĆ, N., ŽIC, E., SUŠANJ, I., TRAVAŠ, V., RUŽIĆ, I., DRAGIČEVIĆ, N., AND KRVAVICA, N. Scientific equipment and research possibilities at the Faculty of Civil Engineering of the University of Rijeka. In *6th Croatian Water Conference with International participation - CROATIAN WATERS ON THE INVESTMENT WAVES* (Opatija, Croatia, 2015), D. Biondić, D. Holjević, and M. Vizner, Eds., Croatian Waters, pp. 1425–1443.
- [18] PEŠA, M., FUIS, I., BABIĆ, S., AND KRVAVICA, N. Road junction "Škurinje" - application of digital photogrammetry in watershed area modeling. *Zbornik radova Građevinskog fakulteta Sveučilišta u Rijeci* 15 (2012), 125–138. (In Croatian).

- [19] RAVLIĆ, N., AND KRVAVICA, N. Hydraulic implications of non-standard solutions in spatially constrained wastewater facilities. In *Environmental Hydraulics, Two Volume Set: Proceedings of the 6th International Symposium on Environmental Hydraulics (ISEH)* (Athens, Greece, 2010), G. Christodoulou and I. Anastasios, Eds., CRC Press, pp. 1035–1040.
- [20] RAVLIĆ, N., KRVAVICA, N., AND MIČETIĆ, I. Modeling of internal hydraulics of water storage tanks with complex geometry. In *Proceedings of 2nd International Symposium on Shallow Flows* (Hong Kong, China, 2008), M. Ghidaoui and Y. Tung, Eds., The Hong Kong University of Science and Technology, pp. 135–139.
- [21] TRAVAŠ, V., AND KRVAVICA, N. Spectral and Monochromatic Approach to the Definition of Hydrodynamic Load on Vertical Piles. *Hrvatske vode* 22, 87 (2014), 13–22. (In Croatian).
- [22] TRAVAŠ, V., KRVAVICA, N., AND RADMAN, I. Numerical analysis of hysteresis in rating curves for open channel flow. *International Journal for Engineering Modelling* 25, 1 (2012), 1–6.
- [23] TRAVAŠ, V., KRVAVICA, N., AND RUBEŠA, J. Modelling of the morphology of open river beds for the implementation of a one-dimensional flow analysis. *Hrvatske vode* 23, 92 (2015), 123–132. (In Croatian).